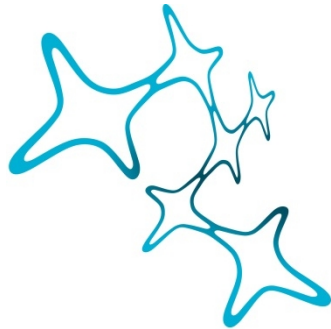


THE EFFECT OF FEEDBACK ON SENSORY PROCESSING IN
THE MOUSE EARLY VISUAL SYSTEM

Gregory Born



Graduate School of
Systemic Neurosciences

LMU Munich



Dissertation der
Graduate School of Systemic Neurosciences
der Ludwig-Maximilians-Universität München

December, 2021

Supervisor

Prof. Dr. Laura Busse

Department of Biology II

Ludwig-Maximilians-Universität München

First Reviewer: Prof. Dr. Laura Busse

Second Reviewer: Prof. Dr. Tobias Rose

Date of Submission: 08.12.2021

Date of Defense: 20.06.2022

Abstract

A central goal of neuroscience is to understand how the brain creates a percept from environmental stimuli. According to the classic view, sensory processing evolves along a feedforward hierarchy where simple representations on lower stages are combined to form increasingly more complex representations on higher stages. Despite explaining many aspects of sensory processing, the model does not consider feedback signals. Feedback signals are provided by neurons that are located on a higher processing stage and whose axons innervate lower processing stages. Although being an abundant motive throughout the brain, the role of feedback for sensory processing remains elusive.

To shed light on this question, we performed electrophysiological recordings in the early visual system of mice. Over the past decade, the mouse has become an important model organism for systems neuroscience, mainly owing to the availability of a large set of genetic tools and its preserved mammalian brain architecture. This includes the thalamo-cortico-thalamic loop, a circuit that is particularly well suited to investigate feedback.

In the two studies presented in the first part of this thesis, we probed response properties of neurons in the mouse dorsolateral geniculate nucleus (dLGN) when corticothalamic (CT) feedback is intact and under conditions in which it is suppressed. Comparing the two conditions, we investigated how CT feedback affects in neurons of mouse dLGN spatial integration (**Born*, Schneider*, Erisken*, et al., Nature Neuroscience, 2021**) and responses to naturalistic stimuli (**Spacek et al., 2021, bioRxiv**). Moreover, we asked to which extent CT feedback mediates behavioral state-dependent processing in dLGN (**Spacek et al., 2021, bioRxiv**).

The second part of the thesis focuses on the origin of CT feedback to dLGN, the primary visual cortex (V1). First, by reviewing current literature, we outline the neural circuits in mouse V1 that underlie visual behavior. In particular, we discuss the extent to which mouse visual behavior relies on the thalamocortical pathway and how feedback modulates sensory processing in V1 (**Katzner et al., 2019, Current Opinion in Neurobiology**). Potentially a signature of top-down influences, we finally describe how evaluating visual cues modulates their representation in V1 (**Wal et al., 2021, Journal of Neuroscience**).

Contents

1	Introduction	1
1.1	Sensory processing	1
1.1.1	Feedforward streams	1
1.1.2	Contextual modulations	2
1.2	The corticothalamic circuit as a model circuit for studying feedback	5
1.2.1	Anatomy	5
1.2.2	Generality	5
1.2.3	Diversity of effects	6
1.3	Layer 6 corticothalamic neurons	7
1.3.1	Direct excitatory connections to relay cells	7
1.3.2	Indirect inhibitory connections to relay cells	7
1.4	Manipulating corticothalamic feedback	8
1.4.1	Traditional approaches	8
1.4.2	Optogenetic methods	9
1.5	Topographic organization of corticothalamic feedback	11
1.6	Effects of cortical feedback on spatial processing in thalamus	12
1.7	Effects of cortical feedback on processing of naturalistic stimuli in thalamus	14
1.8	Differential contributions of corticothalamic feedback and neuromodulation to thalamic processing	15
1.9	Top-down influences on sensory processing in primary visual cortex	16
1.10	Conclusion	17
2	Corticothalamic feedback sculpts visual spatial integration in mouse thalamus	19
3	Robust effects of corticothalamic feedback during naturalistic visual stimulation	55
4	Evaluating visual cues modulates their representation in mouse visual and cingulate cortex	115
5	V1 microcircuits underlying mouse visual behavior	130

6	Discussion	139
6.1	The role of feedback	139
6.1.1	Firing mode	139
6.1.2	Gain control	140
6.1.3	Contextual modulation in mouse V1	141
6.1.4	Predictive coding	142
6.1.5	State-dependent modulations in dLGN	143
6.2	Diversity of L6 CT feedback	145
6.2.1	Anatomical diversity	145
6.2.2	Functional diversity	145
6.3	Manipulating CT feedback	146
6.4	Conclusions and Outlook	147
7	Bibliography	149
8	Supplements	173
8.1	Acknowledgements	173
8.2	List of Publications	174
8.3	Affidavit	175
8.4	Author Contributions	176

1 Introduction

1.1 Sensory processing

Be it the precise kick of a soccer ball or the careful steering of a bike through a crowded street – a main function of the brain is to respond with the appropriate action to stimuli in our environment. To screen both our proximal and our more distal environment the human nervous system comprises six senses: balance, taste, hearing, smell, sight, and touch. The sense of touch contributes to perceiving the surround that is limited to the range of our extremities, while the Andromeda Nebula, a galaxy 2.5 million light-years away from earth, can still be sensed with our naked eye (Wikipedia contributors, 2021).

Each of these senses is implemented by a complex system of nerve cells, neurons, which communicate along a hierarchy (Harris et al., 2019; Felleman and Van Essen, 1991). At the lower end of this hierarchy, ambient stimuli are transformed into electrical signals by sensory receptor cells. In the case of the visual system, photoreceptors in the retina contain light-sensitive proteins, which upon absorption of photons undergo a conformational change. The change in conformation triggers a cascade of effects, which eventually hyperpolarizes the cell and stops the release of the neurotransmitter glutamate (Arshavsky et al., 2002; Fu, 2010).

1.1.1 Feedforward streams

Sensory information travels to downstream targets via different feedforward routes. Feedforward routes are defined by neurons whose axon collaterals leave their original area to establish connections with neurons on a higher processing stage and are contrasted by feedback pathways that send signals into the opposite direction. Amongst the most important feedforward routes is the thalamocortical pathway where signals from the periphery are passed to primary sensory areas in cortex via the thalamus, the so-called gate to cortex (Winer et al., 2005; Sherman and Guillery, 1996). In fact, relay cells in the dorsolateral geniculate nucleus of the thalamus (dLGN) that receive driving signals from retinal ganglion cells, the output units of the retina, provide strong excitation to neurons in layer 4 of primary visual cortex (Felleman and Van Essen, 1991). Along this retino-thalamo-cortical pathway information is carried in segregated channels. In the macaque thalamocortical pathway, for instance, the koniocellular, magnocellular, and parvocellular pathways display different sensitivity to color, contrast, spa-

tial, and temporal features (Livingstone and Hubel, 1988; Nassi and Callaway, 2009).

This strict feedforward hierarchy observed on the anatomical level has long been the working hypothesis for how stimuli are being processed by the brain, also because this hierarchy can be found on the functional level (Lennie, 1998; Herzog and Clarke, 2014) (**Fig. 1**). In the early visual system, single neurons encode a small region in space and respond best to simple visual features, whereas neurons further up the hierarchy have large receptive fields (RF), and respond best to complex stimuli (Wang and Burkhalter, 2007; Siegle et al., 2021). The classical RF of neurons in primate V1, for instance, encodes a region of about 1 deg visual angle and responds best to simple edges (Cavanaugh et al., 2002; Van den Bergh et al., 2010; Martin and Solomon, 2011). At the other end of the hierarchy, the human inferior temporal cortex accommodates the fusiform face area (FFA), a region that selectively engages in the perception of faces (Kanwisher et al., 1997; Tong et al., 2000). Representations in the FFA are invariant to simple transformations of the input, such as the position or the size of the face (Andrews and Ewbank, 2004; Kanwisher and Yovel, 2006).

1.1.2 Contextual modulations

Although feedforward inputs in the visual system determine classical RFs and tuning properties (Lamme and Roelfsema, 2000), and are sufficient for many cognitive processes, such as the fast categorization of visual inputs (Agam et al., 2010; Resulaj et al., 2018; Serre et al., 2007), responses are also affected by contextual modulations. Contextual modulations comprise a myriad of influences, such as those due to attentional processes, perceptual context, expectations, and the animal's behavioral state (e.g. drowsiness vs. alertness), which are associated with distinct processing regimes. Relay cells in the dLGN, for instance, are more likely to display a linear input-output relationship, the tonic-firing mode, when the animal is in an alert state opposed to when it is in a drowsy state (Sherman, 2001; Busse, 2018). Here, responses become more all-or-none-like, a pattern termed the burst-firing mode (Sherman, 2001; Erisken et al., 2014). More specific contextual modulations, on the other hand, include the expectancy of a reward or attentional processes. A signature of spatial attention in the visual system are increased responses of neurons, whose RF location coincides with the location of an attended stimulus, and attenuated responses of neurons, whose RFs lies outside the attended location (Treue and Maunsell, 1996; Desimone and Duncan,

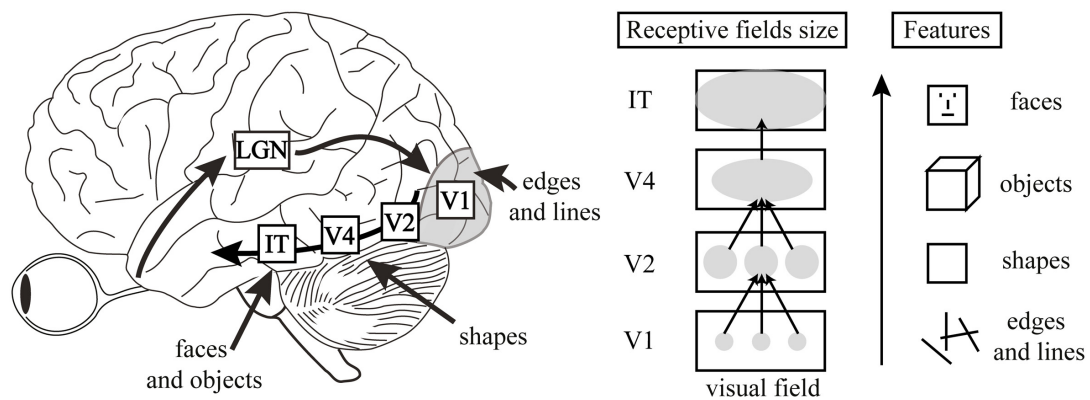


Fig. 1 Feedforward processing in the visual system.

Left: schematic of the ventral feedforward pathway of the visual system. Ganglion cells in the retina send signals to the dLGN, the first-order visual nucleus of the thalamus. Thalamocortical neurons, in turn, relay the information to the primary visual cortex from where it is distributed to higher cortical areas, including areas V2, V4, and the inferior temporal cortex (IT). *Middle:* Neurons at lower processing stages have smaller RFs. RFs of neurons at higher processing stages are larger since they receive converging inputs from several neurons at the lower processing stage. *Right:* Neurons at higher processing stages encode more complex features, while neurons at lower processing stages respond best to simple features; e.g., neurons in V1 are tuned to edges and lines whereas neurons in IT can be tuned to specific faces. The figure is reused from Herzog and Clarke (2014) which is published under the terms of the Creative Commons Attribution License (CC BY).

1995; Moran and Desimone, 1985).

Attentional modulations have a strong impact on perception and behavior. The influence on behavior can be readily observed in simple reaction time paradigms like the Posner task. In the Posner task participants, while fixating their gaze, react more quickly to a target, if the target is presented at a location which has previously been cued. This effect has been found in humans, non-human primates, and mice, and is attributed to covert attention (Wang and Krauzlis, 2018; Posner, 1980; Bowman et al., 1993).

Besides such higher cognitive modulations, neural responses to local stimuli are also affected by the perceptual context of the stimulus scenery. A powerful illustration of this modulation are visual illusions, where the size of a center circle appears to be larger if surrounded by smaller circles than if surrounded by larger circles.

Contextual modulation of neural responses to stimuli cannot be explained by a strict

feedforward hierarchy but needs to rely on different mechanisms. A factor that is at least in part responsible for mediating contextual modulations are neuromodulators like serotonin (Ferguson and Cardin, 2020; Jacob and Nienborg, 2018). Serotonin can be released in a context-dependent manner (De Souza and Van Loon, 1986; Hall et al., 2012; Hanson and Hurley, 2014) and decreases neural responses to sensory stimuli (Jacob and Nienborg, 2018). More closely linked to changes in arousal and attentive states are acetylcholine and norepinephrine (Busse, 2018; Metherate et al., 1992). The most important source of norepinephrine in the brain is the locus coeruleus (LC). Axons from neurons in LC might be partially responsible for depolarizing during locomotion the membrane potentials of neurons in mouse V1 (Polack et al., 2013), leading to higher visually evoked firing rates when the animal is running (Polack et al., 2013; Niell and Stryker, 2010; Keller et al., 2012). Locomotion-associated effects in mouse V1 can also be triggered by stimulating the basal forebrain (Pinto et al., 2013), the main source of cholinergic projections to cortex (Thiele, 2013). In particular, activating cholinergic neurons in the mouse basal forebrain increases visual responses and decorrelates activity of V1 neurons. These changes on the neural level are accompanied by improved behavioral performance in a visual discrimination task (Pinto et al., 2013).

A second mechanism, by which contextual modulations can arise, are feedback and lateral projections (Gilbert and Li, 2013). Indeed, in primate V1, where lateral connections occur predominantly among neurons sharing similar RF properties (Bosking et al., 1997; Malach et al., 1993), they have been associated with contour integration and visual saliency (Stettler et al., 2002; Kapadia et al., 1995). Although lateral connections allow for modulations by stimuli extending beyond the target neuron's classical RF (Gilbert et al., 1996), explaining extraclassical RF modulation in the far surround requires feedback connections (Angelucci and Bressloff, 2006). Feedback projections, on the other hand, are established by neurons that reside in higher processing stages and whose axon collaterals synapse onto neurons on lower processing stages. In the visual system, it has been found that stimulating neurons on higher processing stages either electrically or with optogenetics can induce firing rates in neurons on lower processing stages and trigger behavioral changes that are similar to those associated with attention (Zhang et al., 2014; Moore and Armstrong, 2003).

1.2 The corticothalamic circuit as a model circuit for studying feedback

1.2.1 Anatomy

To study the effects of feedback on sensory processing, an ideal model circuit is corticothalamic (CT) feedback. A main advantage of the CT feedback circuit is its distinct anatomical properties. First, cortical feedback to the first order thalamic nuclei arises solely from neurons contained in layer 6 (L6) of the primary sensory cortices (Sherman and Guillery, 2002). In mice, L6CT neurons express the neurotensin receptor 1 (Ntsr1), which together with the corresponding Cre-lox system allows to specifically manipulate CT feedback (Gong et al., 2007; Bortone et al., 2014; Kim et al., 2014). Second, the source of CT feedback, the primary sensory cortices, and the target, the corresponding thalamic nuclei, are clearly separated. This separation helps to manipulate feedback connections with genetic techniques but also allows to use less specific methods such as cortical cooling, ablation, pharmacological inactivation and transcranial magnetic stimulation (McClurkin and Marrocco, 1984; de Labra et al., 2007; Webb et al., 2002; Wörgötter et al., 1998). Moreover, because of the comparatively long distance between cortex and thalamus and the properties of CT synapses, CT signals arrive at the thalamus with a time delay. Even though these time delays are in the order of milliseconds, they are, especially in model organisms with larger brains, long enough to study the time course of feedback effects (Andolina et al., 2007; Guo et al., 2017).

1.2.2 Generality

The principle organization of CT feedback is conserved across different sensory modalities and species, which offers a high degree of generalization (Alitto and Usrey, 2003). First, in primates, carnivores, and rodents, synapses of L6CT neurons onto thalamic relay cells do not provide a strong driving input but rather exert modulatory influences (Sherman and Guillery, 1998; Sherman, 2007). In line with being modulatory, the small corticogeniculate synapses contact dLGN relay cells at more distal parts of the dendrite compared to axons of retinal ganglion cells and have a lower probability of releasing glutamate (Bickford, 2016; Sherman and Guillery, 1998). A second feature of the corticogeniculate pathway, which is shared among various mammalian species, are segregated processing streams. In primates and carnivores three different types of corticogeniculate cells with distinct morphological and physiological features have been

identified, which can be linked to the parvocellular, magnocellular, and koniocellular or the homologous X, Y, and W streams, respectively (Briggs and Usrey, 2009; Hasse and Briggs, 2017b). Although in rodents, parallel CT feedback pathways have been demonstrated in the somatosensory system (Urbain and Deschenes, 2007; Bokor et al., 2008), functional clustering seems less pronounced along the mouse retino-geniculo-cortical feedforward pathway (Román Rosón et al., 2019; Denman and Contreras, 2016), and might therefore also be less prominent in corticogeniculate feedback projections.

1.2.3 Diversity of effects

Despite being a confined circuit, CT projections allow to study a large repertoire of complex feedback effects. This complexity arises from the fact that CT feedback comprises both a direct excitatory pathway as well as an indirect inhibitory pathway, whose net effect on dLGN relay cells depend on several factors, including stimulus properties and the behavioral state of the animal (Spacek et al., 2021; Sillito and Jones, 2002). Thus, it is not surprising that studying CT feedback has revealed a multitude of top-down mediated effects in thalamic relay cells with respect to both their temporal and spatial RF properties (Jones et al., 2012; Andolina et al., 2013; Alitto and Usrey, 2003; Hasse and Briggs, 2017b), as well as their firing mode (McCormick and von Krosigk, 1992; Godwin et al., 1996).

Finally, although effects of task-mediated attention are more pronounced in higher cortical areas, attentional modulations have also been reported on the level of the thalamus (O'Connor et al., 2002; McAlonan, 2006; Schneider and Kastner, 2009). Magnocellular and parvocellular neurons in primate dLGN, for instance, elicit weaker responses if a stimulus in the neuron's RF is unattended compared to when it is attended (McAlonan et al., 2008). Studying effects of attention on lower levels, like the thalamus, might benefit from the fact that thalamic cells exhibit rather simple response properties that are well studied. This allows to match stimulus properties to the preferences of the recorded neurons. It has been shown that if stimuli engage the recorded neurons optimally, attentional effects are stronger (Gilbert and Sigman, 2007; Hembrook-Short et al., 2017; Martinez-Trujillo and Treue, 2004). The corticothalamic circuit is hence ideally suited to understand how feedback contributes to contextual modulations.

1.3 Layer 6 corticothalamic neurons

1.3.1 Direct excitatory connections to relay cells

Direct input from L6 to thalamic relay cells is excitatory and mediated via glutamatergic synapses (McCormick and von Krosigk, 1992; Sherman, 2001). Although cortical excitatory synapses are usually depressing, connections established by L6CT neurons onto relay cells are facilitatory (Frandolig et al., 2019; Deschenes and Hu, 1990; Jackman et al., 2016). Since the facilitatory effect is weaker in synapses formed by L6CT neurons onto inhibitory neurons in the TRN and because connections established by TRN neurons onto thalamic relay cells are depressing, the net effect of CT feedback is frequency-dependent (Crandall et al., 2015; Kirchgessner et al., 2020). In *in-vitro* recordings of the mouse somatosensory system, it has been shown that low-frequency stimulation of L6CT neurons results in inhibitory feedback effects, whereas high-frequency stimulation leads to net excitation (Crandall et al., 2015). Despite its modulatory nature, the excitatory component of CT feedback can have a strong impact on thalamic sensory processing, e.g. by promoting in relay cells tonic firing mode or boosting responses to small stimuli presented in the center of the relay cell's RF (Sherman, 2001; Webb et al., 2002; Przybylski et al., 2000).

1.3.2 Indirect inhibitory connections to relay cells

Since L6CT neurons are excitatory they can inhibit thalamic relay cells only indirectly, by recruiting inhibitory cells in the thalamic reticular nucleus (TRN) or thalamic interneurons. In the primary sensory nuclei of the rodent thalamus, inhibitory interneurons are low in number or completely absent (Evangelio et al., 2018; Barbaresi et al., 1986). Where present, they however play a dominating role in building local, intrinsic networks (Hirsch et al., 2015). A recent electronmicroscopy study (Morgan and Lichtman, 2020) showed that a single inhibitory interneuron in mouse dLGN spans different functional regions within the visual thalamus, participates in different forms of inhibition, and establishes hundreds of synaptic connections, which together with their ability to participate in dendro-dendritic interactions points to the complexity of their functional role (Morgan and Lichtman, 2020; Crandall and Cox, 2012).

The second source of inhibition which is engaged by CT feedback are neurons in the TRN. The TRN is a sheet-like structure that laterally encompasses the thalamus and

that consists exclusively of GABAergic neurons, which form local networks via gap junctions (Pinault, 2004; Crabtree, 2018). *In vitro* recordings revealed that the synaptic connections between L6CT neurons and TRN neurons are stronger than the modulatory connections formed by CT axons onto relay cells (Golshani et al., 2001; Gentet and Ulrich, 2004). Although *in vivo* studies have yielded conflicting results, ranging from negligible (Jones and Sillito, 1994; Xue et al., 1988) to strong control (Kayama et al., 1984; Li et al., 2013; Montero, 2000) of TRN activity by corticoreticular inputs, TRN has always been associated with top-down processes. Due to this top-down component and its inhibitory effect on other sensory thalamic nuclei, the TRN is thought to be a key structure for attention (Montero, 2000; Wells et al., 2016; Wimmer et al., 2015; Crick, 1984; Guillery et al., 1998).

1.4 Manipulating corticothalamic feedback

1.4.1 Traditional approaches

The CT circuit enjoys a long history of research and over decades the methods to manipulate CT feedback have become more sophisticated. Among the permanent techniques to manipulate CT feedback is the ablation of cortical regions by surgical excision or aspiration (Jones and Sillito, 1994; Gulyas et al., 1990). Aspiration of areas 17 and 18 of cat visual cortex, for instance, has shown that CT feedback shapes spatial integration in dLGN by contributing to surround suppression (Murphy and Sillito, 1987). Critically, removing tissue typically induces widespread effects since passing nerve fibres and blood vessels which supply more distant brain regions are also damaged. Moreover, it is difficult to probe responses from the same neuron under control and experimental conditions since lesions are irreversible.

To overcome the problem of irreversibility, more elaborate techniques have been established, such as transcranial magnetic stimulation, pharmacological interventions or cortical cooling (de Labra et al., 2007; Przybylski et al., 2000; Andolina et al., 2013). While cooling inevitably leads to the reduction of neural activity, the sign of the effect induced by pharmacology depends on the drug. The most widely used substance, muscimole, an agonist for GABA_A-receptors, or lidocaine, a sodium channel blocker, temporarily inactivate neurons at the injection site. Other drugs, including penicillin, lead in the targeted population to an activation (Andolina et al., 2007; Zhang et al., 1997; Ogden, 1960). In this vein, Ogden (1960) used penicillin to activate a large

population of CT neurons in the primary somatosensory cortex of cats. He observed that, post application, evoked responses in the somatosensory relay nuclei were reduced and concluded that CT projections might serve as an inhibitory feedback that helps to establish a sensory focus.

Although introducing reversible methods to the repertoire has substantially improved our understanding of sensory processing in the corticothalamic feedback loop, there remain limitations, which in the case of pharmacological applications comprise the rather slow kinetics of the drug as well as a lack of specificity regarding the targeted cell population (Lomber, 1999).

1.4.2 Optogenetic methods

A recent breakthrough for the perturbation of neural circuits is the advent of optogenetics, a technique that allows the use of light to activate ion-pumps and ion-channels (Fenno et al., 2011; Deisseroth, 2011). Light-gated ion-pumps and channels can be expressed in neurons by either creating transgenic animals or by delivering the opsin-encoding DNA to cells in a particular brain region with a viral vector. In both cases, the expression can be restricted to certain neural populations by choosing a cell-type specific promoter and/or by using recombinase technology such as the Cre-lox system to further narrow down the affected cell type (Zhang et al., 2010; Madisen et al., 2012).

Viruses which are frequently used to transduce neurons are lenti virus, adeno-associated virus (AAV), and glycoprotein-deleted rabies virus (RVΔG). RVΔG act retrogradely, but do not cross synapses, and can thus be used to target neurons, which are projecting to a specific brain region (Wickersham et al., 2007; Ghanem and Conzelmann, 2016). Following this rationale, Hasse and Briggs (2017a) injected an RVΔG into the dLGN of ferrets to express channelrhodopsin-2 (ChR2), a light-gated cation channel, in corticogeniculate neurons. They found that activating corticogeniculate neurons increased in dLGN neurons both spatial and temporal resolution. Despite their popularity, using RVΔG as vehicle for gene delivery comes with limitations, since its cytotoxic properties lead to a significant reduction of the transduced cell population after about two weeks (Wickersham et al., 2007).

Contrarily, AAVs leave the transduced cell intact but lack sufficient packaging capacity to include large promoters, which limits cell type-specific targeting (Zhang et al.,

2010). A solution to this problem is provided by the Cre-dependent AAV expression approach, in which a Cre-dependent AAV is injected into a brain region of a Cre recombinase-driver mouse, so that the opsin expression is restricted to a specific cell-type in the target brain region (Yizhar et al., 2011). In this vein, one can, for instance, deliver ChR2-encoding DNA into the V1 of PVCre-mice, which leads to the expression of ChR2 in all transduced PV+ V1 neurons. Exposing V1 to blue light then activates PV+ inhibitory neurons, which will, in turn, suppress pyramidal cells, including those located in layer 6 (Born et al., 2021; Olsen et al., 2012; Atallah et al., 2012). To more directly manipulate CT feedback, a frequently used model is the Ntsr1-Cre mouse line, in which the enzyme Cre recombinase is with a high specificity of $> 90\%$ expressed in L6CT neurons (Gong et al., 2007; Bortone et al., 2014; Kim et al., 2014).

Although this mouse line allows to specifically target L6CT neurons, using optogenetics to directly suppress activity in neurons remains challenging. Widely used light-activated ion pumps, such as halorhodopsin and archaerhodopsin, require high light-intensity levels (Wiegert et al., 2017), and suffer from reduced efficacy if activated over longer periods (Wiegert et al., 2017; Mattis et al., 2012). Alternatively, recent studies have been focusing on light-activated potassium and chloride channels. Since their equilibrium potential is close to the neuron's resting potential, they can suppress spiking via shunting inhibition (Wiegert et al., 2017). The synthetic potassium channel, BLINK2, for instance, is activated by blue light and remains active over several minutes post illumination, which makes it a powerful tool for long suppression periods (Alberio et al., 2018). Promising light-sensitive anion channels, on the other hand, are the naturally occurring *Guillardia theta* anion-conducting channelrhodopsins (GtACRs), which are highly selective to anions and display large photo-induced currents (Wiegert et al., 2017; Govorunova et al., 2015). Critically, the effect of anion-conducting channels depends on the maturity of the neuron (Kaila et al., 2014) and the specific neural compartment (Turecek and Trussell, 2001; Szabadics, 2006). In immature neurons and presynaptic terminals, where chloride concentrations can be higher, opening GtACRs can lead to neurotransmitter release (Mahn et al., 2016) and trigger antidromic spikes (Malyshev et al., 2017; Wiegert et al., 2017). To avoid eliciting back-propagating action potentials in axons, recently developed soma-targeting GtACRs can be used to reliably suppress activity in L6CT neurons (Mahn et al., 2018).

1.5 Topographic organization of corticothalamic feedback

To facilitate a meaningful modulation of spatial processing in thalamus, CT feedback should be organized topographically, i.e. CT neurons encoding a particular location in space should innervate thalamic relay cells with similar spatial preference. This pattern has been described in the visual system of primates, in which V1 L6CT neurons innervate dLGN neurons with matching RF locations (Ichida and Casagrande, 2002; Angelucci and Sainsbury, 2006). Retinotopic CT feedback connections are, even though less specific, also present in the cat visual system (Murphy et al., 1999; Tsumoto et al., 1978). In rodents, in which corticothalamic interactions are, due to its high degree of structuredness, often probed in the somatosensory system, previous work suggests a topographic arrangement of CT feedback, where the level of specificity depends on the origin. While neurons in the upper layer 6 of a given barrel only innervate neurons belonging to the corresponding barreloid in the VPM, neurons in the lower layer 6 also project to adjacent barreloids (Deschênes et al., 1998; Hoogland et al., 1987; Land et al., 1995). If, analogously, CT projections in the rodent visual system are organized retinotopically remains an open question.

Like the direct feedback connections from V1 to dLGN, cortical projections to the rabbit TRN are also topographically aligned (Crabtree and Killackey, 1989; Montero et al., 1977). By performing in rabbit V1 double injections of proline and methionine, Montero et al. (1977) found that neurons encoding temporal parts of the visual field projected to more lateral and neurons encoding upper parts of the visual field projected to more dorsal regions in visual TRN (visTRN). If mouse visTRN receives cortical inputs that are organized similarly remains elusive. While mouse visTRN shares anatomical features with the visTRN of other mammalian species, i.e. the segregation into lower- and higher-order subregions, the specific arrangement can differ: while in cats, rabbits, and rats the lower-order subregion, receiving input from dLGN and V1, consists of a lateral tier making up about two-thirds of TRN's thickness (Guillery et al., 1998), the lower-order subregion in mouse visTRN consists of the central part of visTRN (Li et al., 2020; Martinez-Garcia et al., 2020). If these anatomical differences also entail a difference in the organization of corticoreticular projections is unknown.

To investigate the organization of CT feedback in mice, we performed triple-color anatomical tracings (**Manuscript 1** - Born et al. (2021)). To this end, we injected into V1 of *Ntsr1*-Cre mice, along an iso-azimuth or an iso-elevation line, small volumes of

three viral vectors. Each viral vector led in transduced L6CT neurons to the expression of a different fluorophore. *Post-mortem* inspection of the fluorescence pattern created by labeled axon terminals in dLGN and visTRN revealed a retinotopic organization of CT feedback projections. In dLGN, azimuth was mapped along the medial-lateral axis with L6CT neurons encoding temporal locations in the visual field innervating more medial parts of the dLGN. Elevation was mapped along the dorsal-ventral axis with axons of L6CT neurons encoding elevated positions terminating in more dorsal regions. This pattern matches the topographic representation of visual space in dLGN (Piscopo et al., 2013). In visTRN, we found elevation to be mainly encoded along the anterior-posterior axis while azimuth mapped along the dorsal-ventral axis. This finding was in line with results obtained from electrophysiological recordings during which we measured in visTRN RFs.

1.6 Effects of cortical feedback on spatial processing in thalamus

The topographic organization of feedback to thalamus allows cortex to differentially modulate its input across space. The effect of these spatial modulations can be assessed by measuring in thalamic neurons spatial integration properties. Two hallmarks of spatial integration are the preferred size of a neuron, i.e. the stimulus size which elicits the strongest response and the level to which the response of a neuron is reduced by a stimulus extending beyond the preferred size, a phenomenon termed surround suppression (Allman et al., 1985; Blakemore and Tobin, 1972; DeAngelis et al., 1994; Knierim and van Essen, 1992; Nelson and Frost, 1978; Gilbert and Wiesel, 1990) (**Fig. 2**). Probing these response properties in dLGN of cats, ferrets, and non-human primates, it has been shown that CT feedback can increase surround suppression and sharpen RFs (Andolina et al., 2013; Hasse and Briggs, 2017a; Jones et al., 2012).

This view, however, has been challenged. First, the effect of CT feedback on spatial integration has traditionally been probed in anesthetized animals. Since anaesthesia affects feedback signals, this impedes interpreting the results and calls for investigations in awake animals (Makino and Komiyama, 2015; Briggs and Usrey, 2011). Second, the results have been questioned by a recent study, which did not find surround suppression in dLGN to be stronger than in the retina, and argues that CT feedback signals are too slow to account for the suppressive component in dLGN (Alitto and Usrey, 2008). Lastly, Bonin (2005) used a network model to simulate normalization effects at

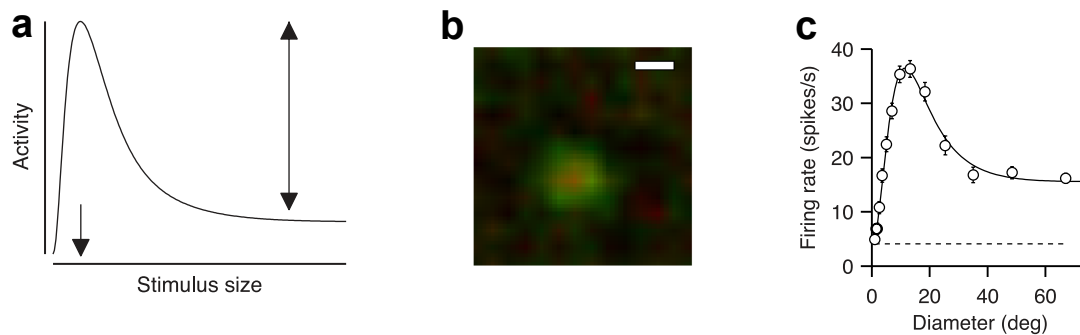


Fig. 2 Neurons in dLGN show surround suppression

(a) Schematic of a size-tuning curve. The small arrow in the lower left corner indicates the preferred size as defined by the stimulus size which elicits the strongest response. The arrow on the right indicates the level of surround suppression that is evoked by a stimulus extending beyond the classical RF. (b) RF of a dLGN neuron as measured with a sparse noise stimulus. *Red*: responses to white squares; *green*: responses to black squares; scale bar: 10 deg. (c) An example size-tuning curve recorded from a dLGN neuron. *Circles*: mean response; *error bars*: standard error of the mean; *solid line*: fit by a Ratio-of-Gaussians model (Cavanaugh et al., 2002). Reprinted with permission from Vaiceliunaite & Busse.

the level of the thalamus and found that surround suppression occurs also for gratings with low spatial and high temporal frequencies - stimulus features which are not well suited to drive cortical responses.

To test if in awake mice CT feedback affects spatial integration, we recorded responses to drifting gratings of different sizes in dLGN neurons of PVCre-mice (**Manuscript 1** - Born et al. (2021)). By optogenetically activating PV+ inhibitory neurons in V1, we suppressed CT feedback in half of the trials. Contrasting size-tuning curves under the two conditions, we found that CT feedback indeed affected spatial integration in dLGN: first, with feedback intact, responses to small stimulus sizes were stronger while responses to large stimulus sizes were weaker, consequently enhancing surround suppression. Moreover, suppressing CT feedback led to an increase in the preferred size. We concluded that CT feedback affects spatial integration in dLGN by sharpening RFs and enhancing surround suppression.

1.7 Effects of cortical feedback on processing of naturalistic stimuli in thalamus

Sensory systems have traditionally been probed with simple, artificial stimuli, yet they have evolved to encode complex inputs, and thus understanding sensory processes will ultimately require investigating sensory responses to naturalistic stimuli (Simoncelli and Olshausen, 2001). Indeed, early exposure to naturalistic stimuli shapes extraclassical RFs of mouse V1 neurons, allowing them to more selectively represent features in natural scenes (Pecka et al., 2014). Using natural scenes to map RFs in mouse V1, their filtering properties were found to be more complex than when probed with artificial stimuli (Walker et al., 2019), and center-surround interactions in neurons of macaque V1 are stronger for preserved natural image statistics (Guo et al., 2005). In particular, the statistics of naturalistic stimuli are well suited to decorrelate responses of neurons in V1 (Vinje and Gallant, 2000), and trigger more reliable responses (Rikhye and Sur, 2015). Similarly, in the ferret primary auditory cortex (Garcia-Lazaro et al., 2006), the cat inferior colliculus (Escabí et al., 2003), and the amphibian papilla of the bullfrog (Rieke et al., 1995), naturalistic sounds are represented more efficiently.

Additionally, naturalistic stimuli might more strongly engage feedback signals. Feedback signals are, according to the framework of predictive coding, said to convey a model of the external world that cancels out redundant feedforward inputs (Lee and Mumford, 2003). Hence, feedback neurons should be best driven by familiar, naturalistic stimuli (Berkes et al., 2011; Rao and Ballard, 1999; Clark, 2013). Supporting this idea, it has been shown that CT feedback responds better to moving than to static stimuli (Sillito and Jones, 2002).

To understand if effects of CT feedback differ between naturalistic and artificial stimuli, we manipulated CT feedback in PVCre-mice and measured responses of dLGN neurons to full-screen drifting gratings and naturalistic movie clips (**Manuscript 2** - Spacek et al. (2021)). Computing a feedback modulation index, we found that, on average, CT feedback enhanced responses to movie clips more strongly than to drifting gratings.

1.8 Differential contributions of corticothalamic feedback and neuromodulation to thalamic processing

Besides feedback signals and lateral connections, another factor contributing to contextual modulation in thalamus is the behavioral state. A mean to assess the effects of behavioral state on activity in the thalamus is to contrast neural response properties during periods of quiescence with response properties during periods of locomotion (Niell and Stryker, 2010). In dLGN, locomotion has been associated with an increase in stimulus evoked activity and spontaneous firing rates, a change in tuning properties, and proportionally fewer spikes fired in bursts (Erisken et al., 2014; Molnár et al., 2021; Aydın et al., 2018).

The origin of these modulatory effects is likely complex: First, behavioral state modulates activity upstream of dLGN relay cells, in boutons of retinal ganglion cells (Liang et al., 2020) and their axons in the optic tract (Schröder et al., 2020). Although the majority of retinal axons in the optic tract, that are modulated by locomotion, displays positive correlations with run speed (Schröder et al., 2020), a calcium imaging study revealed that the effect of arousal on boutons of retinal ganglion cells in dLGN is predominantly suppressive (Liang et al., 2020). Since it is difficult to reconcile this suppressive effect with locomotion-enhanced firing rates in relay cells, state-dependent effects in dLGN might be established directly in the thalamus. Thalamic nuclei are targeted by the neuromodulatory ascending activating system, whose origin lies in brainstem and hypothalamic nuclei that supply amongst others noradrenaline and acetylcholine (ACh) (Lee and Dan, 2012). Indeed, transient application of ACh in cat dLGN enhances responses to optimal stimuli (Sillito et al., 1983) and administration of noradrenaline *in vitro* depolarizes the membrane potential of relay cells (McCormick and Pape, 1990). Finally, effects of behavioral state might be mediated via feedback connections from cortex. Cortical layer 6 is among the layers that is most densely innervated by cholinergic projections (Radnikow and Feldmeyer, 2018), its corticothalamic neurons are depolarized by ACh (Sundberg et al., 2018) and, on average, more active during periods of locomotion (Augustinaite and Kuhn, 2020). Yet, to which extent CT feedback contributes to state-dependent processing in thalamus is an open question.

To understand to which extent state-dependent processing of naturalistic movie clips in mouse dLGN is inherited from cortex, we first probed the effect of CT feedback on responses to naturalistic movie clips (**Manuscript 2** - Spacek et al. (2021)).

We found that when CT feedback was intact, the evoked firing rates were higher while relatively fewer spikes were fired in bursts. Moreover, during trials with CT feedback intact, response patterns were less sparse and less reliable. Interestingly, contrasting control trials in which the animal remained stationary with control trials in which the animal ran, revealed that effects of locomotion on dLGN responses were indeed similar. However, since locomotion-induced effects persisted during V1 suppression, we concluded that state-dependent and CT influences on processing of naturalistic stimuli in dLGN are largely independent.

1.9 Top-down influences on sensory processing in primary visual cortex

While the thalamo-cortico-thalamic loop is an excellent circuit to study the role of feedback for sensory processing, top-down modulations are also prominent in cortex. While cortical layer 4 is the main recipient of feedforward inputs, feedback signals target deep and superficial layers (Larkum, 2013). Interneurons in layer 1 of cat area 17, for instance, receive 90% of their input from long-range feedback connections (Binzegger, 2004) and neurons in area MT project to layer 6 of primate V1 (Sillito et al., 2006; Rockland and Knutson, 2000). In primate V1, feedback signals contribute to extraclassical modulation of the RF (Angelucci and Sainsbury, 2006), including surround suppression (Nassi et al., 2013; Angelucci et al., 2002), help to discriminate figure from background (Hupé et al., 1998; Klink et al., 2017), and mediate non-visual signatures of cognitive processes in V1 activity, such as reward information (Stanisor et al., 2013).

With growing interest in the mouse model, contextual signals have also been reported in murine V1: neurons in mouse V1 display feedback-enhanced surround suppression (Vangeneugden et al., 2019) and figure-ground modulation (Kirchberger et al., 2021), are tuned to specific locations in space (Saleem et al., 2018; Diamanti et al., 2021), and elicit error signals, if visual input deviates from the prediction (Fiser et al., 2016; Khan and Hofer, 2018). The fact that representations in mouse V1 are not limited to visual information, points to its importance for more complex behavior. To gain an overview of how mouse visual behavior depends on microcircuits in V1, we have summarized the recent literature (**Manuscript 3** - Katzner et al. (2019)). In particular, we highlight the role of the thalamo-cortical pathway for mouse visual behavior, describe how visual information is represented within V1, and elaborate on its modulation by

top-down processes.

An important source of top-down inputs to V1 is the anterior cingulate cortex (ACC) (Zhang et al., 2014; Fiser et al., 2016; Leinweber et al., 2017), a large area that is located around the rostrum of the corpus callosum (Devinsky et al., 1995). Its neural activity has been associated with a wide range of cognitive, motor, and affective processes. Deletion of $Ca_v1.2$ channels in mouse ACC, for instance, impairs observational fear learning and weakens behavioral pain responses (Jeon et al., 2010), lesioning mouse ACC leads to a disinhibited response profile in a signal detection task (Hvoslef-Eide et al., 2018), while its photoactivation can improve performance in a visual discrimination task (Zhang et al., 2014). Interestingly, neurons in ACC send topographically organized projections to V1, where they innervate pyramidal cells and different types of inhibitory interneurons, including PV+, SOM+, and VIP+ neurons (Leinweber et al., 2017). To these neurons, ACC axons provide motor signals that might resemble efference copies, enabling the animal to discern self motion from external motion (Leinweber et al., 2017; Khan and Hofer, 2018). If top-down inputs from ACC to V1 convey more specific task-relevant signals, such as the valence of a visual stimulus, remains elusive. To shed light on this question, we recorded in neurons of ACC and V1 while mice evaluated visual cues, one of which signaled a reward (**Manuscript 4** - Wal et al. (2021)). In both ACC and V1, 30% of recorded neurons became selective to one of the two stimuli. While this study shows, that a similar proportion of recorded V1 and ACC neurons developed a stimulus preference, we were not able to resolve if V1 modulations are indeed induced by feedback from ACC. Opposing this idea, selective neurons in ACC were biased towards the rewarded cue, while selectivity in the population of recorded V1 neurons was balanced.

1.10 Conclusion

This thesis comprises four manuscripts which investigate in the mouse early visual system the influence of contextual modulations. In the first part of the thesis (**Manuscript 1, 2** - Born et al. (2021); Spacek et al. (2021)), we studied how corticothalamic feedback affects sensory processing in the mouse dLGN. In particular, we reveal how CT feedback sculpts spatial integration, modulates processing of naturalistic movie clips, and contributes to state-dependent modulations. In the second part, we shift the focus to the primary visual cortex and extend the scope of this work by also considering the

behavioral level. We first summarize recent studies that investigate how mouse visual behavior is mediated by V1 microcircuits (**Manuscript 3** - Katzner et al. (2019)) and emphasize how these microcircuits are shaped by top-down influences. Top-down influences might also be responsible for inducing the effects we describe in our final study where we show that the representation of visual cues is modulated by their evaluation (**Manuscript 4** - Wal et al. (2021)). In sum, this work offers important insights into how visual processing in the early visual system is affected by contextual modulations.

2 Corticothalamic feedback sculpts visual spatial integration in mouse thalamus

This chapter is reproduced from an article published in *Nature Neuroscience*. The article can be found under <https://www.nature.com/articles/s41593-021-00943-0>. The full citation is:

Born, G.,* Schneider-Soupiadis, F. A.*, Erisken, S.*, Vaicelunaite, A., Mobarhan, M. H., Lao, C. L., Spacek, M. A., Einevoll, G. T., & Busse, L. (2021). Corticothalamic feedback sculpts visual spatial integration in mouse thalamus. *Nature Neuroscience*.

Declaration of author contributions

Laura Busse, Sinem Erisken, Gregory Born, Felix A. Schneider-Soupiadis and Agne Vaiceliunaite conceptualized the study. Milad H. Mobarhan and Gaute T. Einevoll developed the methodology. Gregory Born, Sinem Erisken, Felix A. Schneider-Soupiadis, Martin A. Spacek, Mobarhan H. Milad and Laura Busse developed the software. Gregory Born, Felix A. Schneider-Soupiadis, Sinem Erisken and Laura Busse performed the formal analysis. Gregory Born, Felix A. Schneider-Soupiadis, Sinem Erisken, Agne Vaiceliunaite and Martin A. Spacek performed the experimental investigations. Chu Lan Lao provided resources. Martin A. Spacek, Gregory Born, Sinem Erisken, Laura Busse and Felix A. Schneider-Soupiadis curated the data. Gregory Born, Sinem Erisken, Felix A. Schneider-Soupiadis and Laura Busse wrote the original draft. All authors wrote and edited the manuscript. Gregory Born, Felix A. Schneider-Soupiadis, Sinem Erisken and Laura Busse visualized the data. Laura Busse supervised the project, and Laura Busse and Gregory Born acquired funding.

Personal contributions

For Fig. 1, G.B. supported F.S. in carrying out the tracing experiments presented in panels a and b. Data from the same tracing experiments are presented in Fig. 4a, Extended Data Fig. 1, and Extended Data Fig. 7. Moreover, G.B. assisted in recording in the dorsolateral geniculate nucleus (dLGN) responses to drifting gratings in two mice, while optogenetically activating in half of the trials layer 6 (L6) corticothalamic (CT) neurons in the primary visual cortex (V1; Fig. 1d-i). Imaging data recorded in these experiments were also used to quantify relative expression volumes of transduces CT

neurons in V1 L6 and of their axons in the dLGN (Extended Data Fig. 2). Recorded responses of dLGN neurons were further quantified in Extended Data Fig. 3. For Fig. 2h-m, G.B. recorded responses of dLGN neurons in PV-Cre mice in size tuning experiments while optogenetically suppressing CT feedback on half of the trials. Moreover, G.B. analyzed and visualized the data. For Fig. S5a-c, G.B. contributed data recorded in an Ntsr1-Cre mouse to test the effect of optogenetically activating L6 CT neurons on visually evoked responses in V1 neurons. For Fig. 3, G.B. determined the parameters of the extended difference-of-Gaussians model, ran the simulations, and analyzed and visualized the data. For Fig. 4b-c, G.B. conducted retrograde tracing experiments to reveal the TRN neurons that project to dLGN. G.B. performed the surgeries, imaged brain slices and processed the images for visualization. To quantify receptive field properties of visTRN neurons (Fig.4e-m), G.B. conducted sparse-noise and size-tuning experiments. G.B. also analyzed and visualized the data. To measure the effect of CT feedback on response properties of neurons in visTRN, G.B. carried out experiments in which visual stimuli were in half of the trials paired with optogenetic suppression of V1 activity (Fig.5, Extended Data Fig.8, Extended Data Fig. 9, Extended Data Fig. 10). G.B. performed the surgeries, and recorded, analyzed and visualized the data. G.B. helped conceptualize the study and contributed to writing the original draft. G.B. also participated in writing the final manuscript and its editing. Lastly, G.B. acquired funding by receiving an “Add-on Fellowships for Interdisciplinary Life Science” from the Joachim Herz Foundation.

Rights and permissions

”Ownership of copyright in original research articles remains with the Author, and provided that, when reproducing the contribution or extracts from it or from the Supplementary Information, the Author acknowledges first and reference publication in the Journal, the Author retains the following non-exclusive rights: To reproduce the contribution in whole or in part in any printed volume (book or thesis) of which they are the author(s). The author and any academic institution, where they work, at the time may reproduce the contribution for the purpose of course teaching. To reuse figures or tables created by the Author and contained in the Contribution in oral presentations and other works created by them. To post a copy of the contribution as accepted for publication after peer review (in locked Word processing file, of a PDF version thereof) on the Author’s own web site, or the Author’s institutional repository, or the Author’s funding body’s archive, six months after publication of the printed or online edition of

the Journal, provided that they also link to the contribution on the publisher's website. Authors wishing to use the published version of their article for promotional use or on a web site must request in the normal way."

Retrieved from <https://s100.copyright.com/AppDispatchServlet#formTop> on 14.11.2021.



Corticothalamic feedback sculpts visual spatial integration in mouse thalamus

Gregory Born^{1,2,12}, Felix A. Schneider-Soupiadis^{1,2,12}, Sinem Erisken^{1,3,4,12}, Agne Vaiceliunaite³, Chu Lan Lao^{5,6}, Milad H. Mobarhan^{7,8}, Martin A. Spacek¹, Gaute T. Einevoll^{9,10} and Laura Busse^{1,11} ✉

En route from the retina to the cortex, visual information passes through the dorsolateral geniculate nucleus (dLGN) of the thalamus, where extensive corticothalamic (CT) feedback has been suggested to modulate spatial processing. How this modulation arises from direct excitatory and indirect inhibitory CT feedback pathways remains enigmatic. Here, we show that in awake mice, retinotopically organized cortical feedback sharpens receptive fields (RFs) and increases surround suppression in the dLGN. Guided by a network model indicating that widespread inhibitory CT feedback is necessary to reproduce these effects, we targeted the visual sector of the thalamic reticular nucleus (visTRN) for recordings. We found that visTRN neurons have large RFs, show little surround suppression and exhibit strong feedback-dependent responses to large stimuli. These features make them an ideal candidate for mediating feedback-enhanced surround suppression in the dLGN. We conclude that cortical feedback sculpts spatial integration in the dLGN, likely via recruitment of neurons in the visTRN.

According to the classical view of the visual system, information is propagated through a hierarchy of processing stages, which are interconnected via feed-forward projections. The initial feed-forward sweep can contain a considerable amount of information, which is sometimes sufficient to drive perception^{1,2}. Furthermore, feed-forward architectures implemented in artificial neural networks give rise to representations that resemble those in the primate visual processing hierarchy, enabling human-like performance in complex visual tasks³.

While feed-forward architectures can be powerful, anatomical connectivity in the brain is dominated by feedback. Feedback is a prominent and ubiquitous motif in the brain that is observed across areas and species, with descending feedback projections generally outnumbering ascending feed-forward afferents⁴. While this pronounced prevalence implies that feedback projections provide core aspects of neural computation, a consensus regarding the function of feedback to lower-level sensory areas is lacking.

This architectural principle also applies to thalamocortical communication; relay cells in the dLGN of the thalamus receive only 5–10% of their synaptic inputs from retinal afferents, whereas 30% originate from layer 6 CT (L6CT) pyramidal cells in the primary visual cortex (V1)⁵. Yet, dLGN RFs more closely resemble retinal RFs than cortical RFs, supporting the role of CT feedback as a modulator, not driver, of thalamic responses. Still, modulations by CT feedback are expected to be complex, because L6CT pyramidal cells not only provide direct excitation to thalamic relay cells but also provide indirect inhibition by exciting inhibitory neurons in the TRN and local dLGN interneurons. The specific balance of feedback-mediated excitation and indirect inhibition is likely dynamic and flexible, given the distinct stimulus selectivity and synaptic properties in the CT circuit⁶. Most notably, the

retinotopic arrangement of CT projections in the visual system of primates and cats^{7,8} is highly suggestive of a role in modulating spatial processing^{9–13}.

Here, we studied the role of cortical feedback in modulating thalamic spatial integration across the main processing stages of the thalamo–cortico–thalamic loop, V1, dLGN and visTRN. Using viral labeling and channelrhodopsin (ChR2)-assisted functional mapping, we found that V1 corticogeniculate feedback projections in the mouse are retinotopically organized and have spatially specific function. Using optogenetic manipulations to compare the modulation by CT feedback for stimuli of various sizes, we revealed that CT feedback sharpens dLGN RFs and increases surround suppression. Computational modeling and recordings from the TRN provided evidence that CT feedback can augment dLGN surround suppression via the visTRN. We conclude that CT feedback sculpts spatial integration in the dLGN, likely via recruitment of inhibitory neurons in the TRN.

Results

Spatial specificity of corticogeniculate feedback. Modulations of spatial processing could be achieved efficiently if CT feedback was arranged in a retinotopic way. To test whether CT feedback terminal fields in mouse dLGN maintained the retinotopic organization from their V1 origin, we performed triple-color Cre-dependent viral tracing by injecting small volumes of adeno-associated virus (AAV) at different retinotopic positions into V1 of Ntsr1-Cre mice, having >90% specificity for L6CT pyramidal cells (Fig. 1a,b). Visual inspection of thalamic slices revealed that the anterogradely labeled axonal terminal fields of different colors were clearly separated in the dLGN, matched the pattern of expression in V1 and were consistent with the retinotopic organization of the geniculate target region¹⁴ (Fig. 1c and Extended Data Fig. 1). Such spatially precise

¹Division of Neurobiology, Faculty of Biology, LMU Munich, Munich, Germany. ²Graduate School of Systemic Neurosciences (GSN), LMU Munich, Munich, Germany. ³Werner Reichardt Centre for Integrative Neuroscience, University of Tübingen, Tübingen, Germany. ⁴Graduate School of Neural & Behavioural Sciences, International Max Planck Research School, University of Tübingen, Tübingen, Germany. ⁵Department of Physiological Genomics, Biomedical Center (BMC), LMU Munich, Munich, Germany. ⁶Institute of Stem Cell Research, Helmholtz Center Munich, Biomedical Center (BMC), Munich, Germany. ⁷Centre for Integrative Neuroplasticity, University of Oslo, Oslo, Norway. ⁸Department of Biosciences, University of Oslo, Oslo, Norway. ⁹Faculty of Science and Technology, Norwegian University of Life Sciences, Aas, Norway. ¹⁰Department of Physics, University of Oslo, Oslo, Norway. ¹¹Bernstein Centre for Computational Neuroscience, Munich, Germany. ¹²These authors contributed equally: Gregory Born, Felix A. Schneider-Soupiadis, Sinem Erisken.

✉e-mail: busse@bio.lmu.de

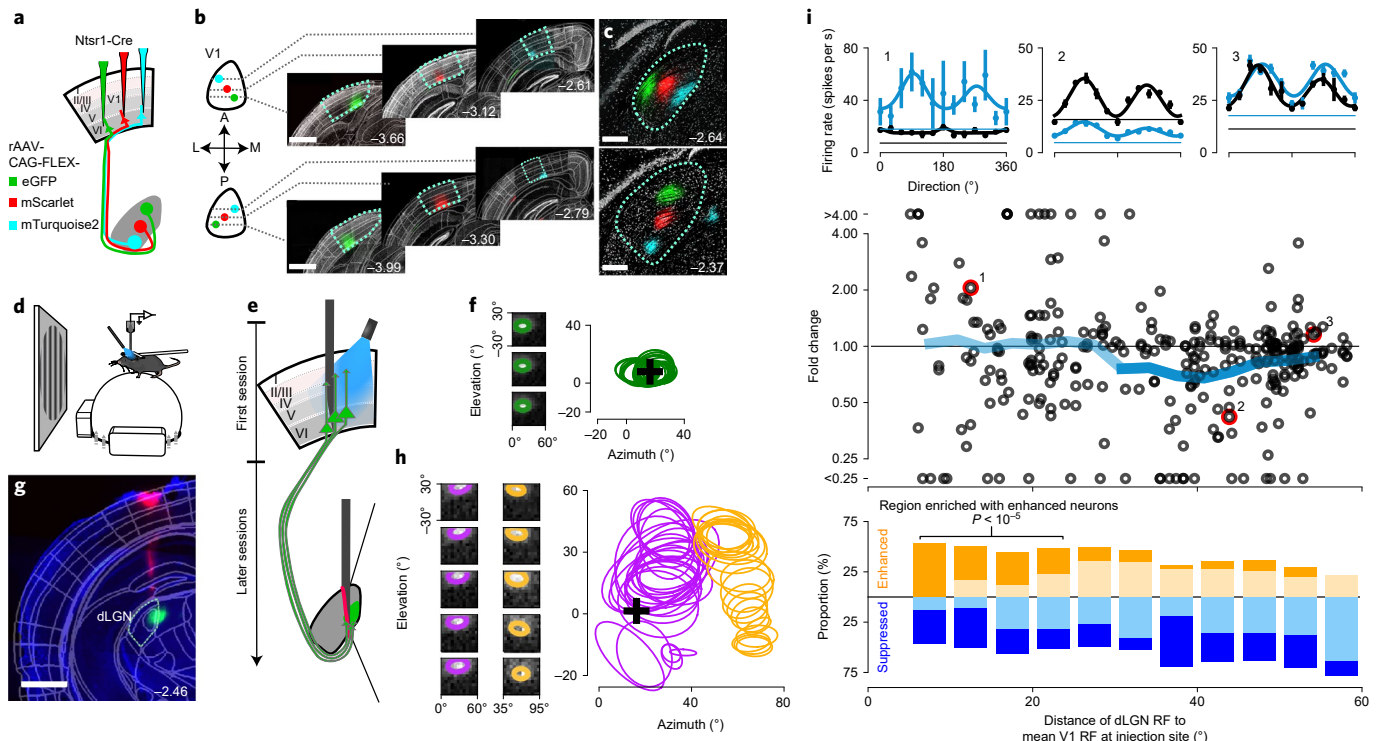


Fig. 1 | Anatomical and functional mapping of L6CT feedback. **a**, Triple-color viral tracing. Transduction of localized populations of V1 L6CT neurons with Cre-dependent AAV-FLEX-enhanced green fluorescent protein (eGFP), AAV-FLEX-mScarlet (red fluorescent protein variant) and AAV-FLEX-mTurquoise2. **b**, Coronal sections of V1 with injections along the V1 axis for azimuth (top) and elevation (bottom); green, eGFP; red, mScarlet; blue, mTurquoise2; gray, Nissl; scale bar, 1 mm; A, anterior; P, posterior; L, lateral; M, medial. **c**, Transduced V1 L6CT axonal terminal fields in the dLGN (top, azimuth axis; bottom, elevation axis); scale bar, 0.25 mm. Observations in **b** and **c** were observed in five mice (Extended Data Fig. 1). **d**, Schematic of in vivo recordings in head-fixed mice. **e**, Schematic of Chr2-assisted functional connectivity mapping. **f**, RF mapping in V1. Left, spatial RFs for three representative channels recorded at the V1 injection site; green, 1σ contours of fitted two-dimensional (2D) Gaussian. Right, all fitted V1 RF contours from the example recording session; black cross, mean RF center. **g**, Representative coronal section showing local axonal termination of V1 L6CT neurons expressing Chr2 tagged with enhanced yellow fluorescent protein (eYFP) in the dLGN; magenta, Dil (recording track); scale bar, 1 mm. **h**, RF mapping in the dLGN. Left, spatial RFs and fitted 1σ contours for representative channels located in the dLGN (two recording sessions, channel order top to bottom on electrode as shown in **e**). Right, fitted dLGN RF contours; black cross, mean RF position from the V1 recording. **i**, Spatial profile of modulations induced by photostimulation of CT feedback. Top, direction-tuning curves for three neurons; blue, photostimulation of L6CT pyramidal cells; black, control conditions; visual stimulus, full-screen sine wave gratings drifting in 1 of 12 directions, with temporal and spatial frequencies coarsely optimized for the recording, 0.75-s duration, photostimulation of 0.085 s before stimulus onset lasting for 0.85 s. Data are presented as means \pm s.e.m. Middle, CT feedback modulation strength (fold change) as a function of retinotopic distance to the mean V1 RF position at the injection site; red circles, neurons shown in the top; blue line, mean of fold change values in overlapping bins (bin size, 15° ; spacing, 3.3°), with the opaque portion delineating the region with significant mean fold change ($n=293$ neurons; $P=6.8 \times 10^{-3}$, two-sided cluster permutation test). Bottom, proportions of significantly enhanced (dark orange), suppressed (dark blue) and unmodulated neurons (pale). Computing the mean V1 RF only based on the lower half of the channels or on those located in L6 as estimated by current source density (CSD) analysis did not qualitatively change the spatial profile. Numbers in **b,c,g** indicate distance from bregma in millimeters.

retinotopic organization, as known from previous work in primates and cats^{7,8}, make CT feedback projections well poised to modulate spatial representations.

To examine whether the retinotopically organized CT feedback can also generate spatially specific functional effects, we next probed the impact of CT feedback on dLGN responses using Chr2-assisted functional mapping (Fig. 1d,e and Extended Data Fig. 2). We expressed Chr2-eYFP in a localized population of L6CT pyramidal cells by injecting a small volume of Cre-dependent AAV expressing Chr2-eYFP into V1 of Ntsr1-Cre mice (Extended Data Fig. 2). After sufficient time for expression, we performed silicon probe recordings in head-fixed mice (Fig. 1d,e). We first targeted the V1 injection site and used a sparse noise stimulus to estimate average RF location of the neurons in the V1 column of the transduced L6CT cells (Fig. 1f). We then turned to the dLGN (Fig. 1g), where RF mapping revealed a smooth retinotopic progression¹⁴, with RFs covering positions from the upper to the lower visual field for consecutive recording

channels along the dorsoventral axis (Fig. 1h). Multiple sessions with different insertions enabled us to measure dLGN RFs located at a wide range of distances from the average RF at the V1 injection site.

We then functionally mapped the spatial profile of CT feedback effects by photostimulating the local population of transduced L6CT pyramidal cells during the presentation of full-screen drifting gratings (Fig. 1i). To avoid potentially confounding, state-dependent response modulations¹⁵, we only considered trials in which the animal was quiescent (speed ≤ 0.25 cm s⁻¹ for $\geq 80\%$ of the trial) for the computation of direction-tuning curves (Fig. 1i) and thus for the evaluation of CT feedback effects, quantified as fold change. Across the population of recorded dLGN neurons, activating CT feedback resulted in both enhancement ($n=112$) and suppression of neuronal responses ($n=181$), with diverse effect sizes. The diversity of effects was not obviously related to recording depth or several aspects of tuning in the recorded dLGN neurons, such as orientation selectivity or contrast sensitivity (Extended Data Fig. 3).

Plotting the responses of individual neurons to CT feedback modulation against their retinotopic distances from the activated L6CT pyramidal cell population, however, revealed a distinct spatial profile (Fig. 1i). While CT feedback had a small overall effect in retinotopically ‘nearby’ regions ($<30^\circ$, transparent blue line), average CT feedback modulation in ‘distant’ regions was predominantly suppressive ($30\text{--}53^\circ$; $P=6.8\times 10^{-3}$, cluster permutation test; opaque blue line). This profile was stable when we reperformed the analysis for partitions of the data across trials and within trials (Extended Data Fig. 3k–n). The small average effect in nearby regions, rather than indicating the absence of modulation, reflected the diversity of effects (Fig. 1i and Extended Data Fig. 3o). Indeed, when we classified neurons into significantly enhanced, suppressed or not modulated by CT feedback groups, we observed that the prevalence of modulation types depended on retinotopic distance ($P=7.2\times 10^{-3}$, chi-squared test). Unlike suppressed neurons ($P=0.43$, chi-squared test), numbers of enhanced neurons varied with retinotopic distance ($P=4.7\times 10^{-4}$, chi-squared test) and were enriched in the sector from 0° to 25° ($P<10^{-5}$, cluster permutation test).

Together with our results of the triple-color viral tracing experiments, these findings demonstrate that L6CT pyramidal cells impact the mouse dLGN in a spatially specific manner. The measured modulation profile is consistent with a circuit architecture in which enhancing influences of CT feedback are more tightly localized, while suppressive influences are dispersed over a wider spatial scale. This spatial profile, in particular the retinotopically distant suppressive region, is suggestive of L6CT feedback shaping dLGN spatial integration.

CT feedback effects on dLGN spatial integration. Having observed that photostimulation of CT feedback can, in principle, induce modulations of geniculate activity with a spatial profile suggestive of shaping spatial integration in the dLGN, we probed whether CT feedback is indeed involved in tuning for stimulus size and surround suppression (Fig. 2). Surround suppression refers to the reduction of a neuron’s activity in response to a stimulus that exceeds the size of its classical RF (Fig. 2d) and is thought to underlie fundamental aspects of visual processing, such as the segregation of visual information and the computation of perceptual salience¹⁶. Furthermore, weakened center-surround interactions seem to be a low-level sensory facet of the compromised ability of individuals with schizophrenia to use context for the interpretation of stimuli¹⁷.

L6CT neurons are known to have low firing rates¹⁸ and to control activity in the V1 cortical column¹³, likely via a translaminar inhibitory interneuron type^{19,20}. Hence, to avoid concerns that direct L6 photoactivation might induce aberrant response patterns or recruit intracortical circuits in a widespread way, we suppressed the activity of L6CT neurons instead. To this end, we used a strategy of reliable and powerful global V1 suppression²¹ by targeting parvalbumin-positive (PV⁺) interneurons, the major class of V1 inhibitory interneurons (Fig. 2a), for Cre-dependent AAV-based expression of ChR2. By recording extracellular activity across the layers of V1, we characterized V1 tuning for stimulus size and surround suppression (Extended Data Fig. 4), and, importantly, we verified that optogenetic activation of PV⁺ neurons indeed suppressed output across the cortical column (Fig. 2b,c). We found that, even in the presence of drifting gratings, which powerfully drive V1 activity under control conditions (Fig. 2b), optogenetic activation of PV⁺ inhibitory interneurons led to suppression of responses in V1 neurons across all layers (Fig. 2c; 0 not included in 95% confidence intervals (95% CIs)).

Having confirmed that photostimulation of PV⁺ interneurons suppressed V1 activity, even in infragranular layers, we turned to the thalamus and recorded from the dLGN (Fig. 2d–m). Because dLGN RF locations in single-electrode penetrations vary widely across simultaneously recorded neurons (Fig. 1h), measuring

complete size-tuning curves (Fig. 2d) for dLGN neurons with RF-centered stimuli is laborious. We therefore focused first on conditions without a visual stimulus, corresponding to 0° conditions in size-tuning experiments, and again restricted our analysis to trials without locomotion (speed of $\leq 0.25\text{ cm s}^{-1}$; Fig. 2d). In light of a previous study showing that mouse dLGN responses to full-screen gratings during V1 suppression were enhanced¹³, we were surprised to observe that, in response to a uniformly gray screen, suppression of V1 for both shorter (250 ms; Fig. 2e(i)) and longer (1 s; Fig. 2e(ii)) periods resulted in reduced geniculate activity. Indeed, firing rates of dLGN neurons during the window of V1 suppression were lower than in the same-sized window before V1 suppression (during = 3.7 spikes per s versus before = 4.9 spikes per s; $n=276$ neurons; $P=1.5\times 10^{-10}$, Wilcoxon signed-rank test; Fig. 2f). Furthermore, closer inspection of the spike patterns (Fig. 2e) centered around V1 suppression revealed a change in dLGN spiking; more specifically, the fraction of spikes fired in bursts approximately doubled (during = 12.4% versus before = 5.0%; $n=236$ neurons; $P=4.4\times 10^{-11}$, Wilcoxon signed-rank test; Fig. 2g). In addition, V1 suppression shifted the distribution of burst lengths toward higher values ($P=3.6\times 10^{-13}$, two-sample Kolmogorov–Smirnov test), including the median burst length (before V1 suppression, median of 2 spikes per burst, $n=835$ bursts; during V1 suppression, median of 3 spikes per burst, $n=1,739$ bursts; $P=1.8\times 10^{-18}$, Mann–Whitney *U*-test; Fig. 2g). Both the decrease in firing rates and the subsequent increase in burst–spike ratio and burst length are consistent with the interpretation that, in the absence of stimulus drive, V1 suppression results in a decrease in feedback-mediated excitation. Such removal of excitation should hyperpolarize dLGN cells, resulting initially in fewer action potentials and later ($\geq 100\text{ ms}$) in bursting, given the hyperpolarization-mediated deactivation of T-type calcium channels. T-type calcium channels, abundant in the thalamus, mediate low-threshold calcium spikes, whose amplitudes are inversely related to membrane potential and are correlated with the number of action potentials in a burst riding its crest²². Complementary to the results of global V1 suppression, we found that photoactivation of L6CT neurons under size 0° conditions (that is, absence of sensory stimulation) was sufficient to enhance tonic firing in the dLGN (Extended Data Fig. 5). Overall, in the absence of visual stimuli, CT feedback seems to exert its effect mainly through the direct excitatory pathway, boosting firing rates and promoting tonic firing.

To probe the effects of CT feedback on spatial integration, we next centered drifting gratings of various sizes on the RF of each dLGN neuron and recorded responses while interleaving trials with and without optogenetic suppression of V1 (Fig. 2h–m). We fit each neuron’s responses under either the control or V1 suppression condition with a descriptive model of size tuning (ratio-of-Gaussians model (RoG; Methods); Fig. 2d,h,i and Extended Data Fig. 6), from which we extracted the preferred size (size at peak response) and suppression strength (suppression index (SI), with 0 indicating no suppression and 1 indicating full suppression). For small stimuli (that is, the preferred size under the control condition), we observed, as in the case of spontaneous activity, that V1 suppression caused a decrease in dLGN responses (control = 22.34 spikes per s versus V1 suppression = 18.09 spikes per s; $n=33$ neurons; $P=0.0018$, Wilcoxon signed-rank test; Fig. 2j). However, for large sizes (that is, the modeled response to a 200° stimulus), we found, in accordance with previous results¹³, the opposite effect; here, dLGN responses increased during V1 suppression (control = 11.69 spikes per s versus V1 suppression = 13.22 spikes per s; $n=33$; $P=0.033$, Wilcoxon signed-rank test; Fig. 2k). Hence, our results indicate that cortical feedback can affect dLGN responses in a contextual manner, enhancing responses to the preferred size while suppressing responses to larger stimuli. To determine whether the size-dependent modulation of dLGN firing rates during V1 suppression translated into changes in spatial integration, we next

examined the size-tuning curves of individual neurons. Indeed, we found that during V1 suppression, dLGN neurons preferred larger sizes (control = 16.27° versus V1 suppression = 20.42° ; $n = 33$; $P = 0.00024$, Wilcoxon signed-rank test; Fig. 2l) and were less surround suppressed (control = 0.62 versus V1 suppression = 0.45; $n = 33$; $P = 7.36 \times 10^{-5}$, Wilcoxon signed-rank test; Fig. 2m).

While V1 suppression did not abolish surround suppression in the dLGN (28 of 33 cells still had an SI ≥ 0.1), our results indicate a substantial involvement of cortical feedback in shaping spatial integration in the dLGN: feedback enhances contextual effects, facilitating responses to the center while suppressing those to the surround, which results in sharper RFs and a stronger center-surround antagonism. While the enhanced small-size responses are consistent with a net depolarizing effect of CT feedback, the increased surround suppression for large sizes is suggestive of CT feedback acting via inhibition.

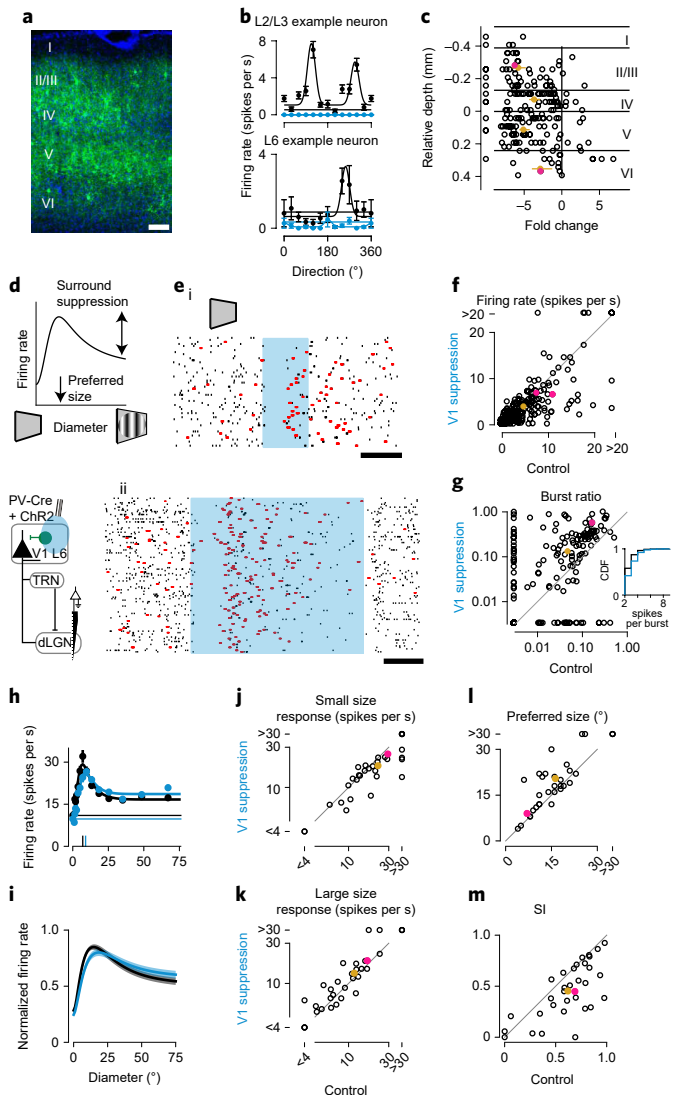
Model of CT feedback effects on dLGN spatial integration.

How might CT feedback shape dLGN spatial integration via inhibition? We first investigated this question through a previously developed mechanistic firing rate model of the dLGN, the extended difference-of-Gaussians model (eDoG)^{23,24} (Fig. 3a and Supplementary Table 1). While the eDoG model makes clear simplifications, for instance by not explicitly considering intracortical connectivity or transformations²³, its conceptually and mathematically simple framework and the availability of a simulation tool²⁴

make it a prime choice to explore how the spatial scale of inhibitory feedback shapes dLGN spatial integration.

To assess how inhibition via CT feedback might increase surround suppression and sharpen the RFs of dLGN neurons, we systematically varied the width of the inhibitory feedback coupling kernel (Fig. 3b) and simulated tuning curves for grating patches of different sizes, with and without CT feedback (Fig. 3b). When we set the width parameter of the inhibitory CT feedback kernel to equal the width of the excitatory CT feedback kernel ($\sigma_{\text{inh fb}} = \sigma_{\text{exc fb}}$), the model failed to replicate our experimentally observed results (Fig. 3b(i)); CT feedback had an overall suppressive effect, reducing responses for all stimulus sizes (22.8% decrease for preferred stimulus size; 23.1% decrease for largest stimulus size) and failed to substantially alter the preferred stimulus size and surround suppression (1.9% increase). We then increased the spatial scale of inhibitory CT feedback to match the spatial scale of feed-forward inhibition ($\sigma_{\text{inh fb}} = \sigma_{\text{inh ff}}$; Fig. 3b(ii)). Now CT feedback began to decrease the preferred size (9.1% decrease) and increase surround suppression (42.7% increase), but it still led to weaker responses overall, even for small sizes (14.6% decrease for preferred stimulus size; 22.9% decrease for largest stimulus size). Only when the width of the inhibitory CT feedback component was sufficiently large ($\sigma_{\text{inh fb}} = 9 \times \sigma_{\text{exc fb}}$; Fig. 3b(iii)) did our simulations yield a pattern comparable to the size-dependent effects observed on average

Fig. 2 | CT feedback effects on dLGN size tuning. **a**, Representative V1 coronal section from a PV-Cre mouse with Cre-dependent AAV-ChR2; green, ChR2-YFP; blue, DAPI; scale bar, 100 μm . **b**, Example direction-tuning curves of neurons in putative L2/L3 (top) or L6 (bottom); visual stimulus, drifting gratings with temporal and spatial frequencies coarsely optimized for the recording, 0.75-s duration; photostimulation, starting 0.1 s before stimulus onset and lasting 0.85 s. **c**, Effect of V1 suppression (fold change across tuning experiments with parameters as described in **b**) as a function of cortical depth relative to the base of L4, estimated by CSD (Methods); gold, layer-wise mean; pink, example neurons. Error bars represent confidence intervals of the mean determined by bootstrapping; $n = 197$ neurons. **d**, Top, schematic size-tuning curve. Bottom, schematic of a recording. **e**, Recordings from the dLGN. Responses of two example dLGN neurons to gray screen (size, 0°) aligned to V1 suppression (shaded blue) are shown; red, burst spikes; black horizontal bar, 200 ms; i, $n = 54$ trials; ii, $n = 105$ trials. In all trials, the run speed was $\leq 0.25 \text{ cm s}^{-1}$. **f**, Firing rates during versus before V1 suppression; $n = 276$ neurons; $P = 1.5 \times 10^{-5}$, two-sided Wilcoxon signed-rank test. **g**, Ratio of burst spikes during versus before V1 suppression; $n = 232$ neurons; $P = 4.1 \times 10^{-11}$, two-sided Wilcoxon signed-rank test. Data points at the margins represent a burst ratio of 0. The inset shows the cumulative distribution function (CDF) of burst lengths during (blue) versus before (black) V1 suppression ($P = 3.6 \times 10^{-13}$, two-sample Kolmogorov-Smirnov test). **h**, Size-tuning curves of an example dLGN neuron. Vertical bars represent preferred size, and horizontal lines represent responses to a blank screen (size, 0°); visual stimulus, drifting gratings with orientation, temporal and spatial frequencies coarsely optimized for the recording, 0.75-s duration; photostimulation, starting 0.04 s before stimulus onset and lasting 0.85 s. **i**, Means of RoG fits for the dLGN population ($n = 33$; shaded areas represent s.e.m.). **j-m**, Comparison of V1 suppression to control conditions for responses to a small-sized stimulus ($P = 0.0018$) (**j**), responses to a large-sized stimulus ($P = 0.03$) (**k**), the preferred size ($P = 0.00024$) (**l**) and SI ($P = 7.4 \times 10^{-5}$) (**m**) (all two-sided Wilcoxon signed-rank tests; $n = 33$ neurons). Error bars represent s.e.m. in **b** and **h**. Pink indicates an example neuron, and gold indicates the population mean in **f** and **g** and **j-m**. Markers of the two neurons indicated in pink almost completely overlap in **g**.



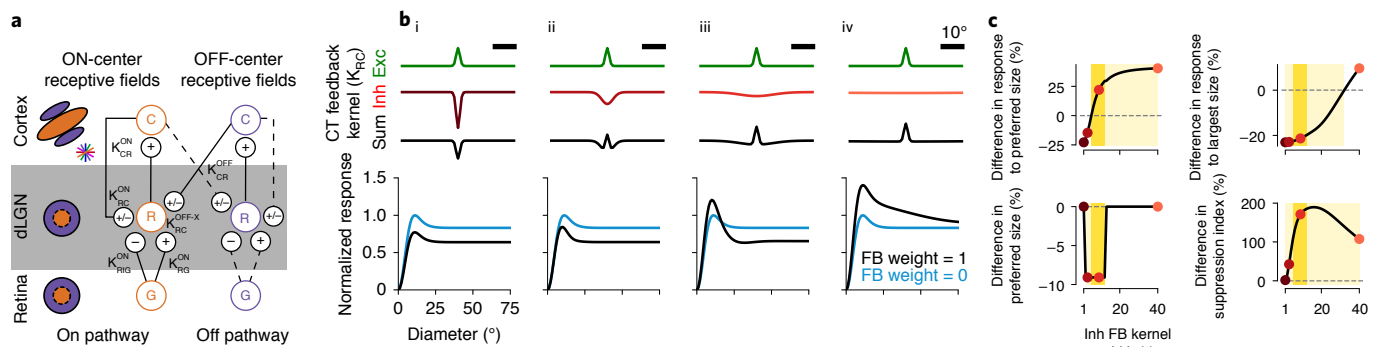


Fig. 3 | Model of CT feedback effects predicts wide inhibitory feedback coupling kernel. **a**, Schematic of the eDoG model²⁴. Center-surround RFs of dLGN relay cells (R) are modeled by feed-forward inputs from retinal ganglion cells (RGCs; G) and feedback inputs from the cortex (C). The three layers are connected by 2D Gaussian coupling kernels (K). RGCs, whose RFs are described by a DoG model, provide excitatory (K_{RG}) and inhibitory (K_{RIG}) feed-forward input to relay cells. CT feedback of both signs (K_{RC}) originates from a population of cortical cells, which receive input from the dLGN relay cells (K_{CR}). **b**, Effects of varying the width of the inhibitory CT feedback coupling kernel on simulated size-tuning curves. Top, excitatory (green) and inhibitory (red) CT feedback coupling kernels and their sum (black). **b**, Same width ($\sigma_{inh\ fb} = \sigma_{exc\ fb}$) (i), same width as inhibitory feed-forward kernel ($\sigma_{inh\ fb} = \sigma_{ff}$) (ii) and two larger widths ($\sigma_{inh\ fb} = 9 \times \sigma_{exc\ fb}$ (iii) and $\sigma_{inh\ fb} = 40 \times \sigma_{exc\ fb}$ (iv)). Note that the area under the curve is the same for all inhibitory feedback coupling kernels. Bottom, simulated dLGN size-tuning curves with cortical feedback intact (black) and abolished (blue). Responses are normalized to the peak response seen under the condition without CT feedback; inh, inhibitory; exc, excitatory; fb, feedback; ff, feed-forward. **c**, Effects of CT feedback for kernel widths between 1° and 40° (varied in 1° steps) on the response magnitude to the preferred (top left) and largest stimulus (top right), the preferred size (bottom left) and surround suppression (bottom right), revealed by zeroing the weight of CT feedback. Red points indicate kernel widths shown in **b**. Light yellow indicates parameter ranges yielding qualitatively similar results to experimental observations (single parameter) and dark yellow represents parameter ranges with valid results across all four variables. Light yellow ranges correspond to $5^\circ \leq \sigma_{inh\ fb} \leq 40^\circ$ (response to preferred size), $1^\circ \leq \sigma_{inh\ fb} \leq 32^\circ$ (response to largest size), $2^\circ \leq \sigma_{inh\ fb} \leq 12^\circ$ (preferred size) and $1^\circ \leq \sigma_{inh\ fb} \leq 40^\circ$ (suppression index). The dark yellow range corresponds to $5^\circ \leq \sigma_{inh\ fb} \leq 12^\circ$.

in the experimental data; while responses to the preferred stimulus size were enhanced (22.0% increase), responses to the largest stimulus size were suppressed (21.4% decrease). In accordance with the experimental data, we also observed that CT feedback decreased the preferred size (9.1% decrease) and strengthened surround suppression (171.2% increase). Finally, when we further increased the spatial scale of the inhibitory feedback kernel ($\sigma_{inh\ fb} = 40 \times \sigma_{exc\ fb}$; Fig. 3b(iv)), CT feedback increased firing rates independently of stimulus size (40.4% increase for preferred stimulus size; 9.7% increase for largest stimulus size) and enhanced surround suppression (107.7% increase) but did not affect the preferred stimulus size (0.0% change).

Analysis of simulations with more fine-grained variation of the width of the inhibitory CT feedback kernel revealed that feedback-induced amplification of responses to the preferred size and strengthening of surround suppression (Fig. 3c) required sufficiently wide kernels. Much wider kernels, however, failed to reproduce both the feedback-induced decrease of responses to larger stimulus sizes and the sharpening of RFs (Fig. 3c). This restricted the parameter range replicating our average experimental results to larger, but spatially confined, inhibitory feedback kernel widths (Fig. 3c). Taken together, our model suggests that cortical feedback enhances contextual effects in the dLGN via an inhibitory component that integrates information over a sufficiently large, yet still localized, spatial scale.

RF properties of mouse visTRN. A candidate circuit through which the cortex could exert widespread inhibitory influence over the dLGN is indirect inhibition via the visTRN (Fig. 4). Present in all mammals, the TRN comprises a sheath of GABAergic neurons surrounding the lateral and anterior parts of the thalamus²⁵. Because the TRN receives input from axon collaterals of both thalamic relay cells and CT neurons, it is in a prime position to modulate the flow of information between the thalamus and the cortex²⁵. Owing to its inhibitory projections to the dLGN, the visTRN has been considered

a ‘guardian of the gate to the cortex’²⁶ and has been implicated in gain control²⁶ and attentional selection^{27,28}.

To better understand how feedback signals from the primary visual cortex arrive in the visTRN, we first characterized the organization of V1 L6CT inputs by analyzing visTRN slices obtained in our triple-color viral tracing experiment (Fig. 4a). For injections along the V1 azimuth axis, we found clearly separated, topographically organized terminal fields within single coronal slices (Fig. 4a). For injections along the V1 elevation axis, the differently colored terminal fields in visTRN were distributed along the anterior–posterior (AP) axis (Extended Data Fig. 7).

To explore whether CT feedback might enhance surround suppression in the dLGN via the visTRN, we next performed silicon probe recordings (Fig. 4b) and tested whether mouse visTRN neurons have appropriate feature selectivity, that is, large, retinotopically organized RFs, responses that increase with stimulus size and little surround suppression. Because the visTRN is located near other thalamic nuclei with visually responsive neurons, we confirmed postmortem via retrograde viral labeling that our visTRN recording sites were in the vicinity of neurons that provided input to the dLGN (Fig. 4c). Indeed, after injection of rAAV2/retro-CMV-GFP (Methods) into the dLGN (Fig. 4c(i)), we found dense GFP expression in the dorsocaudal part corresponding to the visual sector of the TRN^{25,29} (Fig. 4c(ii)), with retrogradely labeled cell bodies localized near the DiI-labeled electrode track (Fig. 4c(iii)). This histological evidence, in combination with the robust visual responses encountered during our recordings, confirmed that we had indeed targeted the visTRN.

We first mapped classical RFs of single visTRN neurons using a sparse noise stimulus (Fig. 4d). RFs of visTRN neurons covered a wide range of sizes, with individual neurons displaying small (Fig. 4d, second from the right: area = 169.3(°)²; $R^2 = 0.92$) or large RFs (Fig. 4d, far right: area = 780.5(°)²; $R^2 = 0.84$). Focusing on RFs obtained within a single penetration (Fig. 4e), we realized that fitted RF centers followed a coarse retinotopy, with neurons recorded at

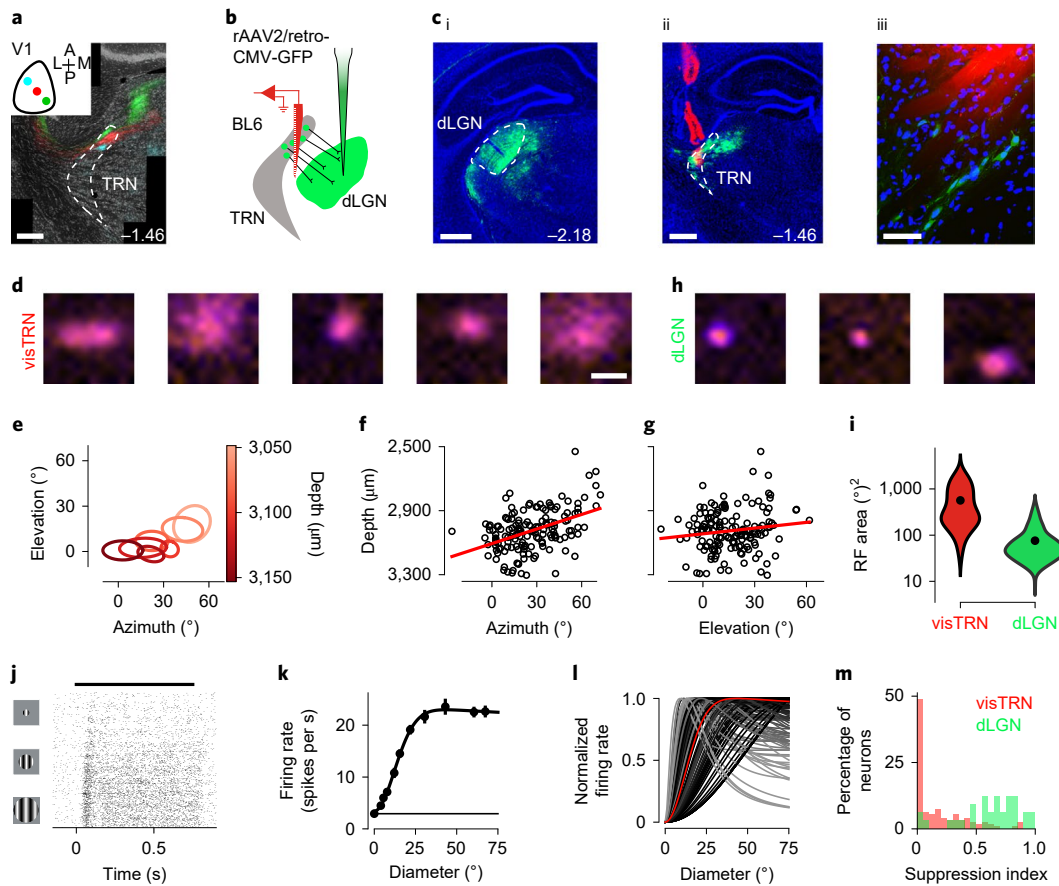


Fig. 4 | Retinotopic organization and RF properties of visTRN neurons. **a**, V1 L6CT terminal fields in the visTRN obtained from triple-color viral injections along the V1 azimuth axis (Fig. 1a and Extended Data Fig. 7). The dashed outline represents the TRN; scale bar, 0.25 mm. Numbers indicate the distance from the bregma in millimeters. The inset represents the V1 injection pattern. Observations were reproduced in four mice, and two additional examples are shown in Extended Data Fig. 7. **b**, Schematic of retrograde viral labeling of visTRN neurons from the dLGN (rAAV2-retro; Methods). **c**, GFP labeling of visTRN neurons in an example mouse. **c**, dLGN injection site (i). The dashed outline indicates the dLGN; scale bar, 0.5 mm. visTRN neurons labeled by retrograde AAV and visTRN recording site are shown (ii), and the dashed outline indicates the TRN; scale bar, 0.5 mm. Magnified view around the tip of the electrode trace from the slice shown in i (iii); scale bar, 50 μ m; blue, DAPI; green, GFP; red, Dil-labeled electrode trace. This pattern was observed in three mice. **d**, Representative images of classical RFs for five example visTRN neurons; orange, OFF response; purple, ON response; scale bar, 20°. **e**, RF fits in an example visTRN recording session ($n=7$ simultaneously recorded neurons). **f**, Comparison of the recording depth and the azimuth coordinate of the RF center for the visTRN population ($n=154$). The red line indicates the linear regression ($R^2=0.2$; $P=5.43 \times 10^{-9}$ (slope)). **g**, Same as **f** but for the elevation coordinate ($R^2=0.02$; $P=0.08$). **h**, Representative images of classical RFs for three dLGN example neurons; scale, same as in **d**. **i**, Comparison of classical RF sizes for recorded visTRN ($n=218$) and dLGN ($n=197$) neurons. Outlines indicate the distribution of classical RF sizes; black, mean; $P=1.0 \times 10^{-51}$, two-sided Mann-Whitney U -test. **j**, Raster plot of an example visTRN neuron recorded in a size-tuning experiment. Trials are sorted by stimulus size with lower rows corresponding to larger sizes; 50 trials per size. The black horizontal bar represents stimulus presentation. **k**, Size-tuning curve corresponding to **j**. The horizontal line indicates response to size 0°. Error bars represent s.e.m. **l**, Size-tuning curves for the visTRN cell population ($n=125$). Strength of surround suppression is represented by darkness of the line; red, example neuron from **j** and **k**. **m**, Distribution of suppression indices for the visTRN (red) and dLGN (green).

deeper, more ventral electrode sites having more central RF locations (Fig. 4e). Both RF azimuth ($n=154$; $P=5.43 \times 10^{-9}$; Fig. 4f) and elevation ($P=0.08$; Fig. 4g) predicted recording depth, but the relationship was considerably stronger for azimuth ($P=0.028$, analysis of covariance (ANCOVA)). Importantly, the retinotopic organization of visTRN neurons seems to match the topographic arrangement of the V1 L6CT feedback terminal fields (compare to Fig. 4a and Extended Data Fig. 7).

While the overall match between retinotopy of the CT innervation and visTRN organization is consistent with preserving spatial information, our simulations predicted inhibitory feedback to be spatially extensive, so we next focused on visTRN RF size. Comparing the classical RF size of the visTRN ($n=218$ neurons; 566.1 ± 37.4 (°)² (mean \pm s.e.m.)); examples in Fig. 4d) with a population of dLGN

neurons measured under the same conditions ($n=197$; 75.9 ± 5.1 (°)²; examples in Fig. 4h) revealed that, despite having overlapping distributions, classical RFs of visTRN neurons were on average 7.5 \times larger ($P=1.0 \times 10^{-51}$, Mann-Whitney U -test) and more variable in size ($P=8.3 \times 10^{-23}$, Brown-Forsythe test; Fig. 4i).

Finally, centered on the RFs, we presented drifting gratings of various sizes and fit the averaged responses in trials without locomotion (run speed < 0.25 cm s⁻¹ for more than half of the trial duration) with the RoG model (Fig. 4j–m). Analogous to our analysis of dLGN size tuning, we used the model fit to determine, for each visTRN neuron, its preferred size and the strength of surround suppression. Like the example neuron (SI, 0.02; Fig. 4j,k), the majority of visTRN neurons experienced little to no surround suppression ($n=125$ visTRN neurons; median SI, 0.06; Fig. 4l,m), a value

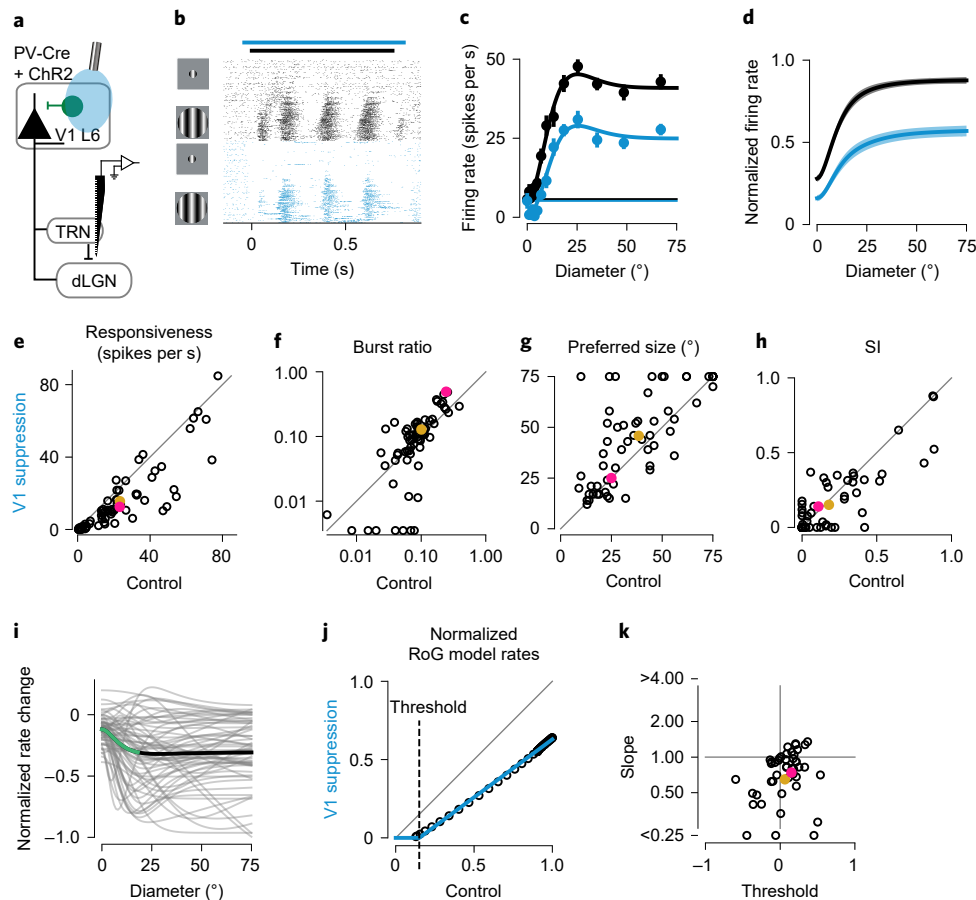


Fig. 5 | Suppression of cortical feedback reduces responses and increases preferred stimulus size in the visTRN. **a**, Schematic of the experimental approach. **b**, Raster plot of a visTRN neuron recorded in a size-tuning experiment. Trials are sorted by feedback condition and stimulus size, with lower rows corresponding to larger stimulus sizes (20 trials per size and feedback condition; black horizontal bar, stimulus presentation; blue horizontal bar, V1 suppression period); visual stimulus, drifting gratings with temporal and spatial frequencies coarsely optimized for the recording, 0.75-s duration; photostimulation, starting 0.04 s before stimulus onset and lasting for 0.85 s. **c**, Size-tuning curves, same neuron as in **b**. Horizontal bars represent response to size 0°, and error bars represent s.e.m. **d**, Means of RoG fits for the visTRN population ($n=63$; shaded areas represent s.e.m.). **e–h**, Mean evoked response ($n=67$; $P=4.9 \times 10^{-10}$) (**e**), burst ratio ($n=67$; $P=0.006$) (**f**), preferred size ($n=61$; $P=0.001$) (**g**) and SIs ($n=61$; $P=0.18$) (**h**) (all two-sided Wilcoxon signed-rank tests) for the visTRN cell population. In **f**, data points at the margins represent neurons whose burst ratios were 0. **i**, Difference between normalized RoG models for V1 suppression and control conditions (gray, single visTRN neurons; black, population mean; green, size range in which a 1° increase in size led to a significant increase in the CT feedback effect (0–18°; $P < 0.05$, bootstrap test; $n=63$). For sizes >18°, the CT feedback effect plateaus. **j**, Threshold-linear fit (blue) to RoG model evaluated in 1° steps (black) for the visTRN neuron in **b** and **c** (slope, 0.74; threshold, 0.15; $R^2=1$). **k**, Slope ($P=2.8 \times 10^{-5}$) and threshold ($n=46$; $P=0.04$, two-sided Wilcoxon signed-rank test) parameters extracted from threshold-linear fits for the visTRN population. Blue represents V1 suppression, and black represents control in **b–d**. In **e–j**, pink indicates an example neuron, and gold indicates the population mean.

significantly smaller than that found in dLGN neurons ($n=33$ dLGN neurons; median SI, 0.69; $P=2.8 \times 10^{-12}$, Mann–Whitney U -test; Fig. 4m). Thus, similar to neurons in the visTRN of carnivores (perigeniculate nucleus)³⁰, mouse visTRN neurons show retinotopic organization, have spatially localized yet large RFs and experience little surround suppression themselves. By responding weakly to small stimuli and strongly during presentation of large stimuli, the properties of inhibitory visTRN neurons are well suited for sculpting dLGN surround suppression.

Effects of CT feedback suppression on the visTRN. To test whether the visTRN would be able to provide CT feedback-mediated indirect inhibition, we measured the responses of visTRN neurons in PV-Cre mice to drifting gratings of varying size while suppressing CT feedback by photoactivating PV⁺ inhibitory interneurons in V1 (Fig. 5a). When we inspected the raster plots (Fig. 5b) and fitted size-tuning curves (RoG model) of single visTRN neurons

(Fig. 5b and Extended Data Fig. 8a–j, again focusing on trials without locomotion), we found that suppressing V1 reduced overall responsiveness. This reduction was robust not only for the neuron shown in Fig. 5b,c (–46.2%) but also for the population of recorded visTRN neurons (V1 suppression = 15.6 ± 2.2 spikes per s and control = 23.4 ± 2.5 spikes per s; $n=67$; $P=4.9 \times 10^{-10}$, Wilcoxon signed-rank test; Fig. 5d,e). Similar to our findings in the dLGN, suppressing V1 also increased visTRN neuron burst ratios (V1 suppression = 12.8% and control = 10.1%; $n=67$ neurons; $P=0.006$, Wilcoxon signed-rank test; Fig. 5f). We conclude from the substantial reduction in responsiveness during V1 suppression that the visTRN is strongly engaged by CT feedback.

More closely inspecting the parameters of the fitted size-tuning curves, we realized that the reduction of visTRN responses during V1 suppression was not uniform across stimulus sizes. Focusing on those visTRN neurons that were still responsive during V1 suppression (mean firing rate ≥ 0.1 spikes per s; 61 of 67 neurons), we

found that V1 suppression increased visTRN preferred size (V1 suppression = $45.8 \pm 2.9^\circ$ and control = $38.5 \pm 2.7^\circ$; $n = 61$ neurons; $P = 0.001$, Wilcoxon signed-rank test; Fig. 5g). This increase indicates that visTRN's peak inhibitory output to the dLGN might shift toward larger stimulus sizes, which could contribute, besides the overall reduction in strength of the inhibitory CT feedback component, to our observation that V1 suppression increased dLGN preferred size (Fig. 2l). While we found the effects of CT feedback on the visTRN to be overall consistent, the remaining variability across the visTRN population was unrelated to several visTRN response properties (Extended Data Fig. 9).

While CT feedback did not change the overall strength of surround suppression in the visTRN (SI during V1 suppression = 0.15 ± 0.03 and control = 0.18 ± 0.03 ; $n = 61$; $P = 0.18$, Wilcoxon signed-rank test; Fig. 5h and Extended Data Fig. 8k), we found that modulation of visTRN responses by CT feedback nevertheless was not constant across stimulus sizes. Inspection of the differences in the normalized fitted size-tuning curves between the two conditions showed that responses to larger stimuli ($>18^\circ$) were more strongly affected by V1 suppression than responses to smaller stimuli ($0-18^\circ$), where the effect of CT feedback steadily increased ($n = 63$; $P < 0.05$, bootstrap test; Fig. 5d,i). Hence, while CT feedback seems to enhance visTRN responses across all stimulus sizes, this enhancement became progressively stronger with increasing stimulus size before reaching a plateau.

What is the nature of the transformation exerted by CT feedback on visTRN responses? To identify to what degree visTRN responses during suppression of CT feedback change in a subtractive or divisive manner³¹, we fit a threshold-linear model (Fig. 5j), which predicts responses during V1 suppression by shifting and scaling responses observed under the control condition. Because V1 suppression cannot lead to negative firing rates, the model additionally contained a threshold for activation. Although it is impossible for this simple model to capture the observed changes in preferred size, it still fitted the effects of V1 suppression on size-tuning curves reasonably well (46 of 63 neurons with $R^2 \geq 0.8$). Focusing on this subset of well-fit neurons, in which V1 suppression had mainly linear effects, we found for both the neuron shown in Fig. 5j ($R^2 = 1$; threshold = 0.15; slope = 0.74; same neuron as in Fig. 5b,c) and the recorded population as a whole (Fig. 5k) a mild subtractive effect (threshold = 0.06 ± 0.04 , mean \pm s.e.m.; $P = 0.04$, Wilcoxon signed-rank test) and a substantial and consistent divisive effect (slope = 0.65 ± 1.13 ; $P = 2.8 \times 10^{-5}$, Wilcoxon signed-rank test; Fig. 5k). Because divisive scaling implies that high firing rates are reduced most, and visTRN neurons have high responses to large stimuli (Fig. 4j-m), this analysis further corroborates our finding that CT feedback strongly engages visTRN activity in response to large stimuli. Such size-dependent recruitment of inhibition via the visTRN by CT feedback might account for our earlier finding that the dLGN's responses to large stimuli are enhanced when CT feedback is suppressed (Fig. 2k). Taken together, the substantial modulation of visTRN responses, and the size-dependent recruitment of inhibitory visTRN responses by CT feedback, make visTRN an ideal candidate for mediating feedback-enhanced surround suppression in the dLGN.

Discussion

Using a combination of viral tracing, bidirectional optogenetic manipulations and computational modeling, we have shown that one role of the retinotopically organized cortical feedback to the mouse dLGN is to sculpt spatial integration by sharpening RFs and enhancing surround suppression. We identified spatially specific, distant suppressive influences of CT feedback, which are most consistent with indirect inhibition. In accordance with simulations in our thalamocortical network model, which indicated that widespread inhibitory CT feedback is required to reproduce our

experimental results, we show that the spatial selectivity of neurons in the visTRN and their size-specific recruitment by CT feedback make them an ideal candidate for mediating feedback-enhanced surround suppression in the dLGN. Therefore, CT feedback, most probably with the involvement of the visTRN, sharpens spatial responses and strengthens contextual modulations in the dLGN.

Spatial integration in the dLGN. Spatial integration in the dLGN is achieved by multiple mechanisms, as surround suppression occurs both up- and downstream of the dLGN. These mechanisms include inheritance from feed-forward retinal input³², augmentation via non-linearities at the retinogeniculate relay³³, recurrent thalamic inhibition³⁴ and CT feedback^{10,11}. The CT feedback-mediated sharpening of RFs and strengthening of the center-surround antagonism that we found in the dLGN of awake mice parallels earlier results in anesthetized cats¹⁰, ferrets¹² and non-human primates^{9,11}. The effects of CT feedback on spatial integration we observed in the dLGN have similar signatures to those of corticocortical feedback^{35,36}, suggesting that the sculpting of spatial integration could represent a canonical function of feedback in the visual system. Finally, CT feedback also sharpens stimulus selectivity in other sensory modalities, such as the primate and rat somatosensory system^{37,38} or the bat echolocation system³⁹.

The role of the TRN. By measuring RF properties in the visTRN and their modulation by CT feedback and by simulating the impact of inhibitory feedback at various spatial scales in a mechanistic dLGN model²⁴, we found evidence that CT feedback can sculpt dLGN spatial integration via the visTRN. While the visTRN has long been implicated in controlling the dLGN²⁶, the specific form of this control has been a matter of debate, ranging from homogenizing dLGN activity ('thermostat hypothesis') to triggering focal rebound excitation in the dLGN ('searchlight hypothesis')^{26,40}. Although our results share with the 'searchlight hypothesis' its component of spatial specificity, they also differ by implying that dLGN spatial selectivity might be enhanced by direct localized excitation from L6CT pyramidal cells acting in concert with indirect, more widespread inhibition from the visTRN. Alternative sources of indirect inhibition in the dLGN are local interneurons³⁴. To disentangle the relative contributions of dLGN interneurons and the visTRN to feedback-enhanced surround suppression in the dLGN, targeted recordings from geniculate interneurons, and an assessment of their modulation by CT feedback, will be a crucial next step.

In contrast to the modulatory effects of CT feedback in the dLGN, we found V1 suppression to substantially reduce visTRN responses. While our estimation of a ~50% V1 contribution to visTRN firing rates during size tuning matches observations in slice preparations⁴¹, the effects of CT feedback suppression on the visTRN in vivo range from strong suppression⁴² to no changes³⁰. A possible explanation for this discrepancy might be that in anesthetized animals, the effects of CT feedback on visTRN responses have been underestimated, because the responsiveness of CT feedback projections might be particularly reduced during anesthesia, and attentional processes recruiting CT feedback are lacking^{28,42}.

Besides the pronounced reduction in responsiveness of visTRN neurons during V1 suppression, we also observed an increase in preferred size. These findings are consistent with at least two mechanisms. Increased visTRN preferred size during V1 suppression might simply reflect the increased preferred size of the dLGN providing feed-forward input to the visTRN. In addition, the increased burst ratio in the visTRN during V1 suppression might also contribute, because the slow, low-threshold calcium current underlying bursts should more efficiently propagate through the TRN's electrical synapses and thus might increase the spatial spread of activation.

For future studies, it will be interesting to compare the impact of CT feedback on lower- and higher-order subnetworks within the

visTRN²⁹ and the dynamic, behavioral state dependence of activity and selectivity of visTRN neurons²⁸.

Manipulating CT feedback. Which alternative circuits could be affected by our reliable²¹, yet global, suppression of CT feedback through PV⁺ activation? Global V1 suppression will also influence corticofugal L5 neurons targeting the superior colliculus (SC), which in turn provide excitatory, driving input to the dLGN⁴³. We regard it, however, as unlikely that the effects observed in our study are mediated via the SC; effects of direct SC suppression on dLGN responses are limited to the dorsal-most 150 μm of the dLGN⁴⁴, and suppressing V1 affects SC responses independently of stimulus size⁴⁵. We also think it is unlikely that intracortical rebound effects at the edge of the cortical area undergoing optogenetic suppression drive our main conclusions, because such effects have not been prominent in previous studies quantifying the lateral extent of cortical suppression²¹. In addition, we have found a consistent spatial pattern of CT feedback effects in the dLGN with both global V1 suppression and L6CT photoactivation, which likely recruit intracortical circuits in different ways. To rule out contributions via polysynaptic circuits during global suppression, it is not sufficient to selectively suppress L6CT pyramidal cells at the level of V1 (refs. ^{13,46}), because their intracortical axon collateral makes privileged connections with a translaminal PV⁺ interneuron subtype in L6 (refs. ^{19,20}), which in turn strongly regulates the gain of the entire V1 column^{13,19,20}. Instead, a more promising next step would be to directly suppress axon terminals of L6CT pyramidal cells at the thalamic target.

Our results contribute to an emerging view, according to which manipulation of L6CT pyramidal cells does not simply produce global gain changes in the dLGN, and photostimulation and photosuppression do not simply produce changes with opposite sign. First, effects of L6CT activation cannot be described by a global gain factor, because these effects have a spatial profile, ranging from facilitation in the dLGN region corresponding to the retinotopic location of the L6 source to suppression beyond. Second, effects of CT feedback on sensory thalamic nuclei are known to be frequency dependent^{6,47}, reflecting the distinct short-term dynamics of synapses in the CT circuit. Complicating the matter further, CT feedback can increase dLGN firing not only via net depolarization but also by sustained hyperpolarization and rebound firing²⁶ through deinactivation of low-threshold, T-type Ca²⁺ channels²² and subsequent bursting.

L6CT pyramidal cells, as targeted by the Ntsr1-Cre line^{19,20}, are not homogeneous but are known to contain at least two subtypes defined by morphology^{19,20,48}, three subtypes defined by electrophysiology and morphology⁴⁸ and four major subtypes defined by transcriptomics⁴⁸. For the mouse, it is currently unknown whether these subtypes differentially contribute to modulation by CT feedback. In the visual system of primates and carnivores, where feed-forward processing along the retino-geniculate-cortical pathway occurs in functionally segregated parallel pathways, CT feedback circuits seem to mimic this organization both in terms of morphology⁴⁹ and function⁵⁰ of L6CT pyramidal cells. Functional cell typing of our dLGN and visTRN population revealed only subtle, if any, differential effects of CT feedback, which might not be so surprising given our strategy of global V1 suppression. In the future, investigating to what extent excitatory and inhibitory feedback pathways are recruited under different stimulus and behavioral conditions, and with specificity for L6CT subtypes, will likely yield more complete answers.

Online content

Any methods, additional references, Nature Research reporting summaries, source data, extended data, supplementary information, acknowledgements, peer review information; details of author contributions and competing interests; and statements of

data and code availability are available at <https://doi.org/10.1038/s41593-021-00943-0>.

Received: 9 June 2020; Accepted: 15 September 2021;
Published online: 11 November 2021

References

- Thorpe, S., Fize, D. & Marlot, C. Speed of processing in the human visual system. *Nature* **381**, 520–522 (1996).
- Resulaj, A., Ruediger, S., Olsen, S. R. & Scanziani, M. First spikes in visual cortex enable perceptual discrimination. *eLife* **7**, e34044 (2018).
- Yamins, D. L. K. & DiCarlo, J. J. Using goal-driven deep learning models to understand sensory cortex. *Nat. Neurosci.* **19**, 356–365 (2016).
- Harris, K. D. & Mrsic-Flogel, T. D. Cortical connectivity and sensory coding. *Nature* **503**, 51–58 (2013).
- Sherman, S. M. & Guillery, R. W. The role of the thalamus in the flow of information to the cortex. *Philos. Trans. R. Soc. B Biol. Sci.* **357**, 1695–1708 (2002).
- Crandall, S. R., Cruikshank, S. J. & Connors, B. W. A corticothalamic switch: controlling the thalamus with dynamic synapses. *Neuron* **86**, 768–782 (2015).
- Tsumoto, T., Creutzfeldt, O. D. & Legéndy, C. R. Functional organization of the corticofugal system from visual cortex to lateral geniculate nucleus in the cat. *Exp. Brain Res.* **32**, 345–364 (1978).
- Ichida, J. M. & Casagrande, V. A. Organization of the feedback pathway from striate cortex (V1) to the lateral geniculate nucleus (LGN) in the owl monkey (*Aotus trivirgatus*). *J. Comp. Neurol.* **454**, 272–283 (2002).
- McClurkin, J. W. & Marrocco, R. T. Visual cortical input alters spatial tuning in monkey lateral geniculate nucleus cells. *J. Physiol.* **348**, 135–152 (1984).
- Murphy, P. C. & Sillito, A. M. Corticofugal feedback influences the generation of length tuning in the visual pathway. *Nature* **329**, 727–729 (1987).
- Jones, H. E. et al. Differential feedback modulation of center and surround mechanisms in parvocellular cells in the visual thalamus. *J. Neurosci.* **32**, 15946–15951 (2012).
- Hasse, J. M. & Briggs, F. Corticogeniculate feedback sharpens the temporal precision and spatial resolution of visual signals in the ferret. *Proc. Natl Acad. Sci. USA* **114**, E6222–E6230 (2017).
- Olsen, S. R., Bortone, D. S., Adesnik, H. & Scanziani, M. Gain control by layer six in cortical circuits of vision. *Nature* **483**, 47–52 (2012).
- Piscopo, D. M., El-Danaf, R. N., Huberman, A. D. & Niell, C. M. Diverse visual features encoded in mouse lateral geniculate nucleus. *J. Neurosci.* **33**, 4642–4656 (2013).
- Erisken, S. et al. Effects of locomotion extend throughout the mouse early visual system. *Curr. Biol.* **24**, 2899–2907 (2014).
- Sachdev, R. N. S., Krause, M. R. & Mazer, J. A. Surround suppression and sparse coding in visual and barrel cortices. *Front. Neural Circuits* **6**, 43 (2012).
- Dakin, S., Carlin, P. & Hemsley, D. Weak suppression of visual context in chronic schizophrenia. *Curr. Biol.* **15**, R822–R824 (2005).
- Vélez-Fort, M. et al. The stimulus selectivity and connectivity of layer six principal cells reveals cortical microcircuits underlying visual processing. *Neuron* **83**, 1431–1443 (2014).
- Bortone, D. S., Olsen, S. R. & Scanziani, M. Translaminal inhibitory cells recruited by layer 6 corticothalamic neurons suppress visual cortex. *Neuron* **82**, 474–485 (2014).
- Frandonig, J. E. et al. The synaptic organization of layer 6 circuits reveals inhibition as a major output of a neocortical sublamina. *Cell Rep.* **28**, 3131–3143 (2019).
- Li, N. et al. Spatiotemporal constraints on optogenetic inactivation in cortical circuits. *eLife* **8**, e48622 (2019).
- Sherman, S. M. Tonic and burst firing: dual modes of thalamocortical relay. *Trends Neurosci.* **24**, 122–126 (2001).
- Einenvoll, G. T. & Plesser, H. E. Extended difference-of-Gaussians model incorporating cortical feedback for relay cells in the lateral geniculate nucleus of cat. *Cogn. Neurodyn.* **6**, 307–324 (2012).
- Mobarhan, M. H. et al. Firing-rate based network modeling of the dLGN circuit: effects of cortical feedback on spatiotemporal response properties of relay cells. *PLoS Comput. Biol.* **14**, e1006156 (2018).
- Crabtree, J. W. Functional diversity of thalamic reticular subnetworks. *Front. Syst. Neurosci.* **12**, 41 (2018).
- Crick, F. Function of the thalamic reticular complex: the searchlight hypothesis. *Proc. Natl Acad. Sci. USA* **81**, 4586–4590 (1984).
- McAlonan, K., Cavanaugh, J. & Wurtz, R. H. Guarding the gateway to cortex with attention in visual thalamus. *Nature* **456**, 391–394 (2008).
- Halassa, M. M. et al. State-dependent architecture of thalamic reticular subnetworks. *Cell* **158**, 808–821 (2014).
- Martinez-Garcia, R. I. et al. Two dynamically distinct circuits drive inhibition in the sensory thalamus. *Nature* **583**, 813–818 (2020).
- Jones, H. E. & Sillito, A. M. The length–response properties of cells in the feline perigeniculate nucleus. *Eur. J. Neurosci.* **6**, 1199–1204 (1994).

31. Béhuret, S., Deleuze, C. & Bal, T. Corticothalamic synaptic noise as a mechanism for selective attention in thalamic neurons. *Front. Neural Circuits* **9**, 80 (2015).
32. Alitto, H. J. & Usrey, W. M. Origin and dynamics of extraclassical suppression in the lateral geniculate nucleus of the macaque monkey. *Neuron* **57**, 135–146 (2008).
33. Alitto, H. J. & Usrey, W. M. Surround suppression and temporal processing of visual signals. *J. Neurophysiol.* **113**, 2605–2617 (2015).
34. Hirsch, J. A., Wang, X., Sommer, F. T. & Martinez, L. M. How inhibitory circuits in the thalamus serve vision. *Annu. Rev. Neurosci.* **38**, 309–329 (2015).
35. Nurminen, L., Merlin, S., Bijanzadeh, M., Federer, F. & Angelucci, A. Top-down feedback controls spatial summation and response amplitude in primate visual cortex. *Nat. Commun.* **9**, 2281 (2018).
36. Vangeneugden, J. et al. Activity in lateral visual areas contributes to surround suppression in awake mouse V1. *Curr. Biol.* **29**, 4268–4275 (2019).
37. Temereanca, S. & Simons, D. J. Functional topography of corticothalamic feedback enhances thalamic spatial response tuning in the somatosensory Whisker/Barrel system. *Neuron* **41**, 639–651 (2004).
38. Ergenzinger, E., Glasier, M., Hahn, J. & Pons, T. Cortically induced thalamic plasticity in the primate somatosensory system. *Nat. Neurosci.* **1**, 226–229 (1998).
39. Zhang, Y., Suga, N. & Yan, J. Corticofugal modulation of frequency processing in bat auditory system. *Nature* **387**, 900–903 (1997).
40. Soto-Sánchez, C., Wang, X., Vaingankar, V., Sommer, F. T. & Hirsch, J. A. Spatial scale of receptive fields in the visual sector of the cat thalamic reticular nucleus. *Nat. Commun.* **8**, 800 (2017).
41. Golshani, P., Liu, X. B. & Jones, E. G. Differences in quantal amplitude reflect GluR4-subunit number at corticothalamic synapses on two populations of thalamic neurons. *Proc. Natl Acad. Sci. USA* **98**, 4172–4177 (2001).
42. Montero, V. M. Attentional activation of the visual thalamic reticular nucleus depends on ‘top-down’ inputs from the primary visual cortex via corticogeniculate pathways. *Brain Res.* **864**, 95–104 (2000).
43. Bickford, M. E., Zhou, N., Krahe, T. E., Govindaiah, G. & Guido, W. Retinal and tectal “Driver-Like” inputs converge in the shell of the mouse dorsal lateral geniculate nucleus. *J. Neurosci.* **35**, 10523–10534 (2015).
44. Ahmadlou, M., Zweifel, L. S. & Heimel, J. A. Functional modulation of primary visual cortex by the superior colliculus in the mouse. *Nat. Commun.* **9**, 3895 (2018).
45. Ahmadlou, M., Tafreshiha, A. & Heimel, J. A. Visual cortex limits pop-out in the superior colliculus of awake mice. *Cereb. Cortex* **27**, 5772–5783 (2017).
46. Spacek, M. A. et al. Robust effects of corticothalamic feedback during naturalistic visual stimulation. Preprint at *bioRxiv* <https://doi.org/10.1101/776237> (2021).
47. Kirchgessner, M. A., Franklin, A. D. & Callaway, E. M. Context-dependent and dynamic functional influence of corticothalamic pathways to first- and higher-order visual thalamus. *Proc. Natl Acad. Sci. USA* **117**, 13066–13077 (2020).
48. Gouwens, N. W. et al. Classification of electrophysiological and morphological neuron types in the mouse visual cortex. *Nat. Neurosci.* **22**, 1182–1195 (2019).
49. Briggs, F., Kiley, C. W., Callaway, E. M. & Usrey, W. M. Morphological substrates for parallel streams of corticogeniculate feedback originating in both V1 and V2 of the Macaque monkey. *Neuron* **90**, 388–399 (2016).
50. Briggs, F. & Usrey, W. M. Parallel processing in the corticogeniculate pathway of the Macaque monkey. *Neuron* **62**, 135–146 (2009).

Publisher's note Springer Nature remains neutral with regard to jurisdictional claims in published maps and institutional affiliations.

© The Author(s), under exclusive licence to Springer Nature America, Inc. 2021

Methods

All procedures complied with the European Communities Council Directive 2010/63/EU and the German Law on the Protection of Animals and were approved by local authorities following appropriate ethics review.

Experiments were performed on three strains of adult mice of both sexes, including C57BL/6J ($n=3$; mean age = 14.2 weeks) and PV-Cre (B6.129P2-*Pvalb^{tm1(cre)Arb}/J*; $n=19$; mean age = 23.3 weeks) obtained from the Jackson Laboratory and Ntsr1-Cre⁵¹ (B6.FVB(Cg)-Tg(*Ntsr1-cre*)GN220Gsat/Mmcd; $n=20$; mean age = 24.4 weeks; MMRRC).

Virus used for triple-color tracing. pAAV-CAG-FLEX-GFP was a gift from M. Parmar (Developmental and Regenerative Neurobiology, Lund University), pAAV-CAG-FLEX-mScarlet was a gift from R. Larsen (Allen Institute for Brain Science; Addgene, 99280; <http://n2t.net/addgene:99280>; RRID: [Addgene_99280](https://doi.org/10.6281/addgene.99280)) and pAAV-TRE-DIO-mTurquoise2 was a gift from V. Gradinaru (Neuroscience and Biological Engineering, California Institute of Technology; Addgene, 99115; <http://n2t.net/addgene:99115>; RRID: [Addgene_99115](https://doi.org/10.6281/addgene.99115))⁵². pAAV-CAG-FLEX-mTurquoise2 was generated in the viral vector facility of the Ludwig-Maximilians-Universität München (LMU) by the restriction digest and ligation method using pAAV-CAG-FLEX-mScarlet as a pAAV backbone, replacing mScarlet with AscI-FseI/Blunt restriction sites and inserting mTurquoise2 (AscI/NheI-Blunt) from pAAV-TRE-DIO-mTurquoise2.

AAV production. High-titer preparations of rAAV2/1 and rAAV2/retro were produced based on the protocol by Zolotukhin and colleagues⁵³ with minor modifications. In brief, HEK 293T cells (ATCC, CRL-3216) were transfected with the CaPO₄ precipitate method. For triple-color viral tracing, the pAAV plasmid, Ad helper (Cell Biolabs, gb AF369965.1) and pRC1 (Cell Biolabs) were applied in an equimolar ratio. For retrograde viral tracing, the plasmids rAAV2-retro (Addgene, 81070)⁵⁴, Ad helper (Cell Biolabs, gb AF369965.1) and pAAV-CMV-GFP (Cell Biolabs, AAV-400) were applied in an equimolar ratio. All plasmids were purified on CsCl gradients. After 72–96 h, the cell pellet was collected with the AAV release solution, 50 U ml⁻¹ benzonase was added and the solution was then incubated for 2 h at 37 °C (water bath). Cells were frozen and thawed in liquid nitrogen to allow rAAV release. Purification of the rAAV vector was done on iodixanol gradients (consisting of 15, 25, 40 and 56% iodixanol), followed by gradient centrifugation at 50,000 r.p.m. for 2 h and 17 min at 22 °C in a Ti70 rotor (Beckman). rAAV was collected from the 40% iodixanol layer with a 5-ml syringe. rAAVs were dialyzed (Slide-A-Lyzer, 10,000 molecular weight cutoff (MWCO), 5 ml) in buffer A overnight to remove iodixanol. An anion-exchange chromatography column (HiTrap Q FF sepharose) equipped with Superloop was connected with the ÄKTAprius Plus chromatography system to collect the eluted fraction. To measure rAAV concentration, the eluted fraction was spun and washed once in PBS-MK Pluronic F68 buffer with a Millipore 30,000 MWCO 6-ml filter unit. rAAVs were stored in a glass vial tube at 4 °C. rAAV titers were measured by SYBR Green quantitative PCR (qPCR) with GFP, SV40 or ITR2 primer⁵⁵. A usual titer was 3 × 10¹⁴ to 5 × 10¹⁶ genome copies per ml.

Surgical procedures. The majority of experiments were performed under Licence ROB-55.2-2532.Vet_02-17-40. Thirty minutes before surgery, an analgesic (metamizole, 200 mg kg⁻¹, subcutaneous (s.c.); MSD Animal Health) was administered. Anesthesia was induced by placing the mice in an induction chamber and exposing them to isoflurane (5% in oxygen; CP-Pharma). Animals were then fixated in a stereotaxic frame (Drill & Microinjection Robot, Neurostar), and the isoflurane level was adjusted (0.5–2% in oxygen) to maintain an appropriate level of anesthesia, as evaluated by the absence of a pedal reflex. During the procedure, the eyes were protected with an ointment (Bepanthen, Bayer), and the animal's body temperature was maintained at 37 °C by means of a closed-loop temperature control system (ATC 1000, WPI Germany). An additional analgesic was then delivered (buprenorphine, 0.1 mg kg⁻¹, s.c.; Bayer). After the animal's head had been shaved, the skin was thoroughly disinfected with iodine solution (Braun), a local analgesic (lidocaine hydrochloride, 7 mg kg⁻¹, s.c.; bela-pharm) was injected under the scalp, and a small incision was made along the midline. Part of the skin covering the skull was removed, and tissue residues were cleaned by administration of a drop of hydrogen peroxide (3%; AppliChem). The animal's head was then adjusted to a skull-flat configuration using four landmarks (bregma, lambda and two points 2 mm to the right and to the left of the midline, respectively). In mice targeted for head bar implantation and electrophysiological measurements, OptiBond FL primer and adhesive (Kerr dental) were applied to the exposed skull, except in locations reserved for subsequent craniotomy and a site approximately 1.5 mm anterior and 1 mm to the right of the bregma, where a miniature reference screw (00-96 × 1/16 stainless steel; Bilaney) soldered to a custom-made connector pin was implanted.

For Cre-dependent triple-color viral tracing, three small craniotomies were drilled over V1 along an iso-azimuth ($n=2$) or iso-elevation ($n=2$) line or along one coronal section ($n=1$) (iso-azimuth: AP (−3.80, −3.30, −2.80), ML (−2.70, −2.40, −2.10); iso-elevation: AP (−3.80, −3.30, −2.80), ML (−2.60, −2.30, −2.00); coronal section: AP (−3.64, ML (−2.66, −2.23, −1.79)). Twenty-five to fifty nanoliters of pAAV-CAG-FLEX-GFP, pAAV-CAG-FLEX-mScarlet and

pAAV-CAG-FLEX-mTurquoise2 (all titers adjusted to 2 × 10¹⁵ genome copies per ml by dilution with a custom-made virus buffer (sterile PBS, 2.6 mM KCl, 1 mM MgCl₂, 0.05% Pluronic F68)) were injected into V1 through the three craniotomies, respectively, at a depth of 900 μm. Injections were performed using a Hamilton syringe (SYR 10 μl 1701 RN no NDL, Hamilton) equipped with a glass pipette controlled by the Injection Robot of the Neurostar Stereotax. The craniotomies were covered with sterile bone wax (AngioTech), and the skin was sutured.

For Cre-dependent expression of ChR2 in PV-Cre and Ntsr1-Cre mice, 2 μl of an AAV (pAAV-EF1a-double floxed-hChR2(H134R)-EYFP-WPRE-HGHpA; Addgene, 20298; with different serotypes and titers, all ≥ 7 × 10¹² viral genomes per ml) was mixed with 0.3 μl of fast green (Sigma-Aldrich). A small craniotomy was performed over V1 at AP −2.8 mm and ML −2.5 mm, AP −2.8 mm and ML −2.3 mm, AP −3.08 mm and ML −2.5 mm or AP −3.28 mm and ML −2.4 mm to enable injection of the prepared mixture. In PV-Cre mice, a total of ~0.2–0.5 μl of the mixture was injected at multiple depths between 1,000 μm and 100 μm below the pial surface. In Ntsr1-Cre mice used for global L6 photostimulation (Extended Data Fig. 5), <0.5 μl was injected at depths between 800 μm and 1,000 μm, approximately targeting L6. In three Ntsr1-Cre mice used for mapping of L6CT feedback (Fig. 1), only ~0.05 μl was injected at a depth of ~900 μm. For retrograde labeling of visTRN cells, 0.5 μl of the AAV vector rAAV2/retro-CMV-GFP (titer, 1.61 × 10¹⁵ genome copies per ml) was mixed with 1.5 μl PBS and 0.3 μl fast green. In three mice, a small craniotomy was performed above the dLGN (AP, −2.3 mm; ML, −2.3 mm), and 0.4 μl of the prepared mixture was injected at a depth of −2.8 mm. Injections were performed using a Hamilton syringe (SYR 10 μl 1701 RN no NDL, Hamilton) equipped with a glass pipette controlled by the Injection Robot of the Neurostar Stereotax.

For all animals planned for electrophysiological recordings (with or without prior virus injection), a custom-made lightweight stainless steel head bar with a cutout for subsequent craniotomy was attached with dental cement (Ivoclar Vivadent) above the posterior part of the skull and on top of the primer/adhesive. At the end of the procedure, the cutout was covered with the silicone elastomer sealant Kwik-Cast (WPI Germany). In some animals, an antibiotic ointment (Imex, Merz Pharmaceuticals) was applied to the borders of the wound.

For all animals, the long-term analgesic (meloxicam, 2 mg kg⁻¹, s.c.; Böhringer Ingelheim) was injected immediately following the surgery and was administered at 24-h intervals for 3 consecutive days. For a period of 5 d after surgery, the animal's health status was assessed with a score sheet.

A smaller number of mice ($n=15$) was treated in accordance with Licence CIN 4/12, in which general surgical procedures were identical to the foregoing with the following exceptions. After induction of anesthesia, mice were additionally injected with atropine (atropine sulfate, 0.3 mg kg⁻¹, s.c.; Braun). The head post consisted of a small S-shaped piece of aluminum, which was cemented to the skull between lambda and bregma and to the right of the midline. Virus was injected with either a Picospritzer (Parker Hannifin) or a Nanoject (Drummond Scientific). Posterior to the head post, overlying the cerebellum, two miniature screws serving as ground and reference were implanted. A well of dental cement was formed over the target recording and stimulation sites and filled with Kwik-Cast. At the end of the procedure, antibiotics (Baytril, 5 mg kg⁻¹, s.c.; Bayer) and a long-term analgesic (Carprofen, 5 mg kg⁻¹, s.c.; Rimadyl, Zoetis) were administered and were given for 3 d after surgery.

To compare visTRN RFs to dLGN RFs (Fig. 4i), we included dLGN recordings from 16 mice (8 PV-Cre and 8 Ntsr1-Cre mice). In six of the Ntsr1-Cre mice, V1 was injected with a virus irrelevant to the purpose of our investigation (AAV-DJ-Ef1a-DIO SwiChR++-EYFP, $n=2$; pAAV_hSyn1-SIO-stGtACR2-FusionRed (Addgene, 105677), $n=4$).

Gradual habituation of the animal to the experimental condition was initiated after at least 7 d of recovery. The habituation phase consisted of 3 d of handling followed by 4 d during which the experimental procedure was simulated. In mice prepared for photostimulation experiments, neural recordings were initiated no sooner than 3 weeks after injection to allow enough time for virus expression. One day before the first recording session, mice were anesthetized in the same way as for the initial surgery. For V1 and dLGN recordings, a craniotomy (ca. 1.5 mm²) was performed above V1 and the dLGN (AP, −2 or −2.5 mm; ML, −2 mm). For visTRN recordings, two smaller craniotomies (ca. 1 mm²) were performed over V1 and the visTRN, respectively (V1: AP −2.8 mm and ML −2.5 mm; visTRN: AP −1.25 mm and ML −2.15 mm, AP −1.25 mm and ML −2.2 mm or AP −1 mm and ML −2 mm). At the end of the procedure, the craniotomy was sealed with Kwik-Cast. To avoid residual drug effects during the recordings, the long-term analgesic Metacam was injected only once at the end of the surgery, unless the mouse showed any sign of distress. Experiments started on the day after craniotomy and were performed daily for as long as the electrophysiological signal remained of high quality.

Electrophysiological recordings and optogenetics. Recording sessions were performed in a secluded chamber that allowed us to perform experiments in the absence of any ambient light source. Animals were head fixed and positioned on an air-cushioned Styrofoam ball that enabled the mouse to move freely. Ball movements were recorded at 90 Hz by two optical computer mice connected to a microcontroller (Arduino Duemilanove). Eye position and pupil size were

recorded under infrared light illumination with a Guppy AVT camera (frame rate, 50 Hz; Allied Vision) interfaced with a zoom lens (Navitar Zoom 6000). Extracellular activity was sampled at 30 kHz (Cerebus, version 6.03.01.00, Blackrock Microsystems). At the beginning of each recording session, the silicone plug covering the craniotomy was removed, and a silicon probe (A1x32Edge-5mm-20-177-A32, A1x32-5mm-25-177, A1x16-3mm-50-177-A16, A1x64-Poly2-6mm-23s-160, NeuroNexus; H3, Cambridge NeuroTech) was positioned above the target site with a micromanipulator (MP-225, Sutter Instrument) and inserted to the appropriate depth (mean recording depth: V1 = 1,040 μm , dLGN = 3,100 μm and visTRN = 3,394 μm) until we encountered vigorous responses to visual stimuli. For recordings from the dLGN and visTRN, we judged the correct position of the electrode based on postmortem histological reconstruction of the electrode track, for which the electrode was stained with a lipophilic fluorescent tracer (DiI, DiD, Invitrogen) on one of the final recording sessions. For recordings from the dLGN, where physiological properties are well known¹⁴, additional indicators were the characteristic progression of RFs from upper to lower visual field along the electrode shank, the neurons' preference for drifting gratings of high temporal frequency and the manifestation of this frequency in the response pattern of the cells (strong F1 response).

To photostimulate PV⁺ inhibitory interneurons or L6CT cells, we interfaced an optic fiber (diameter of 910 μm , Thorlabs, or 480 μm , Doric Lenses) with a blue light-emitting diode (LED) (center wavelength, 470 nm, M470F1, Thorlabs, or center wavelength 465 nm, LEDC2_465/635_SMA, Doric Lenses). The tip of the fiber was placed less than 1 mm above the exposed surface of V1 using a manual micromanipulator. The tip of the head bar holder was surrounded with black metal foil that prevented light from reaching the animal's eyes. For each mouse, the first recording session was conducted in V1 to verify that the photostimulation was effective. Only if light exposure reliably triggered suppression of V1 in PV-Cre mice or activation of L6 in Ntsr1-Cre mice was the animal used for subsequent recordings from the dLGN or visTRN. To elicit reliable effects during each recording session, we adjusted the light intensity of the LED on a daily basis (median intensity of 1.1 mW mm⁻² as measured at the tip of the optic fiber).

Visual stimulation. Visual stimuli were presented on a gamma-corrected liquid crystal display (LCD) monitor (Samsung Sync-Master 2233RZ; 47 × 29 cm, 1,680 × 1,050 resolution at 60 Hz, mean luminance of 50 cd m⁻²) positioned at a distance of 25 cm from the animal's right eye (spanning ~108 × 66°, small angle approximation) and controlled by custom-written software (EXPO, <https://sites.google.com/a/nyu.edu/expo/home>).

RF mapping and identification of cortical layers. We mapped RFs with a sparse noise stimulus, which consisted of non-overlapping black and white squares with a side length of 4 or 5° that were arranged on a grid spanning between 40 and 60° on each side. Stimulus presentation time varied between experiments and ranged from 0.08 to 0.20 s. Whenever possible, subsequent stimuli were presented at RF locations based on multiunit activity (MUAe) extracted from the ongoing recordings by applying a threshold of 4.5 to 6.5 s.d. to the high-pass filtered signals.

To determine the V1 laminar location of the recording sites, we presented full-screen, contrast-reversing checkerboards at 100% contrast, with a check size of 25° and a temporal frequency of 0.5 cycles per s.

Tuning experiments. Drifting gratings adapted in their temporal (0.20–15.00 cycles per s) and spatial frequencies (0.01–0.08 cycles per degree) to the preferences of neurons at the recording site were used to determine selectivity for orientation, contrast and size. Contrast was set to 1 for all gratings except those in contrast-tuning experiments. In all tuning experiments, we assessed spontaneous firing rate by including trials in which only the mean luminance gray screen was presented. Effects of photostimulation were computed using photostimulation windows and corresponding windows in control conditions during stimulus presentation. Across experiments, we used slight variations of stimulus and light durations. In the figure captions, we indicate the parameters of the most common protocol.

To verify the effectiveness of photostimulation, we performed the first recording session for each animal in area V1 using drifting sinusoidal gratings to measure tuning for various stimulus properties, with photostimulation trials interleaved in pseudorandom order. For the analysis of V1 suppression by photoactivating PV⁺ inhibitory interneurons (Fig. 2a–c), we pooled data from direction-tuning experiments ($n = 11$), size-tuning experiments ($n = 19$), and contrast-tuning experiments ($n = 10$). For direction-tuning experiments, grating direction was varied in step sizes of 30° or 45°. Gratings were presented for 0.75 s with photostimulation starting with stimulus onset and lasting for 0.85 s, for 1.5 s with photostimulation starting with stimulus onset and lasting for 1.6 s or for 2 s with photostimulation starting 0.85 s after stimulus onset and lasting for 0.25 s. For size-tuning experiments, gratings ranged in diameter between 0° and 67° (in 11 or 15 steps). Stimuli were presented for either 1.5 s with photostimulation starting with stimulus onset and lasting for 1.6 s or 0.75 s with photostimulation starting 0.21 s after stimulus onset and lasting for 0.25 s. For contrast-tuning experiments, contrast was varied in 13 steps between 0 and 1. Stimuli were presented for 2 s, and photostimulation started 0.85 s after stimulus onset and lasted for 0.25 s.

For the analysis of L6CT activation effects in V1 during photostimulation of Ntsr1⁺ neurons (Extended Data Fig. 5a–c), we again pooled data from direction- ($n = 11$), size- ($n = 11$) and contrast-tuning ($n = 6$) experiments. For direction-tuning experiments, grating direction was varied in step sizes of 30°. Gratings were presented either for 0.75 s with photostimulation starting 0.1 s before stimulus onset and lasting for 0.85 s or for 0.75 s with photostimulation starting 0.15 s after stimulus onset and lasting for 0.25 s. For size-tuning experiments, grating diameter was varied between 0° and 67° in 13 steps. Gratings were presented for 0.75 s with photostimulation starting 0.10 s before stimulus onset and lasting for 0.85 s or for 0.75 s with photostimulation starting 0.15 s after stimulus onset and lasting for 0.25 s. Finally, for contrast-tuning experiments, contrast levels were varied between 0 and 1 in 13 steps. Gratings were presented for 0.75 s with photostimulation starting 0.1 s before stimulus onset and lasting for 0.85 s.

To assess the functional specificity of CT feedback (Fig. 1d–i), we relied on activity measured during orientation-tuning experiments. Sinusoidal gratings drifting in different directions (0–330°, step size = 30°) were presented with and without photostimulation in pseudorandom order. During most experiments ($n = 14$), stimuli were presented for 0.75 s, and photostimulation started 0.085 s before stimulus onset and lasted for 0.85 s. In a small fraction of experiments ($n = 5$), stimuli were presented for 1 s, and photostimulation started 0.15 s before stimulus onset and lasted for 1.35 s.

To assess the effects of V1 suppression on spatial integration in the dLGN ($n = 20$ experiments; Fig. 2h–m), we used drifting gratings with stimulus diameter ranging between 0° and 67° (in 11 or 15 steps). Gratings were presented for 0.75 s with photostimulation starting 0.04 s before stimulus onset and lasting for 0.85 s, for 1.5 s and photoactivation starting 0.03 s before stimulus onset and lasting for 1.6 s or for 0.75 s with photostimulation starting 0.25 s after stimulus onset and lasting for 0.25 s. To probe size tuning in the visTRN ($n = 69$ experiments; Fig. 4j–m), we used sinusoidal or square-wave drifting gratings with diameters ranging between 0° and 67° (in 11 or 15 steps). Stimuli were presented for 0.75 s. In a subset of experiments with paired photoactivation of PV⁺ neurons in V1 ($n = 31$; Fig. 5), photoactivation started 0.04 s before stimulus onset and lasted for 0.85 s.

To measure contrast tuning in the visTRN ($n = 9$ experiments), we presented sinusoidal drifting gratings at different contrasts (in 13 steps). Gratings were presented for 1 s. To measure contrast tuning in the dLGN ($n = 9$ experiments), we presented sinusoidal drifting gratings at different contrasts (in 13 steps). Gratings were presented for 0.75 s (six experiments) or 0.5 s (three experiments).

Spontaneous activity. To probe the effect of suppressing CT feedback on spontaneous activity in the dLGN, we photoactivated PV⁺ neurons in V1 in the absence of visual stimulation ($n = 28$ experiments). Photostimulation periods differed between experiments and ranged from 0.17 s to 1 s.

Histology. To verify recording site and virus expression, we performed histological analyses. For experiments under Licence ROB-55.2-2532.Vet_02-17-40, mice received an analgesic (Metamizole) after the final recording session and were anesthetized with isoflurane and injected (intraperitoneally) with a mixture of medetomidin (Domitor, 0.5 mg kg⁻¹; Vetoquinol), midazolam (Climasol, 5 mg kg⁻¹; Ratiopharm) and fentanyl (Fentadol, 0.05 mg kg⁻¹; Dechra Veterinary Products Deutschland) 30 min later. Under deep anesthesia, mice were then perfused with 4% paraformaldehyde in PBS. Brains were removed, post-fixed in paraformaldehyde for 24 h and rinsed with and stored in PBS at 4°C. Coronal brain slices (40 μm) were cut using a vibratome (Leica VT1200 S, Leica), stained with DAPI solution before (DAPI, Thermo Fisher Scientific; Vectashield H-1000, Vector Laboratories) or after mounting on glass slides (Vectashield DAPI) and cover-slipped. For viral tracing experiments, the perfusion, fixation and slice preparation procedures were identical to those described above, except that brain slices were stained on slides with Invitrogen NeuroTrace DeepRed overnight before being cover-slipped.

A scanning fluorescent microscope (BX61 Systems Microscope, Olympus) was used to inspect slices for the presence of eYFP, GFP, mScarlet, DiI and DiD. Confocal microscopy was performed at the bioimaging core facility of the LMU Biomedical Center with a Leica SP8X WLL microscope equipped with a 405-nm laser, WLL2 laser (470–670 nm) and acousto-optical beam splitter. Images were acquired with a ×63, 1.30-NA glycerol objective. For the different fluorophores, the following fluorescence settings were used: mTurquoise2 (405; 450–480 nm), GFP (490; 492–550 nm), mScarlet (570; 560–600 nm) and NeuroTrace DeepRed (640; 650–700 nm). Recording was performed in three sequences (1, mTurquoise2; 2, GFP, DeepRed; 3, mScarlet) to avoid bleed-through between the channels. All channels were imaged with hybrid photo detectors (HyDs).

For experiments under Licence CIN 4/12, general histological procedures were identical to those described above, except that mice were injected with sodium pentobarbital (Narcoren, 200 mg kg⁻¹ intraperitoneally; Böhringer Ingelheim) before perfusion. Coronal brain slices (50 μm) were obtained by using a vibratome (Microm HM 650V, Thermo Fisher Scientific) and inspected with a Zeiss Imager. Z1m fluorescent microscope (Zeiss).

For atlas registration and three-dimensional (3D) reconstruction, whole-brain images were obtained. Images were processed offline using Fiji^{36,57}. We adjusted individual color channels for better visibility.

3D reconstruction of expression volumes. For 3D reconstruction and volumetric quantification of expression volumes in L6 and the dLGN, brain slice images had to be annotated and mapped to stereotaxic coordinates for each pixel. To this end, brain slice images were registered to the Allen Common Coordinate Framework⁵⁸ using the allenCCF tools software package (<https://github.com/cortex-lab/allenCCF>)⁵⁹. In brief, for each brain slice, best corresponding atlas sections were chosen manually. To find the optimal transform between atlas coordinates and image pixels, reference points between the atlas section and brain slice image were manually set at unambiguous and salient features of the brain, including structures of the hippocampus, ventricle borders along the midline, habenular nuclei, the midline crossing of the corpus callosum, the indent between the ventral end of the hippocampal formation and the hypothalamus, the meeting point between the medial amygdala and the hypothalamus and high curvature turning points of the brain outline. After successful registration, points set manually along the outline of the expression zones were exported in stereotaxic coordinates. Repeating these steps for the brain slices containing the target regions yielded point clouds in 3D space, circumscribing the expression zones in cortex and thalamus. We computed the convex hull of each point cloud as a geometric description of the expression volume. We chose the convex hull because it is unambiguously defined for any set of points and does not require prior assumptions about the shape of the volume. To constrain the expression volume with respect to the potentially non-convex structure of the brain area it occupies, we computed the intersection between the convex hull and the 3D model of the brain area of interest (V1, L6 or dLGN). This process yielded a 3D model of that part of the expression zone, which was embedded in the brain area of interest. The intersection operations and computations of volumes on the 3D models were performed with specialized geometry processing software for Python (PyMesh, <https://github.com/PyMesh>).

Locomotion. For recordings under Licence ROB-55.2-2532.Vet_02-17-40 (Figs. 1i, 2h–m, 4 and 5 and associated Extended Data figures), we computed run speed by using the Euclidean norm of three perpendicular components of ball velocity (roll, pitch and yaw)⁶⁰ and smoothed traces with a Gaussian filter ($\sigma=0.2$ s). For all analyses of electrophysiological data (except RF mapping with the sparse noise stimulus), we only considered trials in which the animal was sitting. Sitting trials were defined as trials in which the speed of the animal remained below 0.25 cm s^{-1} for at least 50% of the time. For recordings performed under Licence CIN 4/12 (Figs. 1k and 2 and associated Extended Data figures), the Gaussian filter differed slightly ($\sigma=0.15$ s), and, hence, sitting trials were defined by a run speed below 1 cm s^{-1} for 80% of the analyzed time window.

Spike sorting. Recordings under protocol ROB-55.2-2532.Vet_02-17-40 (Figs. 1i, 2h–m, 4 and 5 and associated Extended Data figures) were filtered using a fourth-order Butterworth high-pass non-causal filter with a low frequency cutoff of 300 Hz. Any saturation in the signal was removed before clustering responses with the Matlab-based automated spike-sorting software Kilosort⁶¹. The resulting clusters were imported to the Python toolbox Spyke⁶² for manual refinement of clusters. Spyke allows one to select time ranges and channels around clustered spikes for realignment and for representation in 3D space using dimensionality reduction (multichannel principal-component analysis, independent component analysis and/or spike time). In 3D, clusters were further separated by a gradient ascent-based clustering algorithm⁶³. Using exhaustive pairwise comparison of similar clusters, we merged potentially overclustered units. Only clusters whose autocorrelogram displayed a clear refractory period and whose mean voltage trace showed a characteristic spike waveshape were considered for subsequent analyses.

For data recorded under protocol CIN 4/12 (Figs. 1i and 2 and associated Extended Data figures), single neurons in our linear array recordings were isolated by grouping neighboring channels into five equally sized ‘virtual octodes’ (8 channels per group with 2-channel overlap for 32 channel probes). Using an automatic spike detection threshold⁶⁴ multiplied by a factor of 1.5, spikes were extracted from the high-pass-filtered continuous signal for each group separately. The first three principal components of each channel were used for semi-automated isolation of single neurons with KlustaKwik⁶⁵, and the resulting clusters were manually refined with Klusters⁶⁶. Only clusters whose autocorrelogram displayed a clear refractory period and whose mean voltage trace showed a characteristic spike waveshape were further considered. To avoid duplication of neurons extracted from linear probe recordings, we computed cross-correlograms (1-ms bins) between pairs of neurons from neighboring groups. Pairs for which the cross-correlogram’s zero bin was three times larger than the mean of non-zero-bins were considered to be in conflict, and only one was kept.

Extracted single units were assigned to the electrode contact with the largest waveform.

Analysis of MUAe. To obtain robust estimates of RFs at the V1 injection site, we used the envelope of MUAe, which reflects the number and amplitude of spikes close to the electrode and resembles thresholded multiunit data and average single-unit activity⁶⁷. To calculate the MUAe, the median-subtracted, high-pass-filtered signals were full-wave rectified before low-pass filtering (200 Hz) and downsampling to 2,000 Hz (ref. ⁶⁷).

Assignment of units to V1 layers. We assigned units to V1 layers by CSD analyses⁶⁸. The local field potential (LFP) was computed by downsampling the wideband signal to 1,250 Hz. For V1 recordings, the LFP was triggered to contrast reversals of the checkerboard stimulus. The CSD was computed by taking the second spatial derivative of the LFP⁶⁸ and spatially smoothing with a triangular kernel⁶⁹. The contact closest to the earliest CSD polarity inversion was assigned to the base of L4. The remaining contacts were assigned to putative layers based on a cortical thickness of 1 mm and anatomical measurements of relative layer thickness in mouse V1 (ref. ⁷⁰). Note that the depth estimation is limited in resolution to the electrode site spacing (either 25 or 20 μm , depending on probe configuration) both in terms of estimating the base of L4 as well as taking the contact with the largest waveform.

Estimation of anatomical depth in the dLGN. To estimate the anatomical depth of recorded neurons in the dLGN, we considered MUAe. The top-most channel, which showed a clear MUAe RF and was well aligned with the characteristic progression of RFs in the dLGN along the dorsoventral axis¹⁴, was set as the reference channel estimating the dorsal edge of the dLGN during the respective recording session. Single neurons were then assigned the relative depth of the channel with the maximum amplitude of their extracellular waveshape with respect to the reference channel, as determined by the spatial layout of the probe.

Data analysis. All further analyses were conducted with custom-written code in Matlab or Python using the DataJoint framework⁷¹. All statistical tests were two sided.

We calculated mean percent change as

$$\Delta\% (x) = \left(\frac{\sum_{k=1}^n \log_2 \left(\frac{x_{\text{sup}} p_k}{x_{\text{cont}}} \right)}{n} - 1 \right) * 100 \quad (1)$$

Here, x_{sup} and x_{cont} represent the measured variables under the control condition and under the photostimulation condition, respectively, and n is the number of observations.

Descriptive modeling of tuning curves. To characterize neural selectivity, we fit descriptive models and determined goodness of fit by $R^2 = 1 - (SSE/SST)$, where $SSE = \sum (y - \hat{y})^2$ and $SST = \sum (y - \bar{y})^2$.

Receptive field fitting. Receptive field maps obtained in sparse noise experiments were fit with a 2D Gaussian⁷².

$$f(x, y) = \frac{A}{2\pi ab} \exp \left(-\frac{x'^2}{2a^2} - \frac{y'^2}{2b^2} \right) + c \quad (2)$$

Here, A is the maximum amplitude, a and b are half-axes of the ellipse and x' and y' are the transformations of the stimulus coordinates x and y , considering the angle θ and the coordinates of the center (x_c, y_c) of the ellipse, and c is an offset. RF area (Figs. 4d, h, i and 5) was calculated at 1σ .

In analyses where we relied on MUAe activity (Figs. 1f–i and 2h–m), the RF maps were based on MUAe activity between 50 and 100 ms after stimulus onset (both black and white squares). For the comparison of classical RF sizes in the dLGN and visTRN (Fig. 4d, h, i), the RF maps were based on single-unit responses to both bright and dark stimuli. Before fitting the 2D Gaussian, mean responses were normalized by first subtracting the minimum response and then dividing by the range.

Responses in direction-tuning experiments (Figs. 1i and 2b) were fit with a sum of two Gaussians with peaks 180° apart, which could have different amplitudes but equal width and a constant baseline⁷³

$$R(\theta) = R_0 + R_p e^{-\frac{(\theta - \theta_p)^2}{2\sigma^2}} + R_n e^{-\frac{(\theta - \theta_p + 180)^2}{2\sigma^2}} \quad (3)$$

Here, θ is stimulus direction ($0-360^\circ$). The function has five parameters: preferred direction θ_p , tuning width σ , baseline response R_0 , response at the preferred direction R_p and response at the null direction R_n .

Orientation and direction selectivity. Orientation selectivity was quantified according to refs. ^{13,74} as

$$OSI = \frac{\sqrt{(\sum R_k \sin(2\theta_k))^2 + (\sum R_k \cos(2\theta_k))^2}}{\sum R_k} \quad (4)$$

Here, R_k is the response to the k th direction given by θ_k . We determined OSI for each unit during control conditions without optogenetic manipulation.

Direction selectivity index (DSI)⁷⁵ was computed for each unit as

$$DSI = \frac{R_p - R_n}{R_p + R_n + 2R_0} \quad (5)$$

Here, R_p and R_n are the firing rates in the preferred and null directions, respectively, taken from tuning curves fit to responses to drifting gratings in different directions, and R_0 is baseline firing rate independent of orientation. For both *OSI* and *DSI*, we focused on experiments in which responses were sufficiently well fit ($R^2 > 0.8$).

Contrast sensitivity. We fit contrast response functions with a hyperbolic ratio function⁷⁶

$$R_C = R_0 + \frac{R_{\max} * c^n}{c_{50}^n + c^n} \quad (6)$$

where c is the stimulus contrast. The function has four parameters: baseline response R_0 , responsiveness R_{\max} , semisaturation contrast c_{50} and exponent n . To compute contrast response functions, we only considered trials in which the animals were sitting. For the analyses, we focused on experiments in which the response pattern was well captured by the model $R^2 > 0.8$.

Size tuning. To analyze size tuning in the dLGN, we fit responses to drifting gratings of different sizes with a RoG model⁷⁷, where a center Gaussian is normalized by a Gaussian representing the surround, each having their independent amplitude (k) and width (w)

$$R(x) = \frac{K_c L_c(x)}{1 + K_s L_s(x)} \quad (7)$$

$$L_c(x) = \left(\frac{2}{\sqrt{\pi}} \int_0^x e^{-\left(\frac{y}{w_c}\right)^2} dy \right)^2 \quad (8)$$

$$L_s(x) = \left(\frac{2}{\sqrt{\pi}} \int_0^x e^{-\left(\frac{y}{w_s}\right)^2} dy \right)^2 \quad (9)$$

We always constrained $w_c < w_s$.

To analyze spatial integration in the visTRN (Figs. 4j–m and 5), we included an offset (b) and allowed for rectification of the size-tuning curve to better capture spatial integration in neurons whose firing rates were substantially reduced during V1 suppression

$$R(x) = \max \left(0, \frac{k_c L_c(x)}{1 + k_s L_s(x)} + b \right) \quad (10)$$

We subtracted the modeled response to a stimulus size of 0° from the resulting curve and quantified suppression strength with an SI of $SI = (R_{\text{opt}} - R_{\text{supp}})/R_{\text{opt}}$, where R_{opt} is the peak response, and R_{supp} is the response to the largest stimulus diameter (75°). The peak response was defined as the response to the stimulus diameter for which a 1° increment in size failed to increase the modeled firing rate by 0.05%. Similar to previous observations^{78,79}, for size-tuning curves fitted to both dLGN and visTRN responses, we found a negative correlation between preferred size and suppression strength (SI; visTRN: $R^2 = 0.19$, slope of -0.003 , $P = 3.4 \times 10^{-7}$; dLGN: $R^2 = 0.18$, slope of -0.01 , $P = 0.01$; Extended Data Fig. 10d,f).

Quantification of RFs for functional mapping of CT feedback. To quantify average RF location at the V1 injection site (Fig. 1f), we computed an RF map based on MUAe activity for each channel. Channels with poor fits to the 2D Gaussians ($R^2 < 0.4$) were not considered for further analyses. Average V1 RF location was obtained by averaging the center positions over all 2D Gaussians. To quantify the retinotopic distance of dLGN neurons with respect to the V1 injection site, we computed the Euclidean distance between their channels' MUAe RF center and the retinotopic location of the V1 injection site.

Spatial profile of CT feedback. To quantify the spatial profile of CT feedback (Fig. 1i), we used direction-tuning experiments. We focused on visually driven units, defined by evoked firing rates that differed from spontaneous activity by at least 3.29 \times the standard error of the mean for at least one direction, with average firing rates ≥ 0.15 spikes per s. We computed for each unit and direction the log₂ ratio of firing rates with photoactivation to those under the corresponding control condition before averaging across directions.

To assess the spatial profile of CT feedback effects in the dLGN, we grouped neurons according to their retinotopic distance from the V1 injection zone into overlapping bins (15° width, 3.3° spacing; average number of units per bin = 66; minimum number of units per bin = 32, except for the last bin with 7 units), for which we computed the mean. We estimated the 95% CI of the mean effect per bin by resampling with replacement (1,000 iterations). To test for spatial regions with a significant CT feedback effect, we used a cluster-based permutation test⁸⁰. We grouped all neighboring bins with the same sign and mean log₂ ratios that were significantly different from 0 (0 not within 95% CI) into clusters and computed the sum of absolute mean log₂ ratios within those clusters. We then considered the maximum absolute cluster sum value as the test statistic. These steps were then repeated over 1,000 iterations with randomly permuted distance values across all

neurons. The P value was the proportion of random permutations that yielded a cluster sum larger than the one from our original dataset.

Next, we classified single neurons into significantly enhanced, suppressed or unmodulated groups depending on whether their average log₂ ratio was above, below or within the 95% interval of the sampling distribution obtained from permuting the photoactivation labels of trials within directions and recomputing the average log₂ ratio across directions (1,000 iterations). To test whether the proportions of enhanced, suppressed or non-modulated neurons depended on retinotopic distance, we counted the numbers of each modulation type within 5° bins along the retinotopic distance axis, obtaining a 3×11 contingency table. Statistical test for non-uniformity was done using an omnibus chi-squared test, which was followed by post hoc chi-squared tests for each modulation type.

To test whether significantly enhanced neurons were predominantly present close to the injection site, we again applied a cluster-based permutation approach⁸⁰. We first calculated the adjusted standardized residuals (ASR), defined as the difference between the observed counts in the contingency table and the expected counts under the null hypothesis, adjusted for the row and column totals. For the enhanced neurons, we grouped neighboring bins with $|ASR| \geq 1$ for the enhanced neurons into clusters and computed the sum of $|ASR|$ in those clusters. We then considered the maximum cluster sum value as the test statistic. These steps were then repeated over 100,000 iterations with randomly permuted distance values across all neurons. The P value was the proportion of random permutations that yielded a cluster sum larger than the one from our original dataset.

Effects of photostimulation on V1 responses. For the quantification of effects of optogenetic manipulations on V1 responses, we only considered V1 neurons whose maximal firing rate exceeded 0.5 spikes per s in tuning experiments involving either different directions, sizes or contrasts. Furthermore, we excluded neurons that showed a change in the sign of the effect of optogenetic manipulation across experiments. We first computed, for each unit and experiment, average firing rates during photostimulation in trials with optogenetic manipulation and in equivalent time windows in trials of the control condition. We then computed, across experiments, the effect of photostimulation by taking the difference in average rates between the photostimulation condition and the control condition normalized to the rate in the control condition. For the analysis of average effects of V1 suppression by optogenetic activation of PV⁺ inhibitory interneurons, we excluded putative PV⁺ inhibitory interneurons directly driven by the light, defined as a greater than or equal to twofold increase of firing rates in the photostimulation condition compared to the control condition.

Effects of V1 suppression on dLGN responses. To analyze the effects of V1 suppression on dLGN responses, we considered neurons to be located in the dLGN (as opposed to, for example, in the dorsally located hippocampus) if their highest-amplitude extracellular spike waveshape was measured on an electrode channel including and between channels delineating the top and bottom of the dLGN. Top and bottom dLGN channels were defined as the dorsal- and ventral-most channels, respectively, with visually responsive neurons in at least one tuning experiment, involving gratings of either different directions, sizes, temporal frequencies or contrasts. We defined a neuron as being visually responsive in these tuning experiments if (1) the absolute difference between its mean firing rates under at least three conditions within an experiment and the interleaved blank condition was larger than 2.58 \times the standard error of the mean rate under that condition and (2) its maximal firing rate exceeded 0.5 spikes per s.

For the analysis of effects of V1 photostimulation on dLGN responses to medium gray screen (corresponding to a size 0° stimulus; Fig. 2d–g), we excluded neurons that never spiked in a time window around V1 photostimulation ($\pm(0.8\text{ s} + \Delta t_{\text{opto}})$), where Δt_{opto} is the duration of V1 photostimulation. We focused on experiments with a minimum of five trials, during which the animal was sitting during the temporal analysis windows of interest. To assess changes in firing rate, we computed for each unit an average firing rate during the window of V1 photostimulation and during a window of equivalent length immediately preceding light onset. For the analysis of burst ratios, we excluded all neurons that did not spike either in the control or the photostimulation window, as the ratio of burst spikes to all spikes in such cases is not defined. We assessed changes in bursting by computing in the same time windows the ratio of burst spikes to the total number of spikes. Burst spikes were defined according to ref. 81 and required a silent period of at least 100 ms before the first spike in a burst, followed by a second spike with an interspike interval of < 4 ms. Any subsequent spikes with preceding interspike intervals < 4 ms were also considered to be part of the burst. All other spikes were regarded as tonic.

For the analysis of V1 suppression effects on dLGN spatial integration (Fig. 2h–m), we considered neurons for further analysis whose size-tuning curves had an $R^2 \geq 0.7$ and, under the control condition, a mean firing rate of at least 0.15 spikes per s. We discarded experiments in which the stimulus center was placed outside of 1σ of its fitted RF center. We focused on RF fits with $R^2 \geq 0.4$ obtained from units that responded to the sparse noise stimulus with a sufficiently high firing rate (≥ 0.15 spikes per s). If none of the fitted single-unit RFs fulfilled these criteria, we used, if they were well fit ($R^2 \geq 0.4$), RFs computed from MUAe activity. To further assure that neurons were well driven by our stimulus, we only

included neurons whose mean response to the first four stimulus sizes greater than 0° was, under the control condition, at least 5% larger than the response to the blank screen. To evaluate the effects of CT feedback on small stimulus sizes, we considered for each neuron the responses obtained from the model for the preferred size under the control condition. To assess the effect of CT feedback for large stimulus sizes, we compared modeled responses to a 200° stimulus under the two conditions.

RFs in the visTRN and dLGN. To analyze the organization of classical RFs in the visTRN (Fig. 4e–g) and to compare their sizes to those of dLGN neurons (Fig. 4d,h,i), we analyzed responses to sparse noise stimuli. We focused on units with a mean firing rate of at least 0.15 spikes per s and whose RFs were well fit ($R^2 \geq 0.65$ for retinotopy in the visTRN and $R^2 \geq 0.4$ for comparing RF sizes). If for a given unit results from more than one sparse noise experiment fulfilled these criteria, we selected the experiment in which the RF was best captured by the 2D Gaussian (largest R^2 value). To test whether the relation between estimated depth and RF center position was different for azimuth versus elevation, we performed an ANCOVA, which regressed depth on visual angle and included the categorical covariate azimuth versus elevation.

Spatial integration in the visTRN. To analyze spatial integration in the visTRN (Figs. 4j–m and 5), we only considered units whose mean firing rate in the control condition was sufficiently high (≥ 0.15 spikes per s) and whose size-tuning curve in the control condition was well captured by the model $R^2 \geq 0.7$. We further concentrated on experiments in which the stimulus center had been presented inside 1σ of the fitted RF center, focusing on RF fits with $R^2 \geq 0.4$ obtained from units with sufficiently high mean firing rates (≥ 0.15 spikes per s). In cases where a unit fulfilled these criteria for multiple size-tuning experiments, we focused on the experiment in which responses in the control condition were best captured by the RoG model (largest R^2 value).

SI and preferred size were computed as described above. For few units, our definition of the preferred size and the absence of surround suppression led to slightly stronger responses to the largest stimulus than the optimal stimulus diameter, resulting in negative SIs. In such cases, we set the SI to 0.

To rule out that a lack of surround suppression could be explained by the difference between stimulus center and RF center or the difference between monitor center and RF center, we computed linear regressions between the SIs and the two differences (Extended Data Fig. 10). When multiple valid RF mapping experiments were available for a unit, we used the RF with the best model fit (largest R^2 value).

Quantifying effects of V1 suppression on visTRN responses. For the analysis of burst ratios (Fig. 5f), we computed, separately for the control condition and the V1 suppression condition, the ratios of burst spikes to the total number of spikes during sitting trials of a size-tuning experiment. Burst spikes were defined according to ref.⁸² and required a silent period of at least 70 ms before the first spike in a burst, followed by a second spike with an interspike interval of <10 ms. Any subsequent spikes with preceding interspike intervals <10 ms were also considered to be part of the burst. All other spikes were regarded as tonic.

To ensure that SIs and preferred size for size-tuning curves recorded under V1 suppression could be reliably interpreted, we required a minimum mean firing rate of 0.1 spikes per s during V1 suppression for the analyses in Fig. 5g,h. Before computing population size-tuning curves (Fig. 5d), differences in response rate as a function of stimulus size (Fig. 5i), and fitting the threshold-linear model (Fig. 5j,k), we normalized the fitted size-tuning curves by dividing them by the maximum response across the two conditions.

To analyze differences in response rate between control and photostimulation conditions as a function of stimulus size (Fig. 5i), we subtracted for each unit the normalized size-tuning curve (1° resolution) in the control condition from that in the photostimulation condition and took the mean across the population. To test for a significant change in the effect of photostimulation with size, we computed the difference in photostimulation effect for subsequent sizes (1° steps) and used a resampling procedure across neurons (1,000 iterations). If 0 was outside the 97.5th percentile of the resulting distribution of mean differences, we considered the change significant.

To characterize the change in visTRN size tuning induced by suppression of CT feedback (Fig. 5j,k), we predicted visTRN responses to stimuli of different sizes during V1 suppression based on responses under the control condition by fitting a threshold-linear model

$$f(x) = \max(0, m * x + b) \quad (11)$$

If the resulting fit was of good quality ($R^2 \geq 0.8$), we extracted the slope and the threshold parameter (x intercept).

Computational modeling. To explore how dLGN size tuning changes with the spatial scale of the inhibitory CT feedback component, we used the eDoG model²³. This choice of model was motivated by our intention to explore the effects of CT feedback in a conceptually and mathematically simple framework. The eDoG model is a mechanistic firing rate-based model in which visual responses of

dLGN relay cells are computed from direct evaluation of integrals, representing the spatiotemporal receptive field of RGCs and feed-forward and feedback coupling kernels connecting the neurons of the circuit. Despite the relatively simple linear mathematical structure of the model, it nevertheless incorporates two key biological features of the CT feedback: (1) the non-linearity (half-wave rectification) of cortical L6 cells providing feedback and (2) the observation that dLGN cells receive feedback from numerous cortical cells with different orientation selectivities together covering all directions. A key simplification of the framework is that the different cortical populations providing CT feedback can be modeled to be uncoupled at the cortical stage. Thus, the eDoG model does not explicitly consider intracortical connectivity or transformations, such as between the dominant input L4 and L6, from where the CT feedback arises. Rather, such effects are implicitly contained in the choice of effective spatiotemporal feedback coupling kernels.

To perform simulations in the eDoG modeling framework, we computed response curves using the Python toolbox pyLGN²⁴ (Fig. 3). We evaluated the model in its mixed-feedback configuration, where a given dLGN relay cell receives feedback of both signs from cortical cells belonging to the ON and OFF pathways. We took existing code (https://github.com/miladh/edog-simulations/tree/master/size_tuning) that had specified the model parameters following insights from the cat visual system and adjusted them to mimic more closely the properties of the mouse visual system. For the DoG, which represents the receptive field of RGCs, we approximated width parameters based on data recorded from transient OFF α -RGCs⁸³. For the coupling kernels, we scaled the width parameter by a factor of 10, excluding the target inhibitory feedback kernel, which we varied between 1 and 40 in 1° steps. For each inhibitory feedback kernel width, we then generated tuning curves by simulating responses to static gratings of different size (diameter = $0-75^\circ$; step size = 1°) with and without feedback. Feedback was manipulated by setting the weight of the feedback kernels to either 0 (no feedback) or 1. The resulting curves were normalized so that the maximum response in the no feedback condition equaled 1. Preferred size and SI were computed as described for the electrophysiological data.

Statistics and reproducibility. For all electrophysiological experiments, each animal was tested with the full set of stimuli. For experiments in which we manipulated neural activity with optogenetics, we chose a within-study design in which neural responses are probed under the photostimulation and control conditions. Stimulus presentation was pseudorandomized. To avoid making assumptions about the distribution of the data, we used non-parametric tests for statistical comparison. We did not explicitly try to reproduce experiments; however, for statistical tests, we always pooled responses from neurons from multiple recording sessions and animals. No statistical methods were used to predetermine sample sizes, but our sample sizes are similar to those reported in previous publications¹⁵. Criteria for excluding data depended on the analysis and are described in detail in the Methods. In brief, for anatomical tracing studies, we only considered mice in which the cortical expression zone of the virus was focal. For experiments in which we used optogenetics to manipulate CT feedback, we only considered mice in which we observed reliable effects of light stimulation in recordings from V1. For some analyses, we excluded neurons that were not visually responsive or whose response pattern was not captured well by the descriptive model. The investigators were not blinded to allocation during experiments and outcome assessment. Data collection and analysis were not performed blind to the conditions of the experiments.

Reporting Summary. Further information on research design is available in the Nature Research Reporting Summary linked to this article.

Data availability

Except for Fig. 3, all figures were generated from processed data. The data sets are available from https://gin.g-node.org/busse_lab/corticothalamic_spatial_integration.

Code availability

Preprocessed data were analyzed in Matlab and Python using custom-written code. The code to reproduce the figures is available at https://gin.g-node.org/busse_lab/corticothalamic_spatial_integration.

References

- Gong, S. et al. Targeting Cre recombinase to specific neuron populations with bacterial artificial chromosome constructs. *J. Neurosci.* **27**, 9817–9823 (2007).
- Chan, K. Y. et al. Engineered AAVs for efficient noninvasive gene delivery to the central and peripheral nervous systems. *Nat. Neurosci.* **20**, 1172–1179 (2017).
- Zolotukhin, S. et al. Recombinant adeno-associated virus purification using novel methods improves infectious titer and yield. *Gene Ther.* **6**, 973–985 (1999).
- Tervo, D. G. R. et al. A designer AAV variant permits efficient retrograde access to projection neurons. *Neuron* **92**, 372–382 (2016).

55. D'Costa, S. et al. Practical utilization of recombinant AAV vector reference standards: focus on vector genomes titration by free ITR qPCR. *Mol. Ther. Methods Clin. Dev.* **3**, 16019 (2016).
56. Rueden, C. T. et al. ImageJ2: ImageJ for the next generation of scientific image data. *BMC Bioinformatics* **18**, 529 (2017).
57. Schindelin, J. et al. Fiji: an open-source platform for biological-image analysis. *Nat. Methods* **9**, 676–682 (2012).
58. Allen Institute for Brain Science. *Allen Mouse Common Coordinate Framework and Reference Atlas* Technical White Paper (Allen Institute for Brain Science, 2017).
59. Shamash, P., Carandini, M., Harris, K. & Steinmetz, N. A tool for analyzing electrode tracks from slice histology. Preprint at *bioRxiv* <https://www.biorxiv.org/content/10.1101/447995v1> (2018).
60. Dombeck, D. A., Khabbaz, A. N., Collman, F., Adelman, T. L. & Tank, D. W. Imaging large-scale neural activity with cellular resolution in awake, mobile mice. *Neuron* **56**, 43–57 (2007).
61. Pachitariu, M., Steinmetz, N., Kadir, S., Carandini, M. & Harris, K. D. Kilosort: realtime spike-sorting for extracellular electrophysiology with hundreds of channels. Preprint at *bioRxiv* <https://www.biorxiv.org/content/10.1101/061481v1.abstract> (2016).
62. Spacek, M. A., Blanche, T. & Swindale, N. Python for large-scale electrophysiology. *Front. Neuroinform.* **2**, 9 (2009).
63. Swindale, N. V. & Spacek, M. A. Spike sorting for polytodes: a divide and conquer approach. *Front. Syst. Neurosci.* **8**, 6 (2014).
64. Quiroga, R. Q., Nadasdy, Z. & Ben-Shaul, Y. Unsupervised spike detection and sorting with wavelets and superparamagnetic clustering. *Neural Comput.* **16**, 1661–1687 (2004).
65. Henze, D. A. et al. Intracellular features predicted by extracellular recordings in the hippocampus in vivo. *J. Neurophysiol.* **84**, 390–400 (2000).
66. Hazan, L., Zugaro, M. & Buzsáki, G. Klusters, neuroscope, NDManager: a free software suite for neurophysiological data processing and visualization. *J. Neurosci. Methods* **155**, 207–216 (2006).
67. Supèr, H. & Roelfsema, P. R. Chronic multiunit recordings in behaving animals: advantages and limitations. *Prog. Brain Res.* **147**, 263–282 (2005).
68. Mitzdorf, U. Current source-density method and application in cat cerebral cortex: investigation of evoked potentials and EEG phenomena. *Physiol. Rev.* **65**, 37–100 (1985).
69. Nicholson, C. & Freeman, J. A. Theory of current source-density analysis and determination of conductivity tensor for anuran cerebellum. *J. Neurophysiol.* **38**, 356–368 (1975).
70. Heumann, D., Leuba, G. & Rabinowicz, T. Postnatal development of the mouse cerebral neocortex. II. Quantitative cytoarchitectonics of visual and auditory areas. *J. Hirnforsch.* **18**, 483–500 (1977).
71. Yatsenko, D., Walker, E. Y. & Tolia, A. S. DataJoint: a simpler relational data model. Preprint at <https://arxiv.org/abs/1807.11104> (2018).
72. Liu, B.-h et al. Visual receptive field structure of cortical inhibitory neurons revealed by two-photon imaging guided recording. *J. Neurosci.* **29**, 10520–10532 (2009).
73. Katzner, S., Busse, L. & Carandini, M. GABAA inhibition controls response gain in visual cortex. *J. Neurosci.* **31**, 5931–5941 (2011).
74. Bonhoeffer, T., Kim, D.-S., Maloney, D., Shoham, D. & Grinvald, A. Optical imaging of the layout of functional domains in area 17 and across the area 17/18 border in cat visual cortex. *Eur. J. Neurosci.* **7**, 1973–1988 (1995).
75. Niell, C. M. & Stryker, M. P. Highly selective receptive fields in mouse visual cortex. *J. Neurosci.* **28**, 7520–7536 (2008).
76. Albrecht, D. G. & Hamilton, D. B. Striate cortex of monkey and cat: contrast response function. *J. Neurophysiol.* **48**, 21 (1982).
77. Cavanaugh, J. R., Bair, W. & Movshon, J. A. Nature and interaction of signals from the receptive field center and surround in macaque V1 neurons. *J. Neurophysiol.* **88**, 2530–2546 (2002).
78. Van den Bergh, G., Zhang, B., Arckens, L. & Chino, Y. M. Receptive-field properties of V1 and V2 neurons in mice and macaque monkeys. *J. Comp. Neurol.* **518**, 2051–2070 (2010).
79. Sceniak, M. P., Hawken, M. J. & Shapley, R. Visual spatial characterization of macaque V1 neurons. *J. Neurophysiol.* **85**, 1873–1887 (2001).
80. Maris, E. & Oostenveld, R. Nonparametric statistical testing of EEG- and MEG-data. *J. Neurosci. Methods* **164**, 177–190 (2007).
81. Wang, W., Jones, H. E., Andolina, I. M., Salt, T. E. & Sillito, A. M. Functional alignment of feedback effects from visual cortex to thalamus. *Nat. Neurosci.* **9**, 1330–1336 (2006).
82. Wells, M. F., Wimmer, R. D., Schmitt, L. I., Feng, G. & Halassa, M. M. Thalamic reticular impairment underlies attention deficit in *Ptchd1^{+/−}* mice. *Nature* **532**, 58–63 (2016).
83. Ströh, S. et al. Eliminating glutamatergic input onto horizontal cells changes the dynamic range and receptive field organization of mouse retinal ganglion cells. *J. Neurosci.* **38**, 2015–2028 (2018).

Acknowledgements

This research was supported by DFG BU 1808/5-1 (L.B.), DFG SFB870 TP19 (118803580) (L.B.), by an add-on fellowship from the Joachim Herz Stiftung (G.B.), by DFG SFB870 Z04 (118803580) (M. Götz) and by funds awarded to the Centre for Integrative Neuroscience within the framework of German Excellence Initiative (DFG EXC 307). The funders had no role in study design, data collection and analysis, decision to publish or preparation of the manuscript. We thank the Viral Vector Facility of the LMU, in particular I. Mühlhahn for CsCl DNA preparation and A. Wal for recording some of the data in Fig. 2. Confocal microscopy was performed in the bioimaging core facility of the LMU Biomedical Center. We are grateful to M. Sotgia for lab management and support with animal handling, M. Sotgia and H. Wolfrohm for contributing to histology, S. Schörnich for IT support and B. Grothe for providing an excellent research infrastructure.

Author contributions

L.B., S.E., G.B., F.A.S.-S. and A.V. conceptualized the study. M.H.M. and G.T.E. developed the methodology. G.B., S.E., F.A.S.-S., M.A.S., M.H.M. and L.B. developed the software. G.B., F.A.S.-S., S.E. and L.B. performed the formal analysis. G.B., F.A.S.-S., S.E., A.V. and M.A.S. performed the experimental investigations. C.L.L. provided resources. M.A.S., G.B., S.E., L.B. and F.A.S.-S. curated the data. G.B., S.E., F.A.S.-S. and L.B. wrote the original draft. All authors wrote and edited the manuscript. G.B., F.A.S.-S., S.E. and L.B. visualized the data. L.B. supervised the project, and L.B. and G.B. acquired funding.

Competing interests

The authors declare no competing interests.

Additional information

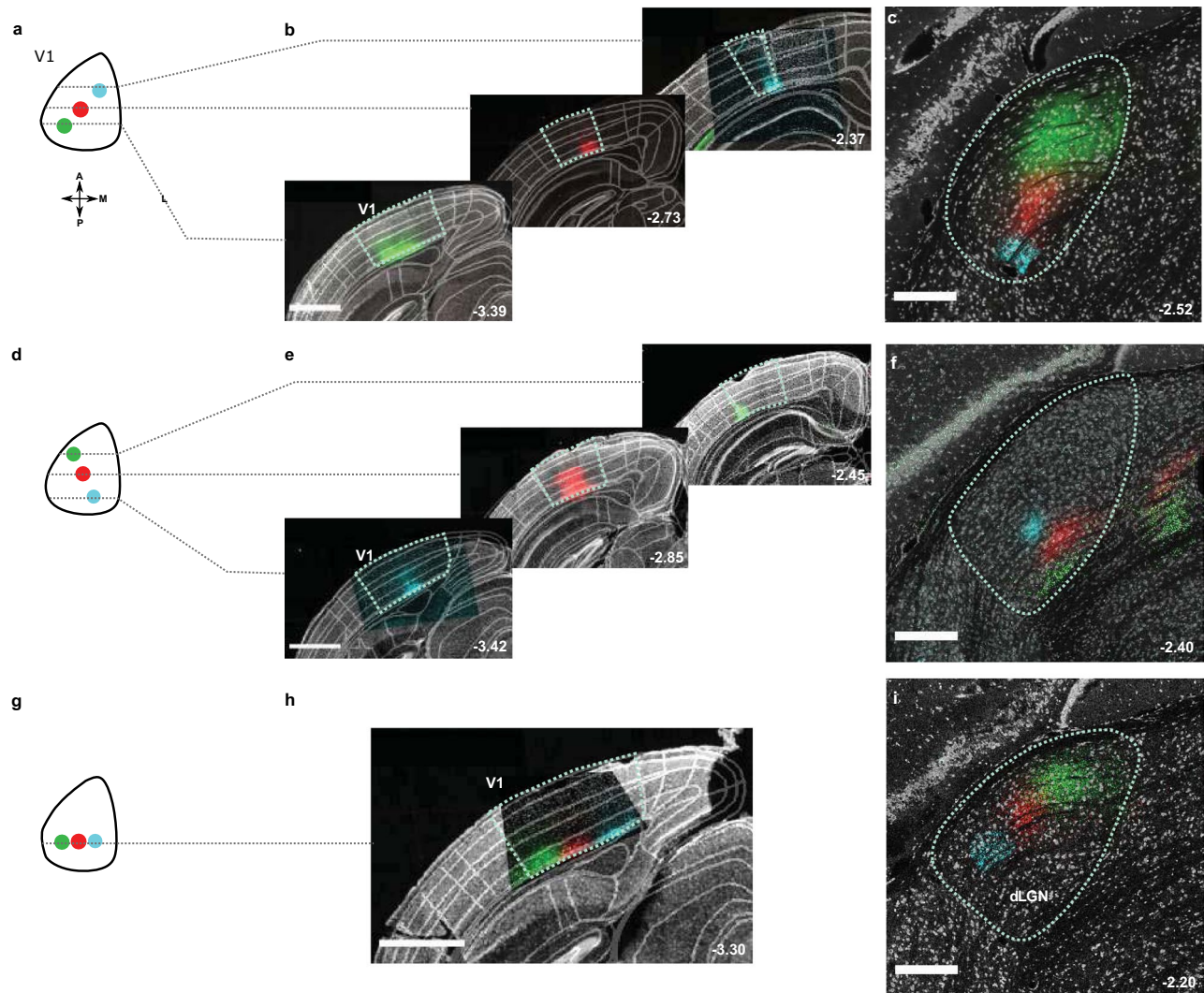
Extended data is available for this paper at <https://doi.org/10.1038/s41593-021-00943-0>.

Supplementary information The online version contains supplementary material available at <https://doi.org/10.1038/s41593-021-00943-0>.

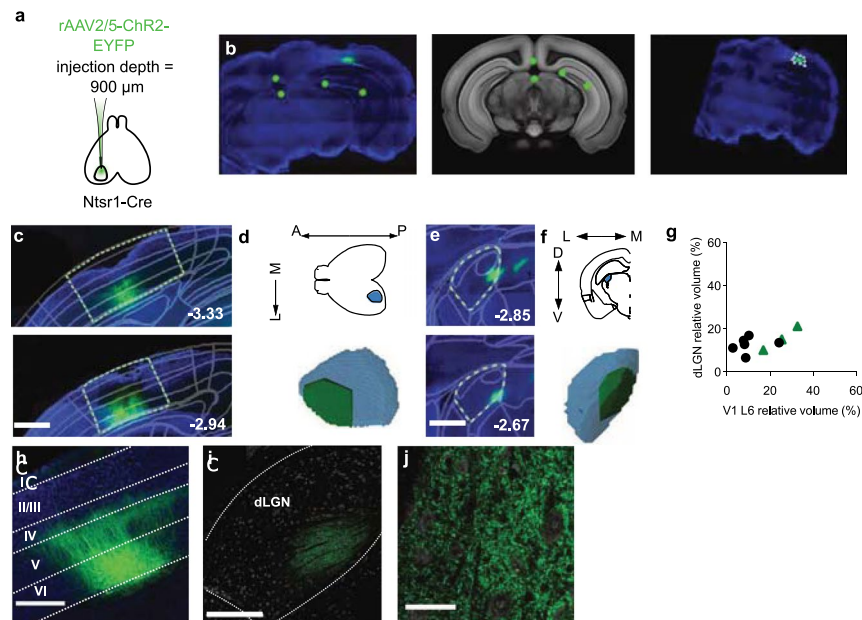
Correspondence and requests for materials should be addressed to Laura Busse.

Peer review information *Nature Neuroscience* thanks the anonymous reviewers for their contribution to the peer review of this work.

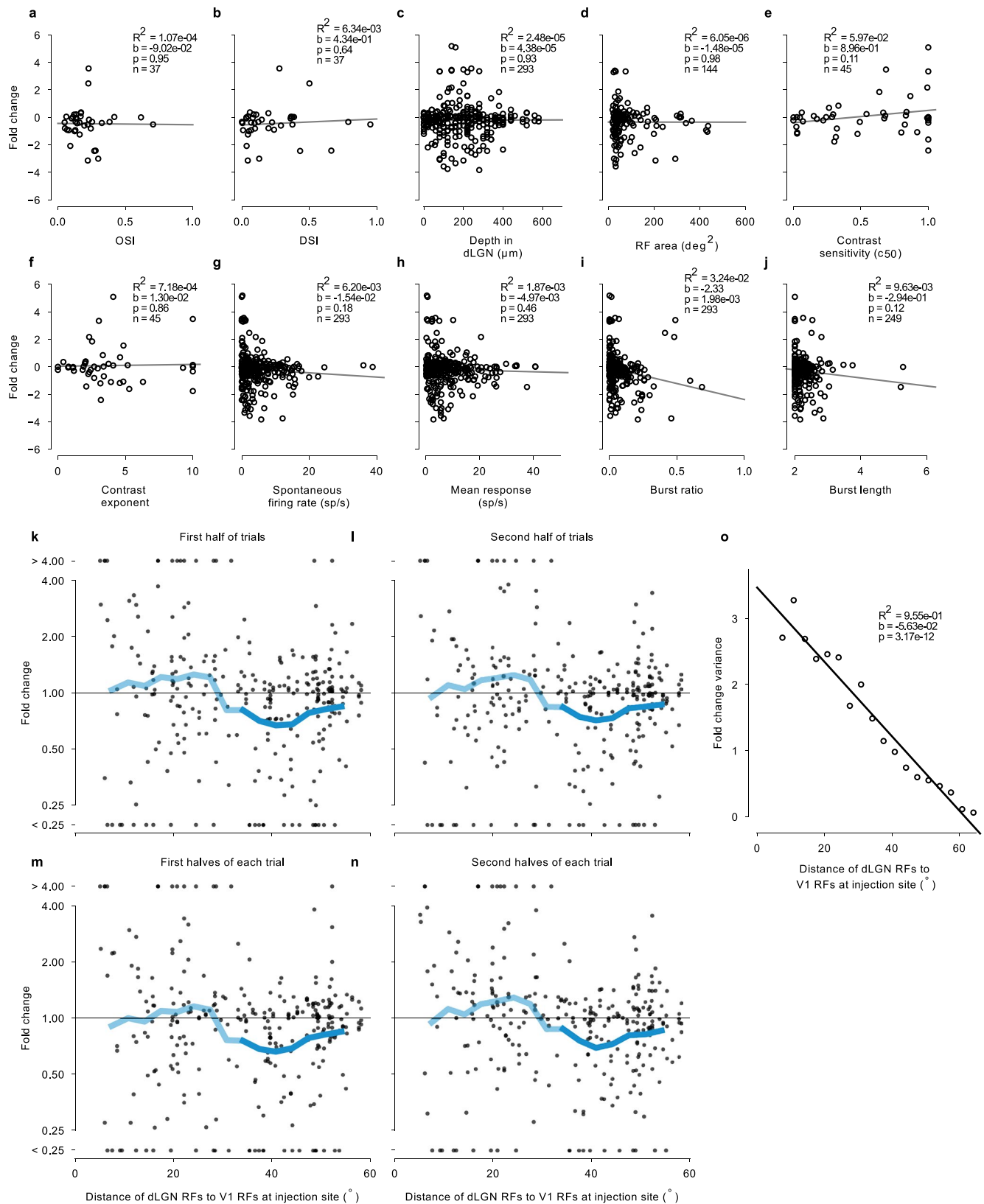
Reprints and permissions information is available at www.nature.com/reprints.



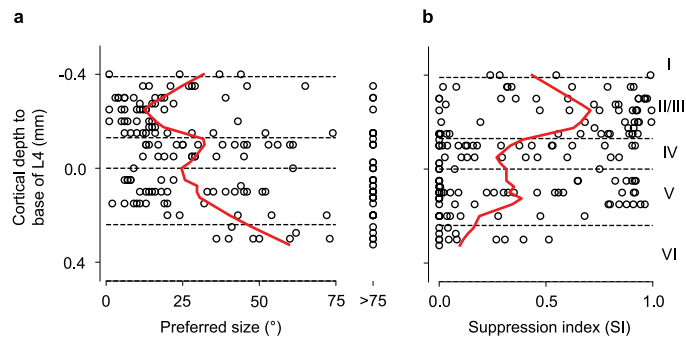
Extended Data Fig. 1 | Results of additional mice used for the analysis of retinotopy of corticothalamic projections. (a) Cartoon of V1 injection sites along the elevation axis. (b) Representative coronal slices with fluorophore expression along the V1 elevation axis. Images are ordered posterior to anterior. (c) Labeled L6CT axonal terminal fields in dLGN. (d–f). Same as (a–c) for another mouse, injected along the V1 azimuth axis. (g–i) Results of another mouse, where V1 injections were placed within a single coronal plane. Narrow-field images of *mTurquoise2* in b,e and *eGFP*, *mScarlet* and *mTurquoise2* in h were acquired with a confocal microscope and manually aligned with the wide-field epifluorescence images of the corresponding brain slices. All panels: numbers indicate distance from bregma. (b,e,h) Scale bar: 1 mm. (c,f,h) Scale bar: 250 μ m. Observations in (b–i) were reproduced in 5 mice.



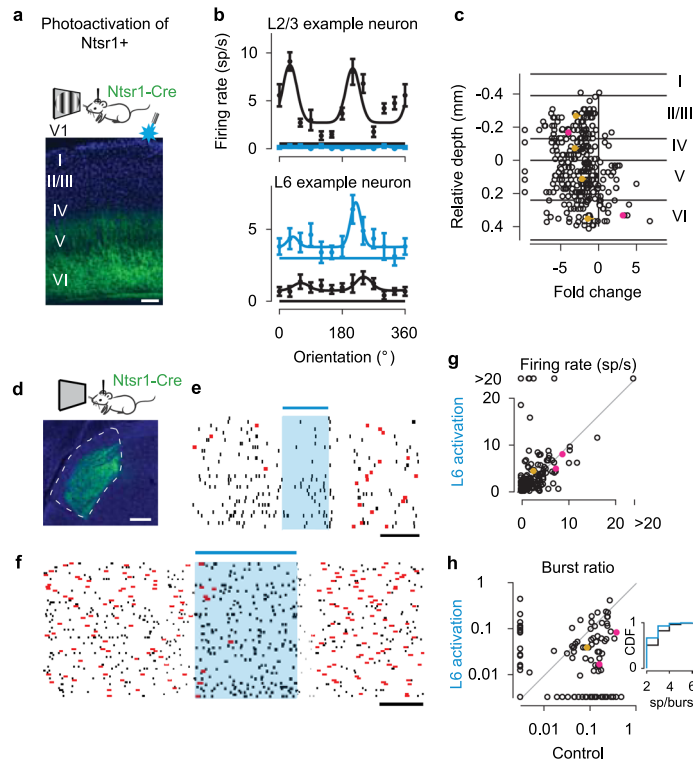
Extended Data Fig. 2 | Quantification of expression volumes. (a) Schematic of the injection: Extended Data Fig. 1). expression of ChR2-eYFP ($n=3$), eGFP ($n=3$) or mScarlet ($n=3$) in a localized population of V1 L6CT pyramidal cells (see also Fig. 1a,b and Extended Data Fig. 1) (b) Pipeline for quantification of expression volumes. (b) *Left*: Manually chosen reference points (*green circles*) on salient features of an example brain-slice image. *Blue*: DAPI; *fainter green*: eYFP. *Middle*: Corresponding locations marked on the manually chosen atlas section from the Allen CCF (see Methods). (c) *Right*: Brain-slice image registered and transformed to the CCF. White points outline the expression zone and are extracted as CCF coordinates. (c-f) Computation of the relative volumes of transduced V1 CT pyramidal cells within L6 ('source volume') and those of their dLGN projections ('target volume') for a representative Ntsr1-Cre mouse. (c) Coronal sections of the V1 injection site, overlaid with fitted area boundaries from the Allen CCF (*gray*). *Green*: ChR2-eYFP. (d) *Top*: Top view of V1 L6 (*blue*) within the cortex (*black contour*). *Bottom*: 3D reconstruction of the expression volume (*green*) within V1 L6 (*blue*), seen from the same perspective as the upper panel ('source volume'). Relative volume: 25%. (e) Coronal sections with transduced L6CT neurons projecting to a restricted volume the dLGN. (f) *Top*: Coronal schematic of dLGN (*blue*) within the brain section (*black contour*). *Bottom*: 3D reconstruction of the expression volume (*green*) within the dLGN (*blue*), seen from the same perspective as the upper panel ('target volume'). Relative volume: 15%. In (c,e), numbers in bottom right corner indicate distance from bregma in mm; scale bar: 0.5 mm. (g) Comparison of the relative expression volumes within V1 L6 ((expression volume within V1 L6)/(total volume of V1 L6)) and dLGN ((expression volume within dLGN)/(total volume of dLGN)) for each mouse. Local injections in V1 yield restricted, spatially specific expression in dLGN with similar relative volumes (mean difference = 0.017, $p=0.55$, resampling, $n=9$ mice). *Black*: mice used for viral tracing experiments; *green*: mice used for ChR2-assisted functional mapping). (h) Example close-up image of L6CT neurons expressing eGFP (*green*). Scale bar: 0.5 mm. (i) Example confocal image of dLGN with eGFP signal in projections from L6CT neurons. Scale bar: 250 μm . (j) Close-up confocal image of L6CT projections in dLGN for same slice as in (i). Scale bar: 25 μm .



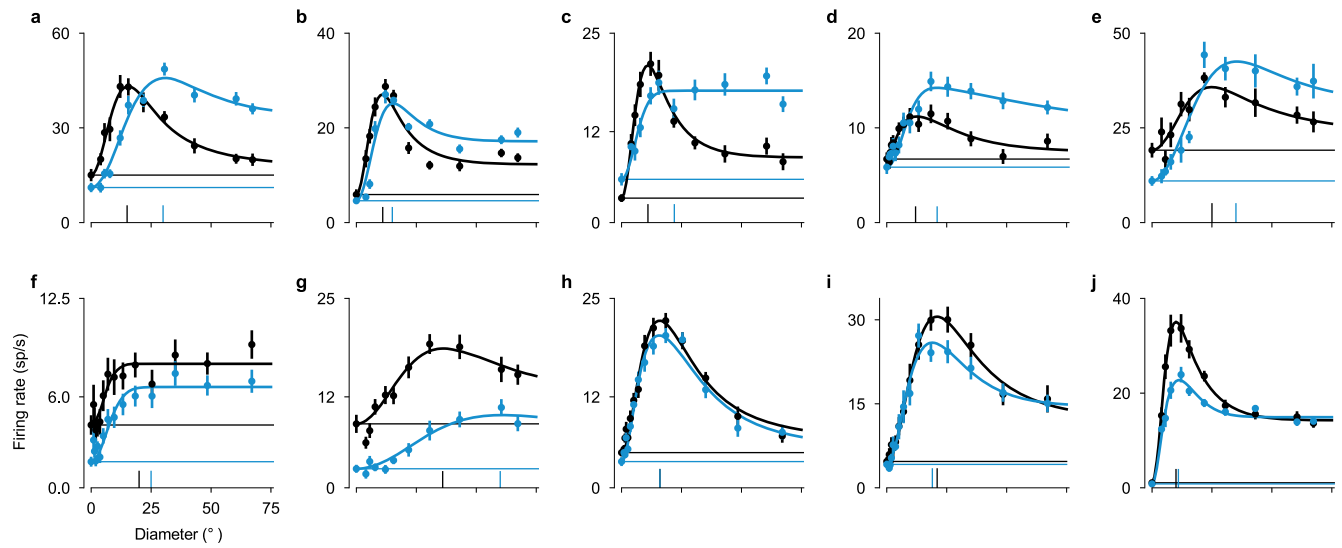
Extended Data Fig. 3 | L6CT photoactivation effects across various classifications of dLGN neurons and stability of distance dependence. Change of firing rate (fold change, \log_2 ratio) as a function of **(a)** orientation selectivity index (OSI, see Methods), **(b)** direction selectivity index (DSI, see Methods), **(c)** estimated depth within dLGN, **(d)** RF area as obtained from sparse noise experiments, **(e)** contrast sensitivity (c_{50}) and **(f)** exponent n of the contrast response function, **(g)** spontaneous firing rate obtained from interleaved blank trials, **(h)** mean response across all drift directions, **(i)** burst ratio, and **(j)** burst length (spikes/burst). Functional properties in (a,b,g-j) are computed from direction tuning experiments. **(k,l)** Spatial profile of modulations induced by photostimulation of CT feedback (see Fig. 1i) retested for the first half and second half of trials in each experiment (*first half*: $p = 0.003$, *second half*: $p = 0.015$). **(m,n)** Same as *k-l* for data partitioned into first and second half of each individual trial (*first half*: $p = 0.016$, *second half*: $p = 0.009$). **(o)** Variance in fold change values across distance in same overlapping bins as in Fig. 1i for all trials. *Black line*: regression fit; *b*: slope; *p*: significance of slope.



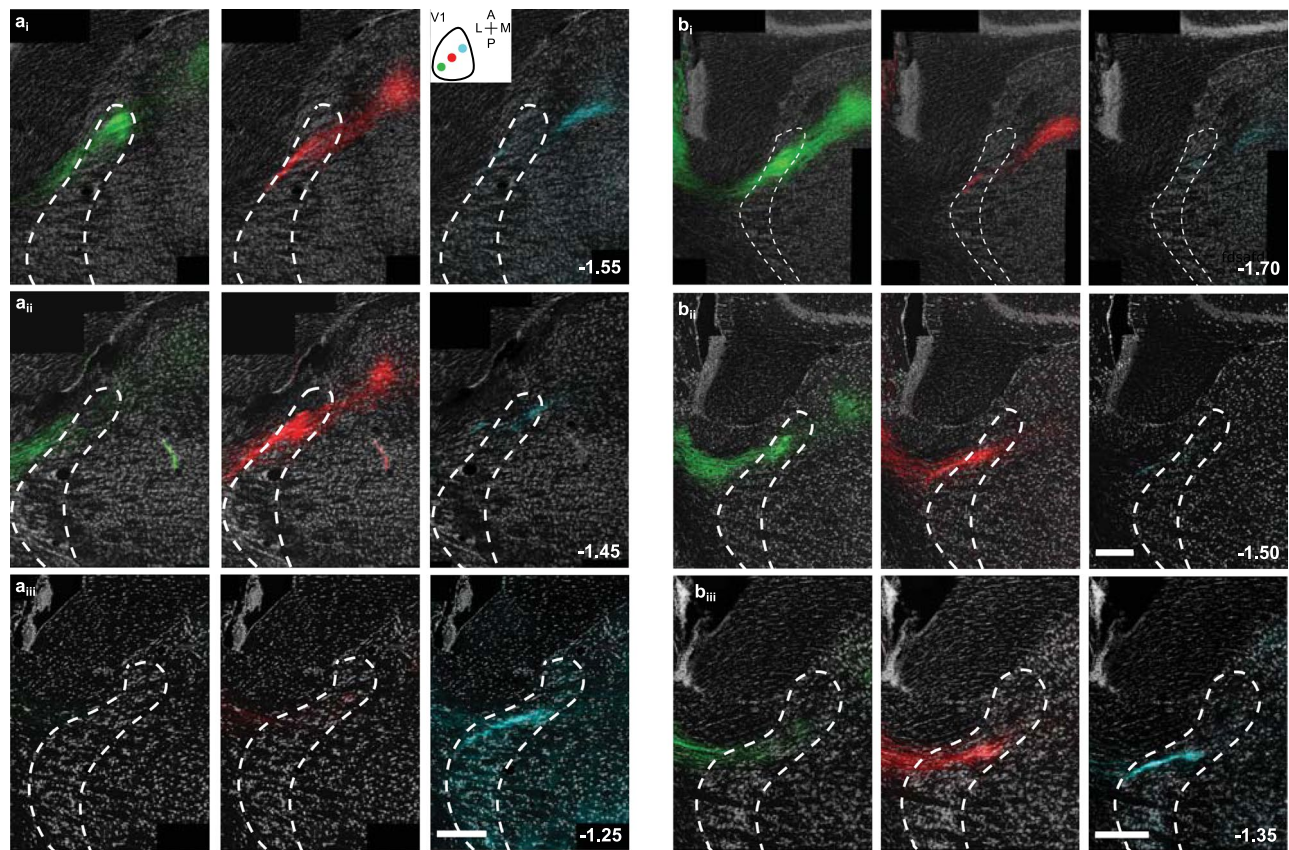
Extended Data Fig. 4 | Neurons in L6 of mouse V1 prefer large stimulus sizes and experience little surround suppression. (a) Distribution of preferred size for neurons ($n=177$) recorded across layers of V1. **(b)** Same as (a) for suppression index. *Dashed horizontal lines:* borders between V1 layers, based on CSD analysis and histological estimates of relative layer thickness (see Methods). *Red:* Smoothed mean computed by local robust regression (MATLAB function 'smooth', method 'rlowess', window size = 0.28 mm).



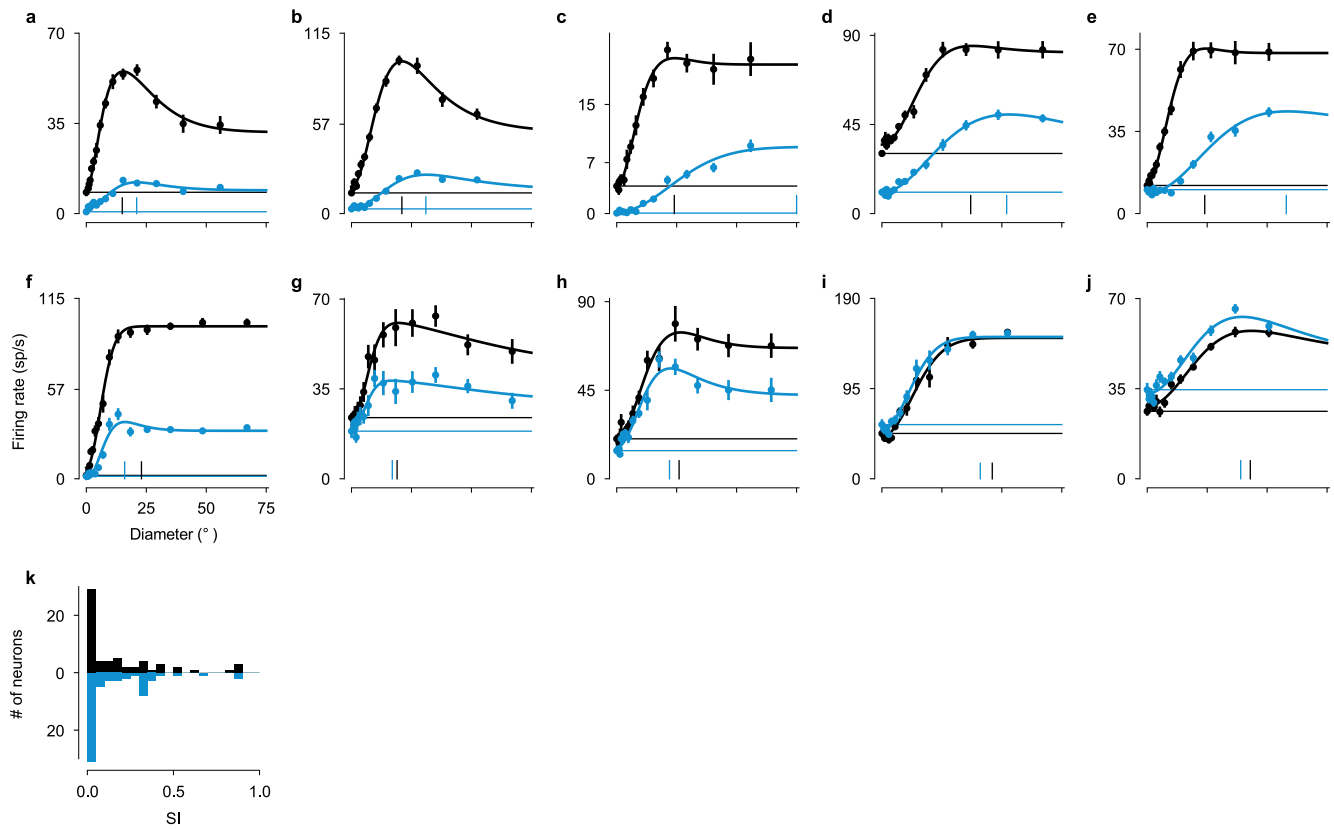
Extended Data Fig. 5 | Photoactivation of L6CT neurons promotes dLGN tonic firing mode. (a) Representative image of a V1 coronal section from a Ntsr1-Cre mouse injected with Cre-dependent AAV-ChR2. Green: ChR2-YFP, blue: DAPI. Scale bar 100 μ m. (b) Example orientation-tuning curves of cells located in putative L2/3 or putative L6 for trials during V1 L6CT photoactivation (blue) and under control conditions (black). Visual stimulus: Drifting gratings with temporal and spatial frequencies coarsely optimized for the recording, duration 0.75 s, photostimulation: starting 0.1 s before stimulus onset, lasting for 0.85 s. Data are presented as mean values \pm s.e.m.. (c) Fold change (that is log₂ ratio of average firing rates for V1 L6CT photoactivation and control conditions across tuning experiments) as a function of cortical depth relative to the base of L4, estimated by CSD (see Methods). Gold: layer-wise mean; pink: example neurons. Error bars: confidence intervals of the mean, determined by bootstrapping. $n = 362$ neurons. (d) Representative image of a dLGN coronal slice, with axons of Ntsr1+ neurons expressing ChR2 in green. (e,f) Recordings from dLGN. Raster plots of two example dLGN neurons during spontaneous activity aligned to V1 L6CT photoactivation (shaded blue). Red: burst spikes, black horizontal bar: 200 ms. (e) $n = 31$ trials, (f) $n = 69$ trials. (g) Firing rates during vs. before V1 L6CT photoactivation. Activation of L6CT neurons yielded diverse results (during: 4.2 sp/s vs. before: 2.7 sp/s; $n = 167$ neurons; $p = 0.4$, two-sided Wilcoxon signed-rank test), consistent with the interpretation of our functional mapping experiments (Fig. 1k). (h) Ratio of burst spikes during vs. before V1 L6CT photoactivation. Activating CT feedback decreased the fraction of spikes fired in bursts (before: 9.04%, during: 3.75%; $n = 139$ neurons; $p = 1.7 \times 10^{-7}$, Wilcoxon signed-rank test). Data points at marginals represent burst ratio = 0. Inset: cumulative distribution of burst lengths during (blue) vs. before (black) V1 L6CT photoactivation. Activating CT feedback shifted the distribution of spikes per burst towards lower values ($p = 7.8 \times 10^{-5}$, two-sample Kolmogorov-Smirnov test).



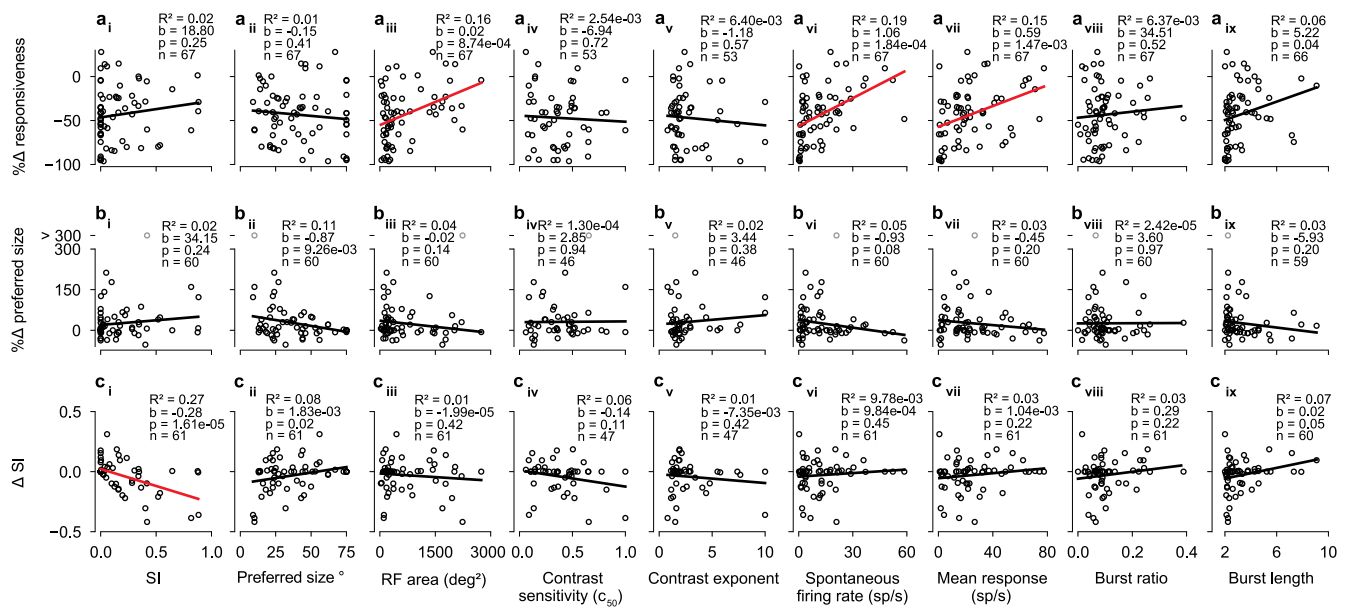
Extended Data Fig. 6 | Size tuning curves of more dLGN example neurons. *Black*: control condition; *Blue*: V1 suppression; horizontal lines: responses to blank screen (size 0 deg); vertical lines: preferred size; error bars represent s.e.m.



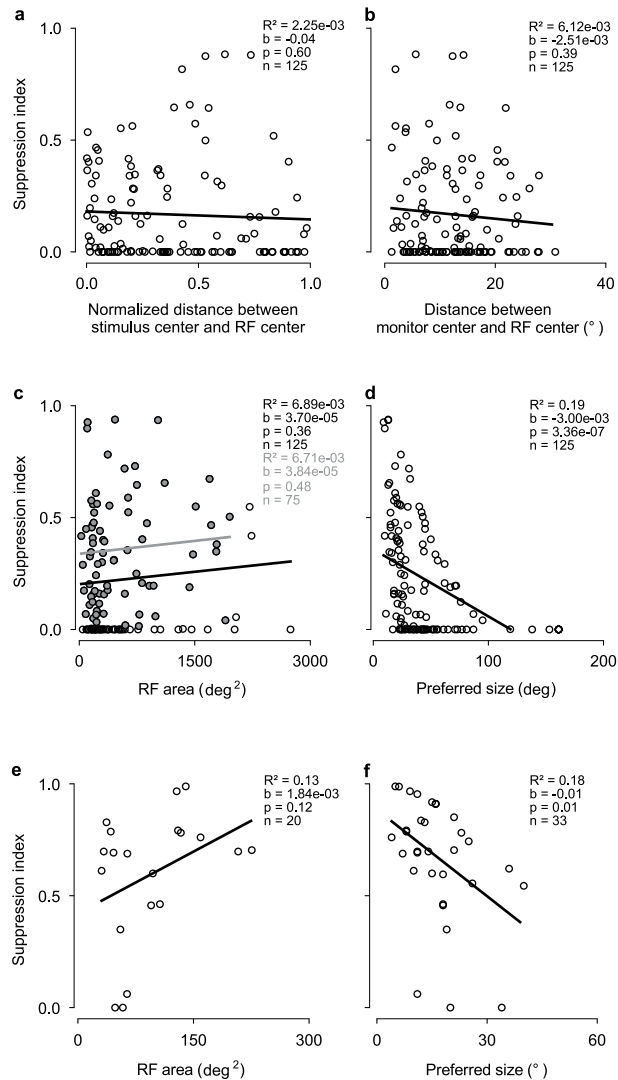
Extended Data Fig. 7 | In visTRN, elevation is predominantly encoded along the anterior-posterior axis. (a_{i-iii}) Innervation pattern in visTRN of axons from L6CT populations transduced with pAAV-CAG-FLEX-EGFP (*green, left*), pAAV-CAG-FLEX-mScarlet (*red, middle*), or pAAV-CAG-FLEX-mTurquoise (*blue, right*). V1 injections were performed along the retinotopic axis representing elevation (*a_i, inset, right*), with EGFP labeling V1 regions representing higher elevations. Confocal images in (a_{i-iii}) are arranged from posterior to anterior (number indicates distance from bregma in mm); images of each row were taken from the same slice, with separate visualization of the three fluorophores. Note that more anterior regions in visTRN contain terminal fields of L6CT axons labeled with mTurquoise, that is representing lower elevations in the visual field; middle regions along the AP axis in visTRN contain terminal fields of L6CT axons labeled with mScarlet, that is representing central elevations in the visual field; more posterior regions in visTRN contain terminal fields of L6CT axons labeled with EGFP, that is representing higher elevations in the visual field. (b_{i-iii}) Same as (a) for a second example mouse. All scale bars 0.25 mm. We observed retinotopic CT projections from V1 to visTRN in 4 mice.



Extended Data Fig. 8 | Size tuning curves of more visTRN example neurons. (a–j) *Black*: control condition; *Blue*: V1 suppression; horizontal lines: responses to blank screen (size 0 deg); vertical lines: preferred size; error bars represent s.e.m. (k) Distribution of suppression indices for the visTRN neuron population ($n = 61$) during control (*black*) and V1 suppression (*blue*). Note that in both conditions the majority of visTRN neurons show little to no surround suppression ($SI < 0.05$).



Extended Data Fig. 9 | The relationship between CT feedback effects on visTRN neurons and their response properties. (a) Percent change in overall responsiveness by CT feedback as a function of SI (a_i) and preferred size (a_{ii}) under control conditions, RF area as measured by a sparse noise stimulus (a_{iii}), contrast sensitivity (c₅₀, a_{iv}) and steepness of the contrast response function (a_v), spontaneous firing rate (a_{vi}), mean response (a_{vii}), burst ratio (a_{viii}), and burst length (a_{ix}) under control conditions of the size tuning experiments. While many relationships are not significant, CT feedback reduces overall responsiveness more for visTRN neurons with small compared to large RFs (a_{iii}), but the explained variance is small, partially because there is a wide array of effects for visTRN neurons with rather small RF coverage. Second, visTRN neurons with higher firing rates, show stronger CT feedback related modulations of firing rate (a_{vi-viii}), pointing towards a multiplicative mechanism. (b,c) Same as (a), for CT feedback effects on preferred size and on surround suppression (SI), respectively. The observation that visTRN neurons with stronger surround suppression in control conditions show more pronounced changes in SI than those with weaker surround suppression (c) could point towards an interesting subpopulation of visTRN neurons, which might represent spatial context and for which this representation is further enhanced by CT feedback. Black/red line: regression fit; b: slope; p: significance of slope.



Extended Data Fig. 10 | Correlations between suppression index and distance of RF center to monitor or stimulus center, and between suppression index and preferred size. (a) Suppression indices for visTRN population ($n = 125$) plotted against the normalized distance between stimulus center and their RF centers (Black line: linear regression; b : slope; p : significance of slope). (b) Suppression indices for visTRN population plotted against the distance between monitor center and their RF centers. (c,d) Strength of surround suppression in visTRN measured during size tuning as a function of RF area mapped with the sparse noise stimulus (c) and as a function of preferred size taken from the size tuning curve (d). Black: regression line including all data points, grey regression line including a restricted set ($S/I > 0.01$ and RF area < 2000 deg²). (e,f) Same as (c-d), for dLGN neurons. Note that in both visTRN (d) and dLGN (f) neurons with larger preferred sizes also tend to have less surround suppression. One caveat regarding the interpretation of this anti-correlation is the limited size of our monitor, which for neurons with larger RFs might not allow for a sufficiently strong stimulation of the surround.

Reporting Summary

Nature Portfolio wishes to improve the reproducibility of the work that we publish. This form provides structure for consistency and transparency in reporting. For further information on Nature Portfolio policies, see our [Editorial Policies](#) and the [Editorial Policy Checklist](#).

Statistics

For all statistical analyses, confirm that the following items are present in the figure legend, table legend, main text, or Methods section.

n/a Confirmed

- The exact sample size (n) for each experimental group/condition, given as a discrete number and unit of measurement
- A statement on whether measurements were taken from distinct samples or whether the same sample was measured repeatedly
- The statistical test(s) used AND whether they are one- or two-sided
Only common tests should be described solely by name; describe more complex techniques in the Methods section.
- A description of all covariates tested
- A description of any assumptions or corrections, such as tests of normality and adjustment for multiple comparisons
- A full description of the statistical parameters including central tendency (e.g. means) or other basic estimates (e.g. regression coefficient) AND variation (e.g. standard deviation) or associated estimates of uncertainty (e.g. confidence intervals)
- For null hypothesis testing, the test statistic (e.g. F , t , r) with confidence intervals, effect sizes, degrees of freedom and P value noted
Give P values as exact values whenever suitable.
- For Bayesian analysis, information on the choice of priors and Markov chain Monte Carlo settings
- For hierarchical and complex designs, identification of the appropriate level for tests and full reporting of outcomes
- Estimates of effect sizes (e.g. Cohen's d , Pearson's r), indicating how they were calculated

Our web collection on [statistics for biologists](#) contains articles on many of the points above.

Software and code

Policy information about [availability of computer code](#)

Data collection

Electrophysiological data were collected with a commercial data acquisition system (Cerebus, Version 6.03.01.00, Blackrock Microsystems). Visual stimuli were generated and presented using Expo (Version 1.5.13, developed and maintained at NYU). Light-stimulation for optogenetic manipulation, tracking of eye position and locomotion was done with custom code written in MatLab (R2014b) and C#.

Data analysis

Most of the data were preprocessed with Kilosort (2016, <https://github.com/cortex-lab/Kilosort>), ran in MatLab (R2019a), and Spyke (version 2.1, <https://github.com/spyke/spyke>). A subset of the data was preprocessed with KlustaKwik (2000, <https://github.com/klusta-team/klustakwik>) and Klusters (version 2.0.0, <https://sourceforge.net/projects/neurosuite/files/sources/>). Data was organized within the DataJoint framework (version 0.12.5, <https://github.com/datajoint>). Data analysis was carried out using custom-written Python (version 3.6) code which will be released upon publication of the manuscript. To quantify expression volumes, we used the allenCCF tools software package (2017, <https://github.com/cortex-lab/allenCCF>) and PyMesh (version 0.3, <https://github.com/PyMesh/PyMesh>). The code for data analysis is available from https://gin.g-node.org/busse_lab/corticothalamic_spatial_integration.

For manuscripts utilizing custom algorithms or software that are central to the research but not yet described in published literature, software must be made available to editors and reviewers. We strongly encourage code deposition in a community repository (e.g. GitHub). See the Nature Portfolio [guidelines for submitting code & software](#) for further information.

Data

Policy information about [availability of data](#)

All manuscripts must include a [data availability statement](#). This statement should provide the following information, where applicable:

- Accession codes, unique identifiers, or web links for publicly available datasets
- A description of any restrictions on data availability
- For clinical datasets or third party data, please ensure that the statement adheres to our [policy](#)

Except for Figure 3, all figures were generated from processed data. These data are available from https://gin.g-node.org/busse_lab/corticothalamic_spatial_integration.

Field-specific reporting

Please select the one below that is the best fit for your research. If you are not sure, read the appropriate sections before making your selection.

Life sciences Behavioural & social sciences Ecological, evolutionary & environmental sciences

For a reference copy of the document with all sections, see [nature.com/documents/nr-reporting-summary-flat.pdf](https://www.nature.com/documents/nr-reporting-summary-flat.pdf)

Life sciences study design

All studies must disclose on these points even when the disclosure is negative.

Sample size	Depending on the analysis, sample size relates to the number of animals or the number of neurons. In both cases, sizes were determined by the standards accepted in the field and by the limits of what can be achieved within a reasonable time. No statistical methods were used to pre-determine sample sizes but our sample sizes are similar to those reported in previous publications (Erisken et al., 2014).
Data exclusions	Criteria for excluding data depended on the analysis and are described in detail in the method section. In brief, for anatomical tracing studies we only considered mice in which the cortical expression zone of the virus was focal. For experiments in which we used optogenetics to manipulate corticothalamic feedback, we only considered mice in which we observed reliable effects of light stimulation in recordings from V1. For some analyses, we excluded neurons which were not visually responsive or whose response pattern was not captured well by the descriptive model.
Replication	We did not try to replicate the exact same results outside our study. However, in our figures we present population averages together with individual data recorded from different neurons in different animals. This demonstrates that the effects are representative and not caused by a small fraction of samples.
Randomization	Except for the comparison of receptive field sizes in visTRN and dLGN, our experiments had a within-subject design, in which each neuron contributes data to each experimental condition.
Blinding	As described under 'Randomization', most of our experiments had a within-subject design. In a within-subject design each neuron is probed under each experimental condition. Blinding is therefore not applicable.

Behavioural & social sciences study design

All studies must disclose on these points even when the disclosure is negative.

Study description	<i>Briefly describe the study type including whether data are quantitative, qualitative, or mixed-methods (e.g. qualitative cross-sectional, quantitative experimental, mixed-methods case study).</i>
Research sample	<i>State the research sample (e.g. Harvard university undergraduates, villagers in rural India) and provide relevant demographic information (e.g. age, sex) and indicate whether the sample is representative. Provide a rationale for the study sample chosen. For studies involving existing datasets, please describe the dataset and source.</i>
Sampling strategy	<i>Describe the sampling procedure (e.g. random, snowball, stratified, convenience). Describe the statistical methods that were used to predetermine sample size OR if no sample-size calculation was performed, describe how sample sizes were chosen and provide a rationale for why these sample sizes are sufficient. For qualitative data, please indicate whether data saturation was considered, and what criteria were used to decide that no further sampling was needed.</i>
Data collection	<i>Provide details about the data collection procedure, including the instruments or devices used to record the data (e.g. pen and paper, computer, eye tracker, video or audio equipment) whether anyone was present besides the participant(s) and the researcher, and whether the researcher was blind to experimental condition and/or the study hypothesis during data collection.</i>

Timing	Indicate the start and stop dates of data collection. If there is a gap between collection periods, state the dates for each sample cohort.
Data exclusions	If no data were excluded from the analyses, state so OR if data were excluded, provide the exact number of exclusions and the rationale behind them, indicating whether exclusion criteria were pre-established.
Non-participation	State how many participants dropped out/declined participation and the reason(s) given OR provide response rate OR state that no participants dropped out/declined participation.
Randomization	If participants were not allocated into experimental groups, state so OR describe how participants were allocated to groups, and if allocation was not random, describe how covariates were controlled.

Ecological, evolutionary & environmental sciences study design

All studies must disclose on these points even when the disclosure is negative.

Study description	Briefly describe the study. For quantitative data include treatment factors and interactions, design structure (e.g. factorial, nested, hierarchical), nature and number of experimental units and replicates.
Research sample	Describe the research sample (e.g. a group of tagged <i>Passer domesticus</i> , all <i>Stenocereus thurberi</i> within Organ Pipe Cactus National Monument), and provide a rationale for the sample choice. When relevant, describe the organism taxa, source, sex, age range and any manipulations. State what population the sample is meant to represent when applicable. For studies involving existing datasets, describe the data and its source.
Sampling strategy	Note the sampling procedure. Describe the statistical methods that were used to predetermine sample size OR if no sample-size calculation was performed, describe how sample sizes were chosen and provide a rationale for why these sample sizes are sufficient.
Data collection	Describe the data collection procedure, including who recorded the data and how.
Timing and spatial scale	Indicate the start and stop dates of data collection, noting the frequency and periodicity of sampling and providing a rationale for these choices. If there is a gap between collection periods, state the dates for each sample cohort. Specify the spatial scale from which the data are taken
Data exclusions	If no data were excluded from the analyses, state so OR if data were excluded, describe the exclusions and the rationale behind them, indicating whether exclusion criteria were pre-established.
Reproducibility	Describe the measures taken to verify the reproducibility of experimental findings. For each experiment, note whether any attempts to repeat the experiment failed OR state that all attempts to repeat the experiment were successful.
Randomization	Describe how samples/organisms/participants were allocated into groups. If allocation was not random, describe how covariates were controlled. If this is not relevant to your study, explain why.
Blinding	Describe the extent of blinding used during data acquisition and analysis. If blinding was not possible, describe why OR explain why blinding was not relevant to your study.
Did the study involve field work?	<input type="checkbox"/> Yes <input type="checkbox"/> No

Field work, collection and transport

Field conditions	Describe the study conditions for field work, providing relevant parameters (e.g. temperature, rainfall).
Location	State the location of the sampling or experiment, providing relevant parameters (e.g. latitude and longitude, elevation, water depth).
Access & import/export	Describe the efforts you have made to access habitats and to collect and import/export your samples in a responsible manner and in compliance with local, national and international laws, noting any permits that were obtained (give the name of the issuing authority, the date of issue, and any identifying information).
Disturbance	Describe any disturbance caused by the study and how it was minimized.

Reporting for specific materials, systems and methods

We require information from authors about some types of materials, experimental systems and methods used in many studies. Here, indicate whether each material, system or method listed is relevant to your study. If you are not sure if a list item applies to your research, read the appropriate section before selecting a response.

Materials & experimental systems

- n/a Involved in the study
- Antibodies
- Eukaryotic cell lines
- Palaeontology and archaeology
- Animals and other organisms
- Human research participants
- Clinical data
- Dual use research of concern

Methods

- n/a Involved in the study
- ChIP-seq
- Flow cytometry
- MRI-based neuroimaging

Antibodies

Antibodies used *Describe all antibodies used in the study; as applicable, provide supplier name, catalog number, clone name, and lot number.*

Validation *Describe the validation of each primary antibody for the species and application, noting any validation statements on the manufacturer's website, relevant citations, antibody profiles in online databases, or data provided in the manuscript.*

Eukaryotic cell lines

Policy information about [cell lines](#)

Cell line source(s) ATCC, IDENTIFIER: CRL-3216

Authentication IDENTIFIER: CRL-3216

Mycoplasma contamination We confirm that cell lines tested negative for mycoplasma contamination.

Commonly misidentified lines (See [ICLAC](#) register) No

Palaeontology and Archaeology

Specimen provenance *Provide provenance information for specimens and describe permits that were obtained for the work (including the name of the issuing authority, the date of issue, and any identifying information). Permits should encompass collection and, where applicable, export.*

Specimen deposition *Indicate where the specimens have been deposited to permit free access by other researchers.*

Dating methods *If new dates are provided, describe how they were obtained (e.g. collection, storage, sample pretreatment and measurement), where they were obtained (i.e. lab name), the calibration program and the protocol for quality assurance OR state that no new dates are provided.*

Tick this box to confirm that the raw and calibrated dates are available in the paper or in Supplementary Information.

Ethics oversight *Identify the organization(s) that approved or provided guidance on the study protocol, OR state that no ethical approval or guidance was required and explain why not.*

Note that full information on the approval of the study protocol must also be provided in the manuscript.

Animals and other organisms

Policy information about [studies involving animals](#); [ARRIVE guidelines](#) recommended for reporting animal research

Laboratory animals Experiments were performed on three strains of adult mice of both sexes: C57BL/6J (n = 3, mean age = 14.2 weeks) and B6;129P2-Pvalbtm1(cre)Arbr/J (n = 19, mean age = 23.3 weeks), both obtained from the Jackson Laboratory and B6.FVB(Cg)-Tg(Ntsr1-cre)GN220Gsat/Mmcd (n = 20, mean age = 24.4 weeks, MMRRC). Animals were housed at ~22.8°C room temperature with an humidity level of ~55% and a reversed 12h light-cycle.

Wild animals No wild animals were used in this study.

Field-collected samples No field collected samples were used in this study.

Ethics oversight All procedures complied with the European Communities Council Directive 2010/63/EU and the German Law on the Protection of Animals, and were approved by local authorities, following appropriate ethics review.

Note that full information on the approval of the study protocol must also be provided in the manuscript.

Human research participants

Policy information about [studies involving human research participants](#)

Population characteristics

Describe the covariate-relevant population characteristics of the human research participants (e.g. age, gender, genotypic information, past and current diagnosis and treatment categories). If you filled out the behavioural & social sciences study design questions and have nothing to add here, write "See above."

Recruitment

Describe how participants were recruited. Outline any potential self-selection bias or other biases that may be present and how these are likely to impact results.

Ethics oversight

Identify the organization(s) that approved the study protocol.

Note that full information on the approval of the study protocol must also be provided in the manuscript.

Clinical data

Policy information about [clinical studies](#)

All manuscripts should comply with the ICMJE [guidelines for publication of clinical research](#) and a completed [CONSORT checklist](#) must be included with all submissions.

Clinical trial registration

Provide the trial registration number from ClinicalTrials.gov or an equivalent agency.

Study protocol

Note where the full trial protocol can be accessed OR if not available, explain why.

Data collection

Describe the settings and locales of data collection, noting the time periods of recruitment and data collection.

Outcomes

Describe how you pre-defined primary and secondary outcome measures and how you assessed these measures.

Dual use research of concern

Policy information about [dual use research of concern](#)

Hazards

Could the accidental, deliberate or reckless misuse of agents or technologies generated in the work, or the application of information presented in the manuscript, pose a threat to:

- | No | Yes | |
|-------------------------------------|--------------------------|----------------------------|
| <input checked="" type="checkbox"/> | <input type="checkbox"/> | Public health |
| <input checked="" type="checkbox"/> | <input type="checkbox"/> | National security |
| <input checked="" type="checkbox"/> | <input type="checkbox"/> | Crops and/or livestock |
| <input checked="" type="checkbox"/> | <input type="checkbox"/> | Ecosystems |
| <input checked="" type="checkbox"/> | <input type="checkbox"/> | Any other significant area |

Experiments of concern

Does the work involve any of these experiments of concern:

- | No | Yes | |
|-------------------------------------|--------------------------|---|
| <input checked="" type="checkbox"/> | <input type="checkbox"/> | Demonstrate how to render a vaccine ineffective |
| <input checked="" type="checkbox"/> | <input type="checkbox"/> | Confer resistance to therapeutically useful antibiotics or antiviral agents |
| <input checked="" type="checkbox"/> | <input type="checkbox"/> | Enhance the virulence of a pathogen or render a nonpathogen virulent |
| <input checked="" type="checkbox"/> | <input type="checkbox"/> | Increase transmissibility of a pathogen |
| <input checked="" type="checkbox"/> | <input type="checkbox"/> | Alter the host range of a pathogen |
| <input checked="" type="checkbox"/> | <input type="checkbox"/> | Enable evasion of diagnostic/detection modalities |
| <input checked="" type="checkbox"/> | <input type="checkbox"/> | Enable the weaponization of a biological agent or toxin |
| <input checked="" type="checkbox"/> | <input type="checkbox"/> | Any other potentially harmful combination of experiments and agents |

ChIP-seq

Data deposition

- Confirm that both raw and final processed data have been deposited in a public database such as [GEO](#).
- Confirm that you have deposited or provided access to graph files (e.g. BED files) for the called peaks.

Data access links <i>May remain private before publication.</i>	<i>For "Initial submission" or "Revised version" documents, provide reviewer access links. For your "Final submission" document, provide a link to the deposited data.</i>
Files in database submission	<i>Provide a list of all files available in the database submission.</i>
Genome browser session (e.g. UCSC)	<i>Provide a link to an anonymized genome browser session for "Initial submission" and "Revised version" documents only, to enable peer review. Write "no longer applicable" for "Final submission" documents.</i>

Methodology

Replicates	<i>Describe the experimental replicates, specifying number, type and replicate agreement.</i>
Sequencing depth	<i>Describe the sequencing depth for each experiment, providing the total number of reads, uniquely mapped reads, length of reads and whether they were paired- or single-end.</i>
Antibodies	<i>Describe the antibodies used for the ChIP-seq experiments; as applicable, provide supplier name, catalog number, clone name, and lot number.</i>
Peak calling parameters	<i>Specify the command line program and parameters used for read mapping and peak calling, including the ChIP, control and index files used.</i>
Data quality	<i>Describe the methods used to ensure data quality in full detail, including how many peaks are at FDR 5% and above 5-fold enrichment.</i>
Software	<i>Describe the software used to collect and analyze the ChIP-seq data. For custom code that has been deposited into a community repository, provide accession details.</i>

Flow Cytometry

Plots

Confirm that:

- The axis labels state the marker and fluorochrome used (e.g. CD4-FITC).
- The axis scales are clearly visible. Include numbers along axes only for bottom left plot of group (a 'group' is an analysis of identical markers).
- All plots are contour plots with outliers or pseudocolor plots.
- A numerical value for number of cells or percentage (with statistics) is provided.

Methodology

Sample preparation	<i>Describe the sample preparation, detailing the biological source of the cells and any tissue processing steps used.</i>
Instrument	<i>Identify the instrument used for data collection, specifying make and model number.</i>
Software	<i>Describe the software used to collect and analyze the flow cytometry data. For custom code that has been deposited into a community repository, provide accession details.</i>
Cell population abundance	<i>Describe the abundance of the relevant cell populations within post-sort fractions, providing details on the purity of the samples and how it was determined.</i>
Gating strategy	<i>Describe the gating strategy used for all relevant experiments, specifying the preliminary FSC/SSC gates of the starting cell population, indicating where boundaries between "positive" and "negative" staining cell populations are defined.</i>

Tick this box to confirm that a figure exemplifying the gating strategy is provided in the Supplementary Information.

Magnetic resonance imaging

Experimental design

Design type	<i>Indicate task or resting state; event-related or block design.</i>
Design specifications	<i>Specify the number of blocks, trials or experimental units per session and/or subject, and specify the length of each trial or block (if trials are blocked) and interval between trials.</i>
Behavioral performance measures	<i>State number and/or type of variables recorded (e.g. correct button press, response time) and what statistics were used to establish that the subjects were performing the task as expected (e.g. mean, range, and/or standard deviation across subjects).</i>

Acquisition

Imaging type(s)

Field strength

Sequence & imaging parameters

Area of acquisition

Diffusion MRI Used Not used

Preprocessing

Preprocessing software

Normalization

Normalization template

Noise and artifact removal

Volume censoring

Statistical modeling & inference

Model type and settings

Effect(s) tested

Specify type of analysis: Whole brain ROI-based Both

Statistic type for inference (See [Eklund et al. 2016](#))

Correction

Models & analysis

n/a	Involved in the study	
<input type="checkbox"/>	<input type="checkbox"/> Functional and/or effective connectivity	
<input type="checkbox"/>	<input type="checkbox"/> Graph analysis	
<input type="checkbox"/>	<input type="checkbox"/> Multivariate modeling or predictive analysis	

Functional and/or effective connectivity

Graph analysis

Multivariate modeling and predictive analysis

3 Robust effects of corticothalamic feedback during naturalistic visual stimulation

This chapter is reproduced from an article published on *bioRxiv*. The article can be found under <https://www.biorxiv.org/content/10.1101/776237v6>. The full citation is:

Spacek, M. A., Born, G., Crombie, D., Bauer, Y., Liu, X., Katzner, S. A., & Busse, L. (2021). Robust effects of cortical feedback on thalamic firing mode during naturalistic stimulation. *bioRxiv*, 776237.

Declaration of author contributions

Laura Busse and Martin A. Spacek conceptualized the study. Martin A. Spacek and Davide Crombie developed the methodology. Martin A. Spacek, Steffen Katzner, Gregory Born, Davide Crombie, Yannik Bauer, and Xinyu Liu wrote the software. Steffen Katzner performed the formal analysis. Martin A. Spacek and Yannik Bauer performed the investigation. Martin A. Spacek, Gregory Born, Davide Crombie, and Laura Busse curated the data. Laura Busse and Gregory Born wrote the original draft. Laura Busse, Steffen Katzner, Martin A. Spacek, Gregory Born, and Davide Crombie reviewed and edited the manuscript. Martin A. Spacek, Gregory Born, and Steffen Katzner visualized the data. Laura Busse acquired funding, supervised, and administered the project.

Personal contributions

For Fig. 1, G.B. processed and visualized histological data showing ChR2 expression in V1 (Fig. 1b) and the electrode tract in the dLGN (Fig. 1c). For Fig.1 – figure supplement 1, G.B. analyzed and visualized the data. Moreover, G.B. took part in building the experimental setup, wrote most of the methods section and contributed to reviewing and editing the manuscript.

Rights and permissions

This article has been published under the CC-BY-NC 4.0 International license.

1 Robust effects of corticothalamic feedback during naturalistic visual 2 stimulation

3 Martin A. Spacek^{a,*}, Gregory Born^{a,b}, Davide Crombie^{a,b}, Yannik Bauer^{a,b}, Xinyu Liu^{a,b},
4 Steffen Katzner^{a,1}, Laura Busse^{a,c,1,*}

5 ^a*Division of Neurobiology, Department Biology II, LMU Munich, Munich, Germany*

6 ^b*Graduate School of Systemic Neurosciences, LMU Munich, Munich, Germany*

7 ^c*Bernstein Centre for Computational Neuroscience, Munich, Germany*

8 Abstract

Neurons in the dorsolateral geniculate nucleus (dLGN) of the thalamus are contacted by a large number of feedback synapses from cortex, whose role in visual processing is poorly understood. Past studies investigating this role have mostly used simple visual stimuli and anesthetized animals, but corticothalamic (CT) feedback might be particularly relevant during processing of complex visual stimuli, and its effects might depend on behavioral state. Here, we find that CT feedback robustly modulates responses to naturalistic movie clips by increasing response gain and promoting tonic firing mode. Compared to these robust effects for naturalistic movies, CT feedback effects on firing rates were less consistent for grating stimuli. Finally, while CT feedback and locomotion affected dLGN responses in similar ways, we found their effects to be largely independent. We propose that CT feedback and behavioral state use separate circuits to modulate visual information on its way to cortex in a stimulus-dependent manner.

9 Introduction

10 Mammalian vision is based on a hierarchy of processing stages that are connected by
11 feedforward circuits projecting from lower to higher levels, and by feedback circuits projecting
12 from higher to lower levels. Feedforward processing is thought to create feature selectivity
13 [1, 2] and invariance to translation, scale, or rotation [2–5], to ultimately enable object
14 recognition [6]. Hypotheses about the functional role of feedback circuits include top-down
15 attention, working memory, prediction, and awareness [7–12]. Compared to theories of
16 feedforward processing, however, there is little consensus on the specific function of feedback
17 connections [13, 14].

*Correspondence: m.spacek@lmu.de (MAS), busse@bio.lmu.de (LB)

¹Senior authors

18 Feedback in the mammalian visual system targets brain areas as early as the dorsolateral
19 geniculate nucleus (dLGN) of the thalamus, where up to 30% of synaptic connections onto
20 relay cells are established by corticothalamic (CT) feedback [15]. Direct CT feedback is
21 thought to arise from V1 layer 6 (L6) CT pyramidal cells [16, 17], whose role in visual pro-
22 cessing has remained elusive for a number of reasons. L6 CT pyramidal cells have notoriously
23 low firing rates [18–23] and their deep location within cortex makes them a difficult target for
24 *in-vivo* single cell functional imaging [24] and cell-type specific manipulations using optoge-
25 netics [25]. L6 CT pyramidal cells are also challenging to identify in extracellular recordings
26 due to the heterogeneity of L6 neurons [16]. The action of CT feedback on dLGN activity
27 is generally considered modulatory rather than driving [26], as CT feedback inputs contact
28 the distal dendrites of relay cells via mGluR1 metabotropic receptors [27], implying rather
29 slow and long-lasting effects on dLGN processing. Since L6 CT pyramidal cells provide both
30 direct excitation and indirect inhibition of dLGN via the thalamic reticular nucleus (TRN)
31 and dLGN inhibitory interneurons [17, 28], the effects of CT feedback are expected to be
32 complex.

33 Despite the massive number of CT inputs to dLGN, the functional impact of CT feedback
34 remains unclear [29, 30]. In the literature, diverse methods of manipulation with different
35 temporal scales, specificity and overall sign (activation vs. suppression), have yielded diverse
36 and even conflicting results. CT feedback, for instance, has been shown to modulate genicu-
37 late spatial integration [31–39], temporal processing [37, 40], response gain [38, 41–43], and
38 transitions between tonic and burst firing modes [44, 45]. Other studies, however, found that
39 manipulation of CT feedback did not change some or any of these dLGN response properties
40 [25, 37, 46–48].

41 Most of these previous studies have probed the effects of CT feedback with artificial stim-
42 ulti, and mostly in anesthetized animals; CT feedback, however, might be most relevant for
43 processing of dynamic naturalistic information and during wakefulness. From a conceptual
44 perspective, if the role of feedback was to provide context based on an internal model built
45 from the statistics of the world [49–52], natural stimuli would be expected to best comply
46 with this model, and hence better drive these feedback mechanisms. Indeed, it has previously
47 been suggested that CT feedback might be more strongly engaged for moving compared to
48 stationary stimuli [17], and for complex dynamic noise textures than simple moving bars
49 [53], consistent with a potential role in figure-ground processing [33, 54, 55]. Furthermore,
50 since the responsiveness of feedback projections [56, 57], including those originating from V1
51 CT neurons [30], seem to be strongly reduced by anesthesia, it is critical for an acceleration
52 of our understanding to examine CT feedback effects in awake animals.

53 Here, we recorded spiking activity in dLGN of awake mice and investigated how CT feed-

54 back affected dLGN responses to naturalistic movie clips. In order to achieve reliable, tem-
55 porally precise, and reversible suppression of CT feedback, we conditionally expressed chan-
56 nelrhodopsin2 (ChR2) in V1 parvalbumin-positive (PV+) inhibitory interneurons, whose
57 activation can efficiently suppress cortical output [41, 58]. We found that V1 suppression
58 had consistent modulatory effects on dLGN responses to movie clips, which could largely be
59 captured by divisive transformations. Effects of CT feedback on dLGN responses to grating
60 stimuli were more diverse, highlighting the stimulus-dependency of CT feedback effects. Fi-
61 nally, while geniculate responses during V1 suppression resembled those during quiescence,
62 we found effects of CT feedback and behavioral state to be largely independent. Overall, our
63 results demonstrate that visual information en route to cortex can be reliably modulated by
64 extra-retinal influences such as cortical feedback and locomotion, which are likely conveyed
65 via different modulatory pathways.

66 Results

67 *CT feedback robustly modulates dLGN responses to naturalistic movie clips*

68 To investigate the impact of CT feedback on visual processing of naturalistic stimuli, we
69 presented to head-fixed mice full-screen movie clips and compared responses of dLGN neurons
70 during optogenetic suppression of V1 activity to a control condition with CT feedback left
71 intact (**Fig. 1**). The responses of individual dLGN neurons to naturalistic movie clips
72 were characterized by distinct response events that were narrow in time and reliable across
73 trials (**Fig. 1d, top**, example neuron). Consistent with the notion that CT feedback has a
74 modulatory rather than driving role [59], even during V1 suppression the temporal response
75 pattern remained discernible (Pearson correlation $r = 0.54$, $p < 10^{-6}$, **Fig. 1d,e**). Yet, as
76 illustrated in the example neuron, with CT feedback intact, firing rates were higher and burst
77 spikes were less frequent (**Fig. 1e, left**). As a consequence, the distributions of instantaneous
78 firing rates in the two conditions were significantly different (KS test, $p < 10^{-6}$), and were
79 more skewed during V1 suppression than with CT feedback intact ($\gamma = 2.02$ vs. 1.22; **Fig. 1e**,
80 **right**).

81 We observed similar effects in the recorded population of dLGN neurons, where CT feed-
82 back enhanced overall responses and promoted tonic mode firing. Indeed, while mean firing
83 rates varied almost 4 orders of magnitude across the population (~ 0.1 –100 spikes/s), they
84 were higher with CT feedback intact than with feedback suppressed (13.1 vs. 10.6 spikes/s;
85 linear multilevel-model (LMM): $F_{1,173.1} = 12.5$, $p = 0.0005$; **Fig. 1f**). In addition, CT feed-
86 back also influenced more fine-grained properties of geniculate responses. First, with CT
87 feedback, the mean proportion of spikes occurring as part of a burst event was about half of
88 what we observed during suppression (0.050 vs. 0.090; LMM: $F_{1,177.9} = 45.6$, $p = 1.9 \times 10^{-10}$;

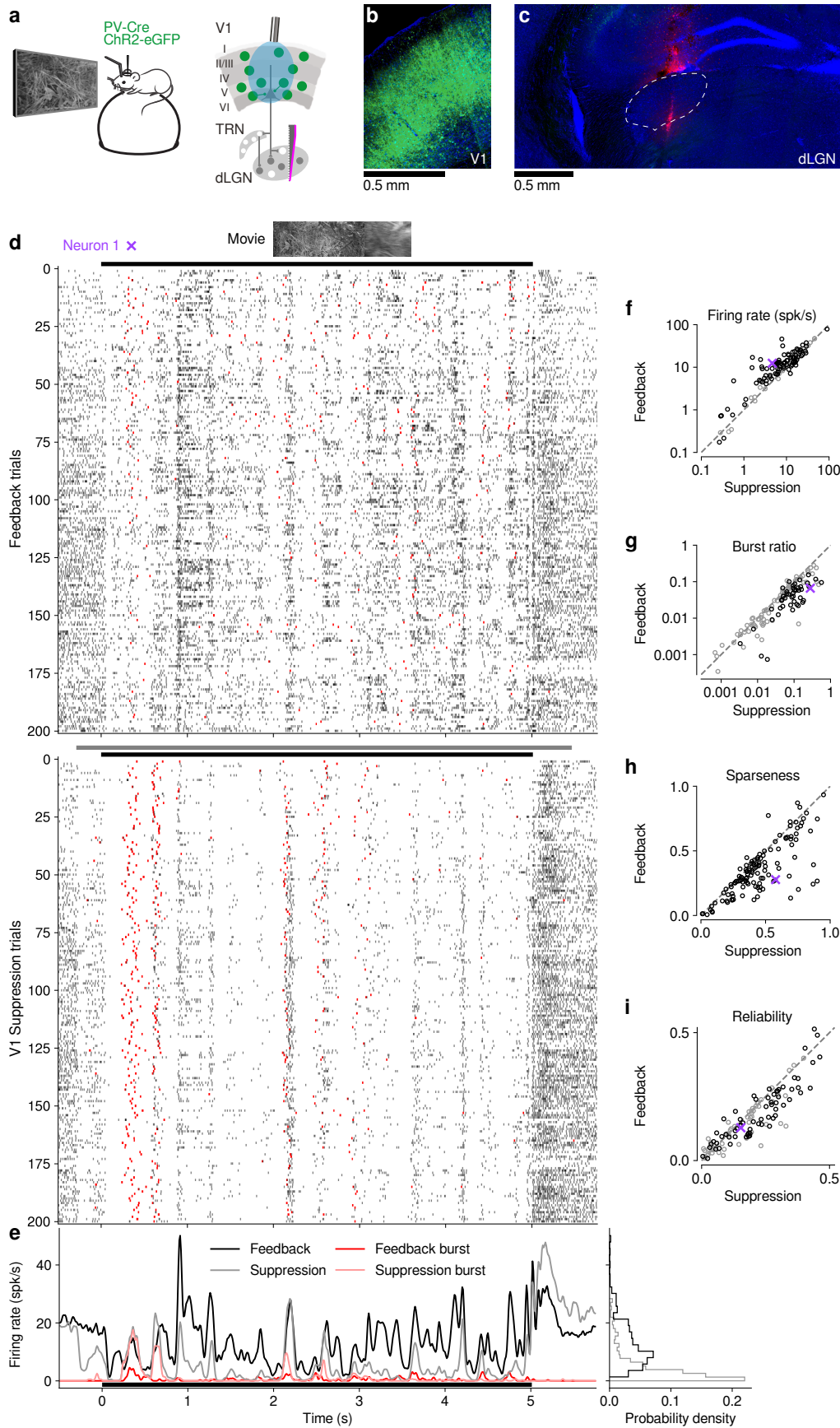


Figure 1 (Previous page) CT feedback modulates dLGN responses to full-screen naturalistic movie clips. **(a)** *Left*: Schematic of experimental setup. Head-fixed mice were placed on a floating Styrofoam ball and visual stimuli were presented on a screen located ~ 25 cm away from the animal. *Right*: ChR2 was conditionally expressed in PV+ inhibitory interneurons (*green*) in all layers of V1 using a viral approach. Extracellular silicon electrode recordings were performed in dLGN with and without optogenetic suppression of V1. **(b)** Coronal section close to the V1 injection site for an example PV-Cre mouse (*blue*: DAPI; *green*: eYFP; Bregma: -3.4 mm). **(c)** Coronal section at the dLGN (white outline) recording site, same animal as in (b). For post-mortem confirmation of the electrode position, the back of the probe was stained with DiI (*magenta*) for one of the recording sessions (*blue*: DAPI; Bregma: -1.82 mm). **(d)** Raster plots of an example neuron for 200 presentations of a 5 s naturalistic movie clip, with CT feedback intact (control condition, *top*) and during V1 suppression (*bottom*). *Red*: burst spikes; *black bar*: movie clip presentation; *gray bar*: V1 suppression. **(e)** *Left*: PSTHs for both the feedback (*black*) and V1 suppression (*gray*) conditions. Superimposed are PSTHs of burst spikes only, separately for feedback (*red*) and suppression (*pale red*) conditions. *Right*: Corresponding instantaneous firing rate distributions. **(f–i)** Comparison of CT feedback vs. suppression conditions for mean firing rate (f), burst ratio (g), temporal sparseness (h), and response reliability (i), all calculated for the duration of the movie clip. Sparseness captures the activity fraction of a neuron, re-scaled between 0 and 1 [60]. Response reliability is defined as the mean Pearson correlation of all single trial PSTH pairs [61]. For sample sizes, see [Table 1](#). *Purple*: example neuron. Black markers in (f,g,i) indicate neurons with individually significant effects (Welch’s t-test). See also [Fig. 1-Supplement 1](#) and [Fig. 1-Supplement 2](#).

89 [Fig. 1g](#)). Second, consistent with the distributions of firing rate for the example neu-
90 ron ([Fig. 1e, right](#)) and related to the relative increase of responsiveness in the population
91 ([Fig. 1-Supplement 2d](#)), responses to the naturalistic movie clips with CT feedback intact
92 were, on average, less sparse (0.35 vs. 0.54; LMM: $F_{1,170.1} = 55.4$, $p = 4.7 \times 10^{-12}$; [Fig. 1h](#)),
93 indicating that neurons fired less selectively across the frames of the movie. Finally, we also
94 examined the effect of CT feedback on response reliability. To quantify reliability, we com-
95 puted the Pearson correlation coefficient of a neuron’s responses between each pair of the 200
96 stimulus repeats per condition, and averaged the correlation coefficients over all pair-wise
97 combinations [61]. With CT feedback intact, mean response reliability was lower than with-
98 out feedback (0.15 vs. 0.18; LMM: $F_{1,166.9} = 22.5$, $p = 4.4 \times 10^{-6}$; [Fig. 1i](#)). Except for the
99 effects on sparseness, the feedback effects on responses to naturalistic movies were unrelated
100 to changes in firing rates ([Fig. 1-Supplement 2c–g](#)). The increased trial-to-trial reliability
101 during V1 suppression could not be explained by higher stability in eye positions, because,
102 first, variability in eye position was comparable between conditions with CT feedback intact
103 vs. suppressed ([Fig. 1-Supplement 2h](#)), and second, effects of CT feedback on neural re-
104 liability were unrelated to changes in variability in eye position ([Fig. 1-Supplement 2i](#)).
105 Splitting the dLGN population into putative cell types according to several functional char-
106 acteristics and location within dLGN revealed few differences in how global V1 suppression
107 affected firing rates and bursting ([Fig. 1-Supplement 3](#)). Finally, we repeated our exper-
108 iments with more specific optogenetic suppression after selectively expressing the inhibitory
109 opsin stGtACR2 [62] in V1 Ntsr1+ neurons, which correspond to $\geq 90\%$ to L6 CT neurons

110 [63, 64] (**Fig. 1-Supplement 4**). These control experiments with specific suppression of
111 L6 CT neurons during viewing of naturalistic movies yielded identical conclusions (**Fig. 1-**
112 **Supplement 4a–h**). Taken together, our results indicate that CT feedback can modulate
113 responses of dLGN neurons to naturalistic movie clips. The modulations are consistent with
114 a net depolarizing effect, which supports higher firing rates and more linear, tonic firing
115 mode with higher dynamic range, at the expense of sparseness, trial-to-trial reliability, and
116 signal-to-noise.

117 *V1 suppression decreases dLGN responses to naturalistic movies by reducing response gain*

118 To better understand the effects of V1 suppression on dLGN firing rate, we next asked
119 whether the observed reduction in responsiveness could be explained by a divisive and/or
120 subtractive change (**Fig. 2**). Using repeated random subsampling cross-validation, we fit
121 a simple threshold linear model (**Fig. 2a, inset**) to timepoint-by-timepoint responses in
122 suppression vs. feedback conditions, and extracted the slope and threshold of the fit for
123 each subsample (**Fig. 2b,d**). In the two example neurons shown in **Fig. 2a–d**, the fitted
124 slope was significantly smaller than 1 (neuron 2: median slope of 0.66, 95% CI: 0.63–0.69,
125 **Fig. 2b**; neuron 1: median slope of 0.37, 95% CI: 0.32–0.41, **Fig. 2d**), while the threshold
126 (x -intercept) was either small or not significantly different from 0 (neuron 2: median of
127 1.58, 95% CI: 0.39–2.91; neuron 1: median of -0.14 , 95% CI: -1.49 – 0.89). We obtained
128 similar results for the population of recorded neurons, where V1 suppression decreased the
129 neurons' responses to naturalistic movie clips via a substantial change in response gain
130 (slope of 0.76 ± 0.1 ; LMM) without a significant shift in baseline (threshold of 0.013 ± 1.3 ;
131 LMM; **Fig. 2e**). This demonstrates that V1 suppression influences responses in dLGN to
132 naturalistic movie clips predominantly via a divisive effect.

133 We noticed that the threshold linear model could predict the effects of V1 suppression
134 better for some neurons than for others. We therefore explored whether poor fits of the
135 model might be related to our finding that V1 suppression can trigger non-linear, burst-
136 mode firing. For instance, the threshold-linear model accurately captured the responses of
137 example neuron 2 (median $R^2 = 0.90$, cross-validated; **Fig. 2a,b**), which exhibited little
138 bursting during V1 suppression (burst ratio: 0.007). Neuron 1, in contrast, had a higher
139 burst ratio during suppression (0.28) and the prediction (*blue*) sometimes overestimated or
140 underestimated peaks in the actual response (*gray*), such that the percentage of explained
141 variability was rather low (median $R^2 = 0.29$, cross-validated, **Fig. 2c,d**).

142 Indeed, across the population of recorded cells, the model goodness of fit (median R^2 ,
143 cross-validated) during V1 suppression was inversely related to the burst ratio (slope of
144 -1.4 ± 0.23 ; LMM; **Fig. 2f**), consistent with the notion that the highly non-linear, all-

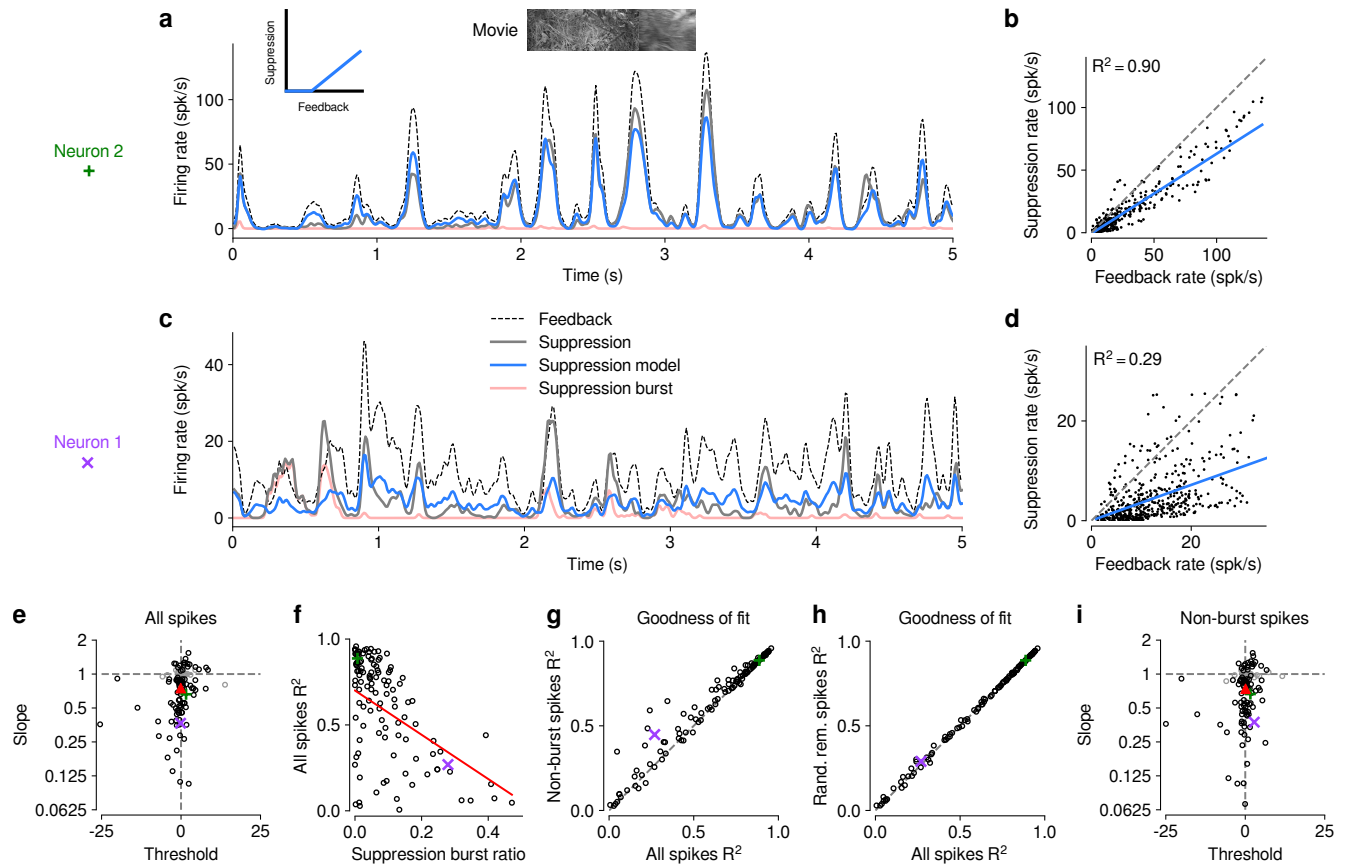


Figure 2 The effect of V1 suppression on dLGN responses to naturalistic movie clips is predominantly divisive.

(a) PSTHs of an example neuron during CT feedback (*black, dotted*) and V1 suppression (*gray*) conditions, for a random subset of 50% of trials per condition not used for model fitting. Responses during the suppression condition are approximated by the threshold linear model (*blue*) based on responses during the feedback condition. *Pale red*: PSTH during V1 suppression consisting only of burst spikes. *Inset*: cartoon of threshold linear model. (b) Timepoint-by-timepoint comparison of instantaneous firing rates of the PSTHs (derived from the 50% of trials not used for fitting) during the suppression vs. feedback conditions. PSTH data points are plotted at 0.01 ms resolution. *Blue line*: threshold linear model fit. (c,d) Same as (a,b) for a second example neuron (same as in Fig. 1d,e). (a,b) and (c,d) each contain data from 1 representative subsample. (e) Slope and threshold parameters for all neurons. Each point represents the median for each neuron across 1000 random subsamples of trials. Black points indicate neurons with slopes significantly different from 1 (95% CI). (f) Cross-validated model prediction quality (median R^2) vs. burst ratio during V1 suppression. *Red line*: LMM fit. (g) Model prediction quality with and without removal of burst spikes. (h) Model prediction quality with and without removal of an equivalent number of tonic spikes. (i) Same as (e) but with burst spikes removed. (e-h) *Purple, green*: example neurons; *red triangle*: LMM estimate of the mean.

145 or-none-like burst mode firing [65] cannot be captured by the threshold-linear model. To
 146 further investigate the impact of bursting on response transformations by CT feedback, we re-
 147 computed the PSTHs for each neuron during V1 suppression after removing all burst spikes.
 148 Removal of burst spikes allowed our model to capture the effects of V1 suppression even
 149 better (all spikes: mean $R^2 = 0.60$; non-burst spikes: mean $R^2 = 0.63$; LMM: $F_{1,152.8} = 5.9$,
 150 $p = 0.016$; Fig. 2g). Importantly, this increase in model performance was not simply a

151 consequence of removing a certain proportion of spikes that originally needed to be predicted:
152 discarding an equivalent number of randomly selected tonic spikes did not yield improved
153 fit quality (random tonic spikes removed: mean $R^2 = 0.60$; LMM: $F_{1,153.8} = 0.017$, $p =$
154 0.9 ; **Fig. 2h**). While burst spikes thus cannot be captured by the threshold-linear model,
155 removing burst spikes did not change our conclusion that the effect of CT feedback on movie
156 responses was predominantly divisive (slope: 0.75 ± 0.09 ; threshold: 0.22 ± 1.33 ; LMM;
157 **Fig. 2i**), likely because burst events were much rarer than tonic spikes (see also **Fig. 1g**)
158 [66]. Indeed, firing mode (all spikes vs. non-burst spikes) had no effect on either slope
159 (LMM: $F_{1,153.7} = 0.57$, $p = 0.45$) or threshold estimates (LMM: $F_{1,150.5} = 0.21$, $p = 0.65$) of
160 the simple linear model.

161 *CT feedback modulates dLGN responses evoked by drifting gratings*

162 Previous studies have investigated the effects of CT feedback using artificial stimuli,
163 such as gratings and bars [25, 34, 41, 44]. To relate our findings to these studies, and
164 to investigate the role of stimulus type, we next examined the effects of V1 suppression
165 during the presentation of drifting gratings (**Fig. 3**). To approximate the visual stimulus
166 configuration used for naturalistic movie clips, we presented full-screen gratings drifting
167 in one of 12 different orientations, and selected a pseudo-random subset of trials for V1
168 suppression. As expected, we found that responses of single dLGN neurons in the control
169 condition with CT feedback intact could be modulated at the temporal frequency (TF,
170 4 cyc/s) of the drifting grating (**Fig. 3a₁, b₁**). Similar to previous studies in mouse dLGN
171 [67–69], we also encountered some dLGN neurons with tuning for grating orientation or
172 direction (**Fig. 3a₂, b₂**).

173 Remarkably, V1 suppression had mixed effects on dLGN responses to drifting gratings.
174 Example neuron 1, for instance, had lower firing rates with CT feedback intact, both in the
175 orientation tuning (**Fig. 3a₂**) and the cycle-averaged response to the preferred orientation
176 (**Fig. 3a₃**). In addition, with CT feedback intact, there were markedly fewer burst spikes.
177 In contrast, example neuron 3 responded more strongly with CT feedback intact (**Fig. 3b₂,**
178 **b₃**). Such diverse effects of CT feedback were representative of the recorded population
179 (**Fig. 3c**): V1 suppression during grating presentation significantly reduced responses for
180 some neurons, but significantly increased responses for others, such that the average firing
181 rates in the two conditions were almost identical (feedback: 14.8 spikes/s, suppression: 15.1
182 spikes/s) and statistically indistinguishable (LMM: $F_{1,88.7} = 0.05$, $p = 0.83$). In contrast to
183 these diverse effects on firing rate, but similar to our findings for naturalistic movie clips,
184 intact CT feedback was consistently associated with less bursting (burst ratios of 0.041 vs.
185 0.15; LMM: $F_{1,90.8} = 42.6$, $p = 3.8 \times 10^{-9}$; **Fig. 3d**). Also similar to our findings for movies,

186 there was no relationship between the strength of feedback effects on firing rate and on
187 bursting (**Fig. 4-Supplement 1a**).

188 Beyond studying overall changes in responsiveness and firing mode, we next asked how
189 CT feedback affected the tuning for grating orientation of dLGN neurons. It is known from
190 previous studies [67, 69–72] that mouse dLGN neurons show various degrees of orientation
191 tuning, ranging from few strongly tuned neurons, potentially relaying tuned input from the
192 retina [70], to a larger group with orientation bias [67, 72]. We computed orientation tuning
193 curves separately for feedback and suppression conditions. For neuron 1, intact CT feedback
194 was associated not only with lower average firing rates, but also poorer selectivity (OSIs of
195 0.14 vs. 0.25; **Fig. 3a₂**). In contrast, for neuron 3, orientation selectivity was similar during
196 feedback and suppression conditions (OSIs of 0.1 vs. 0.09; **Fig. 3b₂**). These results were
197 representative of the population, where CT feedback affected orientation selectivity in diverse
198 ways, with virtually no difference in population means (feedback OSI: 0.13; suppression:
199 0.12; LMM: $F_{1,88.7} = 0.31$, $p = 0.58$; **Fig. 3e**; see also [25, 46, 47, 72]). For neurons with
200 $OSI > 0.02$ and well-fit orientation tuning curves ($R^2 > 0.5$), preferred orientation during
201 feedback and suppression conditions was largely similar, except for some cases where it
202 shifted (**Fig. 3f**). As was the case for movie stimulation, for grating stimulation, splitting the
203 dLGN population into putative cell types according to several functional characteristics and
204 their location within dLGN revealed few consistent differences in how global V1 suppression
205 affected firing rates and bursting (**Fig. 3-Supplement 1**). Taken together, although the
206 effects of V1 suppression on firing rate seem more diverse in magnitude and sign for grating
207 stimuli, the similarity of orientation selectivity between CT feedback conditions suggests
208 underlying changes in gain, in accordance to what we observed for naturalistic movies.

209 Inspecting the spike rasters at different orientations, we realized that responses of geniculate
210 neurons appeared to be more strongly modulated at the grating’s temporal frequency
211 during V1 suppression than when feedback was intact (**Fig. 3a₁**). To test whether V1 sup-
212 pression affected the ability of dLGN neurons to follow the gratings’ temporal modulation,
213 for each neuron we computed the amplitude of the response at the stimulus frequency (F_1
214 component) relative to the mean response (F_0 component) [73, 74] and found that F_1/F_0
215 ratios were indeed lower when feedback was intact (1.08 vs. 1.22; LMM: $F_{1,90.5} = 15.8$,
216 $p = 0.00014$; **Fig. 3g**). To explore the impact of CT feedback on the first harmonic re-
217 sponse in more detail, we examined the cycle average responses to the preferred orientation,
218 and asked how CT feedback affected response phase. Similar to the results obtained for
219 the example neurons (**Fig. 3a₃**, **Fig. 3b₃**), we found that V1 suppression could advance
220 response phase (**Fig. 3h**). This phase advance occurred more often for neurons whose re-
221 sponses during V1 suppression included a substantial proportion of burst spikes (**Fig. 3i**,

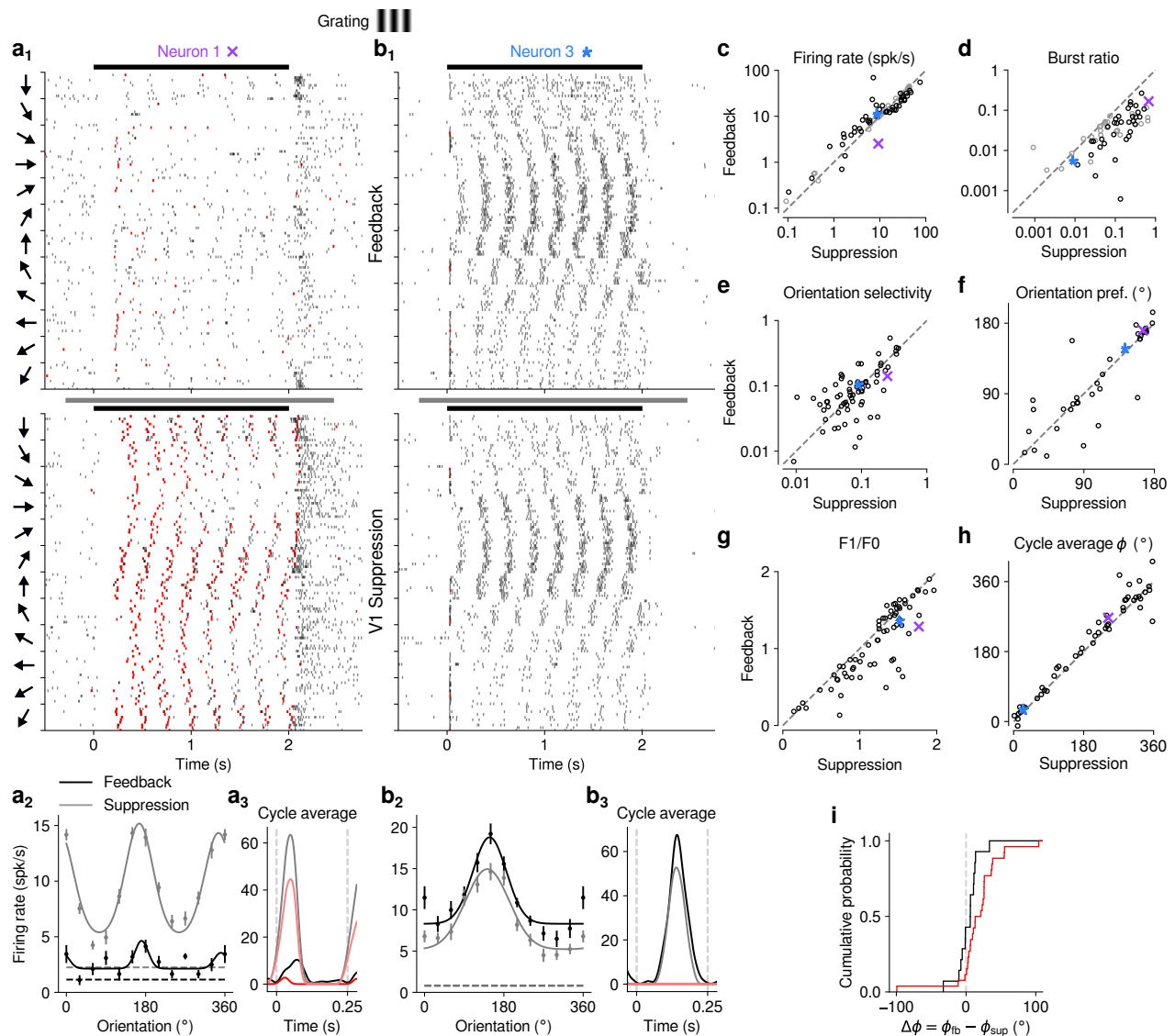


Figure 3 CT feedback modulates dLGN responses to drifting gratings.

(a) Responses of example neuron 1 (same as in Fig. 1d,e and Fig. 2c,d) to full-screen, drifting gratings. (a₁) Raster plot in response to drifting gratings, with trials sorted by grating orientation (10 trials per orientation, 30° steps). Red: burst spikes. (a₂) Corresponding orientation tuning curve. Dashed lines represent spontaneous firing rates in response to medium gray screen. Error bars: standard error of the mean. (a₃) Cycle average response to preferred orientation. Black, gray: cycle average constructed from all spikes. Red, pale red: cycle average constructed from burst spikes only. Black, red: CT feedback intact; gray, pale red: V1 suppression. (b) Same as (a), for example neuron 3. (c–h) Comparison of conditions with CT feedback intact vs. V1 suppression, for mean firing rate (c), burst ratio (d), orientation selectivity index (OSI) (e), preferred orientation θ (f), F_1/F_0 (g), and cycle average phase ϕ (h). Purple, blue: example neurons. Black markers in (c,d) indicate neurons with individually significant effects (Welch's t-test). (i) Cumulative distribution of cycle average phase differences between feedback and suppression conditions. Black: neurons with little burst spiking (ratio of cycle average peak for burst spikes to cycle average peak for all spikes < 0.1); red: neurons with substantial burst spiking (ratio of cycle average peak for burst spikes to cycle average peak for all spikes ≥ 0.1).

222 *red*; 25 of 29 neurons showed phase advance, $p = 0.0001$, binomial test) than for neurons
223 whose V1 suppression responses had little or no bursting (**Fig. 3i**, *black*; 11 of 21 neurons
224 advanced, $p = 1$, binomial test). Together with earlier work using intracellular recordings
225 at different levels of holding membrane potential in anesthetized cats [75], these analyses
226 demonstrate that the phase advance is driven by the dynamics of burst spiking. Finally,
227 similar to our re-assessment of CT feedback effect on responses to naturalistic movies, our
228 conclusions regarding the effects of CT feedback on grating responses did not change when
229 we repeated our experiments using a selective suppression of Ntsr1+ neurons with stGtACR2
230 [62] (**Fig. 1-Supplement 4i–o**).

231 *Effects of CT feedback on dLGN firing rates are more consistent and overall stronger for*
232 *full-screen movies than full-screen gratings*

233 Our analyses suggest that the impact of CT feedback on firing rates might be overall
234 stronger for naturalistic movie stimuli than for gratings. To test this hypothesis, we focused
235 on the subset of neurons recorded with both types of stimuli. Indeed, when we compared
236 feedback modulation indices (FMIs) of firing rates, we found that FMI was on average
237 more positive for movies than for gratings (0.15 vs. 0.053; LMM: $F_{1,38} = 5.21$, $p = 0.028$;
238 **Fig. 4a**). Remarkably, in 10/39 neurons (**Fig. 4a**, dark lines) V1 suppression decreased
239 firing rates for movies (positive movie FMI), but increased firing rates for gratings (negative
240 grating FMI). The opposite effect only occurred in 3/39 neurons (dark dashed lines). These
241 findings were not a consequence of differences in firing rates that might have already been
242 present in conditions with CT feedback intact (**Fig. 4-Supplement 1b**), and were also
243 not a consequence of the longer duration of V1 suppression during movie clips (**Fig. 4-**
244 **Supplement 1c,d**).

245 Differences in CT feedback effects on firing rates to full-screen gratings and movies might
246 be related to feedback-mediated changes in bursting, which might be stimulus-dependent
247 [75, 76] and can drive high frequency firing. To test this hypothesis, we compared CT
248 feedback modulation of burst ratio for gratings vs. movie clips, and found that V1 suppression
249 indeed induced stronger bursting for gratings than for movies (**Fig. 4-Supplement 1e**).
250 However, for both movies (**Fig. 1-Supplement 2c**) and gratings (**Fig. 4-Supplement**
251 **1a**), CT feedback effects on firing rates were unrelated to those on bursting. Thus, while
252 suppression of CT feedback engages bursting overall more strongly for gratings than movies,
253 this differential recruitment does not seem to account for differences in CT feedback-related
254 modulations of firing rates for movies vs. grating stimuli.

255 Alternatively, CT feedback might operate differently on full-screen movie vs. grating
256 stimuli, because the stimuli themselves might differentially engage CT feedback to modulate

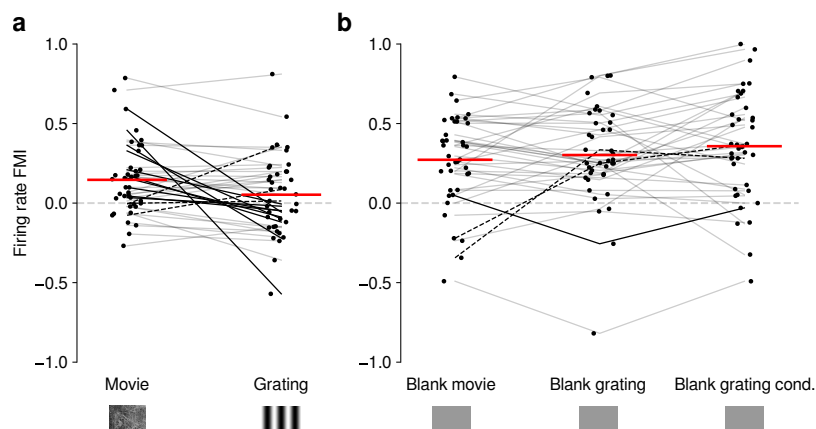


Figure 4 Effects of CT feedback on dLGN firing rate depend on stimulus type.

(a) Comparison of the strength of CT feedback effects on firing rate (feedback modulation index, FMI) during presentation of full-screen movie clips and gratings. (b) Comparison of the strength of CT feedback effect on firing rate for blank stimuli interleaved with movies or gratings. Red: mean (LMM), dark lines: changes in sign of feedback modulation effect with stimulus type from positive for movies to negative for gratings (solid) and vice versa (dashed). See also [Fig. 4-Supplement 1](#).

257 dLGN processing. Differential engagement of CT feedback might be related to differences
258 in multiple aspects of the two stimulus types, for instance contrast, spatial and temporal
259 frequency, or spatial context. With respect to spatial context, a substantial body of lit-
260 erature has indicated that one role of CT feedback is to enhance dLGN center-surround
261 antagonism [31–35, 37, 39, 77, 78]. Such center-surround antagonism might be stimulus de-
262 pendent: recordings in area V1 have demonstrated that the strength of surround modulation
263 dynamically changes with the statistics of naturalistic stimuli, and on average is less than
264 the surround modulation exerted by large-sized iso-oriented gratings [79].

265 To test whether CT feedback effects differ for movies and gratings due to differential
266 modulation of dLGN surround suppression, one would ideally compare responses to movies
267 and gratings of optimal size, which evoke little surround suppression, in addition to responses
268 to both types of full-screen stimuli, which evoke more surround suppression, all while ma-
269 nipulating CT feedback. However, due to limited recording time and the impracticality
270 of centering movies and gratings over the retinotopically dispersed RFs in dLGN ([Fig. 1-](#)
271 [Supplement 1b](#)) [67], we did not collect responses to optimally sized stimuli. However,
272 our recordings did include periods of blank screen, which minimally recruit surround mech-
273 anisms. These were short (~ 0.3 s) periods directly preceding each full-screen movie and
274 grating trial (see e.g. [Fig. 1d](#) and [Fig. 3a₁](#)), as well as blank trials interleaved as one
275 condition in the grating experiments. Applying our analyses to these various blank stimuli
276 ([Fig. 4b](#), [Fig. 4-Supplement 1g–i](#)), we found that CT feedback enhanced mean firing rates
277 regardless of blank type or blank period duration (positive firing rate FMIs, mean FMIs: 0.27
278 vs. 0.30 vs. 0.36; LMM: $F_{2,76} = 1.69$, $p = 0.19$; [Fig. 4b](#)). This CT feedback-related average

279 enhancement for blank stimuli was even stronger than the enhancement observed during
280 movie presentation (LMM: $F_{1,116} = 15.1$, $p = 0.0002$), and stronger than the mixed effects
281 during grating presentation (LMM: $F_{1,116} = 34.9$, $p = 3.6 \times 10^{-8}$). Since the CT feedback
282 effects on these various blank stimuli (see also **Fig. 4-Supplement 1e–1**) did not depend on
283 blank period duration or whether blanks were embedded in grating or movie experiments,
284 we interpret these findings to represent differential, stimulus-dependent engagement of CT
285 feedback.

286 These findings are consistent with the interpretation that CT feedback most strongly
287 enhances firing rates to blanks in both movie and grating experiments, because the recruit-
288 ment of suppressive mechanisms via the indirect inhibitory CT feedback circuit is minimal.
289 In contrast, presentation of iso-oriented full-screen gratings likely invokes stronger suppres-
290 sive feedback mechanisms, such that overall CT feedback influences would be comprised of
291 a mix of direct excitation and indirect inhibition. Suppressing cortex during presentation of
292 full-screen gratings would thus result in reduced excitation, but also release from inhibition,
293 such that the two effects on firing rate might cancel out. Finally, if indirect inhibitory in-
294 fluences of CT feedback were recruited less by full-screen naturalistic movies, CT feedback
295 effects on firing rates would more strongly reflect the influences of the direct, excitatory CT
296 feedback circuit. Taken together with previous studies in anesthetized cats demonstrating
297 that CT feedback-mediated enhancement of dLGN surround suppression can depend on the
298 orientation alignment of center and surround [33, 55], these findings suggest that the strength
299 and sign of CT feedback gain might be stimulus-dependent and potentially sensitive to the
300 statistics of the center and the surround stimulation.

301 *Effects of locomotion on dLGN responses resemble effects of CT feedback, but are largely*
302 *independent*

303 Previous studies have reported that responses of mouse dLGN neurons to grating stimuli
304 are modulated by locomotion [80–82]. To assess how these findings extend to more complex
305 stimuli, we separated the trials with CT feedback intact according to the animals' loco-
306 motion behavior. When we examined the spike rasters and PSTHs of example neuron 1 in
307 control conditions with CT feedback intact (**Fig. 5a,b**), we found that, despite preserved
308 temporal features of the responses (Pearson correlation $r = 0.72$ between run and sit PSTHs,
309 $p < 10^{-6}$), firing rates were higher overall during locomotion than stationary periods. Addi-
310 tionally, during locomotion, the distribution of firing rates was less skewed ($\gamma = 1.15$ vs. 1.45
311 during stationary trials), with a decrease in low and an increase in medium firing rates (KS
312 test, $p < 10^{-6}$). This pattern was also observed in the population of dLGN neurons, where
313 firing rates were consistently higher for trials with locomotion compared to trials when the

314 animal was stationary (12.7 vs. 9.7 spikes/s; LMM: $F_{1,194.1} = 15.4$, $p = 0.00012$; **Fig. 5c**).
315 Similar to previous reports using gratings [80, 83], we found that bursting was lower during
316 locomotion than stationary periods (0.045 vs. 0.068; LMM: $F_{1,185.4} = 28.5$, $p = 2.7 \times 10^{-7}$;
317 **Fig. 5d**). Beyond these established measures, using movie clips allowed us to test the effects
318 of locomotion on additional response properties: trials with locomotion were associated with
319 lower sparseness (0.40 vs. 0.47; LMM: $F_{1,181.9} = 22.7$, $p = 3.8 \times 10^{-6}$; **Fig. 5e**) and lower
320 trial-to-trial reliability (0.14 vs. 0.17; LMM: $F_{1,190.0} = 10.1$; $p = 0.0018$; **Fig. 5f**). This
321 locomotion-related decrease of reliability could be related to, but is likely not fully explained
322 by, the increase in eye movements typically associated with running (**Fig. 5-Supplement**
323 **1h,i**) [80, 84]. These analyses demonstrate that in dLGN, processing of naturalistic movie
324 clips is robustly modulated by locomotion. Curiously, in all aspects tested, these modula-
325 tions by locomotion had the same signatures as those of CT feedback: increased firing rates,
326 reduced bursting, and decreased sparseness and trial-to-trial reliability.

327 Since the effects of CT feedback and locomotion closely resembled each other, and since
328 L6CT neurons themselves are modulated by locomotion [85], are the effects of locomotion
329 on dLGN responses inherited via feedback from cortex? To test this hypothesis, we next
330 focused on only those trials with V1 suppression and repeated the separation according to
331 locomotion (**Fig. 5g-h**). These analyses revealed that effects of locomotion persisted, even if
332 CT feedback was suppressed (**Fig. 5i-l**; firing rate: 9.7 vs. 7.5 spikes/s; LMM: $F_{1,183.2} = 18.1$,
333 $p = 3.3 \times 10^{-5}$; burst ratio: 0.084 vs. 0.12 spikes/s; LMM: $F_{1,193.1} = 28.3$, $p = 2.8 \times 10^{-7}$;
334 sparseness: 0.47 vs. 0.56; LMM: $F_{1,179.5} = 54.7$, $p = 5.1 \times 10^{-12}$; reliability: 0.14 vs. 0.18;
335 LMM: $F_{1,187.5} = 22.0$, $p = 5.3 \times 10^{-6}$).

336 Finally, to test more directly the relationship between effects of behavioral state and CT
337 feedback, we compared CT feedback and running-related modulations on a neuron-by-neuron
338 basis. First, we hypothesized that if effects of locomotion on dLGN responses were inherited
339 from primary visual cortex, such effects should vanish during V1 suppression (**Fig. 6a₀**).
340 However, consistent with our observations above (**Fig. 5i-l**), even during V1 suppression,
341 running-related modulations were significantly different from 0 (firing rate run modulation
342 index (RMI): 0.18 ± 0.06 ; burst ratio: -0.17 ± 0.12 ; sparseness: -0.12 ± 0.04 ; reliability:
343 -0.11 ± 0.08 ; **Fig. 6a₁₋₄**). In fact, the degree of running modulation was correlated between
344 feedback and suppression conditions (firing rate: slope of 0.51 ± 0.12 ; burst ratio: slope of
345 0.38 ± 0.2 ; sparseness: slope of 0.44 ± 0.14 ; reliability: slope of 0.50 ± 0.15 ; **Fig. 6a₁₋₄**).
346 Interestingly, for firing rates and burst ratios, locomotion effects were slightly stronger, on
347 average, with CT feedback intact compared to V1 suppression (firing rate RMI: 0.23 vs.
348 0.20; LMM: $F_{1,168.3} = 4.3$, $p = 0.04$, **Fig. 6a₁**; burst ratio RMI: -0.25 vs. -0.17 ; LMM:
349 $F_{1,154.7} = 6.3$, $p = 0.013$, **Fig. 6a₂**), indicating that these two modulatory influences likely

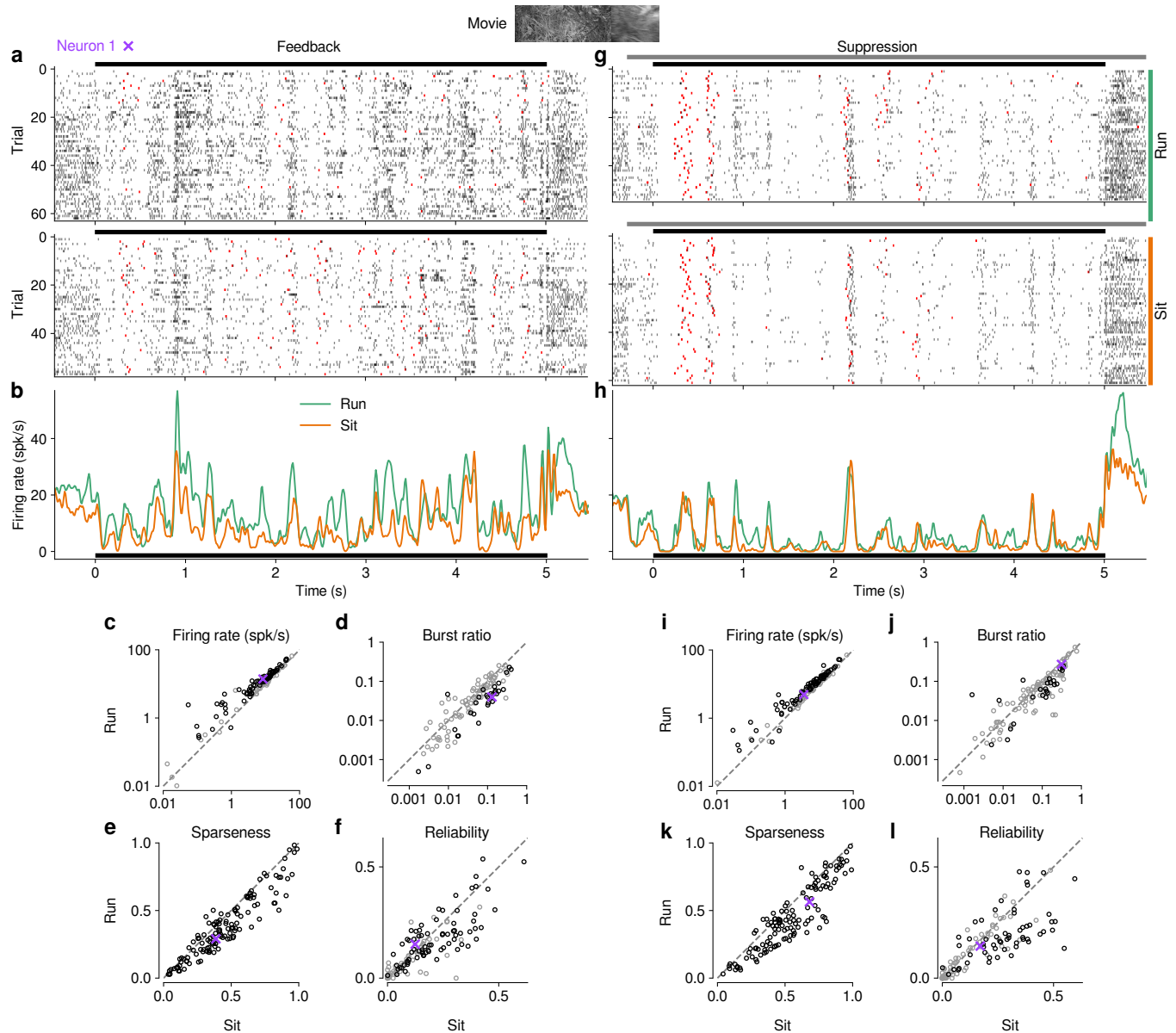


Figure 5 Effects of locomotion on dLGN responses resemble those of CT feedback, but persist even during V1 suppression.

(a) Spike raster of example neuron 1 (same as Fig. 1d) in response to a naturalistic movie clip during locomotion and stationary trials with CT feedback intact. *Top*: trials with run speed > 1 cm/s; *bottom*: trials with run speed < 0.25 cm/s, both for at least > 50% of each trial. *Red*: burst spikes. (b) Corresponding PSTHs. *Green*: locomotion, *orange*: stationary; *black bar*: duration of movie clip. (c–f) Comparison of firing rates (c), burst ratio (d), sparseness (e), and trial-to-trial reliability (f) during locomotion and stationary trials. Black markers in (c,d,f) correspond to individually significant observations (Welch’s t-test). (g–l) Same as (a–f), for locomotion and stationary trials during V1 suppression. See also Fig. 5-Supplement 1.

350 interact.

351 We next tested the hypothesis that CT feedback might have a stronger impact during
352 active behavioral states than during quiescence. Indeed, it has previously been shown that
353 during brain states associated with anesthesia, the responsiveness of feedback circuits is
354 particularly reduced [30, 56, 57]. One might therefore predict that during quiescence, if
355 feedback circuits were already completely disengaged, we should not be able to observe
356 further effects of V1 suppression (**Fig. 6b₀**). This was clearly not the case, because CT
357 feedback effects were correlated across behavioral states (firing rate: slope of 0.72 ± 0.10 ; burst
358 ratio: slope of 0.34 ± 0.15 ; sparseness: slope of 0.85 ± 0.12 ; reliability: slope of 0.43 ± 0.14 ;
359 **Fig. 6b₁₋₄**). In addition, and similar to the slightly stronger RMIs during feedback, we
360 discovered a locomotion-dependent CT feedback effect for firing rates and burst ratios. CT
361 feedback effects were slightly stronger, on average, during locomotion than during quiescence
362 (firing rate FMI: 0.18 vs. 0.15; LMM: $F_{1,172.8} = 3.5$, $p = 0.065$; **Fig. 6b₁**; burst ratio FMI:
363 -0.27 vs. -0.19 ; LMM: $F_{1,166.9} = 6.8$, $p = 0.0097$; **Fig. 6b₂**). This subtle interaction
364 between behavioral state and CT feedback effects might relate to a previous finding, where
365 careful dissection of brain states by depth of anesthesia had already suggested that the
366 effects of transient cortical inactivation on dLGN responses were more evident during lighter
367 anesthesia, i.e., during desynchronized cortical activity [43]. Our ability to observe effects of
368 V1 suppression in dLGN while the animal was stationary suggests that CT feedback circuits
369 are engaged even under conditions of behavioral quiescence and underscores that effects of
370 CT feedback and behavioral state are largely independent.

371 Finally, if modulations by CT feedback and behavioral state exploited the same circuitry,
372 neurons experiencing strong modulation by V1 suppression should also be strongly affected
373 by locomotion (**Fig. 6c₀**). Contrary to this prediction, we found that effects of CT feedback
374 (FMI) and behavioral state (RMI) were uncorrelated (firing rate: slope of 0.054 ± 0.13 ; burst
375 ratio: slope of -0.11 ± 0.13 ; sparseness: slope of -0.053 ± 0.21 ; reliability: slope of $-0.095 \pm$
376 0.12 ; **Fig. 6c₁₋₄**). Together, these comparisons demonstrate that effects of behavioral state
377 associated with locomotion and effects of CT feedback are largely independent.

378 Discussion

379 In this study, we used naturalistic movies to reveal that corticothalamic feedback can have
380 substantial and consistent effects on dLGN responses. First, we show that V1 suppression
381 reduces time-varying dLGN firing rates, and leads to increases in bursting, sparseness and
382 trial-to-trial reliability. While changes of time-varying responses to movies were generally
383 well predicted via a divisive reduction in response gain, a simple threshold-linear model
384 could not capture the full spectrum of V1 suppression effects, in particular the nonlinearities

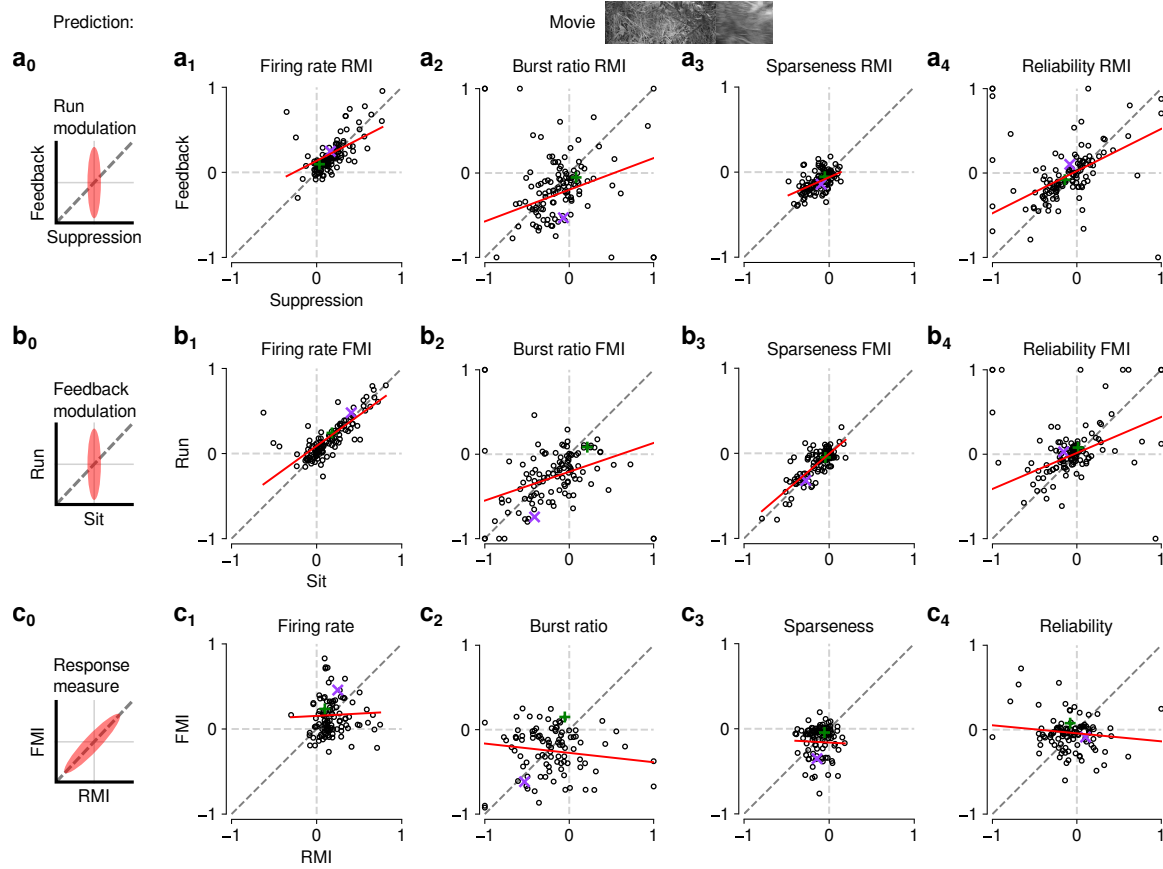


Figure 6 The effects of CT feedback and locomotion on movie responses are largely independent.

(**a**₀–**c**₀) Predicted relationships between modulation indices and response measures in different conditions, assuming dependence in the effects of CT feedback and locomotion. (**a**) Comparison of modulation by running (RMI) during CT feedback intact and V1 suppression for firing rates (**a**₁), burst ratio (**a**₂), sparseness (**a**₃), and reliability (**a**₄). Running effects were quantified with a run modulation index (RMI), where $RMI = (\text{running} - \text{sitting}) / (\text{running} + \text{sitting})$. (**b**) Comparison of modulation by CT feedback (FMI) during locomotion and stationary periods for firing rates (**b**₁), burst ratio (**b**₂), sparseness (**b**₃), and reliability (**b**₄). (**c**) Comparison of modulation by feedback (FMI) and modulation by running (RMI) for firing rates (**c**₁), burst ratio (**c**₂), sparseness (**c**₃), and reliability (**c**₄). Red: LMM fit. Green, purple: example neurons from Fig. 2a,b.

385 arising from burst spiking. Second, we demonstrate that effects of V1 suppression on firing
386 rate were more consistent and therefore stronger overall for naturalistic movies than for
387 gratings, potentially related to the differential engagement of CT feedback as a function
388 of stimulus context. Third, we show that CT feedback effects on dLGN activity closely
389 resemble effects of behavioral state, as assessed by locomotion. We demonstrate, however,
390 that the effects of V1 suppression on firing rate, bursting, sparseness and reliability are largely
391 independent of modulations by behavioral state, and importantly, that effects of locomotion
392 persist even when V1 activity is suppressed. Together, these findings demonstrate that
393 behavioral modulations of dLGN activity are not simply inherited from cortex. Overall, our
394 findings highlight that dLGN activity can be reliably modulated by two extra-retinal sources
395 – cortical feedback and locomotion – which exert their influences via largely separate routes.

396 To manipulate CT feedback, we chose a global V1 suppression approach based on opto-
397 genetic activation of ChR2 expressed in local PV+ inhibitory interneurons [41, 46–48, 86].
398 ChR2-based activation of local PV+ inhibitory interneurons results in reliable, continu-
399 ous, and strong suppression of V1 L6 CT neurons, compared to alternative optogenetic
400 approaches involving direct photosuppression of L6 CT neurons using archaerhodopsin and
401 halorhodopsin [25, 41]. These light-driven pumps pose challenges in terms of light power
402 requirements, temporal decay of sensitivity, and effects on intracellular ion homeostasis
403 [62, 86]. While silencing by excitation of inhibitory interneurons can exploit the robust
404 effects of GABA-mediated inhibition in cortical circuits, it comes with a limitation in speci-
405 ficity. In addition to the direct L6 → thalamus circuit, indirect, polysynaptic effects might
406 be exerted via alternative routes. One example is L5 corticofugal pyramidal cells projecting
407 to the superior colliculus (SC), where tectogeniculate neurons in the superficial layers pro-
408 vide retinotopically organized, driving inputs to the dorsolateral shell region of the dLGN
409 [87]. To address this lack of specificity, in control experiments, we replaced photoactivation
410 of PV+ neurons with direct, selective suppression of V1 Ntsr1+ neurons, which overlap by
411 at least 90% with L6 CT pyramidal cells [63, 64]. Since photosuppression via the novel
412 light-gated chloride channel stGtACR2 [62] did not alter any of our conclusions regarding
413 the effects of CT feedback on dLGN responses, we assume that the effects of V1 suppression
414 to a large degree reflect the specific impact of the L6 CT circuit. L6 CT neurons, however,
415 have an intracortical axon collateral making privileged connections with a translaminar PV+
416 interneuron subtype in L6 [63, 88], which in turn strongly regulates the gain of the entire
417 V1 column [41, 63, 88]. Since suppression of L6 CT neurons increases the gain in V1 [41],
418 and since this is the opposite of the global effects of V1 suppression via PV+ activation, it
419 is unlikely that the observed modulations of dLGN are largely driven by alternative circuits.
420 Nevertheless, decisively ruling out alternative circuits would require the selective suppression

421 of L6 CT axon terminals at the thalamic target.

422 Cortical layer 6 is well known for its especially high diversity of neuronal cell types
423 [16]. Even within the population of L6 CT pyramidal cells there is heterogeneity, with at
424 least 2 subtypes defined by morphology [88–90], 3 subtypes defined by electrophysiology
425 and morphology [90], and 4 major subtypes defined by transcriptomics [89, 90]. Whether
426 these subtypes mediate different aspects of feedback modulations is currently unknown. In
427 the visual system of primates and carnivores, CT feedback circuits seem to be organized
428 into distinct streams [91–93] whose functional organization mimics that of the feedforward
429 streams. Whether the known subtypes in mice can convey independent, stream-specific
430 information is currently unknown, partly because already at the level of feedforward pro-
431 cessing, the notion of streams in mouse dLGN is a matter of ongoing debate [94, 94–97], and
432 response properties are diverse [67, 68, 98]. Our own assessment of CT feedback effects re-
433 vealed few systematic differences for various dLGN cell-type classifications. Such an absence
434 of differences, however, is not surprising, because our manipulation approaches nonspecific-
435 cally suppressed all L6 CT neuron subtypes. Once genetic targeting of L6 CT subtypes is
436 possible [99, 100], it will be important to test the stream-specificity of CT feedback in the
437 mouse.

438 Our analyses of the time-varying firing rates in response to naturalistic movies revealed
439 that V1 suppression results in a robust decrease of geniculate response gain. Divisive CT
440 feedback effects have also been previously reported for contrast response functions of parvo-
441 cellular dLGN neurons in anesthetized macaques [42]. Such divisive gain modulations were
442 commonly thought to arise from shunting inhibition, as opposed to hyperpolarizing inhibi-
443 tion. From simulations, however, it has become clear that in the suprathreshold regime,
444 the effect of shunting synapses is also subtractive [101], even if voltage-dependent inhibitory
445 conductances are considered [102]. Instead, a crucial element to produce gain modulations
446 seems to be changes in the level of synaptically driven V_m fluctuations, often called “synaptic
447 noise” [103–105]. Indeed, *in vivo* V1 recordings suggest that the combined impact of changes
448 in V_m fluctuations, input resistance, and depolarization is needed to produce gain changes
449 [106]. These cellular properties are altered by both feedback [105] and neuromodulation
450 [107], not only in cortex [108] but also in the corticothalamic system [109]. Here, “synap-
451 tic noise” together with varying degrees of T-type channel recruitment has been shown to
452 change the slope of the input-output function and alter the temporal filtering characteristics
453 of thalamic relay cells [109, 110]. Thus, by providing variable synaptic input and affecting
454 membrane depolarization, CT feedback might be in a prime position to dynamically tune
455 the gain of the thalamic relay; elucidating the underlying cellular mechanisms will be an
456 important step in the future.

457 In addition to potentially contributing to the observed gain modulations, “synaptic noise”
458 from CT feedback may also help explain the less precise and less reliable dLGN responses
459 we observed when feedback was left intact. Specifically, V1 neurons are known to exhibit
460 about double the trial-to-trial variability of simultaneously recorded dLGN neurons [111], and
461 eliminating variable cortical input might reveal the even greater reliability of feed-forward
462 retinal inputs [111].

463 Our analyses of movie and grating response characteristics showed that V1 suppression
464 robustly and consistently biased geniculate activity towards burst firing mode. Burst firing
465 mode occurs when dLGN neurons undergo sustained (≥ 100 ms) hyperpolarization [65],
466 which allows for the de-inactivation of low-threshold T-type calcium channels abundant in
467 thalamus [112]. Previous intracellular recordings in cat dLGN have revealed that cortical
468 ablation can hyperpolarize the resting membrane potential of dLGN relay cells by ~ 9 mV,
469 enough to push them into burst-firing mode [113]. Conversely, direct optogenetic activation
470 of L6 CT neurons in primary somatosensory cortex has been shown to decrease burst mode
471 firing [114]. In burst firing mode, reminiscent of the effects we observed during V1 suppres-
472 sion, dLGN spontaneous activity is low [65], stimulus-evoked responses show phase-advance
473 [75, 115] and high trial-to-trial reliability [115]. The increase in trial-to-trial response re-
474 liability we observed during V1 suppression might therefore be explained not only by the
475 removal of a more variable input as mentioned above [111], but also by a shift towards burst
476 mode, where retinogeniculate communication efficacy is elevated [116].

477 Theories about the function of thalamic firing modes can also provide a useful framework
478 for interpreting the effects of CT feedback we observed here, in particular since the greater
479 precision and trial-to-trial reliability of responses during V1 suppression might be unexpected
480 at first glance. Thalamic burst mode is often linked with “inattentive states”, where the
481 sudden appearance or change of a visual stimulus from non-preferred to preferred RF contents
482 [117–119] can reliably trigger a thalamic burst. Bursting is associated with high signal-to-
483 noise, well-suited for stimulus detection [65, 120]. In addition, thalamic burst mode is known
484 to augment the efficacy of retinal input to drive spiking in dLGN [116], and increases the
485 probability of relay between thalamus and cortex, because bursts drive large postsynaptic
486 potentials [121]. This in turn might lead to depolarizing CT feedback, switching the thalamus
487 to tonic mode and allowing more faithful, linear relay of information with a higher dynamic
488 range, better suited for encoding of more finely graded details [65, 109]. Sherman has
489 termed this process a “wake-up-call” for cortex [65, 117], which could represent a neural
490 implementation of bottom-up attention in dLGN [122]. To understand if CT feedback is
491 indeed recruited for detailed perceptual analyses, an essential next step would be to measure
492 the activity of L6 CT neurons under behaviorally relevant conditions. Interestingly, in the

493 auditory system, activation of L6 CT feedback has been shown to influence sound perception,
494 with enhancements of sound detection or discrimination behavior, depending on the relative
495 timing between CT spiking and stimulus onset [123]. Beyond having broad impact on coding
496 regimes and transmission, bursting in thalamus is also known to have specific computational
497 properties, such as efficiently encoding high- and low-frequency information in parallel [124].

498 So far, most studies using naturalistic stimuli to probe dLGN responses have been per-
499 formed in anesthetized animals and have not considered CT feedback [117–119, 125–127].
500 Similarly, most studies investigating the impact of CT feedback have relied on artificial
501 stimuli [25, 34, 41, 44]. Combining both manipulations to directly compare the effects of
502 CT feedback during naturalistic movies and gratings, we found evidence that CT feedback
503 modulates firing rates at the geniculate level in a stimulus-dependent fashion. For artificial
504 stimuli, such as gratings and bars, it has long been known that CT feedback can enhance
505 dLGN surround suppression by increasing responses to small stimuli and reducing responses
506 to large stimuli [31–35, 37, 39, 77, 78]. Such CT feedback mediated enhancement of sur-
507 round suppression might result from recruitment of a more narrow direct excitatory and a
508 wider indirect inhibitory CT feedback component according to grating size [78], with the
509 balance shifting more towards direct excitation for small gratings and more towards indirect
510 inhibition for large gratings. Size, however, is likely not the only determinant of relative re-
511 cruitment of CT feedback circuits: for instance, V1 ablation or pharmacological suppression
512 in anesthetized cats leads to more prominent reductions of dLGN surround suppression for
513 iso- vs. cross-oriented gratings [33, 55], suggesting an additional role of stimulus context. For
514 naturalistic stimuli with complex context, measurements in area V1 have already demon-
515 strated that surround suppression is generally lower than for iso-oriented gratings, and is
516 flexibly invoked depending on the specific statistics in the RF center and surround [79]. The
517 differential effect of CT feedback on dLGN firing rates for full-screen naturalistic movies
518 and iso-oriented gratings observed in our study might therefore be parsimoniously explained
519 by differences in the relative strength of direct excitatory and indirect inhibitory CT feed-
520 back. It would be of prime interest to measure, in future experiments, size tuning curves
521 with and without CT feedback using different stimuli, such as naturalistic movies, iso- and
522 cross-oriented gratings. Given our results, we predict that CT feedback would affect firing
523 rate responses to full-screen cross-oriented gratings more similarly to full-screen naturalistic
524 movies than would iso-oriented gratings.

525 By measuring the effects of V1 suppression during different behavioral states, and by
526 measuring locomotion effects with and without CT feedback, we found that locomotion and
527 CT feedback had similar effects on dLGN responses, but operated via largely separate cir-
528 cuits. The independence of modulations by CT feedback and behavioral state is remarkable:

529 neuromodulation accompanying locomotion also affects cortical layer 6, which receives dense
530 cholinergic afferents from basal forebrain [128], and mouse V1 L6 CT neurons increase action
531 potential firing in slice recordings upon bath application of ACh [129]. Potentially related,
532 many V1 L6 CT neurons themselves increase activity during locomotion or arousal [85, 130].
533 While it is therefore unclear why such modulations of V1 L6 CT neurons only contribute
534 relatively little to the dLGN locomotion effects, our result is similar to recent findings in
535 superior colliculus (SC), where locomotion-related response modulations were also indepen-
536 dent of V1 feedback [131]. If not inherited from CT feedback [see also 132, 133], which
537 alternative circuits could mediate the effects of locomotion in dLGN [80–82]? Locomotion is
538 accompanied by arousal [134], which in turn involves various neuromodulatory influences [re-
539 viewed in 135]. For instance, norepinephrine from the locus coeruleus (LC) and acetylcholine
540 (ACh) from the midbrain are known to act directly on the thalamus [reviewed in 136, 137]
541 and could drive some of the arousal-related depolarizing effects on firing rate independent of
542 cortical feedback, for instance by blocking a long-lasting Ca^{2+} -dependent K^+ current [138].
543 In addition, electrical stimulation of the LC [139] and the parabrachial region (PBR) [140]
544 within the mesencephalic locomotor region (MLR), and direct application of noradrenergic
545 [141] and cholinergic [137, 142] agonists within dLGN, are sufficient to reduce thalamic burst
546 mode firing. Finally, at least part of the locomotion effects in dLGN might also be related
547 to modulations of retinal output [131, 143]. Indeed, two-photon calcium imaging of retinal
548 ganglion cell boutons in dLGN [143] and SC [131] revealed that their activity can be mod-
549 ulated by locomotion, albeit with an overall suppressive effect. In future studies, it will be
550 key to further dissect the contributions of retinal, cortical and potentially collicular modu-
551 lations, and the different neuromodulatory sources of behavioral state-related modulations
552 in thalamic targets.

553 Acknowledgments

554 This research was supported by the German Research Foundation (DFG) SFB870 TP19
555 (LB), DFG BU 1808/5-1 (LB), DFG SFB 1233, Robust Vision: Inference Principles and
556 Neural Mechanisms, TP 13, project number: 276693517 (LB), and by an add-on fellowship
557 of the Joachim Herz Stiftung (GB). We thank D. Metzler for discussions regarding the
558 multi-level modeling, M. Sotgia for lab management and support with animal handling
559 and histology, S. Schörnich for IT support, and B. Grothe for providing excellent research
560 infrastructure.

561 Materials and Methods

562 All procedures complied with the European Communities Council Directive 2010/63/EC
563 and the German Law for Protection of Animals, and were approved by local authorities,
564 following appropriate ethics review.

565 *Surgical procedures*

566 Experiments were carried out in 6 adult PV-Cre mice (median age at first recording ses-
567 sion: 23.5 weeks; B6;129P2-Pvalb^{tm1(cre)}Arbr/J; Jackson Laboratory) and 3 adult Ntsr1-Cre
568 mice (median age: 29.4 weeks; B6.FVB(Cg)-Tg(Ntsr1-cre)GN220Gsat/Mmcd; MMRRC)
569 of either sex. Thirty minutes prior to the surgical procedure, mice were injected with an
570 analgesic (Metamizole, 200 mg/kg, sc, MSD Animal Health, Brussels, Belgium). To induce
571 anesthesia, animals were placed in an induction chamber and exposed to isoflurane (5% in
572 oxygen, CP-Pharma, Burgdorf, Germany). After induction of anesthesia, mice were fixated
573 in a stereotaxic frame (Drill & Microinjection Robot, Neurostar, Tuebingen, Germany) and
574 the isoflurane level was lowered (0.5%–2% in oxygen), such that a stable level of anesthesia
575 could be achieved as judged by the absence of a pedal reflex. Throughout the procedure,
576 the eyes were covered with an eye ointment (Bepanthen, Bayer, Leverkusen, Germany) and
577 a closed loop temperature control system (ATC 1000, WPI Germany, Berlin, Germany) en-
578 sured that the animal's body temperature was maintained at 37° C. At the beginning of the
579 surgical procedure, an additional analgesic was administered (Buprenorphine, 0.1 mg/kg, sc,
580 Bayer, Leverkusen, Germany) and the animal's head was shaved and thoroughly disinfected
581 using iodine solution (Braun, Melsungen, Germany). Before performing a scalp incision
582 along the midline, a local analgesic was delivered (Lidocaine hydrochloride, sc, bela-pharm,
583 Vechta, Germany). The skin covering the skull was partially removed and cleaned from
584 tissue residues with a drop of H₂O₂ (3%, AppliChem, Darmstadt, Germany). Using four
585 reference points (bregma, lambda, and two points 2 mm to the left and to the right of
586 the midline respectively), the animal's head was positioned into a skull-flat configuration.
587 The exposed skull was covered with OptiBond FL primer and adhesive (Kerr dental, Ras-
588 tatt, Germany) omitting three locations: V1 (AP: -2.8 mm, ML: -2.5 mm), dLGN (AP:
589 -2.3 mm, ML: -2 mm), and a position roughly 1.5 mm anterior and 1 mm to the right
590 of bregma, designated for a miniature reference screw (00-96 X 1/16 stainless steel screws,
591 Bilaney) soldered to a custom-made connector pin. 2 μ L of the adeno-associated viral vec-
592 tor rAAV9/1.EF1a.DIO.hChR2(H134R)-eYFP.WPRE.hGH (Addgene, #20298-AAV9) was
593 dyed with 0.3 μ L fast green (Sigma-Aldrich, St. Louis, USA). After performing a small
594 craniotomy over V1, in PV-Cre mice a total of \sim 0.5 μ L of this mixture was injected across
595 the entire depth of cortex (0.05 μ L injected every 100 μ m, starting at 1000 μ m and ending at

596 100 μm below the brain surface), using a glass pipette mounted on a Hamilton syringe (SYR
597 10 μL 1701 RN no NDL, Hamilton, Bonaduz, Switzerland). In V1 of Ntsr1-Cre mice, we in-
598 jected 0.35 μL of stGtACR2 (pAAV_hSyn1-SIO-stGtACR2-FusionRed, Addgene, #105677;
599 0.05 μL injected every 100 μm , starting at 1000 μm and ending at 500 μm below the brain
600 surface). A custom-made lightweight stainless steel head bar was positioned over the poste-
601 rior part of the skull such that the round opening in the bar was centered on V1/dLGN. The
602 head bar was attached with dental cement (Ivoclar Vivadent, Ellwangen, Germany) to the
603 primer/adhesive. The opening was later filled with the silicone elastomer sealant Kwik-Cast
604 (WPI Germany, Berlin, Germany). At the end of the procedure, an antibiotic ointment
605 (Imex, Merz Pharmaceuticals, Frankfurt, Germany) or iodine-based ointment (Braunodi-
606 von, 10%, B. Braun, Melsungen, Germany) was applied to the edges of the wound and a
607 long-term analgesic (Meloxicam, 2 mg/kg, sc, Böhringer Ingelheim, Ingelheim, Germany)
608 was administered and for 3 consecutive days. For at least 5 days post-surgery, the animal's
609 health status was assessed via a score sheet. After at least 1 week of recovery, animals were
610 gradually habituated to the experimental setup by first handling them and then simulat-
611 ing the experimental procedure. To allow for virus expression, neural recordings started no
612 sooner than 3 weeks after injection. On the day prior to the first day of recording, mice
613 were fully anesthetized using the same procedures as described for the initial surgery, and a
614 craniotomy (ca. 1.5 mm²) was performed over dLGN and V1 and re-sealed with Kwik-Cast
615 (WPI Germany, Berlin, Germany). As long as the animals did not show signs of discom-
616 fort, the long-term analgesic Metacam was administered only once at the end of surgery, to
617 avoid any confounding effect on experimental results. Recordings were performed daily and
618 continued for as long as the quality of the electrophysiological signals remained high.

619 *Electrophysiological recordings, optogenetic suppression of V1, perfusion*

620 Head-fixed mice were placed on an air-cushioned Styrofoam ball, which allowed the ani-
621 mal to freely move. Two optical computer mice interfaced with a microcontroller (Arduino
622 Duemilanove) sampled ball movements at 90 Hz. To record eye position and pupil size, the
623 animal's eye was illuminated with infrared light and monitored using a zoom lens (Navitar
624 Zoom 6000) coupled with a camera (Guppy AVT camera; frame rate 50 Hz, Allied Vision,
625 Exton, USA). Extracellular signals were recorded at 30 kHz (Blackrock microsystems). For
626 each recording session, the silicon plug sealing the craniotomy was removed. For V1 record-
627 ings, a 32 or 64 channel silicon probe (Neuronexus, A1x32-5mm-25-177, A1x32Edge-5mm-
628 20-177-A32 or A1x64-Poly2-6mm-23s-160) was lowered into the brain to a median depth of
629 1025 μm . For dLGN recordings, a 32 channel linear silicon probe (Neuronexus A1x32Edge-
630 5mm-20-177-A32) was lowered to a depth of \sim 2300–3611 μm below the brain surface. We

631 judged recording sites to be located in dLGN based on the characteristic progression of RFs
632 from upper to lower visual field along the electrode shank [67] (**Fig. 1-Supplement 1b**), the
633 presence of responses strongly modulated at the temporal frequency of the drifting gratings
634 (F1 response), and the preference of responses to high temporal frequencies [67, 144]. For
635 *post hoc* histological reconstruction of the recording site, the electrode was stained with DiI
636 (Invitrogen, Carlsbad, USA) for one of the final recording sessions.

637 For photostimulation of V1 PV+ inhibitory interneurons, an optic fiber (910 μm diam-
638 eter, Thorlabs, Newton, USA) was coupled to a light-emitting diode (LED, center wavelength
639 470 nm, M470F1, Thorlabs, Newton, USA; or center wavelength 465 nm, LEDC2_465/635_SMA,
640 Doric Lenses, Quebec, Canada) and positioned with a micromanipulator less than 1 mm
641 above the exposed surface of V1. A black metal foil surrounding the tip of the head bar
642 holder prevented the photostimulation light from reaching the animal's eyes. To ensure that
643 the photostimulation was effective, the first recording session for each mouse was carried
644 out in V1. Only if the exposure to light reliably induced suppression of V1 activity was
645 the animal used for subsequent dLGN recordings. For gratings, photostimulation started
646 either 0.1 s before stimulus onset and ended 0.1 s after stimulus offset (2 experiments),
647 or photostimulation started 0.3 s before stimulus onset and ended 0.2 s after stimulus off-
648 set (11 experiments), or photostimulation started 0.3 s before stimulus onset and ended
649 0.45 s after stimulus offset (12 experiments). For movie clips, photostimulation started ei-
650 ther 0.1 s before stimulus onset and ended 0.1 s after stimulus offset (2 experiments), or
651 photostimulation started 0.3 s before stimulus onset and ended 0.45 s after stimulus offset
652 (45 experiments). LED light intensity was adjusted on a daily basis to evoke reliable ef-
653 fects (median intensity: 13.66 mW/mm^2 for activating ChR2 in PV-Cre mice, and 10.84
654 mW/mm^2 for activating stGtACR2 in Ntsr1-Cre mice, as measured at the tip of the optic
655 fiber). Since the tip of the fiber never directly touched the surface of the brain, and since the
656 clarity of the surface of the brain varied (generally decreasing every day following the cran-
657 iotomy), the light intensity delivered even to superficial layers of V1 was inevitably lower.
658 Importantly, changes in dLGN firing rates induced by V1 suppression (FMI, see below) did
659 not differ, on average, from those induced by behavioral state (RMI, see below) (firing rate:
660 FMI 0.20 vs. RMI 0.15, LMM: $F_{1,145.7} = 3.02$, $p = 0.08$; burst ratio: FMI -0.27 vs. RMI
661 -0.28 , $F_{1,124.0} = 0.002$, $p = 0.97$; sparseness: FMI -0.12 vs. RMI -0.14 , $F_{1,144.9} = 1.03$,
662 $p = 0.31$; reliability: FMI -0.084 vs. -0.037 , $F_{1,183.0} = 1.96$, $p = 0.16$; **Fig. 6c**), indicating
663 that optogenetic stimulation effects were not outside the physiological range.

664 After the final recording session, mice were first administered an analgesic (Metamizole,
665 200 mg/kg, sc, MSD Animal Health, Brussels, Belgium) and following a 30 min latency
666 period were transcardially perfused under deep anesthesia using a cocktail of Medetomidin

667 (Domitor, 0.5 mg/kg, Vetoquinol, Ismaning, Germany), Midazolam (Climasol, 5 mg/kg, Ra-
668 tiopharm, Ulm, Germany) and Fentanyl (Fentadon, 0.05 mg/kg, Dechra Veterinary Products
669 Deutschland, Aulendorf, Germany) (ip). A few animals, which were treated according to
670 a different license, were anesthetized with sodium pentobarbital (Narcoren, 400 mg/kg, ip,
671 Böhringer Ingelheim, Ingelheim, Germany). Perfusion was first done with Ringer's lactate
672 solution followed by 4% paraformaldehyde (PFA) in 0.2 M sodium phosphate buffer (PBS).

673 *Histology*

674 To verify recording site and virus expression, we performed histological analyses. Brains
675 were removed, postfixed in PFA for 24 h, and then rinsed with and stored in PBS at 4°
676 C. Slices (40 μm) were cut using a vibrotome (Leica VT1200 S, Leica, Wetzlar, Germany),
677 mounted on glass slides with Vectashield DAPI (Vector Laboratories, Burlingame, USA),
678 and coverslipped. A fluorescent microscope (BX61, Olympus, Tokyo, Japan) was used to
679 inspect slices for the presence of yellow fluorescent protein (eYFP) and DiI. Recorded images
680 were processed using FIJI [145, 146].

681 *Visual stimulation*

682 Visual stimuli were presented on a liquid crystal display (LCD) monitor (Samsung Sync-
683 Master 2233RZ, 47×29 cm, 1680×1050 resolution at 60 Hz, mean luminance 50 cd/m²)
684 positioned at a distance of 25 cm from the animal's right eye (spanning $\sim 108\times 66^\circ$, small
685 angle approximation) using custom written software (EXPO, [https://sites.google.com/a/nyu.
686 edu/expo/home](https://sites.google.com/a/nyu.edu/expo/home)). The display was gamma-corrected for the presentation of artificial stimuli,
687 but not for movies (see below).

688 To measure receptive fields (RFs), we mapped the ON and OFF subfields with a sparse
689 noise stimulus. The stimulus consisted of nonoverlapping white and black squares on a
690 square grid, each flashed for 200 ms. For dLGN recordings, the square grid spanned 60° on
691 a side, while individual squares spanned 5° on a side. For a single experiment the vertical
692 extent was reduced to 50°. For subsequent choices of stimuli, RF positions and other tuning
693 preferences were determined online after each experiment based on multiunit activity, i.e.
694 high-pass filtered signals crossing a threshold of 4.5 to 6.5 SD.

695 We measured single unit orientation preference by presenting full-screen, full-contrast
696 drifting sinusoidal gratings of either 12 (23 experiments) or 8 (2 experiments) different,
697 pseudo-randomly interleaved orientations (30° or 45° steps). For dLGN recordings, spatial
698 frequency was either 0.02 cyc/° (17 experiments) or 0.04 cyc/° (8 experiments) and temporal
699 frequency was either 2 Hz (2 experiments) or 4 Hz (23 experiments). One blank condition
700 (i.e., mean luminance gray screen) was included to allow measurements of spontaneous ac-
701 tivity. The stimulus duration was either 2 s (23 experiments) or 5 s (2 experiments), with

702 an interstimulus interval (ISI) of 2.4 s (21 experiments) or 1.25 s (2 experiments). For two
703 Ntsr1-Cre experiments, ISIs varied and were either 0.58 s or 1.09 s.

704 For laminar localization of neurons recorded in V1, we presented a full-screen, contrast-
705 reversing checkerboard at 100% contrast, with a spatial frequency of either 0.01 cyc/° (2 ex-
706 periments) or 0.02 cyc/° (5 experiments) and a temporal frequency of 0.5 cyc/s.

707 Movies were acquired using a hand-held consumer-grade digital camera (Canon Power-
708 Shot SD200) at a resolution of 320×240 pixels and 60 frames/s. Movies were filmed close to
709 the ground in a variety of wooded or grassy locations in Vancouver, BC, and contained little
710 to no forward/backward optic flow, but did contain simulated gaze shifts (up to 275°/s),
711 generated by manual camera movements (for example movies, see [Fig. 1-Video 1](#) and
712 [Fig. 1-Video 2](#)). Focus was kept within 2 m and exposure settings were set to automatic.
713 The horizontal angle subtended by the camera lens was 51.6°. No display gamma correction
714 was used while presenting movies, since consumer-grade digital cameras are already gamma
715 corrected for consumer displays [147]. For presentation, movies were cut into 5 s clips and
716 converted from color to grayscale. Movie clips were presented full-screen with an ISI of
717 1.25 s (43 experiments). For two Ntsr1-Cre experiments, ISIs varied and were either 0.58 s
718 or 1.08 s. white noise: Different clips were presented in pseudorandom order,

719 *Spike sorting*

720 To obtain single unit activity from extracellular recordings, we used the open source,
721 Matlab-based, automated spike sorting toolbox Kilosort [148]. Resulting clusters were man-
722 ually refined using Spyke [149], a Python application that allows the selection of channels
723 and time ranges around clustered spikes for realignment, as well as representation in 3D
724 space using dimension reduction (multichannel PCA, ICA, and/or spike time). In 3D, clus-
725 ters were then further split via a gradient-ascent based clustering algorithm (GAC) [150].
726 Exhaustive pairwise comparisons of similar clusters allowed the merger of potentially over-
727 clustered units. For subsequent analyses, we inspected autocorrelograms and mean voltage
728 traces, and only considered units that displayed a clear refractory period and a distinct spike
729 waveshape. All further analyses were carried out using the DataJoint framework [151] with
730 custom-written code in Python.

731 *Response characterization*

732 We used current source density (CSD) analysis for recordings in area V1 to determine
733 the laminar position of electrode contacts. To obtain the LFP data we first down-sampled
734 the signal to 1 kHz before applying a bandpass filter (4–90 Hz, 2nd-order Butterworth filter).
735 We computed the CSD from the second spatial derivative of the local field potentials [152],
736 and assigned the base of layer 4 to the contact that was closest to the earliest CSD polarity

737 inversion. The remaining contacts were assigned to supragranular, granular and infragranular
738 layers, assuming a thickness of ~ 1 mm for mouse visual cortex [153].

739 In recordings targeting dLGN, we used the envelope of multi-unit spiking activity (MUAe)
740 [154] to determine RF progression (Fig. 1-Supplement 1b). Briefly, we full-wave rectified
741 the high-pass filtered signals (cutoff frequency: 300 Hz, 4th-order non-causal Butterworth
742 filter) before performing common average referencing by subtracting the median voltage
743 across all channels in order to eliminate potential artifacts (e.g. movement artifacts). We
744 then applied a low-pass filter (cutoff frequency: 500 Hz, Butterworth filter) and down-
745 sampled the signal to 2 kHz. Recording sessions for which RFs did not show the retinotopic
746 progression typical of dLGN (Fig. 1-Supplement 1b) [67] were excluded from further
747 analysis.

748 Each unit's peristimulus time histogram (PSTH, i.e., the response averaged over trials)
749 was calculated by convolving a Gaussian of width $2\sigma = 20$ ms with the spike train collapsed
750 across all trials, separately for each condition.

751 We defined bursts according to [75], which required a silent period of at least 100 ms before
752 the first spike in a burst, followed by a second spike with an interspike interval < 4 ms. Any
753 subsequent spikes with preceding interspike intervals < 4 ms were also considered to be part
754 of the burst. All other spikes were regarded as tonic. We computed a burst ratio (the number
755 of burst spikes divided by the total number of spikes) and compared this ratio in conditions
756 with CT feedback intact vs. V1 suppression or during locomotion vs. stationary conditions.
757 PSTHs for burst spikes were calculated by only considering spikes that were part of bursts
758 before collapsing across trials and convolving with the Gaussian kernel (see above). PSTHs
759 for non-burst spikes were calculated in an analogous way.

760 To quantify the effect of V1 suppression on various response properties, we defined the
761 feedback modulation index (FMI) as

$$\text{FMI} = \frac{\text{feedback} - \text{suppression}}{\text{feedback} + \text{suppression}} \quad (1)$$

762 *Characterization of responses to naturalistic movie clips*

763 Signal to noise ratio (SNR) was calculated according to [155] by

$$\text{SNR} = \frac{\text{Var}[\langle C_r \rangle_t]}{\langle \text{Var}[C]_t \rangle_r} \quad (2)$$

764 where C is the T by R response matrix (time samples by stimulus repetitions) and $\langle \rangle_x$ and
765 $\text{Var}[\]_x$ denote the mean and variance across the indicated dimension, respectively. If all trials
766 were identical such that the mean response was a perfect representative of the response, SNR

767 would equal 1.

768 The sparseness S of a PSTH was calculated according to [60] by

$$S = \left(1 - \frac{\left(\sum_{i=1}^n r_i/n \right)^2}{\sum_{i=1}^n r_i^2/n} \right) \left(\frac{1}{1 - 1/n} \right) \quad (3)$$

769 where $r_i \geq 0$ is the signal value in the i^{th} time bin, and n is the number of time bins.
770 Sparseness ranges from 0 to 1, with 0 corresponding to a uniform signal, and 1 corresponding
771 to a signal with all of its energy in a single time bin.

772 Response reliability was quantified according to [61] as the mean pairwise correlation
773 of all trial pairs of a unit's single trial responses. Single trial responses were computed by
774 counting spikes in 20 ms, overlapping time bins at 1 ms resolution. Pearson's correlation was
775 calculated between all possible pairs of trials, and then averaged across trials per condition.

776 To detect response peaks in trial raster plots and measure their widths, clustering of spike
777 times collapsed across trials was performed using the gradient ascent clustering (GAC) algo-
778 rithm [150], with a characteristic neighborhood size of 20 ms. Spike time clusters containing
779 less than 5 spikes were discarded. The center of each detected cluster of spike times was
780 matched to the nearest peak in the PSTH. A threshold of $\theta = b + 3$ Hz was applied to the
781 matching PSTH peak, where $b = 2 \text{ median}(x)$ is the baseline of each PSTH x . Peaks in the
782 PSTH that fell below θ were discarded, and all others were kept as valid peaks. Peak widths
783 were measured as the temporal separation of the middle 68% (16th to 84th percentile) of
784 spike times within each cluster.

785 To determine whether V1 suppression changes dLGN responses in a divisive or subtractive
786 manner, we fit a threshold-linear model using repeated random subsampling cross-validation.
787 To this end, we first selected a random set of 50% of the trials for each condition for fitting
788 to the timepoint-by-timepoint responses a threshold linear model given by $R_{supp} = s R_{fb} + b$,
789 where $R_{supp} > 0$, with s representing the slope and b the offset. Fitting was done using
790 non-linear least squares (`scipy.optimize.curve_fit`). Throughout **Fig. 2**, we report the
791 resulting x -intercept as the threshold. We evaluated goodness of fit (R^2) for the other 50% of
792 trials not used for fitting. We repeated this procedure 1000 times and considered threshold
793 and slope as significant if the central 95% of their distribution did not include 0 and 1,
794 respectively.

795 *Characterization of responses to drifting gratings*

796 For display of spike rasters (**Fig. 3**), trials were sorted by condition. We computed
797 orientation tuning curves by fitting a sum of two Gaussians of the same width with peaks
798 180° apart:

$$R(\theta) = R_0 + R_p e^{-\frac{(\theta - \theta_p)^2}{2\sigma^2}} + R_n e^{-\frac{(\theta - \theta_p + 180)^2}{2\sigma^2}} \quad (4)$$

799 In this expression, θ is stimulus orientation (0 – 360°). The function has five parameters:
800 preferred orientation θ_p , tuning width σ , baseline response (offset independent of orientation)
801 R_0 , response at the preferred orientation R_p , and response at the null orientation R_n .

802 Orientation selectivity was quantified according to [41, 156] as

$$\text{OSI} = \frac{\sqrt{(\sum R_k \sin(2\theta_k))^2 + (\sum R_k \cos(2\theta_k))^2}}{\sum R_k} \quad (5)$$

803 where R_k is the response to the k th direction given by θ_k . We determined OSI for each unit
804 during both feedback and suppression conditions.

805 We computed the first harmonic of the response R from the spike trains according to [74]
806 to obtain the amplitude and phase of the best-fitting sinusoid, which has the same temporal
807 frequency as the stimulus. For each trial, we calculated

$$R = (1/D) \sum_k \cos(2\pi f t_k) + i \sin(2\pi f t_k) \quad (6)$$

808 where D is the stimulus duration, f is the temporal frequency of the stimulus, and the t_k
809 are the times of the individual spikes. We excluded the first cycle to avoid contamination
810 by the onset response. For (**Fig. 3g**), we calculated average amplitude F_1 by obtaining
811 the absolute value of the complex number R on each trial, before averaging across trials,
812 to avoid potential confounds due to differences in response phase across conditions. For
813 the comparison of response phase, we focused on the orientation which elicited the maximal
814 cycle average response across both feedback and suppression conditions.

815 *Cell typing*

816 Units were classified as suppressed by contrast (SbC) or not suppressed by contrast (non-
817 SbC) by comparing their mean firing rates during full-screen drifting grating presentation to
818 their mean firing rates during blank-screen presentation. Units were classified as SbC if they
819 were visually responsive to gratings (see below) and had a median z-scored response across
820 orientation conditions of ≤ -3 during at least one grating experiment. Otherwise, units
821 were classified as non-SbC. SbC units seem to constitute a sizeable fraction in our dataset,

822 which is similar to our previous results [68], where SbC was also found to be among the
823 overrepresented retinal ganglion cell (RGC) types providing input to dLGN.

824 To identify electrode channels within the putative shell/core of the dLGN, we concen-
825 trated on the RF progression as assessed with MUAe maps that were constructed using
826 sparse noise experiments. Because RF progression is mainly along elevation, amplitudes of
827 MUAe for each channel were collapsed across azimuth and then range normalized. Channels
828 with normalized amplitudes higher than an empirically set threshold (0.4) were considered
829 part of dLGN. Non-detected channels located between detected channels were added. We
830 considered neurons to be located in putative dLGN shell if their mean spike waveform had
831 the largest amplitude on one of the uppermost 20% of electrode channels classified as falling
832 within dLGN.

833 Direction selectivity index (DSI, [157]) was calculated for each unit as

$$\text{DSI} = \frac{R_p - R_n}{R_p + R_n + 2R_0} \quad (7)$$

834 where R_p and R_n are the firing rates in the preferred and null directions, respectively, ex-
835 tracted from tuning curves fit to drifting grating responses (see above), and R_0 is baseline
836 firing rate independent of orientation.

837 The RF distance from the center of the screen was calculated for each unit by finding
838 the position of the MUAe RF for the channel on which the unit's mean spike waveform had
839 the largest amplitude.

840 *Exclusion criteria*

841 Neurons with mean evoked firing rates < 0.01 spikes/s were excluded from further anal-
842 ysis. For movie clips, only neurons with $\text{SNR} \geq 0.015$ in at least one of the conditions in
843 an experiment were considered. Of this population, 2 neurons were excluded from the anal-
844 ysis of the parameters returned by the threshold linear model, because their R^2 was < 0 .
845 For gratings, we converted firing rates in response to each orientation to z-scores relative
846 to responses to the mean luminance gray screen. We only considered visually responsive
847 neurons, with an absolute z-scored response ≥ 2.5 to at least 1 orientation. For the analysis
848 of response phase, we only considered neurons with a peak of the cycle average response of
849 at least 10 Hz in both feedback and suppression conditions, and an F_1/F_0 ratio of at least
850 0.25.

851 *Locomotion*

852 We used the Euclidean norm of three perpendicular components of ball velocity (roll,
853 pitch and yaw) to compute animal running speed. For the analysis of neural responses as a

854 function of behavioral state, locomotion trials were defined as those for which speed exceeded
855 1 cm/s for at least 50% of the stimulus presentation, and stationary trials as those for which
856 speed fell below 0.25 cm/s for at least 50% of the stimulus presentation. To quantify the
857 effect of running vs. sitting on various response properties, the run modulation index (RMI)
858 was defined as

$$\text{RMI} = \frac{\text{running} - \text{sitting}}{\text{running} + \text{sitting}} \quad (8)$$

859 Although other measures of behavioral state such as pupil size indicate that the animal
860 may be in an active/ aroused state outside of periods of locomotion [134, 158, 159], we have
861 chosen to use locomotion to categorize trials for several reasons. Firstly, it is clear from
862 the aforementioned studies that the largest changes in neural activity (at the level of the
863 visual cortex) occur as a function of locomotion. Secondly, because pupil size and locomotion
864 fluctuations are highly correlated [80], using one measure or the other would likely result in a
865 similar separation of trials. Finally, our naturalistic movie stimuli contain dynamic changes
866 in luminance, which drive changes in pupil size that would act as a confound to behavioral
867 state classification.

868 *Eye Tracking*

869 The stimulus viewing eye was filmed using an infrared camera under infrared LED il-
870 lumination. Pupil position was extracted from the videos using a custom, semi-automated
871 algorithm. Briefly, each video frame was equalized using an adaptive bi-histogram equaliza-
872 tion procedure, and then smoothed using median and bilateral filters. The center of the pupil
873 was detected by taking the darkest point in a convolution of the filtered image with a black
874 square. Next, the peaks of the image gradient along lines extending radially from the center
875 point were used to define the pupil contour. Lastly, an ellipse was fit to the contour, and the
876 center of this ellipse was taken as the position of the pupil. A similar procedure was used
877 to extract the position of the corneal reflection (CR) of the LED illumination. Eye blinks
878 were automatically detected and the immediately adjacent data points were excluded. Ad-
879 justable algorithm parameters were set manually for each experiment. Output pupil position
880 time-courses were lightly smoothed, and unreliable segments were automatically removed ac-
881 cording to *a priori* criteria. Finally, the CR position was subtracted from the pupil position
882 to eliminate translational eye movements, and pupil displacement in degrees relative to the
883 baseline (median) position was determined by

$$\theta = 2 \frac{\arcsin(d/2)}{r} \quad (9)$$

884 where d is the distance between the pupil and the baseline position, and $r = 1.25$ mm is
885 the radius of the eye [160]. Angular displacement was computed separately for x and y
886 directions.

887 Eye position standard deviation was computed by first taking the standard deviation
888 of the horizontal eye position at each time point across trials, and then averaging over the
889 5 s during which the visual stimulus was presented. We focused on horizontal eye position
890 because horizontal and vertical eye movements tend to occur in tandem under head-fixed
891 conditions, and the horizontal position variance is larger [161], thus serving as a better proxy
892 for variance in 2D. For each experiment, trials were sorted either by the presence of optoge-
893 netic suppression of CT feedback (**Fig. 1-Supplement 2h**), or by the behavioral state of
894 the animal as described above (**Fig. 5-Supplement 1h**). The eye position standard devia-
895 tion FMI and RMI (**Fig. 1-Supplement 2i** and **Fig. 5-Supplement 1i**) were calculated
896 in the same manner as for the neural response properties.

897 *Statistical methods*

898 To assess statistical significance, we fitted and examined multilevel linear models [162].
899 Such models take into account the hierarchical structure present in our data (i.e., neurons
900 nested in experiments, experiments nested in recording sessions, recordings sessions nested
901 in animals), and eliminate the detrimental effect of structural dependencies on the likelihood
902 of Type I errors (false positive reports) [163]. By considering the nested structure of the
903 data, multilevel models also eliminate the need for “pre-selecting” data sets, such as one
904 out of several experiments repeatedly performed on the same neurons. Whenever we have
905 several experiments per neuron, we include all of them, and also show them in the scatter
906 plots (“observations”). We provide the sample size for each analysis in **Table 1**. In fitting
907 the models, we accounted for repeated measures by including random effects for animals,
908 recording sessions, experiments, and neurons. We fit these models in R [164], using the
909 *lme4* package [165]. We estimated F-values, their degrees of freedom, and the corresponding
910 p-values using the Satterthwaite approximation [166] implemented by the *lmerTest* package
911 [167]. Throughout, uncertainty in estimated regression slopes is represented as $slope \pm x$,
912 where x is $2 \times$ the estimated standard error of the slope.

913 *Data and code availability*

914 Data and source code used to generate the figures in the manuscript will be made available
915 on Dryad.

	Observations	Neurons	Mice
Figure 1f–i	124	65	6
Figure 2e–h	119	63	6
Figure 3c–e,g	68	44	4
Figure 3f	36	28	4
Figure 3h–i	50	35	3
Figure 4a–b	39	39	4
Figure 5c–e	130	66	6
Figure 5f,i–l	129	66	6
Figure 6a ₁ ,a ₃	126	64	6
Figure 6a ₂	109	58	6
Figure 6a ₄	111	63	6
Figure 6b ₁ ,c ₃	123	63	6
Figure 6b ₂	110	58	6
Figure 6b ₄	109	62	6
Figure 6c ₁ ,c ₃ ,c ₄	109	59	6
Figure 6c ₂	101	56	6
Figure 1S2a	124	65	6
Figure 1S2b,g	108	57	6
Figure 1S2c	117	63	6
Figure 1S2d–f	118	64	6
Figure 1S2h	22	n/a	6
Figure 1S2i	124	64	6
Figure 1S3a,c	39	39	4
Figure 1S3b	63	63	6
Figure 1S3d	54	54	6
Figure 1S3e	64	64	6
Figure 1S3f,h	38	38	4
Figure 1S3g	62	62	6
Figure 1S3i	53	53	6
Figure 1S3j	63	63	6
Figure 1S4e–h	64	59	3
Figure 1S4l,n	110	73	3
Figure 1S4m	98	71	3
Figure 3S1a,c,e	44	44	4
Figure 3S1b	63	63	6

Figure 3S1d	36	36	4
Figure 3S1f,h,j	42	42	4
Figure 3S1g	40	40	4
Figure 3S1i	35	35	4
Figure 4S1a	65	42	4
Figure 4S1b	43	43	4
Figure 4S1c-d, g, j	124	65	6
Figure 4S1e	36	36	3
Figure 4S1f	29	29	3
Figure 4S1h-i,k	68	44	4
Figure 4S1l	66	43	4
Figure 5S1a	130	66	6
Figure 5S1b,g	102	56	6
Figure 5S1c	107	57	6
Figure 5S1d,f	129	65	6
Figure 5S1e,i	125	65	6
Figure 5S1h	30	n/a	6

Table 1 Breakdown of sample sizes (N) for the analyses of neural data. See text for details.

916 **Author contributions**

917 Conceptualization, L.B. and M.A.S; Methodology, M.A.S., D.C.; Software, M.A.S., S.K.,
918 G.B., D.C., Y.B., X.L.; Formal Analysis, S.K.; Investigation, M.A.S., Y.B.; Data Curation,
919 M.A.S., G.B., D.C., L.B.; Writing – Original Draft, L.B., G.B.; Writing – Review & Editing,
920 L.B., S.K., M.A.S., G.B., D.C.; Visualization, M.A.S., G.B., S.K.; Supervision, L.B.; Project
921 Administration, L.B.; Funding Acquisition, L.B.

922 **Competing interests**

923 The authors declare no competing interests.

924 References

- 925 1. Lien, A. D. & Scanziani, M. Cortical direction selectivity emerges at convergence of
926 thalamic synapses. *Nature* **558**, 80–86 (2018).
- 927 2. Hubel, D. H. & Wiesel, T. N. Receptive fields, binocular interaction and functional
928 architecture in the cat’s visual cortex. *J. Physiol.* **160**, 106–154 (1962).
- 929 3. Chance, F. S., Nelson, S. B. & Abbott, L. F. Complex cells as cortically amplified
930 simple cells. *Nat. Neurosci.* **2**, 277–282 (1999).
- 931 4. Riesenhuber, M. & Poggio, T. Hierarchical models of object recognition in cortex. *Nat.*
932 *Neurosci.* **2**, 1019–1025 (1999).
- 933 5. Riesenhuber, M. & Poggio, T. Models of object recognition. *Nat. Neurosci.* **3**, 1199–
934 1204 (2000).
- 935 6. DiCarlo, J. J., Zoccolan, D. & Rust, N. C. How Does the Brain Solve Visual Object
936 Recognition? *Neuron* **73**, 415–434 (2012).
- 937 7. Squire, R. F., Noudoost, B., Schafer, R. J. & Moore, T. Prefrontal contributions to
938 visual selective attention. *Annu. Rev. Neurosci.* **36**, 451–466 (2013).
- 939 8. Roelfsema, P. R. & de Lange, F. P. Early Visual Cortex as a Multiscale Cognitive
940 Blackboard. *Annu. Rev. Vis. Sci.* **2**, 131–151 (2016).
- 941 9. Bastos, A. M. *et al.* Canonical microcircuits for predictive coding. *Neuron* **76**, 695–711
942 (2012).
- 943 10. Lamme, V. A. F. & Roelfsema, P. R. The distinct modes of vision offered by feedforward
944 and recurrent processing. *Trends Neurosci.* **23**, 571–579 (2000).
- 945 11. Takahashi, N., Oertner, T. G., Hegemann, P. & Larkum, M. E. Active cortical dendrites
946 modulate perception. *Science* **354**, 1587–1590 (2016).
- 947 12. Larkum, M. A cellular mechanism for cortical associations: An organizing principle for
948 the cerebral cortex. *Trends Neurosci.* **36**, 141–151 (2013).
- 949 13. Heeger, D. J. Theory of cortical function. *Proc. Natl. Acad. Sci. U.S.A.* **114**, 1773–1782
950 (2017).
- 951 14. Gilbert, C. D. & Li, W. Top-down influences on visual processing. *Nat. Rev. Neurosci.*
952 **14**, 350–63 (2013).

- 953 15. Sherman, S. M. & Guillery, R. W. The role of the thalamus in the flow of information
954 to the cortex. *Philos. Trans. Royal Soc. B* **357**, 1695–708 (2002).
- 955 16. Briggs, F. Organizing principles of cortical layer 6. *Front. Neural Circuits* **4**, 3 (2010).
- 956 17. Sillito, A. M. & Jones, H. E. Corticothalamic interactions in the transfer of visual
957 information. *Philos. Trans. Royal Soc. B* **357**, 1739–1752 (2002).
- 958 18. Vélez-Fort, M. *et al.* The stimulus selectivity and connectivity of layer six principal
959 cells reveals cortical microcircuits underlying visual processing. *Neuron* **83**, 1431–43
960 (2014).
- 961 19. Stoelzel, C. R., Bereshpolova, Y., Alonso, J.-M. & Swadlow, H. A. Axonal Conduction
962 Delays, Brain State, and Corticogeniculate Communication. *J. Neurosci.* **37**, 6342–6358
963 (2017).
- 964 20. Crandall, S. R., Patrick, S. L., Cruikshank, S. J. & Connors, B. W. Infrabarrels
965 Are Layer 6 Circuit Modules in the Barrel Cortex that Link Long-Range Inputs and
966 Outputs. *Cell Rep.* **21**, 3065–3078 (2017).
- 967 21. Oberlaender, M. *et al.* Cell Type-Specific Three-Dimensional Structure of Thalamo-
968 cortical Circuits in a Column of Rat Vibrissal Cortex. *Cereb. Cortex* **22**, 2375–2391
969 (2012).
- 970 22. Swadlow, H. A. Efferent neurons and suspected interneurons in S-1 vibrissa cortex of
971 the awake rabbit: Receptive fields and axonal properties. *J. Neurophysiol.* **62**, 288–308
972 (1989).
- 973 23. Pausin, F. P. & Krieger, P. A Corticothalamic Circuit for Refining Tactile Encoding.
974 *Cell Rep.* **23**, 1314–1325 (2018).
- 975 24. Andermann, M. L. *et al.* Chronic cellular imaging of entire cortical columns in awake
976 mice using microprisms. *Neuron* **80**, 900–13 (2013).
- 977 25. Denman, D. J. & Contreras, D. Complex effects on in vivo visual responses by specific
978 projections from mouse cortical layer 6 to dorsal lateral geniculate nucleus. *J. Neurosci.*
979 **35**, 9265–9280 (2015).
- 980 26. Sherman, S. M. & Guillery, R. W. On the actions that one nerve cell can have on
981 another: Distinguishing “drivers” from “modulators”. *Proc. Natl. Acad. Sci. U.S.A.*
982 **95**, 7121–7126 (1998).

- 983 27. Godwin, D. W. *et al.* Ultrastructural Localization Suggests that Retinal and Cortical
984 Inputs Access Different Metabotropic Glutamate Receptors in the Lateral Geniculate
985 Nucleus. *J. Neurosci.* **16**, 8181–8192 (1996).
- 986 28. Usrey, W. M. & Sherman, S. M. Corticofugal circuits: Communication lines from the
987 cortex to the rest of the brain. *J. Comp. Neurol.* **527**, 640–650 (2018).
- 988 29. Briggs, F. & Usrey, W. M. Emerging views of corticothalamic function. *Curr. Opin.*
989 *Neurobiol.* **18**, 403–407 (2008).
- 990 30. Briggs, F. & Usrey, W. M. Corticogeniculate feedback and visual processing in the
991 primate. *J. Physiol.* **589**, 33–40 (2011).
- 992 31. Wang, W., Andolina, I. M., Lu, Y., Jones, H. E. & Sillito, A. M. Focal Gain Control
993 of Thalamic Visual Receptive Fields by Layer 6 Corticothalamic Feedback. *Cerebral*
994 *Cortex* **28**, 267–280 (2018).
- 995 32. Andolina, I. M., Jones, H. E. & Sillito, A. M. Effects of cortical feedback on the spatial
996 properties of relay cells in the lateral geniculate nucleus. *J. Neurophysiol.* **109**, 889–899
997 (2013).
- 998 33. Cudeiro, J. & Sillito, A. M. Spatial frequency tuning of orientation-discontinuity-
999 sensitive corticofugal feedback to the cat lateral geniculate nucleus. *J. Physiol.* **490** (
1000 **Pt 2**), 481–492 (1996).
- 1001 34. Murphy, P. C. & Sillito, A. M. Corticofugal feedback influences the generation of length
1002 tuning in the visual pathway. *Nature* **329**, 727–729 (1987).
- 1003 35. Webb, B. S. *et al.* Feedback from V1 and inhibition from beyond the classical receptive
1004 field modulates the responses of neurons in the primate lateral geniculate nucleus.
1005 *Visual Neurosci.* **19**, 583–592 (2002).
- 1006 36. Nolt, M. J., Kumbhani, R. D. & Palmer, L. A. Suppression at High Spatial Frequencies
1007 in the Lateral Geniculate Nucleus of the Cat. *J. Neurophysiol.* **98**, 1167–1180 (2007).
- 1008 37. Hasse, J. M. & Briggs, F. Corticogeniculate feedback sharpens the temporal precision
1009 and spatial resolution of visual signals in the ferret. *Proc. Natl. Acad. Sci. U.S.A.* **114**,
1010 E6222–E6230 (2017).
- 1011 38. Rivadulla, C., Martínez, L. M., Varela, C. & Cudeiro, J. Completing the corticofugal
1012 loop: A visual role for the corticogeniculate type 1 metabotropic glutamate receptor.
1013 *J. Neurosci.* **22**, 2956–2962 (2002).

- 1014 39. Jones, H. E. *et al.* Differential feedback modulation of center and surround mechanisms
1015 in parvocellular cells in the visual thalamus. *J. Neurosci.* **32**, 15946–15951 (2012).
- 1016 40. Andolina, I. M., Jones, H. E., Wang, W. & Sillito, A. M. Corticothalamic feedback
1017 enhances stimulus response precision in the visual system. *Proc. Natl. Acad. Sci. U.S.A.*
1018 **104**, 1685–1690 (2007).
- 1019 41. Olsen, S. R., Bortone, D. S., Adesnik, H. & Scanziani, M. Gain control by layer six in
1020 cortical circuits of vision. *Nature* **483**, 47–52 (2012).
- 1021 42. Przybyszewski, A. W., Gaska, J. P., Foote, W. & Pollen, D. A. Striate cortex increases
1022 contrast gain of macaque LGN neurons. *Visual Neurosci.* **17**, 485–494 (2000).
- 1023 43. Wörgötter, F., Eyding, D., Macklis, J. D. & Funke, K. The influence of the corticotha-
1024 lamic projection on responses in thalamus and cortex. *Philos. Trans. Royal Soc. B* **357**,
1025 1823–1834 (2002).
- 1026 44. Wang, W., Jones, H. E., Andolina, I. M., Salt, T. E. & Sillito, A. M. Functional
1027 alignment of feedback effects from visual cortex to thalamus. *Nat. Neurosci.* **9**, 1330–
1028 1336 (2006).
- 1029 45. de Labra, C. *et al.* Changes in Visual Responses in the Feline dLGN: Selective Thalamic
1030 Suppression Induced by Transcranial Magnetic Stimulation of V1. *Cereb. Cortex* **17**,
1031 1376–1385 (2007).
- 1032 46. Li, Y.-T., Ibrahim, L. A., Liu, B.-H., Zhang, L. I. & Tao, H. W. Linear transformation
1033 of thalamocortical input by intracortical excitation. *Nat. Neurosci.* **16**, 1324–30 (2013).
- 1034 47. Lien, A. D. & Scanziani, M. Tuned thalamic excitation is amplified by visual cortical
1035 circuits. *Nat. Neurosci.* **16**, 1315–23 (2013).
- 1036 48. King, J. L., Lowe, M. P., Stover, K. R., Wong, A. A. & Crowder, N. A. Adaptive
1037 Processes in Thalamus and Cortex Revealed by Silencing of Primary Visual Cortex
1038 during Contrast Adaptation. *Curr. Biol.* **26**, 1295–1300 (2016).
- 1039 49. Berkes, P., Orbán, G., Lengyel, M. & Fiser, J. Spontaneous Cortical Activity Reveals
1040 Hallmarks of an Optimal Internal Model of the Environment. *Science* **331**, 83–87
1041 (2011).
- 1042 50. Lee, T. S. & Mumford, D. Hierarchical Bayesian inference in the visual cortex. *JOSA*
1043 *A* **20**, 1434–1448 (2003).

- 1044 51. Rao, R. P. N. & Ballard, D. H. Predictive coding in the visual cortex: A functional
1045 interpretation of some extra-classical receptive-field effects. *Nat. Neurosci.* **2**, 79–87
1046 (1999).
- 1047 52. Clark, A. Whatever next? Predictive brains, situated agents, and the future of cognitive
1048 science. *Behav. Brain. Sci.* **36**, 181–204 (2013).
- 1049 53. Gulyás, B., Lagae, L., Eysel, U. & Orban, G. A. Corticofugal feedback influences the
1050 responses of geniculate neurons to moving stimuli. *Exp. Brain Res.* **79**, 441–446 (1990).
- 1051 54. Poltoratski, S., Maier, A., Newton, A. T. & Tong, F. Figure-Ground Modulation in
1052 the Human Lateral Geniculate Nucleus Is Distinguishable from Top-Down Attention.
1053 *Curr. Biol.* **29**, 2051–2057 (2019).
- 1054 55. Sillito, A. M., Cudeiro, J. & Murphy, P. C. Orientation sensitive elements in the
1055 corticofugal influence on centre-surround interactions in the dorsal lateral geniculate
1056 nucleus. *Experimental Brain Research* **93**, 6–16 (1993).
- 1057 56. Makino, H. & Komiyama, T. Learning enhances the relative impact of top-down pro-
1058 cessing in the visual cortex. *Nat. Neurosci.* **18**, 1116–1122 (2015).
- 1059 57. Keller, A. J., Roth, M. M. & Scanziani, M. Feedback generates a second receptive field
1060 in neurons of the visual cortex. *Nature* 1–5 (2020).
- 1061 58. Atallah, B. V., Bruns, W., Carandini, M. & Scanziani, M. Parvalbumin-Expressing
1062 Interneurons Linearly Transform Cortical Responses to Visual Stimuli. *Neuron* **73**,
1063 159–170 (2012).
- 1064 59. Sherman, S. M. Thalamus plays a central role in ongoing cortical functioning. *Nat.*
1065 *Neurosci.* **19**, 533–541 (2016).
- 1066 60. Vinje, W. E. & Gallant, J. L. Sparse coding and decorrelation in primary visual cortex
1067 during natural vision. *Science* **287**, 1273–1276 (2000).
- 1068 61. Goard, M. & Dan, Y. Basal forebrain activation enhances cortical coding of natural
1069 scenes. *Nat. Neurosci.* **12**, 1444–1449 (2009).
- 1070 62. Mahn, M. *et al.* High-efficiency optogenetic silencing with soma-targeted anion-
1071 conducting channelrhodopsins. *Nat. Commun.* **9**, 4125 (2018).
- 1072 63. Bortone, D. S., Olsen, S. R. & Scanziani, M. Translaminar inhibitory cells recruited by
1073 layer 6 corticothalamic neurons suppress visual cortex. *Neuron* **82**, 474–85 (2014).

- 1074 64. Kim, J., Matney, C. J., Blankenship, A., Hestrin, S. & Brown, S. P. Layer 6 corticotha-
1075 lamic neurons activate a cortical output layer, layer 5a. *Journal of Neuroscience* **34**,
1076 9656–64 (2014).
- 1077 65. Sherman, S. M. Tonic and burst firing: dual modes of thalamocortical relay. *Trends*
1078 *Neurosci* **24**, 122–126 (2001).
- 1079 66. Guido, W. & Weyand, T. Burst responses in thalamic relay cells of the awake behaving
1080 cat. *Journal of Neurophysiology* **74**, 1782–1786 (1995).
- 1081 67. Piscopo, D. M., El-Danaf, R. N., Huberman, A. D. & Niell, C. M. Diverse visual
1082 features encoded in mouse lateral geniculate nucleus. *J. Neurosci.* **33**, 4642–56 (2013).
- 1083 68. Román Rosón, M. *et al.* Mouse dLGN Receives Functional Input from a Diverse Popu-
1084 lation of Retinal Ganglion Cells with Limited Convergence. *Neuron* **102**, 1–15 (2019).
- 1085 69. Marshel, J. H., Kaye, A. P., Nauhaus, I. & Callaway, E. M. Anterior-posterior direction
1086 opponency in the superficial mouse lateral geniculate nucleus. *Neuron* **76**, 713–20
1087 (2012).
- 1088 70. Cruz-Martín, A. *et al.* A dedicated circuit links direction-selective retinal ganglion cells
1089 to the primary visual cortex. *Nature* **507**, 358–61 (2014).
- 1090 71. Zhao, X., Chen, H., Liu, X. & Cang, J. Orientation-selective responses in the mouse
1091 lateral geniculate nucleus. *Journal of Neuroscience* **33**, 12751–63 (2013).
- 1092 72. Scholl, B., Tan, A. Y. Y., Corey, J. & Priebe, N. J. Emergence of orientation selectivity
1093 in the Mammalian visual pathway. *J. Neurosci.* **33**, 10616–24 (2013).
- 1094 73. Skottun, B. C. *et al.* Classifying simple and complex cells on the basis of response
1095 modulation. *Vision Res.* **31**, 1079–1086 (1991).
- 1096 74. Carandini, M., Heeger, D. J. & Movshon, J. A. Linearity and Normalization in Simple
1097 Cells of the Macaque Primary Visual Cortex. *J. Neurosci.* **17**, 8621–8644 (1997).
- 1098 75. Lu, S. M., Guido, W. & Sherman, S. M. Effects of membrane voltage on receptive field
1099 properties of lateral geniculate neurons in the cat: Contributions of the low-threshold
1100 Ca²⁺ conductance. *Journal of Neurophysiology* **68**, 2185–2198 (1992).
- 1101 76. Grubb, M. S. & Thompson, I. D. Visual Response Properties of Burst and Tonic
1102 Firing in the Mouse Dorsal Lateral Geniculate Nucleus. *Journal of Neurophysiology*
1103 **93**, 3224–3247 (2005).

- 1104 77. McClurkin, J. W. & Marrocco, R. T. Visual cortical input alters spatial tuning in
1105 monkey lateral geniculate nucleus cells. *The Journal of Physiology* **348**, 135–152 (1984).
- 1106 78. Born, G. *et al.* Corticothalamic feedback sculpts visual spatial integration in mouse
1107 thalamus. *bioRxiv* 2020.05.19.104000 (2021).
- 1108 79. Coen-Cagli, R., Kohn, A. & Schwartz, O. Flexible gating of contextual influences in
1109 natural vision. *Nature Neuroscience* **18**, 1648–1655 (2015).
- 1110 80. Erisken, S. *et al.* Effects of Locomotion Extend throughout the Mouse Early Visual
1111 System. *Curr. Biol.* **24**, 2899–2907 (2014).
- 1112 81. Aydın, Ç., Couto, J., Giugliano, M., Farrow, K. & Bonin, V. Locomotion modulates
1113 specific functional cell types in the mouse visual thalamus. *Nat. Commun.* **9**, 4882
1114 (2018).
- 1115 82. Williamson, R. S., Hancock, K. E., Shinn-Cunningham, B. G. & Polley, D. B. Loco-
1116 motion and Task Demands Differentially Modulate Thalamic Audiovisual Processing
1117 during Active Search. *Curr. Biol.* **25**, 1885–1891 (2015).
- 1118 83. Niell, C. M. & Stryker, M. P. Modulation of Visual Responses by Behavioral State in
1119 Mouse Visual Cortex. *Neuron* **65**, 472–479 (2010).
- 1120 84. Bennett, C., Arroyo, S. & Hestrin, S. Subthreshold Mechanisms Underlying State-
1121 Dependent Modulation of Visual Responses. *Neuron* **80**, 350–357 (2013).
- 1122 85. Augustinaite, S. & Kuhn, B. Complementary Ca²⁺ Activity of Sensory Activated
1123 and Suppressed Layer 6 Corticothalamic Neurons Reflects Behavioral State. *Current*
1124 *Biology* (2020).
- 1125 86. Wiegert, J. S., Mahn, M., Prigge, M., Printz, Y. & Yizhar, O. Silencing Neurons:
1126 Tools, Applications, and Experimental Constraints. *Neuron* **95**, 504–529 (2017).
- 1127 87. Bickford, M. E., Zhou, N., Krahe, T. E., Govindaiah, G. & Guido, W. Retinal and Tec-
1128 tal “Driver-Like” Inputs Converge in the Shell of the Mouse Dorsal Lateral Geniculate
1129 Nucleus. *J. Neurosci.* **35**, 10523–10534 (2015).
- 1130 88. Frandolig, J. E. *et al.* The Synaptic Organization of Layer 6 Circuits Reveals Inhibition
1131 as a Major Output of a Neocortical Sublamina. *Cell Reports* **28**, 3131–3143.e5 (2019).
- 1132 89. Tasic, B. *et al.* Adult mouse cortical cell taxonomy revealed by single cell transcrip-
1133 tomics. *Nature Neuroscience* **19**, 335–346 (2016).

- 1134 90. Gouwens, N. W. *et al.* Classification of electrophysiological and morphological neuron
1135 types in the mouse visual cortex. *Nature Neuroscience* **22**, 1182–1195 (2019).
- 1136 91. Briggs, F., Kiley, C. W., Callaway, E. M. & Usrey, W. M. Morphological Substrates
1137 for Parallel Streams of Corticogeniculate Feedback Originating in Both V1 and V2 of
1138 the Macaque Monkey. *Neuron* **90**, 388–399 (2016).
- 1139 92. Hasse, J. M., Bragg, E. M., Murphy, A. J. & Briggs, F. Morphological heterogene-
1140 ity among corticogeniculate neurons in ferrets: Quantification and comparison with a
1141 previous report in macaque monkeys. *Journal of Comparative Neurology* **527**, 546–557
1142 (2019).
- 1143 93. Briggs, F. & Usrey, W. M. Parallel Processing in the Corticogeniculate Pathway of the
1144 Macaque Monkey. *Neuron* **62**, 135–146 (2009).
- 1145 94. Chen, C., Bickford, M. E. & Hirsch, J. A. Untangling the Web between Eye and Brain.
1146 *Cell* **165**, 20–21 (2016).
- 1147 95. Denman, D. J. & Contreras, D. On Parallel Streams through the Mouse Dorsal Lateral
1148 Geniculate Nucleus. *Frontiers in Neural Circuits* **10** (2016).
- 1149 96. Morgan, J. L., Berger, D. R., Wetzell, A. W. & Lichtman, J. W. The Fuzzy Logic of
1150 Network Connectivity in Mouse Visual Thalamus. *Cell* **165**, 192–206 (2016).
- 1151 97. Zhuang, J. *et al.* The spatial structure of feedforward information in mouse primary
1152 visual cortex. *bioRxiv* 2019.12.24.888156 (2019).
- 1153 98. Liang, L. *et al.* A Fine-Scale Functional Logic to Convergence from Retina to Thalamus.
1154 *Cell* **173**, 1343–1355.e24 (2018).
- 1155 99. Graybuck, L. T. *et al.* Enhancer viruses for combinatorial cell-subclass-specific labeling.
1156 *Neuron* (2021).
- 1157 100. Mich, J. K. *et al.* Functional enhancer elements drive subclass-selective expression from
1158 mouse to primate neocortex. *Cell Reports* **34**, 108754 (2021).
- 1159 101. Holt, G. R. & Koch, C. Shunting Inhibition Does Not Have a Divisive Effect on Firing
1160 Rates. *Neural Computation* **9**, 1001–1013 (1997).
- 1161 102. Doiron, B., Longtin, A., Berman, N. & Maler, L. Subtractive and Divisive Inhibition:
1162 Effect of Voltage-Dependent Inhibitory Conductances and Noise. *Neural Computation*
1163 **13**, 227–248 (2001).

- 1164 103. Hô, N. & Destexhe, A. Synaptic Background Activity Enhances the Responsiveness of
1165 Neocortical Pyramidal Neurons. *Journal of Neurophysiology* **84**, 1488–1496 (2000).
- 1166 104. Shu, Y., Hasenstaub, A., Badoual, M., Bal, T. & McCormick, D. A. Barrages of
1167 Synaptic Activity Control the Gain and Sensitivity of Cortical Neurons. *Journal of*
1168 *Neuroscience* **23**, 10388–10401 (2003).
- 1169 105. Chance, F. S., Abbott, L. F. & Reyes, A. D. Gain Modulation from Background
1170 Synaptic Input. *Neuron* **35**, 773–782 (2002).
- 1171 106. Cardin, J. A., Palmer, L. A. & Contreras, D. Cellular Mechanisms Underlying Stimulus-
1172 Dependent Gain Modulation in Primary Visual Cortex Neurons In Vivo. *Neuron* **59**,
1173 150–160 (2008).
- 1174 107. Disney, A. A., Aoki, C. & Hawken, M. J. Gain Modulation by Nicotine in Macaque
1175 V1. *Neuron* **56**, 701–713 (2007).
- 1176 108. Ferguson, K. A. & Cardin, J. A. Mechanisms underlying gain modulation in the cortex.
1177 *Nature Reviews Neuroscience* 1–13 (2020).
- 1178 109. Béhuret, S., Deleuze, C. & Bal, T. Corticothalamic Synaptic Noise as a Mechanism for
1179 Selective Attention in Thalamic Neurons. *Frontiers in Neural Circuits* **9** (2015).
- 1180 110. Wolfart, J., Debay, D., Le Masson, G., Destexhe, A. & Bal, T. Synaptic background
1181 activity controls spike transfer from thalamus to cortex. *Nature Neuroscience* **8**, 1760–
1182 1767 (2005).
- 1183 111. Kara, P., Reinagel, P. & Reid, R. C. Low Response Variability in Simultaneously
1184 Recorded Retinal, Thalamic, and Cortical Neurons. *Neuron* **27**, 635–646 (2000).
- 1185 112. Jahnsen, H. & Llinás, R. Voltage-dependent burst-to-tonic switching of thalamic cell
1186 activity: An in vitro study. *Arch. Ital. Biol.* **122**, 73–82 (1984).
- 1187 113. Dossi, R. C., Nuñez, A. & Steriade, M. Electrophysiology of a slow (0.5–4 Hz) intrinsic
1188 oscillation of cat thalamocortical neurones in vivo. *J. Physiol.* **447**, 215–234 (1992).
- 1189 114. Mease, R. A., Krieger, P. & Groh, A. Cortical control of adaptation and sensory relay
1190 mode in the thalamus. *Proc. Natl. Acad. Sci. U.S.A.* **111**, 6798–6803 (2014).
- 1191 115. Alitto, H. J., Weyand, T. G. & Usrey, W. M. Distinct Properties of Stimulus-Evoked
1192 Bursts in the Lateral Geniculate Nucleus. *Journal of Neuroscience* **25**, 514–523 (2005).

- 1193 116. Alitto, H., Rathbun, D. L., Vandeleest, J. J., Alexander, P. C. & Usrey, W. M. The
1194 Augmentation of Retinogeniculate Communication during Thalamic Burst Mode. *J.*
1195 *Neurosci.* **39**, 5697–5710 (2019).
- 1196 117. Lesica, N. A. & Stanley, G. B. Encoding of Natural Scene Movies by Tonic and Burst
1197 Spikes in the Lateral Geniculate Nucleus. *J. Neurosci.* **24**, 10731–10740 (2004).
- 1198 118. Lesica, N. A. *et al.* Dynamic Encoding of Natural Luminance Sequences by LGN Bursts.
1199 *PLoS Biol.* **4** (2006).
- 1200 119. Wang, X. *et al.* Feedforward Excitation and Inhibition Evoke Dual Modes of Firing in
1201 the Cat’s Visual Thalamus during Naturalistic Viewing. *Neuron* **55**, 465–478 (2007).
- 1202 120. Whitmire, C. J., Waiblinger, C., Schwarz, C. & Stanley, G. B. Information Coding
1203 through Adaptive Gating of Synchronized Thalamic Bursting. *Cell Reports* **14**, 795–
1204 807 (2016).
- 1205 121. Swadlow, H. A. & Gusev, A. G. The impact of ‘bursting’ thalamic impulses at a
1206 neocortical synapse. *Nature Neuroscience* **4**, 402–408 (2001).
- 1207 122. Hochstein, S. & Ahissar, M. View from the Top: Hierarchies and Reverse Hierarchies
1208 in the Visual System. *Neuron* **36**, 791–804 (2002).
- 1209 123. Guo, W., Clause, A. R., Barth-Marion, A. & Polley, D. B. A Corticothalamic Circuit
1210 for Dynamic Switching between Feature Detection and Discrimination. *Neuron* **95**,
1211 180–194 (2017).
- 1212 124. Mease, R. A., Kuner, T., Fairhall, A. L. & Groh, A. Multiplexed Spike Coding and
1213 Adaptation in the Thalamus. *Cell Rep.* **19**, 1130–1140 (2017).
- 1214 125. Dan, Y., Atick, J. J. & Reid, R. C. Efficient coding of natural scenes in the lateral
1215 geniculate nucleus: experimental test of a computational theory. *J. Neurosci.* **16**, 3351–
1216 3362 (1996).
- 1217 126. Lesica, N. A. *et al.* Adaptation to Stimulus Contrast and Correlations during Natural
1218 Visual Stimulation. *Neuron* **55**, 479–491 (2007).
- 1219 127. Mante, V., Frazor, R. A., Bonin, V., Geisler, W. S. & Carandini, M. Independence of
1220 luminance and contrast in natural scenes and in the early visual system. *Nat. Neurosci.*
1221 **8**, 1690–1697 (2005).

- 1222 128. Radnikow, G. & Feldmeyer, D. Layer- and Cell Type-Specific Modulation of Excitatory
1223 Neuronal Activity in the Neocortex. *Frontiers in Neuroanatomy* **12** (2018).
- 1224 129. Sundberg, S. C., Lindström, S. H., Sanchez, G. M. & Granseth, B. Cre-expressing neu-
1225 rons in visual cortex of Ntsr1-Cre GN220 mice are corticothalamic and are depolarized
1226 by acetylcholine. *Journal of Comparative Neurology* **526**, 120–132 (2018).
- 1227 130. Swadlow, H. A. & Weyand, T. G. Corticogeniculate neurons, corticotectal neurons,
1228 and suspected interneurons in visual cortex of awake rabbits: Receptive-field properties,
1229 axonal properties, and effects of EEG arousal. *Journal of Neurophysiology* **57**, 977–1001
1230 (1987).
- 1231 131. Schröder, S. *et al.* Arousal Modulates Retinal Output. *Neuron* **107**, 487–495.e9 (2020).
- 1232 132. Murata, Y. & Colonnese, M. T. Thalamus Controls Development and Expression of
1233 Arousal States in Visual Cortex. *J. Neurosci.* **38**, 8772–8786 (2018).
- 1234 133. Nestvogel, D. B. & McCormick, D. A. Visual Thalamocortical Mechanisms of Waking
1235 State Dependent Activity and Alpha Oscillations. *bioRxiv* 2021.04.14.439865 (2021).
- 1236 134. Vinck, M., Batista-Brito, R., Knoblich, U. & Cardin, J. A. Arousal and Locomo-
1237 tion Make Distinct Contributions to Cortical Activity Patterns and Visual Encoding.
1238 *Neuron* **86**, 740–754 (2015).
- 1239 135. Zaghera, E. & McCormick, D. A. Neural control of brain state. *Current Opinion in*
1240 *Neurobiology* **29**, 178–186 (2014).
- 1241 136. Lee, S.-H. & Dan, Y. Neuromodulation of Brain States. *Neuron* **76**, 209–222 (2012).
- 1242 137. McCormick, D. A. Neurotransmitter actions in the thalamus and cerebral cortex and
1243 their role in neuromodulation of thalamocortical activity. *Progress in Neurobiology* **39**,
1244 337–388 (1992).
- 1245 138. Sherman, S. M. & Koch, C. The control of retinogeniculate transmission in the mam-
1246 malian lateral geniculate nucleus. *Experimental Brain Research* **63**, 1–20 (1986).
- 1247 139. Holdefer, R. N. & Jacobs, B. L. Phasic stimulation of the locus coeruleus: Effects on
1248 activity in the lateral geniculate nucleus. *Experimental Brain Research* **100**, 444–452
1249 (1994).

- 1250 140. Lu, S. M., Guido, W. & Sherman, S. M. The brain-stem parabrachial region controls
1251 mode of response to visual stimulation of neurons in the cat's lateral geniculate nucleus.
1252 *Visual Neuroscience* **10**, 631–642 (1993).
- 1253 141. Funke, K., Pape, H. C. & Eysel, U. T. Noradrenergic modulation of retinogeniculate
1254 transmission in the cat. *The Journal of Physiology* **463**, 169–191 (1993).
- 1255 142. Sillito, A. M., Kemp, J. A. & Berardi, N. The cholinergic influence on the function of
1256 the cat dorsal lateral geniculate nucleus (dLGN). *Brain Research* **280**, 299–307 (1983).
- 1257 143. Liang, L. *et al.* Retinal Inputs to the Thalamus Are Selectively Gated by Arousal.
1258 *Current Biology* **30**, 3923–3934 (2020).
- 1259 144. Grubb, M. S. & Thompson, I. D. Quantitative Characterization of Visual Response
1260 Properties in the Mouse Dorsal Lateral Geniculate Nucleus. *J. Neurophysiol.* **90**, 3594–
1261 3607 (2003).
- 1262 145. Rueden, C. T. *et al.* ImageJ2: ImageJ for the next generation of scientific image data.
1263 *BMC Bioinf.* **18** (2017).
- 1264 146. Schindelin, J. *et al.* Fiji: An open-source platform for biological-image analysis. *Nat.*
1265 *Methods* **9**, 676–682 (2012).
- 1266 147. Poynton, C. A. Rehabilitation of gamma. In Rogowitz, B. E. & Pappas, T. N. (eds.)
1267 *Human Vision and Electronic Imaging III*, vol. 3299, 232–249 (International Society
1268 for Optical Engineering, San Jose, CA, 1998). URL [http://www.poynton.com/PDFs/
1269 Rehabilitation_of_gamma.pdf](http://www.poynton.com/PDFs/Rehabilitation_of_gamma.pdf).
- 1270 148. Pachitariu, M., Steinmetz, N. A., Kadir, S. N., Carandini, M. & Harris, K. D. Fast
1271 and accurate spike sorting of high-channel count probes with KiloSort. In Lee, D. D.,
1272 Sugiyama, M., Luxburg, U. V., Guyon, I. & Garnett, R. (eds.) *Advances in Neural*
1273 *Information Processing Systems 29*, 4448–4456 (Curran Associates, Inc., 2016).
- 1274 149. Spacek, M. A., Blanche, T. J. & Swindale, N. V. Python for large-scale electrophysiol-
1275 ogy. *Front. Neuroinform.* **2**, 9 (2009). URL <http://swindale.ecc.ubc.ca/code>.
- 1276 150. Swindale, N. V. & Spacek, M. A. Spike sorting for polytrodes: a divide and conquer
1277 approach. *Front. Syst. Neurosci.* **8**, 6 (2014).
- 1278 151. Yatsenko, D., Walker, E. Y. & Tolia, A. S. DataJoint: A simpler relational data model.
1279 *arXiv* **1807**, 11104 (2018).

- 1280 152. Mitzdorf, U. Current source-density method and application in cat cerebral cortex:
1281 Investigation of evoked potentials and EEG phenomena. *Physiol. Rev.* **65**, 37–100
1282 (1985).
- 1283 153. Heumann, D., Leuba, G. & Rabinowicz, T. Postnatal development of the mouse cere-
1284 bral neocortex. II. Quantitative cytoarchitectonics of visual and auditory areas. *J.*
1285 *Hirnforsch.* **18**, 483–500 (1977).
- 1286 154. van der Togt, C., Spekreijse, H. & Supèr, H. Neural responses in cat visual cortex
1287 reflect state changes in correlated activity. *Eur. J. Neurosci.* **22**, 465–475 (2005).
- 1288 155. Baden, T. *et al.* The functional diversity of retinal ganglion cells in the mouse. *Nature*
1289 **529**, 345–350 (2016).
- 1290 156. Bonhoeffer, T., Kim, D.-S., Malonek, D., Shoham, D. & Grinvald, A. Optical Imaging
1291 of the Layout of Functional Domains in Area 17 and Across the Area 17/18 Border in
1292 Cat Visual Cortex. *Eur. J. Neurosci.* **7**, 1973–1988 (1995).
- 1293 157. Niell, C. M. & Stryker, M. P. Highly selective receptive fields in mouse visual cortex.
1294 *J Neurosci* **28**, 7520–7536 (2008).
- 1295 158. Reimer, J. *et al.* Pupil Fluctuations Track Fast Switching of Cortical States during
1296 Quiet Wakefulness. *Neuron* **84**, 355–362 (2014).
- 1297 159. McGinley, M. J., David, S. V. & McCormick, D. A. Cortical Membrane Potential
1298 Signature of Optimal States for Sensory Signal Detection. *Neuron* **87**, 179–192 (2015).
- 1299 160. Remtulla, S. & Hallett, P. A schematic eye for the mouse, and comparisons with the
1300 rat. *Vision Res.* **25**, 21–31 (1985).
- 1301 161. Sakatani, T. & Isa, T. Quantitative analysis of spontaneous saccade-like rapid eye
1302 movements in c57bl/6 mice. *Neuroscience research* **58**, 324–331 (2007).
- 1303 162. Gelman, A. & Hill, J. *Data Analysis Using Regression and Multilevel/Hierarchical Mod-*
1304 *els.* Analytical Methods for Social Research (Cambridge University Press, Cambridge,
1305 2007).
- 1306 163. Aarts, E., Verhage, M., Veenvliet, J. V., Dolan, C. V. & van der Sluis, S. A solution
1307 to dependency: Using multilevel analysis to accommodate nested data. *Nat. Neurosci.*
1308 **17**, 491–496 (2014).

- 1309 164. R Core Team. *R: A Language and Environment for Statistical Computing*. R Found-
1310 dation for Statistical Computing, Vienna, Austria (2017). URL [https://www.R-project.](https://www.R-project.org/)
1311 [org/](https://www.R-project.org/).
- 1312 165. Bates, D., Mächler, M., Bolker, B. & Walker, S. Fitting Linear Mixed-Effects Models
1313 Using **lme4**. *J. Stat. Softw.* **67** (2015).
- 1314 166. Luke, S. G. Evaluating significance in linear mixed-effects models in R. *Behav. Res.*
1315 *Methods* **49**, 1494–1502 (2017).
- 1316 167. Kuznetsova, A., Brockhoff, P. B. & Christensen, R. H. B. **lmerTest** Package: Tests in
1317 Linear Mixed Effects Models. *J. Stat. Softw.* **82** (2017).

1318 **Supplementary Information**

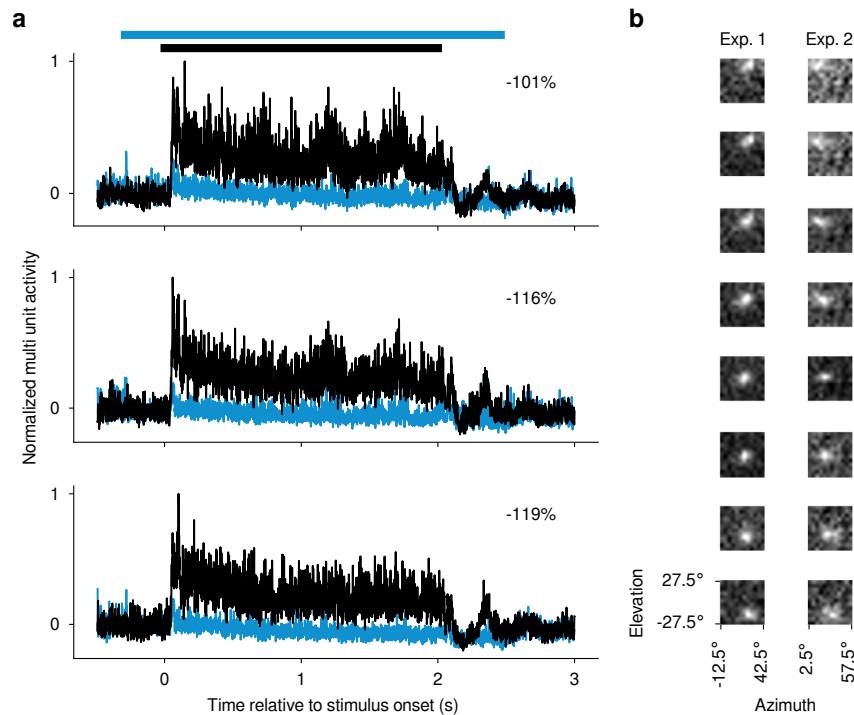


Figure 1-Supplement 1 Confirmation of optogenetic suppression of V1 responses and targeting dLGN for recordings.

(a) MUAe responses [154] to 2 s drifting gratings recorded in one experiment for three example channels. All three channels were located, as determined by current source density analysis [152], in the infragranular layers of V1. *Black*: Mean MUAe responses across control trials; *blue*: MUAe responses in trials with optogenetic activation of PV+ inhibitory interneurons. Normalized MUAe was computed by subtracting the mean activity across both conditions in a 200 ms time window prior to light onset before normalizing to the maximum response across the two conditions. Percentages indicate mean reduction in MUAe over the stimulus presentation period. *Black bar*: stimulus period; *blue bar*: photoactivation period. (b) MUAe-based RFs for channels located in dLGN during two example RF mapping experiments. Each panel represents one channel, with the top channel being located most dorsally and the bottom channel most ventrally in the dLGN. RFs were computed as the mean response to a change in contrast at a given monitor position in a time window ranging from 50 ms after stimulus onset to 100 ms after stimulus offset. Brighter pixels indicate higher activity. The emerging characteristic pattern with more ventrally located channels representing locations lower in the visual field was used to confirm successful targeting of dLGN.

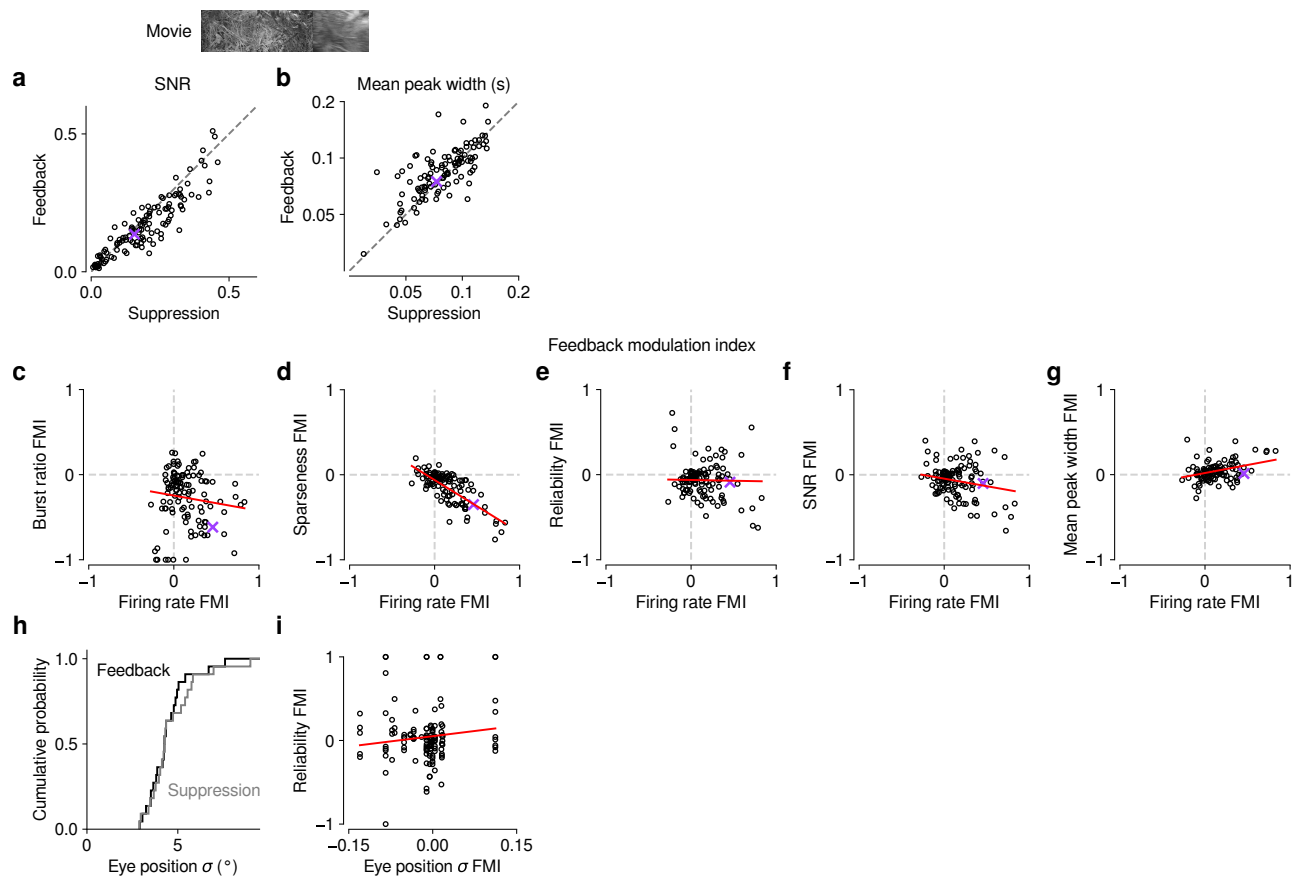


Figure 1-Supplement 2 Effects of CT feedback on additional parameters of responses to naturalistic movies and relationship with firing rate.

(a,b) Comparison of CT feedback vs. V1 suppression conditions for PSTH signal-to-noise ratio (SNR) (a) and mean peak width (b). SNR was computed as in [155], and compares the variance of the trial-averaged PSTH across time relative to the single-trial variance across time, averaged across stimulus repeats. If all trials are identical such that the PSTH is a perfect representation of each trial's response, SNR equals 1. The width of PSTH peaks that exceeded a threshold amplitude was measured as the temporal separation of the middle 68% of spikes clustered as part of each peak (see Methods). Narrow peaks are a proxy for high temporal precision of responses. With CT feedback intact, mean SNR was lower (0.15 vs. 0.18, LMM: $F_{1,180.6} = 11.2$, $p = 0.00098$) and mean peak width was higher (0.087 vs. 0.081, LMM: $F_{1,154.15} = 7.0$, $p = 0.0091$). (c-g) Relationship between CT feedback effects on firing rate and burst ratio (c), sparseness (d), reliability (e), SNR (f), and mean peak width (g). Feedback effects were quantified with a feedback modulation index (FMI), where $FMI = (\text{feedback} - \text{suppressed}) / (\text{feedback} + \text{suppressed})$. CT feedback-related changes in firing rate can to a large degree account for the changes in sparseness (LMM: slope of -0.62 ± 0.11 ; (d)). Importantly, for all other measures, there was no systematic relation to the feedback manipulation of firing rates because slopes were either non-significant or close to 0 (burst ratio, LMM: slope of -0.18 ± 0.29 ; reliability, LMM: -0.018 ± 0.19 ; SNR, LMM: slope of -0.18 ± 0.18 ; mean peak width, LMM: slope of 0.19 ± 0.11 ; estimated slope $\pm 2 \times$ the estimated standard error). (h) Cumulative distribution of variance in eye position with CT feedback intact (black) and suppressed (gray). Eye position standard deviation was, on average, slightly greater during V1 suppression than during feedback (4.5° vs. 4.3° , LMM: $F_{1,21} = 4.4$, $p = 0.049$, $N = 22$ experiments from 6 mice). (i) The strength of CT feedback effects on reliability is unrelated to the strength of feedback effects on eye position (LMM: slope 0.83 ± 1.27). The results from (h) and (i) are inconsistent with the hypothesis that CT feedback effects on trial-to-trial reliability can be explained by changes in eye position variance.

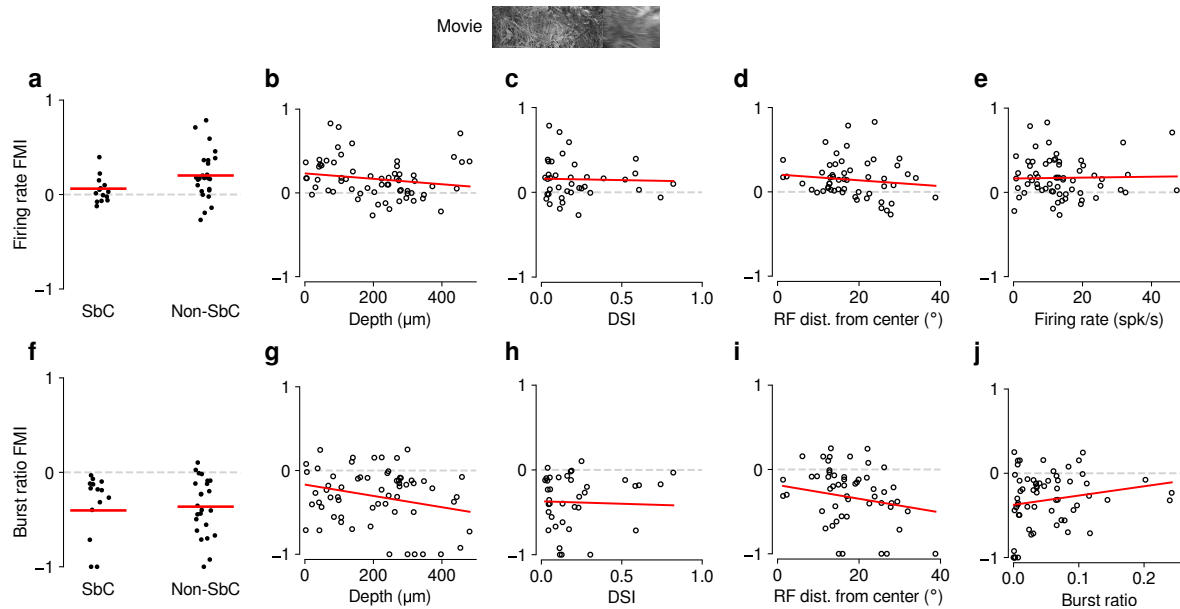


Figure 1-Supplement 3 Feedback effects during movie presentation are largely independent of functional cell type classification.

The dLGN is a non-homogeneous nucleus, consisting of different neuronal cell types [67, 68]. To test if the effect of CT feedback depended on functional cell type, we performed functional cell typing of neurons in various ways. None of the classifications yielded significant results. (a) Firing rate FMI distributions during movie presentation, with units classified according to whether or not they were suppressed by contrast (SbC) [67, 68]. Units were defined as SbC if their mean firing rates to uniform equiluminant gray screen were $\geq 3\times$ that of a full-contrast stimulus. CT feedback effects on firing rates tended to be lower for SbC neurons compared to the rest of the population, but not significantly (SbC: 0.062 vs. non-SbC: 0.20; LMM: $F_{1,37.0} = 3.51$, $p = 0.069$). (b) Firing rate FMI during movie presentation, plotted against estimated depth of each unit in dLGN (slope -0.00032 ± 0.00046). (c) Same as (b), but with units plotted against the direction selectivity index (DSI) [157] of each unit (slope -0.034 ± 0.37). (d) Same as (c), but with units plotted against the distance of their RFs from the center of the screen (slope -0.0035 ± 0.0083). We considered distance from center of screen as a proxy for RF coverage by the visual stimuli, which we hypothesized might modulate CT feedback effects through its known effects on spatial integration [78]. (e) Same as (d), but with units plotted against their mean firing rate during the feedback intact condition (slope 0.00052 ± 0.006). This indicates that the CT feedback modulation of firing rates does not depend on overall firing rate, i.e. that neurons do not share the same gain factor (see also Fig. 2e,i). (f-j) Same as (a-e), but for burst ratio (-0.40 (SbC) vs. -0.36 (non-SbC); LMM: $F_{1,30.8} = 0.42$, $p = 0.52$; depth: slope -0.00067 ± 0.0006 ; DSI: slope -0.057 ± 0.3 ; RF distance: slope -0.0081 ± 0.01 ; burst ratio: slope 1.1 ± 1.3). In summary, except for modest trends of differential CT feedback modulations of SbC neurons, we did not find any difference in how feedback affected the various subpopulations. The general similarity of CT feedback effects across classifications might be related to a lack of power (cell-typing in high-dimensional space requires high neuron counts) and to the global suppression approach.

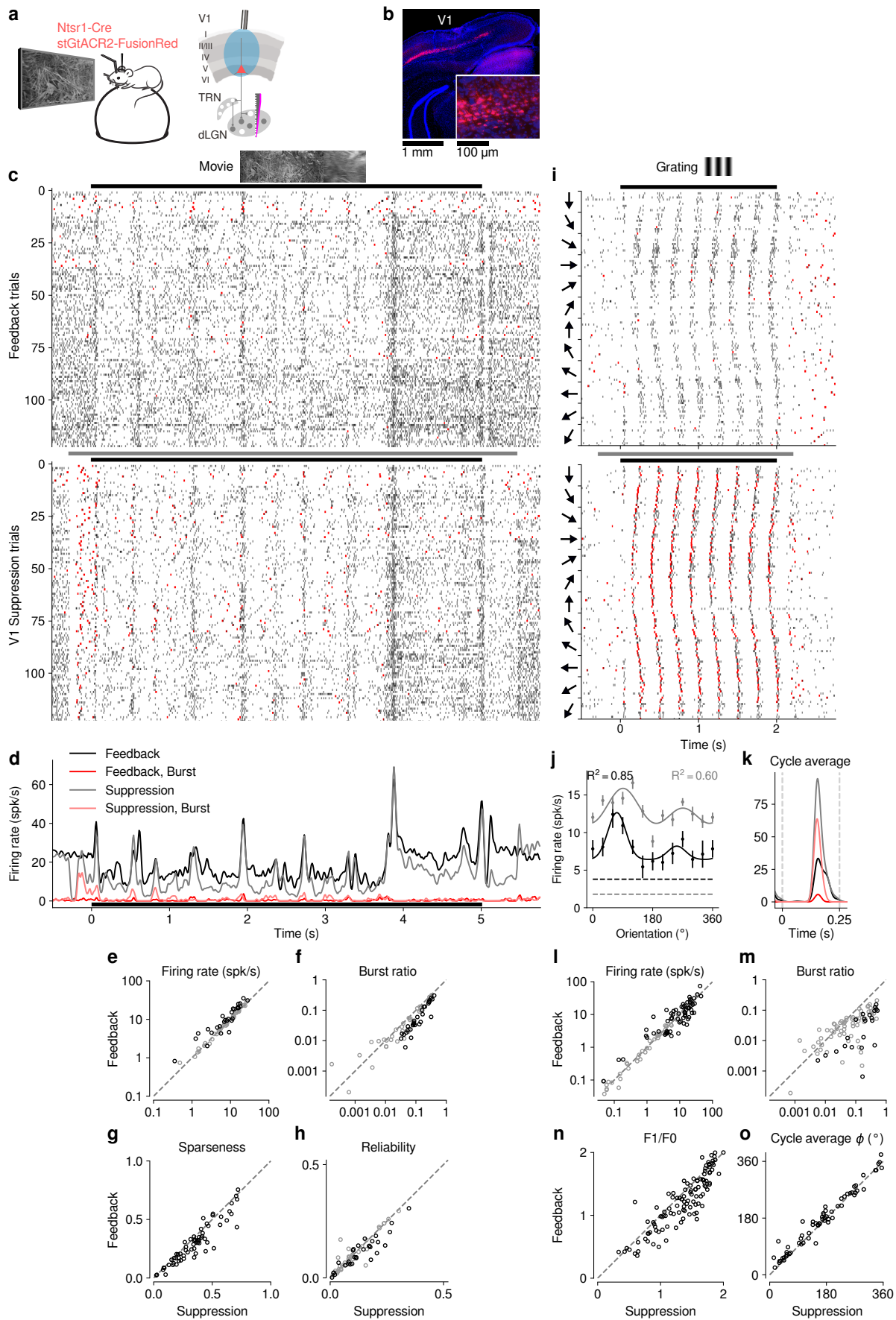


Figure 1-Supplement 4 (Previous page) Selective optogenetic suppression of L6 CT feedback in Ntsr1-Cre yielded similar results as global V1 suppression via PV+ activation.

(a) Schematic of experimental approach. The chloride-conducting, inhibitory opsin stGtACR2 [62] was conditionally expressed in V1 Ntsr1+ neurons (red) using a viral approach. Extracellular silicon electrode recordings were performed in dLGN with and without optogenetic suppression of V1. (b) Coronal section of V1 for an example Ntsr1-Cre mouse, showing transduced Ntsr1+ neurons (magenta) located in the deep layers of V1. Blue: cell nuclei stained with DAPI. Inset: magnified view with expression of stGtACR2 largely restricted to somata. (c) Movie raster plots during feedback and suppression for an example neuron. (d) Corresponding PSTHs. (e-h) Comparison of CT feedback vs. suppression conditions for mean firing rate (e), burst ratio (f), temporal sparseness (g), and response reliability (h), all calculated for the duration of the movie clip. Similar to our results for global V1 suppression, CT feedback enhanced firing rates (10.4 (feedback) vs. 9.0 spikes/s (suppression); LMM: $F_{1,68.3} = 9.2$, $p = 0.0034$), reduced bursting (0.083 vs. 0.12; LMM: $F_{1,67.7} = 57.6$, $p = 1.3 \times 10^{-10}$), reduced sparseness (0.31 vs. 0.36; LMM: $F_{1,68.1} = 37.9$, $p = 4.4 \times 10^{-8}$), and reduced trial-to-trial reliability (0.10 vs. 0.11; LMM: $F_{1,66.3} = 5.1$, $p = 0.027$). (i) Grating raster plots sorted by orientation, during CT feedback and suppression conditions for a different example neuron. (j,k) Corresponding orientation tuning curves and cycle average responses to preferred orientation. (l-o) Comparison of feedback vs. suppression conditions for mean firing rate (l), burst ratio (m), F_1/F_0 (n), and cycle average phase ϕ (o). Similar to our results for global V1 suppression, CT feedback had no consistent effect on firing rate (11.10 (feedback) vs. 11.09 spikes/s (suppression); LMM: $F_{1,137.9} = 0.0001$, $p = 0.99$), but reduced bursting (0.04 vs. 0.12; LMM: $F_{1,127.5} = 43.7$, $p = 9.4 \times 10^{-10}$), and reduced F_1/F_0 (1.2 vs. 1.3; LMM: $F_{1,142.9} = 13.0$, $p = 0.00043$). Black symbols in (e,f,h,l,m) indicate individually significant neurons (Welch's t-test).

Figure 1-Video 1 First example 5 s movie clip used for visual stimulation.

Figure 1-Video 2 Second example 5 s movie clip used for visual stimulation.

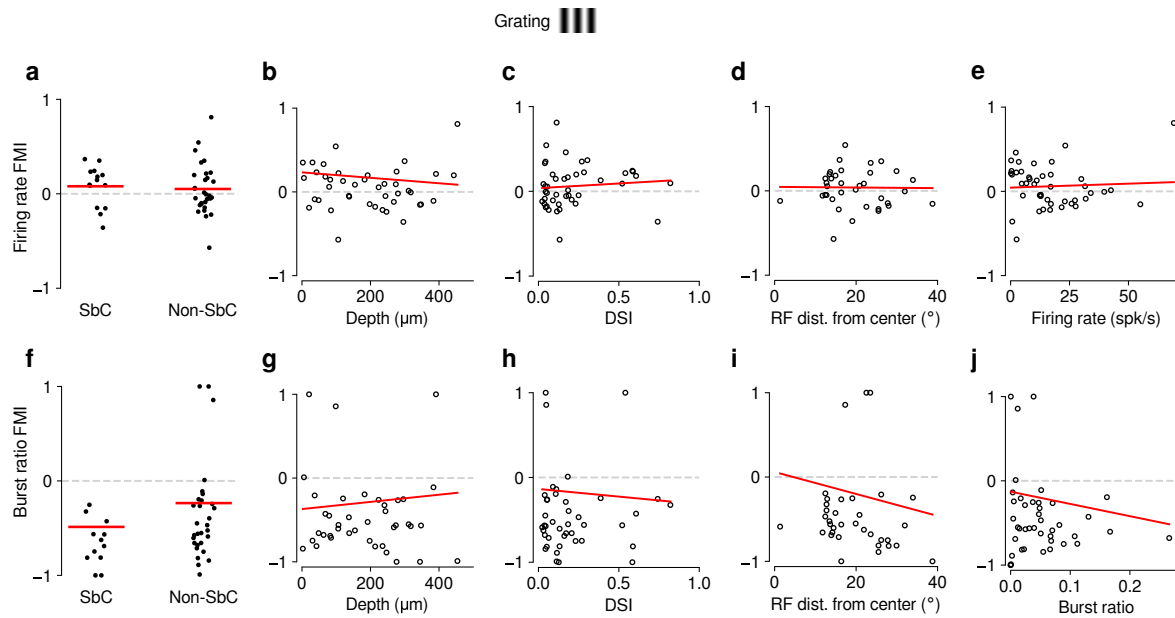


Figure 3-Supplement 1 As for movies (**Fig. 1-Supplement 3**), feedback effects during grating presentation are largely independent of functional cell type classification.

(**a–e**) Same as **Fig. 1-Supplement 3a–e** but for drifting gratings (0.08 (SbC) vs. 0.05 (non-SbC); LMM: $F_{1,42} = 0.12$, $p = 0.73$; depth: slope -0.00032 ± 0.0005 ; DSI: slope 0.11 ± 0.4 ; RF distance: slope -0.0004 ± 0.01 ; firing rate: slope 0.0009 ± 0.005). (**f–j**) Same as **Fig. 1-Supplement 3f–j** but for drifting gratings (-0.49 (SbC) vs. -0.24 (non-SbC); LMM: $F_{1,34.0} = 3.77$, $p = 0.061$; depth: slope 0.00043 ± 0.0012 ; DSI: slope -0.18 ± 0.6 ; RF distance: slope -0.013 ± 0.03 ; burst ratio: slope -1.5 ± 2.2).

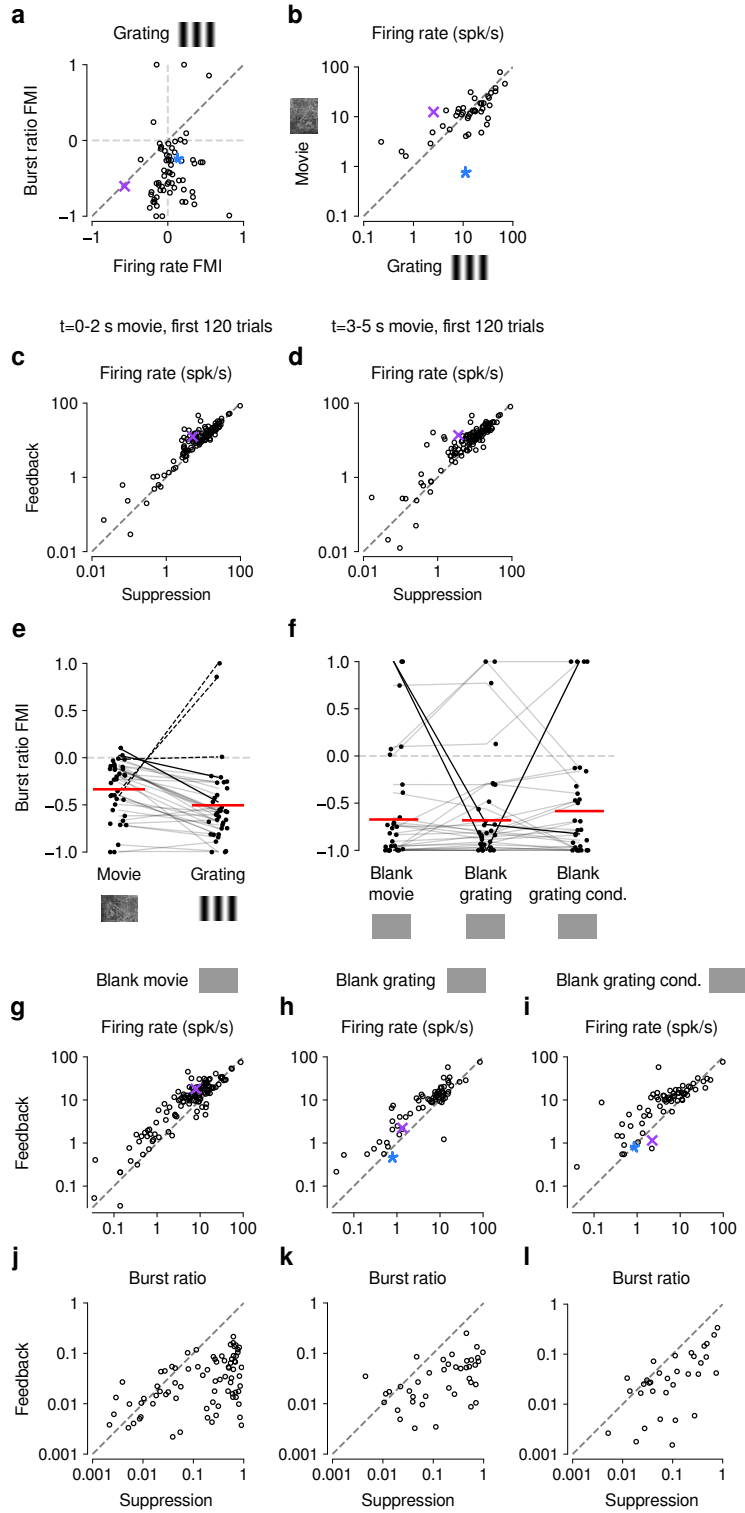


Figure 4-Supplement 1 (Previous page) Control analyses assessing the difference in CT feedback effects for gratings and movies.

(a) Similar to our results for movies (**Fig. 1-Supplement 2c**), CT feedback modulation of grating burst ratio was unrelated to CT feedback modulation of firing rate (LMM: slope of 0.029 ± 0.41). (b) With CT feedback intact, movies and gratings evoked firing rates of similar magnitude (13.3 spikes/s vs. 16.3 spikes/s, LMM: $F_{1,42} = 4.1$, $p = 0.05$). This rules out the possibility that larger CT feedback effects for movies are related to stronger firing rates already present in the baseline condition with CT feedback intact. (c) dLGN firing rates for movies were consistently higher during the CT feedback intact vs. V1 suppression condition, even when restricted to only the first 2 s and 120 trials of movie stimulation, for more direct comparison with grating stimulation (main effect of feedback, LMM: $F_{1,429.1} = 13.0$, $p = 0.0004$). (d) Same as (c), but for the last 2 s of movie stimulation. The effect of V1 suppression was indistinguishable during the first two and the last two seconds of the movie clips (interaction feedback \times analysis window, LMM: $F_{1,429.1} = 0.54$, $p = 0.46$). Higher consistency of effects of V1 feedback suppression on firing rates for naturalistic movies thus cannot be explained by the longer duration or greater number of movie trials (5 s, 200 trials) than grating trials (2 s, 120 trials). (e) V1 suppression increases bursting more strongly during presentation of gratings than movies (burst ratio FMI of -0.34 (movies) vs. -0.5 (gratings); LMM: $F_{1,35} = 5.7$, $p = 0.023$). (f) V1 suppression increases bursting to a similar degree during short blank screen periods preceding movie and grating stimulus trials, and during blank grating conditions (burst ratio FMI of -0.67 (pre-movies) vs. -0.68 (pre-gratings) vs. -0.58 (blank grating condition); LMM: $F_{2,56} = 0.43$, $p = 0.65$). Burst ratio FMI depended only weakly on stimulus type (movie vs. grating, average of all blank conditions, LMM: $F_{2,126.2} = 2.8$, $p = 0.067$). (g,h,i) Comparison of firing rates during CT feedback vs. V1 suppression for short blank periods preceding movies and gratings, and during blank grating conditions. In all cases, CT feedback is associated with enhanced firing rates (blank pre-movies: firing rates 12.9 spikes/s (feedback) vs. 8.9 spikes/s (V1 suppression); LMM: $F_{1,178.7} = 24.2$, $p = 2.0 \times 10^{-6}$; blank pre-gratings: firing rates 11.5 spikes/s (feedback) vs. 7.9 spikes/s (V1 suppression); LMM: $F_{1,86.4} = 13.2$, $p = 0.0005$; blank grating condition: firing rates 11.4 spikes/s (feedback) vs. 8.5 spikes/s (V1 suppression); LMM: $F_{1,86.3} = 6.4$, $p = 0.01$). (j,k,l) Same as (g,h,i), but for burst ratio. In all cases, CT feedback is associated with less bursting (blank pre-movies: burst ratios 0.024 (feedback) vs. 0.22 (V1 suppression); LMM: $F_{1,185.7} = 96.5$, $p = 2.2 \times 10^{-16}$; blank pre-gratings: burst ratios 0.036 (feedback) vs. 0.22 (V1 suppression); LMM: $F_{1,93.0} = 38.1$, $p = 1.8 \times 10^{-8}$; blank grating condition: burst ratios 0.047 (feedback) vs. 0.14 (V1 suppression); LMM: $F_{1,83.0} = 24.4$, $p = 4.0 \times 10^{-6}$). (e,f) Red horizontal lines: means estimated by LMM.

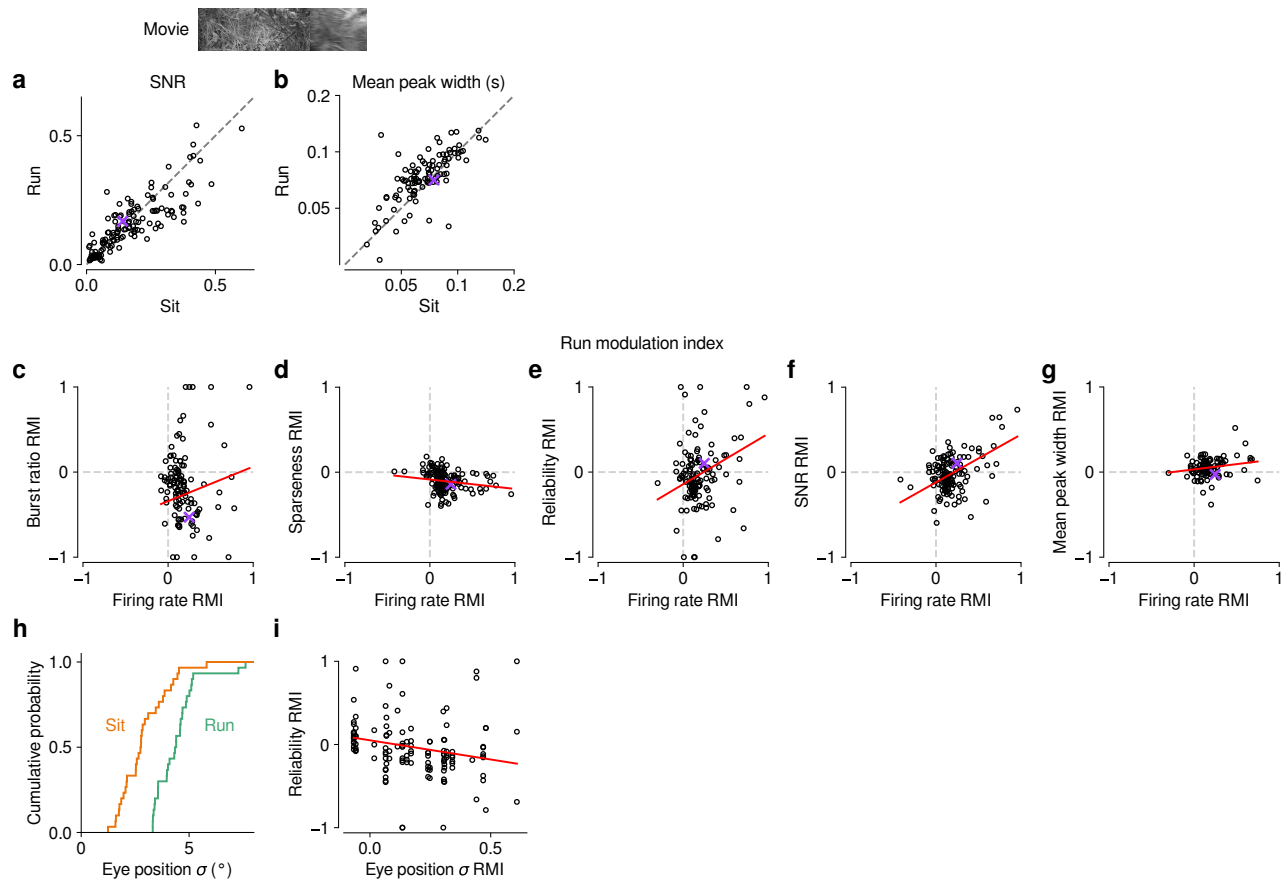


Figure 5-Supplement 1 Effects of locomotion on additional parameters of responses to naturalistic movie clips and relationship with firing rate.

(a,b) Comparison between trials with locomotion and stationary periods for (a) SNR [155] and (b) width of response peaks. During locomotion, SNR was lower (0.14 vs. 0.16, LMM: $F_{1,174.1} = 5.6$, $p = 0.019$) and mean peak width was broader (0.08 vs. 0.07, LMM: $F_{1,146.2} = 13.1$, $p = 0.0004$). (c–g) Relationship between locomotion effects (RMI) on firing rate of burst ratio (c), sparseness (d), reliability (e), SNR (f), and mean peak width (g). Locomotion-related changes in firing rate can to some degree account for the changes in reliability (LMM: slope of 0.59 ± 0.38) and SNR (LMM: slope of 0.56 ± 0.20). Slopes were non-significant for burst ratio (LMM: slope of 0.41 ± 0.43), sparseness (LMM: slope of -0.11 ± 0.11) and mean peak width (LMM: slope of 0.12 ± 0.14). (h) Cumulative distribution of trial-averaged eye-position standard deviation for stationary (orange) and locomotion (green) trials. Eye-position standard deviation was first calculated for each time point across trials, and then averaged across time points. In line with previous reports [80, 84], standard deviation of eye position was, on average, larger during locomotion than during stationary periods (4.4° vs. 2.9° , LMM: $F_{1,49} = 50.3$, $p = 4.8 \times 10^{-9}$, $N = 60$ experiments from 6 mice). (i) Locomotion-related trial-to-trial reliability co-varied with locomotion-related changes in eye position standard deviation (LMM: slope of -0.46 ± 0.38); however, the expected difference in reliability RMI corresponding to a 1 standard deviation difference in eye position σ RMI is -0.082 , which is much smaller than the residual standard deviation of 0.28 unexplained by the regression. Therefore, changes in eye position during locomotion cannot account for most of the reduced reliability of responses during locomotion (Fig. 5f).

4 Evaluating visual cues modulates their representation in mouse visual and cingulate cortex

This chapter is reproduced from an article published in *The Journal of Neuroscience*. The article can be found under <https://www.jneurosci.org/content/41/15/3531.abstract>. The full citation is:

Wal, A., Klein, F. J., Born G., Busse, L., & Katzner, S. (2021). Evaluating visual cues modulates their representation in mouse visual and cingulate cortex. *Journal of Neuroscience*, 41(15), 3531–3544.

Declaration of author contributions

Alexandra Wal, Frederike J. Klein, and Gregory Born performed the research. Alexandra Wal, Frederike J. Klein, Gregory Born, and Laura Busse edited the paper. Laura Busse and Steffen Katzner designed the research. Steffen Katzner analyzed the data and wrote the paper.

Personal contributions

For Fig.6A, G.B. processed and visualized histological data. To try to dissociate the valence (no reward vs. reward) from the shape (diamond vs. square) of the stimulus, G.B. ran experiments in which the stimulus-reward contingencies were reversed after a few recording sessions. These data are not shown in the manuscript. Lastly, G.B. contributed to editing the manuscript.

Rights and permissions

”Authors grant JNeurosci a license to publish their work and copyright remains with the author. For articles published after 2014, the Society for Neuroscience (SfN) retains an exclusive license to publish the article for 6 months; after 6 months, the work becomes available to the public to copy, distribute, or display under the terms of the Creative Commons Attribution 4.0 International License (CC-BY). This license allows data and text mining, use of figures in presentations, and posting the article online, provided that the original article is credited.”

Retrieved from <https://www.jneurosci.org/content/rights-permissions> on 14.11.2021.

Evaluating Visual Cues Modulates Their Representation in Mouse Visual and Cingulate Cortex

Alexandra Wal,^{2,3} Frederike Johanna Klein,²  Gregory Born,^{1,3,4}  Laura Busse,^{1,5} and  Steffen Katzner^{1,2}

¹Division of Neurobiology, Department Biology II, LMU Munich, Martinsried 82152, Germany, ²Werner Reichardt Centre for Integrative Neuroscience, University of Tübingen, Tübingen 72076, Germany, ³Graduate Training Centre of Neuroscience, International Max Planck Research School, Tübingen 72076, Germany, ⁴Graduate School of Systemic Neuroscience, LMU Munich, Martinsried 82152, Germany, and ⁵Bernstein Centre for Computational Neuroscience Munich, Martinsried 82152, Germany

Choosing an action in response to visual cues relies on cognitive processes, such as perception, evaluation, and prediction, which can modulate visual representations even at early processing stages. In the mouse, it is challenging to isolate cognitive modulations of sensory signals because concurrent overt behavior patterns, such as locomotion, can also have brainwide influences. To address this challenge, we designed a task, in which head-fixed mice had to evaluate one of two visual cues. While their global shape signaled the opportunity to earn reward, the cues provided equivalent local stimulation to receptive fields of neurons in primary visual (V1) and anterior cingulate cortex (ACC). We found that mice evaluated these cues within few hundred milliseconds. During this period, ~30% of V1 neurons became cue-selective, with preferences for either cue being balanced across the recorded population. This selectivity emerged in response to the behavioral demands because the same neurons could not discriminate the cues in sensory control measurements. In ACC, cue evaluation affected a similar fraction of neurons; emerging selectivity, however, was stronger than in V1, and preferences in the recorded population were biased toward the cue promising reward. Such a biased selectivity regime might allow the mouse to infer the promise of reward simply by the overall level of activity. Together, these experiments isolate the impact of task demands on neural responses in mouse cerebral cortex, and document distinct neural signatures of cue evaluation in V1 and ACC.

Key words: behavior; mouse vision; prefrontal cortex; task-dependent modulation; visual cortex

Significance Statement

Performing a cognitive task, such as evaluating visual cues, not only recruits frontal and parietal brain regions, but also modulates sensory processing stages. We trained mice to evaluate two visual cues, and show that, during this task, ~30% of neurons recorded in V1 became selective for either cue, although they provided equivalent visual stimulation. We also show that, during cue evaluation, mice frequently move their eyes, even under head fixation, and that ignoring systematic differences in eye position can substantially obscure the modulations seen in V1 neurons. Finally, we document that modulations are stronger in ACC, and biased toward the reward-predicting cue, suggesting a transition in the neural representation of task-relevant information across processing stages in mouse cerebral cortex.

Introduction

Goal-directed behavior, such as standing in line for a restaurant table, relies on cognitive processes allowing us to recognize the current situation, evaluate the costs and benefits of potential actions, and eventually decide on a specific course of action, here, keep standing or move on. The neural signals reflecting such cognitive processes are often studied in parietal (Shadlen and Kiani, 2013; Hanks et al., 2015; Goard et al., 2016; Licata et al., 2017; Krumin et al., 2018; Pho et al., 2018) and frontal areas of cerebral cortex (Duan et al., 2015; Hanks et al., 2015; Goard et al., 2016; Kim et al., 2016; Murray and Rudebeck, 2018; Pho et al., 2018), yet they can have widespread impact, reaching down to the earliest stages of cortical sensory processing (Chen et al., 2008; Briggs et al., 2013; Saleem et al., 2018). Measuring how

Received July 14, 2020; revised Feb. 12, 2021; accepted Feb. 17, 2021.

Author contributions: A.W., F.J.K., and G.B. performed research; A.W., F.J.K., G.B., and L.B. edited the paper; L.B. and S.K. designed research; S.K. analyzed data; S.K. wrote the paper.

This work was supported by a Starting Independent Researcher grant from the European Research Council awarded to S.K. (281885 PERCEPT) and by funds awarded to the Centre for Integrative Neuroscience within the framework of the German Excellence Initiative (DFG EXC 307). G.B. was supported by Deutsche Forschungsgemeinschaft grant DFG BU 1808/5-1. We thank Agne Klein (nee Vaiceliunaite) and Petya Georgieva for help with the experiments.

F. J. Klein's present address: Ernst Strüngmann Institute for Neuroscience, Frankfurt, Germany.

The authors declare no competing financial interests.

Correspondence should be addressed to Steffen Katzner at steffen.katzner@lmu.de.

<https://doi.org/10.1523/JNEUROSCI.1828-20.2021>

Copyright © 2021 the authors

cognition affects sensory responses is essential to understand how the same physical stimulus can give rise to different percepts.

Cognition has long been known to shape responses of visual neurons; its impact has most elegantly been demonstrated in nonhuman primates, where the level of behavioral control remains unmatched. Excellent examples are studies on covert attention (for review, see Maunsell, 2015; Moore and Zirnsak, 2017), where monkeys are trained to direct, without moving their eyes, attention to a visual stimulus. Attentional effects are then isolated by comparing conditions with identical sensory stimulation, levels of engagement, task difficulty, and behavioral responses. How cognition influences early vision is increasingly studied in the mouse (Gavornik and Bear, 2014; Zhang et al., 2014; Poort et al., 2015; Wimmer et al., 2015; Fiser et al., 2016; Goard et al., 2016; Henschke et al., 2020; Speed et al., 2020); turning to the mouse brings powerful genetic tools, but reaching a level of behavioral control strong enough to isolate cognition is a challenge. A standard paradigm for mice is the Go/No-go task with head fixation, where the mouse is required to respond to a specific stimulus, and withhold the response to other stimuli (e.g., Andermann et al., 2010; Histed et al., 2012; Lee et al., 2012; Glickfeld et al., 2013; Goard et al., 2016; Montijn et al., 2016; Ramesh et al., 2018; Neske et al., 2019). These tasks have the advantage that mice can learn them in reasonable time. However, if the animal's behavioral report, or the sensory drive provided by each stimulus, grossly differs between Go and No-go conditions, it can be difficult to isolate neural signatures of cognition. Any such efforts can be further complicated by the fact that rodents perform eye movements when viewing visual stimuli (Sakatani and Isa, 2007; Wallace et al., 2013; Samonds et al., 2018).

Here, we focus on one cognitive process, evaluating visual cues, and study how this process affects stimulus representations in V1 and ACC of the mouse. We trained mice to engage in goal-directed behavior, where the commitment to a potentially rewarding action had to rely on visual cues. These cues differed in terms of global shape but provided equivalent stimulation to locally confined receptive fields (RFs) in cortex. Under equivalent visual stimulation, with controlled locomotion behavior and matched eye positions, we found that, during cue evaluation, about one-third of V1 neurons responded more strongly to one or the other of the two locally identical visual cues, and their preferences were evenly split. In ACC, cue evaluation affected activity in a similar fraction of neurons; here, however, the effect was substantially stronger and preferences in the recorded population were biased in favor of the cue promising reward. Together, these results reveal distinct signatures of cue evaluation in mouse visual and cingulate cortex.

Materials and Methods

We used 19 mice (3–4 months old, 11 males and 8 females): 9 of the C57BL/6J WT strain and 10 of the PV-Cre strain *B6;129P2-Pvalbtm1 (cre)Arbr/J* (JAX stock #008069). All procedures were conducted in compliance with the European Communities Council Directive 2010/63/EC and the German Law for Protection of Animals; they were approved by the local authorities following appropriate ethics review.

Surgical protocol. Anesthesia was induced with isoflurane (3%) and maintained throughout the surgery (1.5%). A small S-shaped aluminum headpost was attached to the anterior part of the skull (OptiBond FL primer and adhesive, Kerr dental; Tetric EvoFlow dental cement, Ivoclar vivadent); two miniature screws (00-96 × 1/16 stainless-steel screws, Bilaney) were implanted over the cerebellum serving as reference and

ground for electrophysiological recordings. Before surgery, an analgesic (buprenorphine, 0.1 mg/kg s.c.) was administered, and the eyes were protected with ointment (Bepanthen). The animal's temperature was kept at 37°C via a feedback-controlled heating pad (WPI). Antibiotics (Baytril, 5 mg/kg s.c.) and a longer-lasting analgesic (Carprofen, 5 mg/kg s.c.) were administered for 3 d after surgery. Mice were given 7 days to recover before they were habituated to the experimental setup. Before electrophysiological recordings, a craniotomy (1.5 mm²) was performed over V1 (3 mm lateral to the midline, 1.1 mm anterior to the transverse sinus) (Wang et al., 2011) or ACC (0.3 mm lateral to the midline, 0.2 mm anterior to bregma) (Zhang et al., 2014). The craniotomy was sealed with Kwik-Cast (WPI), which was removed and reapplied before and after each recording session.

In PV-Cre mice, we expressed channelrhodopsin (ChR2) by injecting the adeno-associated viral vector rAAV5.EF1a.DIO.hChR2(H134R)-EYFP.WPRE.hGH (Penn Vector Core, University of Pennsylvania). The vector was injected through a small craniotomy into V1 of anesthetized mice. We used a Picospritzer III (Parker) to inject the virus at multiple depths while gradually retracting the pipette. We expressed ChR2 to identify, in our recorded population, inhibitory interneurons (Kvitsiani et al., 2013). The number of identified interneurons was too small, however, to provide a substantial contribution to this report.

Histology. Histologic reconstructions were used to verify recording sites from ACC. Before recording from ACC, electrodes were coated with a yellow-shifted fluorescent lipophilic tracer (DiI; DiI18(3), Invitrogen). After recordings were terminated, mice were perfused transcardially and the brain was fixed in a 4% PFA/PBS solution for 24 h, before being stored in PBS. Brains were sliced at 50 μm using a vibratome (Microm HM 650 V, Thermo Scientific), mounted on glass slides with Vectashield DAPI (Vector Laboratories), and coverslipped. Slides were inspected for blue DAPI and yellow DiI using a fluorescent microscope (Zeiss Imager.Z1m).

Experimental setup and visual stimulus. Mice were put on an air-suspended Styrofoam ball ($n = 11$) or a mounted plastic disk ($n = 8$) and head-fixed by clamping their headpost to a rod. Movements of the ball were recorded at 90 Hz by two optical mice connected to a microcontroller (Arduino Duemilanove); disk rotation was measured with a rotary encoder sampling at 100 Hz (MA3-A10-125-N Magnetic Encoder, Pewatron). A computer-controlled syringe pump (Aladdin AL-1000, WPI) delivered precise amounts of water through a drinking spout, which was positioned in front of the animal's snout. The drinking spout was present only during the foraging task experiments and was removed during measurements in sensory control conditions. Eye movements were monitored under infrared illumination using a zoom lens (Navitar Zoom 6000) coupled to a camera (Guppy AVT, frame rate 50 Hz). The setup was enclosed with a black fabric curtain. Visual stimuli were generated with custom-written software (<https://sites.google.com/a/nyu.edu/expo/home>) and presented on an LCD monitor (Samsung 2233RZ, display size 47 × 30 cm, refresh rate 120 Hz, mean luminance of 50 cd/m²). The monitor was positioned 20–25 cm from the animal's eyes at an angle of 15–40 degrees, relative to the mouse AP axis. Luminance nonlinearities of the display were corrected with an inverse γ lookup table, which was regularly obtained by calibration with a photometer. Stimuli were downward-drifting sinusoidal gratings at 50% contrast. Temporal frequency was 1.5 Hz, spatial frequency 0.02–0.05 cycles/degree. Gratings were 40–55 degrees diameter in size, and framed by either a black square or diamond.

Behavioral training. After recovery from the surgery, mice were placed on a water restriction schedule until their weight dropped to ~85% of their *ad libitum* body weight. During this time, mice were habituated to head fixation on the ball or disk and delivery of water through the spout. The animals' weight and fluid consumption were monitored and recorded on each day, and the mice were checked for potential signs of dehydration. After the weight had stabilized, the mice were trained in daily sessions on the visual task. Training sessions were typically performed 5 d a week. On days without training, mice received water supplementation of 25 ml/kg body weight.

Electrophysiological recordings. After mice had learned the task, extracellular recordings were performed with 32-channel linear silicon

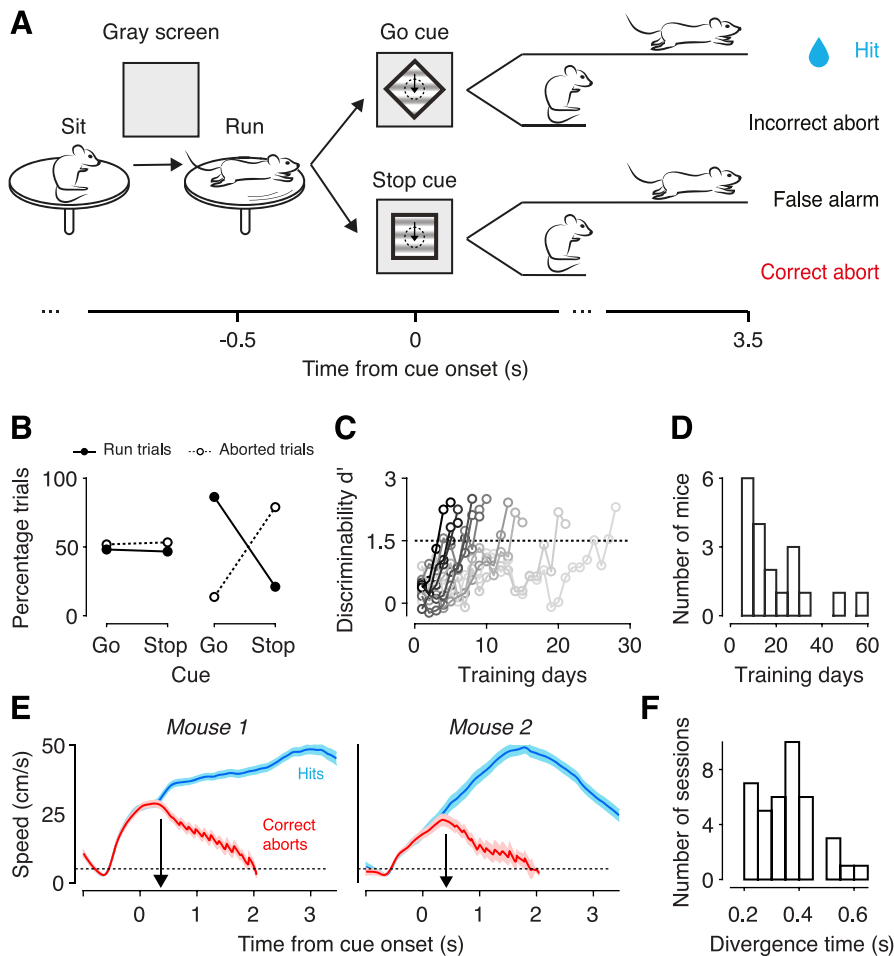


Figure 1. Behavioral task and performance. **A**, Schematic of the behavioral task. Mice were head-fixed using an implanted headpost (not shown). Running for 0.5 s above a speed threshold of 5 cm/s triggered the presentation of one of two visual cues that were identical, except for their overall shape, and were positioned such that they covered multiple RFs (dotted circle) of V1 neurons. Arrows indicate drift direction of the grating. By extending the run for 3.5 s in response to the Go cue, the mouse could earn a fluid reward (hit). By slowing down in response to the Stop cue, the mouse could terminate the current trial (correct abort) and initiate a new trial. The cue was presented until the end of a trial. **B**, Behavioral performance for 1 example mouse (M85) during an early (left) and late training stage (right). **C**, Learning curves of 10 example mice. Mice were considered trained when $d' \geq 1.5$ for 2 consecutive sessions. **D**, Summary of training sessions across our sample of mice ($n = 19$). **E**, Trial-averaged speed traces for hits (blue) and correct aborts (red) aligned to the presentation of the cue, from a single session of 2 trained mice (M312; M323). Shaded area represents SEM. Dashed lines indicate running speed threshold. Arrows indicate the point in time, at which the two traces significantly diverged (left: 365 ms; right: 414 ms). **F**, Summary of running speed divergence times across all sessions, in which we measured neural responses during task performance ($n = 42$ sessions from 13 mice).

probes (Neuronexus, A1x32-5 mm-25-177-A32). Electrodes were inserted perpendicular to the brain surface and lowered to $\sim 800 \mu\text{m}$ (V1) or $1200 \mu\text{m}$ (ACC) below the surface. Wideband extracellular signals were digitized at 30 kHz (Blackrock Microsystems) and analyzed using the NDManager software suite. To isolate single neurons from linear arrays, we grouped adjacent channels into 5 equally sized “virtual octrodes” (8 channels per group with 2 channels overlap). Using an automatic spike detection threshold (Quiroga et al., 2004), spikes were extracted from the high-pass filtered continuous signal for each group separately. The first three principal components of each channel were used for automatic clustering with KlustaKwik (K. D. Harris, <http://klusta-team.github.io/klustakwik>), which was followed by manual refinement of clusters (Hazan et al., 2006). For the analyses of neural data, we only considered high-quality single-unit activity, judged by rate stability, distinctiveness of spike wave shape, and cleanness of the refractory period in the autocorrelogram. In our final set of neurons, overall firing rates were distributed according to a log-normal distribution (Buzsaki and Mizuseki, 2014). Only 0.14% (median) of single-unit waveforms violated a refractory period of 2 ms. The median rate of interspike interval

violations was 0.15, computed for an assumed refractory period of 2 ms and reflecting the relative firing rate of hypothetical neurons generating these violations (Hill et al., 2011). Overall cluster quality was assessed by fitting separate Gaussian mixture models in principal component analysis space between all pairs of units (Hill et al., 2011) on our “virtual octrodes,” which revealed a median summed false positive rate of 0.14 (probability that a waveform assigned to cluster 1 was generated by cluster 2), and a median summed false negative rate of 0.08 (probability that a waveform assigned to cluster 2 was generated by cluster 1).

RF mappings and orientation tuning. We mapped RFs of V1 neurons with a sparse noise stimulus, consisting of 5 degree, full-contrast black and white squares, which were flashed on a gray background for 150 ms at a random location on a virtual 12×12 grid. Neural responses were fitted with 2D Gaussians to determine RF center, separately for ON and OFF subfields (Liu et al., 2010). To guide the placement of the stimuli, we estimated RF parameters online, relying on threshold crossings of spiking activity at each recording channel. Stimuli were then positioned to cover as many RFs as possible. For the analyses shown in Figure 4A, we considered RFs as well defined if the 2D Gaussian explained at least 30% of the variance in the neural response.

We computed orientation tuning curves by fitting a sum of two Gaussians of the same width with peaks 180 degrees apart (Jurjut et al., 2017). For the analysis shown in Figure 4B, we considered neurons well tuned if the sum of Gaussians explained at least 50% of response variance.

Current source density (CSD) analysis. As described by Jurjut et al. (2017), we computed the CSD from the second spatial derivative of the local field potential (Mitzdorf, 1985) in response to periodic visual stimulation. We smoothed the CSD in space using a triangular kernel (Nicholson and Freeman, 1975) and used a value of 0.4 S/m as measure of cortical conductivity (Logothetis et al., 2007) to approximate the CSD in units of nanoamperes per cubic millimeter. We assigned the contact closest to the earliest polarity inversion to the base of layer 4 (Schroeder et al., 1998). The remain-

ing contacts were assigned to putative supragranular, granular, and infragranular layers based on a cortical thickness of 1 mm and anatomic measurements of the relative thickness of individual layers in mouse V1 (Heumann et al., 1977).

Behavioral task. We successfully trained $n = 19$ mice on the cue evaluation task shown in Figure 1A. For $n = 12$ mice, the diamond was the Go cue and the square the Stop cue; for the remaining mice ($n = 7$), this assignment was reversed. The cues were presented in a randomized sequence. After keeping still for at least 80 ms, the mice could trigger cue onset by running for a duration of 500 ms above a speed threshold of 5 cm/s, during which a mean-luminance gray screen was shown. The Go cue signaled a delayed fluid reward (5 μl), which the mouse could earn by continuing to run above threshold for an additional 3.5 s. Running in response to the Stop cue was not rewarded; therefore, the most economical action for the mouse was to terminate such trials by stopping, and immediately initiate a new trial. Cues were present until a trial was correctly or incorrectly terminated. To measure V1 activity in the absence of visual stimulation, running triggered, on a fraction of trials, a mean-

luminance gray screen without any cue. A single session consisted of 300–600 trials divided into blocks of 100 trials; diamond, square, and blank screen appeared on 43%, 43%, and 14%, respectively, of all trials.

Because trials were actively initiated by the mouse, the interstimulus intervals were variable. After a hit, mice took some time to consume the reward before they initiated a new trial (median interstimulus interval: 8.3 s, interquartile range: 3.6 s, minimum: 4.2 s, $n = 2173$ trials from 63 experiments). After correct aborts, in contrast, mice initiated trials more quickly, but the interstimulus interval never fell below 1 s (median: 2.3 s, interquartile range: 1.5 s, minimum: 1.1 s, $n = 1445$ trials).

Sensory control measurements. After the mice had completed all task blocks, we ran a sensory control condition, in which a periodic sequence of the stimuli was shown, independent of the animals' behavior. To set apart this sensory control condition, the mice could not initiate a trial by running. Instead, the stimuli were simply flashed in a randomized, periodic sequence. Each stimulus was shown for 2 s, followed by a 1 s presentation of a mean-luminance gray screen. No reward was given during these controls. To further emphasize the difference to the task condition, the lick spout was removed. Analogous to the task condition, we showed, on a fraction of trials, a mean-luminance gray screen without any stimulus. Sensory control experiments consisted of 100–500 trials; square, diamond, and blank screen appeared on 40%, 40%, and 20%, respectively, of all trials.

Measurements of eye position. We detected the pupil with a custom-written program developed with the Bonsai framework (Lopes et al., 2015). Briefly, we applied a threshold to turn each camera frame into a binary image, performed a morphologic opening operation, identified the most circle-like object as the pupil, and fitted a circle to determine the position of its center. We computed relative pupil displacements by subtracting, for each frame, the pupil position from a default position, defined as the grand average eye position across all stimuli and task conditions. To convert pupil displacements to angular displacements, we assumed that the center of eye rotation was 1.041 mm behind the pupil (Stahl et al., 2000). We defined saccades as changes in eye position ≥ 2 degrees. Considering that the average mouse saccade lasts 50 ms (Sakatani and Isa, 2007), we detected saccades by taking the difference of mean eye position 60 ms before and after each time point.

Measurements of locomotion. For the air-suspended ball, running speed was computed as the Euclidean norm of three perpendicular components (roll, pitch, and yaw) of ball velocity (Dombeck et al., 2007). For the running disk, we converted deg/s to cm/s by considering the radius from the center of the mouse to the center of the disk, which typically was between 5 and 6 cm.

Experimental design and statistical analysis. We relied on the open-source framework DataJoint for creating data analysis pipelines (Yatsenko et al., 2018) and the R project for statistical analysis (R Core Team, 2017). We used a within-subject (i.e., repeated-measures) design, such that every mouse participated in each condition (visual task, sensory control measurements). Neural data were also collected within subjects; that is, responses of each neuron were measured under all behavioral conditions. Where appropriate, we therefore performed within-subject ANOVAs, or tests relying on dependent samples. Details of the statistical procedures, and sample sizes are described in the following subsections.

Running behavior. For each session of each mouse, we extracted run-speed profiles for individual trials and aligned them to stimulus onset to identify and exclude invalid trials, in which task engagement might have been suboptimal. For aborted trials, we took as termination time the point in time, relative to stimulus onset, where running speed dropped below the threshold of 5 cm/s, and considered trials invalid if termination time was faster than 500 ms (13.6% of 5253 trials) or slower than 2 s (9.0%). We also considered a trial invalid if its running speed profile differed markedly from the average profile across trials of the same type (i.e., across all hits, or all correct aborts). It “differed markedly” if the maximum running speed within 500 ms after stimulus onset was lower than the mean across trials \times SEM. The factor x varied across mice and sessions and ranged from 2 to 5, excluding 1.8% of the trials. After removing invalid trials, we then determined, for hits and correct aborts, the period of stimulus presentation, during which running

speed was indistinguishable. We compared distributions of running speed at every point in time, and took as “point of speed divergence” the first of three consecutively significant time points (Kolmogorov–Smirnov test, $p < 0.01$).

Behavioral discrimination performance. To quantify and track behavioral performance, we computed, from hits and false alarm rates, a discriminability index d' , defined as $Z_N - Z_{SN}$, after $Z_N = 1 - p(\text{false alarm})$ and $Z_{SN} = 1 - p(\text{hit})$ were turned into z scores using the inverse of the cumulative normal distribution (Gescheider, 1997). In case of extreme performance levels (hits or false alarm rates of 0 or 1), we computed d' using the log-linear approach described by Stanislaw and Todorov (1999). We considered mice as trained, if d' across task blocks was ≥ 1.5 for at least 2 consecutive days. From trained mice, we only considered neural responses, eye positions, or speed profiles that were measured in task blocks where $d' \geq 1.5$.

Eye position. For each session and each mouse, we extracted eye positions for individual trials and aligned them to stimulus onset. Within each session's time window of constant running speed (based on the speed divergence times shown in Fig. 1F), we removed trials containing saccades and then determined, for each trial, the average eye position across time. We compiled 2D (horizontal, vertical) distributions of eye positions, separately for each stimulus and task condition. We matched the number of trials across conditions in each eye position bin by finding the smallest number of trials across conditions and deleting, where necessary, excess trials from the corresponding bin in the other three conditions. By matching the number of trials, we made sure that we removed any potential bias in terms of eye position across all task and sensory control conditions. We varied bin width across mice and sessions from 1.4 to 6.4 degrees, with the exception of a single session in 1 mouse, where bin width was 19.2 degrees. We chose bin widths to maximize the number of surviving trials under the constraint that the resulting distributions of eye positions were statistically indistinguishable across stimulus and task conditions ($p \geq 0.1$). Statistical testing, however, was then performed on raw eye positions (i.e., without any binning). To assess statistical significance, we compared all four distributions of eye positions using the multisample variant of the nonparametric Anderson–Darling test (Scholz and Stephens, 1987). This is an omnibus test (i.e., it provides a single test statistic to assess whether multiple distributions differ from each other). Sessions for which $p < 0.1$, or the number of surviving trials < 10 , were considered “unmatchable” and excluded from the analyses of V1 responses (13 of 25 sessions, see Fig. 2G). After matching eye positions, the mean number of trials per condition was 28.75 ± 3.8 , averaged across sessions. To assess statistical significance of mean saccade rates (see Fig. 2C), we performed a repeated-measures ANOVA, including the within-subject factors task condition (task vs sensory control) and stimulus type (Go vs Stop).

Neural data. We obtained neural data during task performance from $n = 13$ mice in 42 sessions. In 9 mice (25 sessions), we recorded spiking activity in area V1. Sessions for which we were unable to match eye positions were excluded from further analyses, resulting in a final V1 dataset of 5 mice (12 sessions). In these sessions, we recorded 411 single neurons. We computed single-trial firing rates by convolving spike trains with a Gaussian kernel (resolution 1 ms, width 70 ms). We first identified neurons that were visually responsive: we compared, across trials, time-averaged firing rates in 5 ms bins between stimulus and blank screen conditions and considered a neuron visually responsive if its response to a stimulus, during task and sensory control, was significantly larger than its response to the blank screen in at least 10 consecutive bins within a window of 1 s (Wilcoxon rank sum test, $p < 0.05$). Of $n = 264$ visually driven neurons, we only included those for which we had at least 10 trials per stimulus and task condition after matching eye positions ($n = 247$). To quantify how well each neuron could discriminate the stimuli, we performed ideal observer analyses (Macmillan and Creelman, 2005), separately for task and sensory control conditions. We split single-trial firing rates based on stimulus type, focused on the time window where running speed was indistinguishable during task performance, averaged across time, and determined the area under the receiver operating characteristic (area under the curve [AUC]). To assess statistical significance, we repeated 1000 times the random selection of

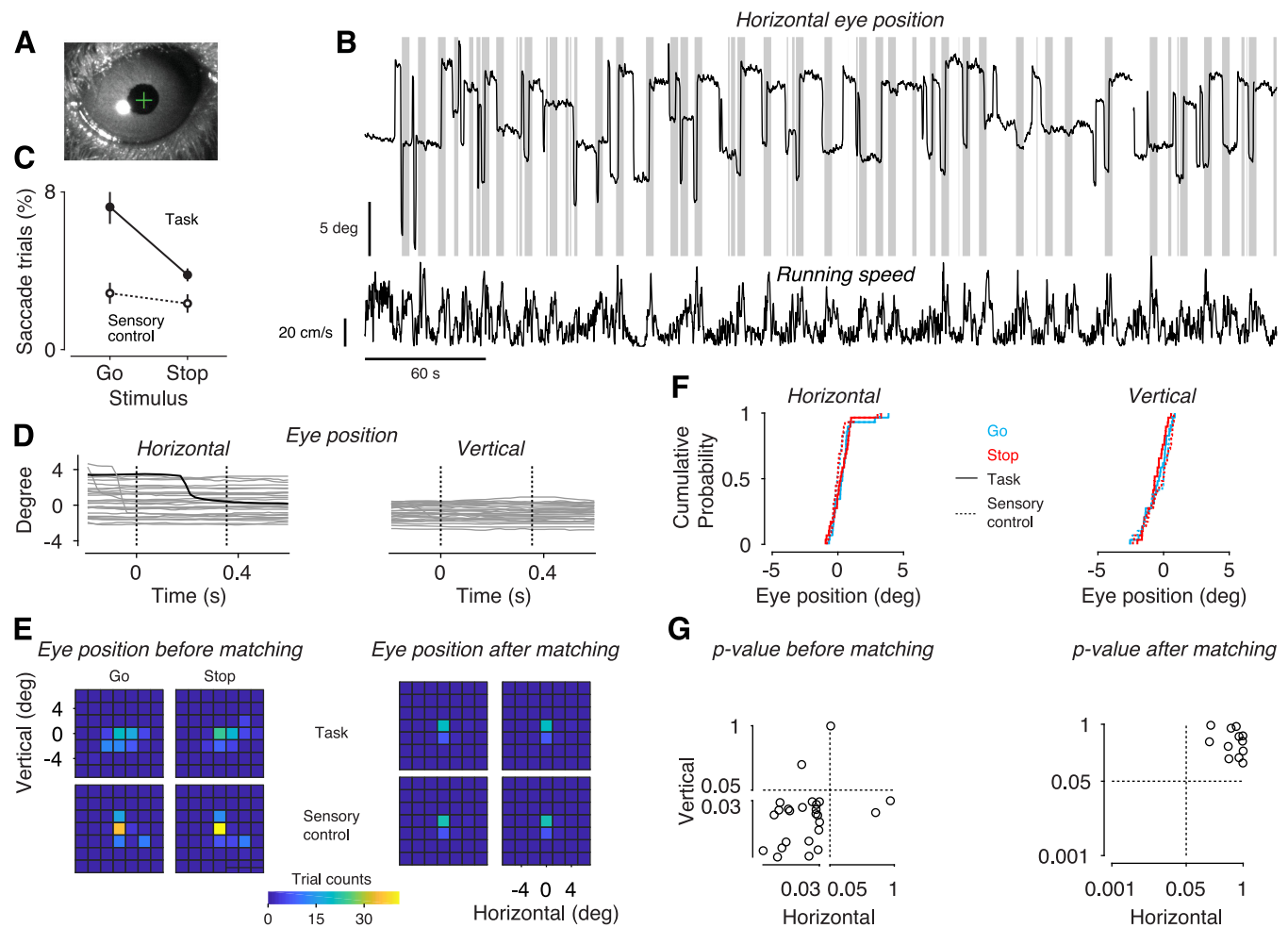


Figure 2. Eye movements occurred frequently and varied systematically across behavioral conditions; differences across conditions were eliminated by selecting subsets of trials with matched eye positions. **A**, Example image acquired by the eye-tracking camera. White spot represents cornea reflection of infrared LED. Green cross represents estimate of pupil center. **B**, Top, Horizontal eye position recorded in one example session. Gray bars represent time periods during which a cue was presented on the screen. Bottom, Running speed. In a small fraction of trials, stimulus presentation was omitted even if the speed threshold was crossed (blank screen trials to assess visual responsiveness). **C**, Average percentage of trials with at least one saccade, during task and sensory control condition, separately for the two stimuli ($n = 42$ sessions from 13 mice). Saccade activity was determined during the time window of equal running speed. Error bars indicate SEM after accounting for variability across sessions (Loftus and Masson, 1994). **D**, Single-trial eye positions during task performance, relative to the presentation of the cue (time 0). Black trace represents a trial with a saccade. Dotted vertical lines span the time period of cue evaluation in this session, during which running speed was indistinguishable. **E**, 2D histograms of eye positions shown in **D**, binned after removing saccades and averaging across the time window of constant running speed; bin width 2 degrees. Left, Number of trials as a function of eye position for each combination of stimulus and task condition. Right, Same, after matching eye positions by randomly deleting excess trials. **F**, Cumulative distributions, without binning, of horizontal (left) and vertical (right) eye positions after matching, for each stimulus and task condition. The four distributions in each panel are statistically indistinguishable (Anderson–Darling omnibus test, $p > 0.1$). **A**, **B**, **D–F**, Mouse M85, session 62. **G**, Summary, across all sessions. Each session's omnibus p value summarizes the statistical significance of any difference between the four distributions. Left, Before matching ($n = 25$ sessions from 9 mice), in which we recorded from V1. Right, Subset of sessions that survived eye position matching ($n = 12$ sessions from 5 mice).

trials by eye position matching and created, for each neuron, a distribution of AUC values. We took the mean AUC across repeats as measure of neural discriminability and considered it significant if chance performance (0.5) was outside the central region of the CI. In the sensory control condition, our criterion was lax: We used a 90% CI to catch neurons that showed any trend toward differential responses. Using a lax criterion was important because we wanted to make sure that the neurons we examined responded in the same way to stimulation of their classical and extraclassical RFs. In the task condition, our criterion was conservative: we used a 99% CI to identify those neurons that could reliably discriminate the stimuli. Based on these statistics, we excluded neurons that could discriminate the stimuli in the sensory control condition, and asked how many of the remaining, nonselective, neurons ($n = 115$) could discriminate the stimuli within the context of the task.

Although we selected neurons based on their AUC value in the sensory control condition, and then reassessed AUCs during task performance, our observed effects cannot be reduced to the statistical phenomenon known as “regression to the mean” (e.g., Barnett et al.,

2005). By requiring that neurons could not discriminate the stimuli during the sensory control, we selected those neurons whose AUC values were very close to the overall population mean, which was at 0.51. If they then showed any significance during the task, they actually “regressed away” from the population mean (see, e.g., Fig. 3G,H). We also tested for regression-to-the-mean effects at the level of individual neurons. We took the V1 neurons that could not discriminate the stimuli during the control condition ($n = 115$; Fig. 3H), split the dataset into odd and even trials, and computed AUC values for each subset of trials. Reassuringly, AUC values that were nonsignificant for the subset of even trials remained so for the subset of odd trials, and vice versa. In stark contrast, comparing the subsets of even trials from sensory control and task condition still revealed significant task-related modulation in 25 of 115 neurons. A similar fraction (21 of 115) showed task-dependent modulation when we compared the odd trials from the sensory control and task conditions. A smaller fraction overall, with these control analyses, is to be expected, given the reduction in power that comes with using only half of the trials. Together, these control analyses show that the task-

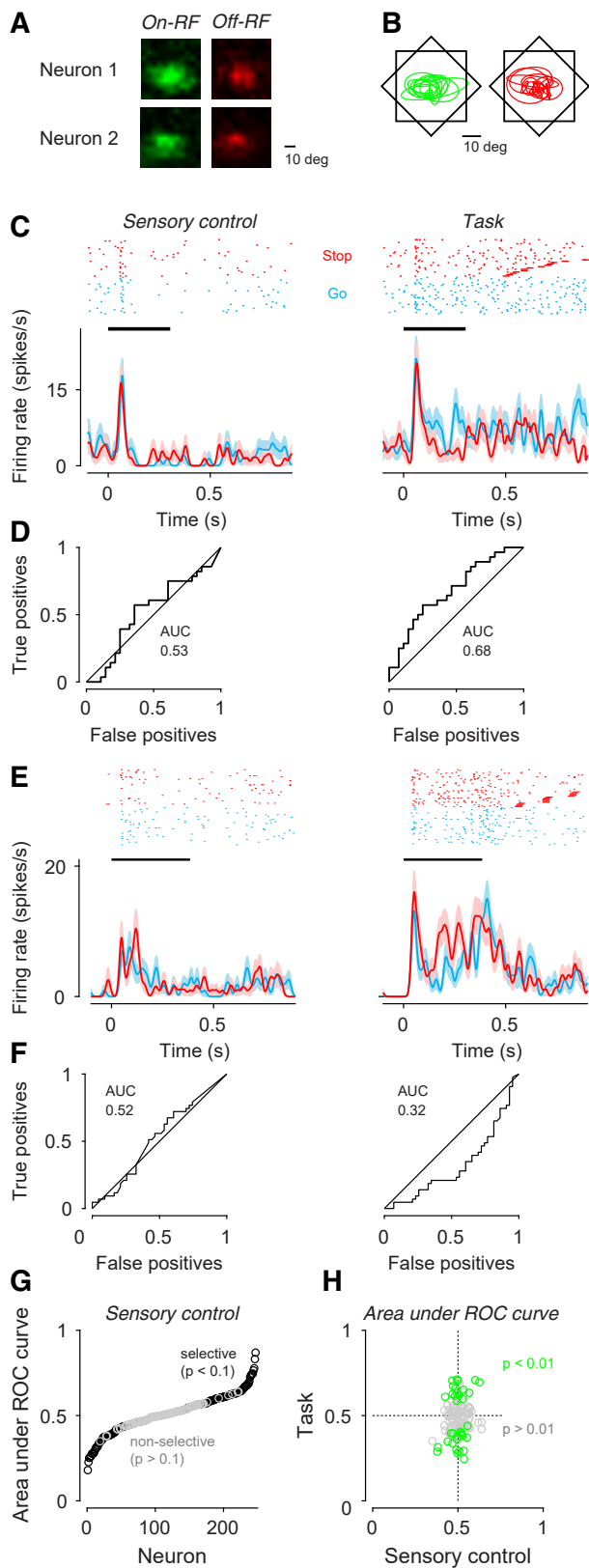


Figure 3. Cue evaluation can modulate responses of V1 neurons to locally identical visual stimulation. **A**, ON and OFF RF subregions for two example V1 neurons. **B**, RF contours of simultaneously recorded V1 neurons in one example session ($n = 14$); stimulus outlines are drawn in black. **C**, Spike rasters and density functions in response to the Go (blue) and Stop stimulus (red) for one example neuron (M127-78-28) measured in the sensory control (left) and task condition (right). Thick marks in task raster represent end of trial. Black horizontal bar represents time window used for the analyses of neural data, defined by the period during which running speed in the task was indistinguishable. **D**, ROC curves quantifying how

dependent modulations we observed are not simply a statistical artifact introduced by taking two successive measurements from the same neuron.

To assess how strongly eye position matching contributed to our result, we reran our analyses of discriminability by randomly selecting subsets of trials, but independent of eye position. Everything else was kept identical, including the trial numbers and the computation of AUC values. Using identical trial numbers was important because it rules out that any changes in variability might be related to an unequal number of trials. To compare counts of significant neurons between matched and nonmatched datasets, we used a χ^2 test. To assess the variability of single-neuron AUC distributions, we determined their SDs and compared distributions of SDs between matched and nonmatched datasets using a two-sample Kolmogorov–Smirnov test.

Because of a bug in the stimulus presentation program, the phase of the gratings during sensory control measurements was shifted by 90 degrees, relative to the phase of the stimuli during the cue evaluation task. We therefore repeated all analyses by shifting the time window in the sensory control condition, such that the stimulus phases were identical across conditions. The results were essentially the same and the conclusions unaffected: With matched eye positions, the number of cells that could discriminate during the task was 30.07% (16.99% responded more strongly to the Go stimulus, 13.07% more strongly to the Stop stimulus). Without matching, this percentage dropped to 9.8% (5.88% responded more strongly to the Go stimulus, 3.92% more strongly to the Stop stimulus). The drop in percentages was highly significant ($p < 0.00001$, χ^2 test), and the SDs of single-neuron AUC distributions were smaller under matched than unmatched eye positions ($p < 0.00001$, two-sample Kolmogorov–Smirnov test).

To test whether the results observed in V1 might be caused by changes in spatial integration because of running, we focused on the sensory control condition, in which mice showed variability in running behavior. For each trial, we computed the mean speed in a time window of 0.5 s after stimulus onset, and determined whether the mouse was running (speed > 1 cm/s) or stationary (speed ≤ 1 cm/s). Where possible, we split trials based on running behavior, and drew 1000 times, without replacement, random subsets of trials. For each neuron, we compiled distributions of AUC values, separately for running versus sitting. We considered a neuron's discriminability to be affected by running if the mean AUC value for running was outside the central 95% of the AUC distribution for sitting.

In 3 mice (14 sessions), we recorded spiking activity from ACC. During ACC recordings, we did not track eye positions; all other aspects of task structure and analyses were kept identical to the V1 recordings described above. We excluded neurons with < 1 spike/s and bootstrapped CIs for AUC values ($n = 1000$ replications). If many ACC neurons showed visual responses that were sensitive to differences in eye positions, we might have underestimated the number of neurons that can discriminate the stimuli during the task, just as in V1 with unmatched eye positions. We also tested whether stratifying V1 data by matching eye positions introduced a bias in terms of a specific brain state or arousal level. We examined two prominent proxies for brain state: pupil size and spectral content of the local field potential. We found that both were largely similar between trials with matched and unmatched eye positions. These analyses confirmed that matching for eye positions in V1 recordings did not select for a specific brain state, and justify the comparison of V1 to ACC recordings, where responses were not stratified by eye position.

←
 well this neuron could discriminate Go and Stop stimuli during the sensory control (left) and task condition (right). **E**, **F**, Same, but for a second example neuron (M85-56-8). **G**, Population summary of AUC values during sensory control condition. Neurons showing any trend toward differential responses ($p < 0.1$) are excluded from further analyses (black data points, $n = 132$). Gray represents nonselective neurons ($n = 115$). **H**, Discrimination performance (AUC) of nonselective neurons (gray data points in **G**) during task performance. Green represents neurons that can reliably discriminate the cues ($p < 0.01$) ($n = 35$).

Results

To isolate how visual processing is modulated by behavioral demands, we designed a task, in which mice had to evaluate visual cues to decide on an appropriate action (Fig. 1). We placed head-fixed mice on a treadmill in front of a monitor, where they could harvest a reward by running in response to one, but not the other, of two visual cues (Fig. 1A). The cues had different global shapes (diamond vs square), such that they could be discriminated by the mice, but they were composed of the same, downward-drifting grating to provide identical visual stimulation to neurons targeted for recordings in visual cortex. The mice initiated each trial by moving forward on the treadmill, which triggered the presentation of a randomly selected cue. One cue (Go) promised a fluid reward, which the mouse could earn by continuing to run for an additional 3.5 s. A 3.5 s run in response to the Go cue was considered a hit; a 3.5 s run in response to the other cue (Stop) was considered a false alarm. At any point in time, the mouse could terminate the current trial by slowing down, and immediately start over; these terminated trials were considered correct or incorrect aborts (Fig. 1A). With this task and stimulus design, we sought to isolate how visual processing is affected by the process of evaluating cues because (1) across cue conditions, the animal's running behavior was identical around the time of cue onset and (2) those neurons, whose classical RFs (Fig. 1A, dotted circles) were contained within the stimulus aperture, should receive equivalent visual stimulation. Which of those neurons indeed received equivalent visual signals was determined in a sensory control condition, in which we flashed the same stimuli in a randomized, periodic sequence, unrelated to the animals' behavior. In this condition, the mice were not engaged: they could not control the onset of a cue, nor could they earn rewards by running.

After a few training sessions, mice had learned to discriminate the cues and earn rewards (Fig. 1B–D). Naive mice performed at chance level (Fig. 1B, left). Trained mice, in contrast, achieved high hit rates and low false alarm rates (right). From hit and false alarm rates, we computed d' (Gescheider, 1997) to quantify and track behavioral performance (Fig. 1C,D). Some mice reached a criterion level of 1.5 within few days (Fig. 1C, dark traces); other mice needed multiple weeks (bright traces). On average, mice reached criterion levels of performance after 18.9 ± 3.3 training days (mean \pm SEM, $n = 19$). Once the mice had learned the task, they showed stereotypical running behavior, which reliably reflected the reward assignments (Fig. 1E,F). Consider, for instance, the 2 example mice shown in Figure 1E. Running above threshold for 0.5 s triggered the onset of the cue (time 0). After presentation of the Go cue, speed remained high or even increased as the mice went for the reward (hit trials, blue traces); after presentation of the Stop cue, in contrast, running speed quickly dropped (correct aborts, red traces).

How long does it take a mouse to evaluate a visual cue and decide on a specific course of action? We took the point in time, at which the speed profiles diverged as an estimate for the duration of this process. We determined, for each individual session, the time window during which running speed was indistinguishable between cue conditions (Fig. 1E,F). We performed these analyses on a subset of 13 mice, from which we recorded neural responses during task performance. Across these recording sessions, behavioral performance remained well above criterion level (mean $d' = 2.82 \pm 0.08$, $n = 42$ sessions). We compiled distributions of running speeds across trials, separately for hits and correct aborts, and compared these distributions at every point in time.

We took as point of speed divergence the first of three consecutive time points, where the distributions of running speed significantly differed (Kolmogorov–Smirnov test, $p < 0.01$). For the two sessions shown in Figure 1E, running speeds were indistinguishable during the first 365 (left) or 414 ms (right) of stimulus presentation. The time points of speed divergence varied across sessions with an average of 347 ± 16 ms (Fig. 1F; $n = 42$ sessions from 13 mice). We took these estimates as a behavioral marker for the average duration of the cue evaluation process, and used them to define the time window of interest for the analyses of cortical responses. Restricting the analyses to this time window also ensured that the two behavioral conditions were comparable in terms of locomotion behavior. Controlling locomotion is important because it can affect sensory responses in the mouse visual system (Niell and Stryker, 2010; Bennett et al., 2013; Saleem et al., 2013; Erisken et al., 2014; Pakan et al., 2016; Dadarlat and Stryker, 2017; Aydın et al., 2018; Clancy et al., 2019; Musall et al., 2019).

We next examined eye movements during cue evaluation and found systematic differences in saccades and eye positions between the cue conditions (Fig. 2). We recorded videos of the eye to track pupil position (Fig. 2A) and observed frequent eye movements (Fig. 2B). They mostly occurred along the horizontal direction and often seemed related to the trial structure (gray vertical bars mark cue presentations). We expected eye movements in our task because mice initiated trials by running (Fig. 2B, bottom), which increases the frequency of eye movements in head-fixed mice (Niell and Stryker, 2010; Keller et al., 2012; Ayaz et al., 2013; Bennett et al., 2013). Because running behavior was comparable during evaluation of Go and Stop cues, we expected eye movements of similar frequencies. However, when we identified saccades and aligned them to cue onset, we found clear differences in saccade frequency between cue conditions: more saccades occurred during the presentation of the Go cue than during the Stop cue, but only during the task (Fig. 2C; $n = 42$ sessions from 13 mice, interaction between cue and task: $F_{(1,41)} = 8.27$, $p = 0.0064$, repeated-measures ANOVA). Follow-up analyses confirmed that, during the task, saccades occurred more often for the Go cue than for the Stop cue (7.1 vs 3.8%, $F_{(1,41)} = 15.48$, $p = 0.00032$). In the control condition, however, the percentage of saccades was indistinguishable (2.8 vs 2.3%, $F_{(1,41)} = 2.71$, $p = 0.11$). In both task and control conditions, saccades were linked to transitions from slowing down to speeding up (data not shown), potentially reflecting intended head movements (Meyer et al., 2020).

To remove any differences in eye position between cue conditions for subsequent analyses of V1 responses, we next identified subsets of trials where eye position was equivalent between all task and sensory control conditions (Fig. 2D–G). For each recording session, we focused on the cue evaluation period where running speed was comparable between the cue conditions (Fig. 1E,F), and matched distributions of eye positions (Roelfsema et al., 1998). We illustrate this procedure for one example session (Fig. 2D–F). First, we removed all trials containing one or more saccades during the cue evaluation window (Fig. 2D, black trace). From the remaining trials (gray), we constructed histograms of time-averaged eye positions, separately for each stimulus in the task and sensory control condition (Fig. 2E, left). We then matched the number of trials in each eye-position bin by finding the minimum number across all four conditions and removing, where necessary, a random selection of excess trials from the other conditions (Fig. 2E, right). To confirm that this matching procedure removed any differences in eye positions, we compared, without binning, their cumulative distributions across all four conditions and found that they were indistinguishable (Fig.

2F, horizontal position: $p=0.77$; vertical position: $p=0.36$; Anderson–Darling test). Applying this procedure to our entire dataset, we found that, before matching, the distributions of eye position differed systematically in every single session (Fig. 2G, left, $n=25$ sessions from 9 mice). In 12 sessions obtained from 5 mice, however, we could match eye positions without falling below a minimum number of 10 trials for each combination of stimulus and task condition (Fig. 2G, right, all $p > 0.1$). These are the sessions with equivalent visual input to the mouse's eye during task performance and in the sensory control condition; we focused on those for the analyses of V1 responses.

Having identified time windows of equal running speed and subsets of trials with equalized visual input reaching the eye, we analyzed how V1 neurons were modulated during cue evaluation (Fig. 3). We first identified those neurons, which could not discriminate the cues in the sensory control condition. To increase our chances that the two cues provided the same visual stimulation we had mapped, at the beginning of each recording session, RFs of the recorded V1 neurons ($n=9$ mice, Fig. 3A) and had positioned the two cues during the task such that they fully covered multiple RFs (Fig. 3B). *Post hoc*, we tested which neurons indeed received comparable stimulation by comparing responses to the cues in the sensory control condition (Fig. 3C–F, left). To quantify whether individual neurons could discriminate between the two cues, we determined how well an ideal observer could decode stimulus identity. We separated single-trial firing rates evoked by Go versus Stop cues, determined mean firing rates during the window of constant running speed (black horizontal bars in Fig. 3C,E), and computed the area under the receiver operating characteristic (AUC) (Macmillan and Creelman, 2005) (Fig. 3D,F, left). To make sure that the magnitude of the AUC value did not depend on the specific subset of trials that survived our eye-position stratification procedure, we repeated random stratification and AUC computation 1000 times, creating, for each neuron, a distribution of AUC values. We took the mean of this distribution as measure of discriminability. To select only those neurons for further analyses that could not discriminate between the cues, we applied a conservative criterion and excluded all neurons that showed any trend for differential responses to the cues in the sensory control condition (chance performance = 0.5 was outside the central 90% of the AUC distribution, i.e., $p < 0.1$). This left us with 115 neurons, for which, similar to both example neurons (Fig. 3C–F, left; AUC = 0.53 and 0.52, both $p > 0.1$), the AUC was not significantly different from chance performance in the sensory control condition (Fig. 3G, gray data points).

Focusing on those neurons whose RFs received comparable sensory drive from the locally identical cues (Fig. 3G, gray; 115 of 247 neurons), we then examined how they represented the two cues during task performance. Consider, for instance, the example neurons shown in Figure 3C–F. Despite similar responses in the sensory control condition (left panels), both neurons could reliably discriminate these locally identical visual signals when the mouse had to extract the meaning of the cues. Neuron 1 responded more strongly to the Go than to the Stop cue (Fig. 3C,D, right panels, AUC = 0.68, $p < 0.01$). Neuron 2 showed the opposite effect (Fig. 3E,F, right panels, AUC = 0.32, $p < 0.01$). Choosing again a conservative criterion, we considered discriminability during the task as significant if chance performance was outside the central 99% of the AUC distribution ($p < 0.01$), and found that discriminability emerged, during cue evaluation, in a substantial fraction of V1 neurons. Specifically, among the nonselective neurons, which failed to discriminate

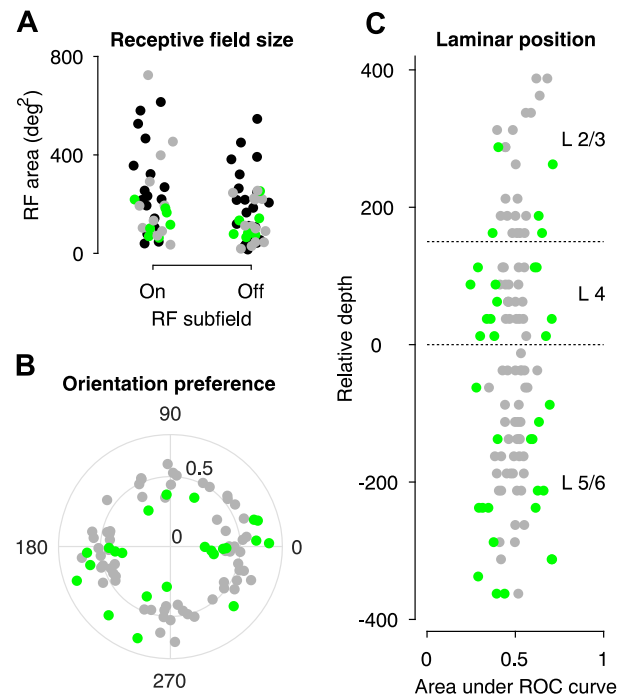


Figure 4. Basic physiological properties of V1 neurons, separated by whether or not they were modulated during cue evaluation. **A**, RF area of ON/OFF subregions, separately for shape-selective neurons (black, $n=42$), nonselective neurons that were not modulated during cue evaluation (gray, $n=25$), and nonselective neurons that were modulated during cue evaluation (green, $n=14$). **B**, Strength of modulation (AUC value) as a function of direction preference. Conventions as in **A**, but $n=23$ (green) and $n=64$ (gray). Stimulus direction is 0. Inner circle represents chance performance (AUC = 0.5). Outer circle represents AUC = 1. **C**, Strength of modulation (AUC value) across cortical depth, $n=115$. Borders between supra-granular, granular, and infragranular layers (dashed lines) are based on CSD analyses of simultaneously recorded local field potentials.

between Go and Stop cue in the sensory control condition, 30.4% reliably signaled the identity of the stimulus during task performance (Fig. 3H, green, $n=35$). About half of these neurons responded more strongly to the Go stimulus (AUC > 0.5, $n=16$), and the remaining neurons responded more strongly to the Stop stimulus (AUC < 0.5, $n=19$). These data show that responses in mouse V1 to locally identical stimuli can indeed reflect the process of evaluating visual cues.

To gain insight into potential differences between the neurons modulated by cue evaluation and those unaffected, we examined basic physiological parameters and compared them between these populations (Fig. 4). The majority (85%) of neurons that were modulated during cue evaluation had RF areas that were smaller than the mean of the entire population (189.2 ± 17.1 , $n=81$ well-defined RFs), indicating that modulation by cue evaluation was not restricted to neurons with relatively large RFs (Fig. 4A). Indeed, neurons that were modulated during cue evaluation (Fig. 4A, green data points) had significantly smaller RF areas than neurons that were shape-selective (Fig. 4A, black data points, $p=0.046$, two-sample Kolmogorov–Smirnov test). We also asked whether the strength of modulation would depend on the neurons' orientation preference but found no evidence for any such relation: orientation preferences of neurons modulated during cue evaluation (green, $n=23$ well-tuned neurons) were distributed around the circle, with no indication of a particular peak (Fig. 4B, Rayleigh test of uniformity, $p=0.69$). Finally, we examined laminar positions and found that modulated neurons were present across the depth of cortex, with no apparent clustering (Fig. 4C, $n=115$).

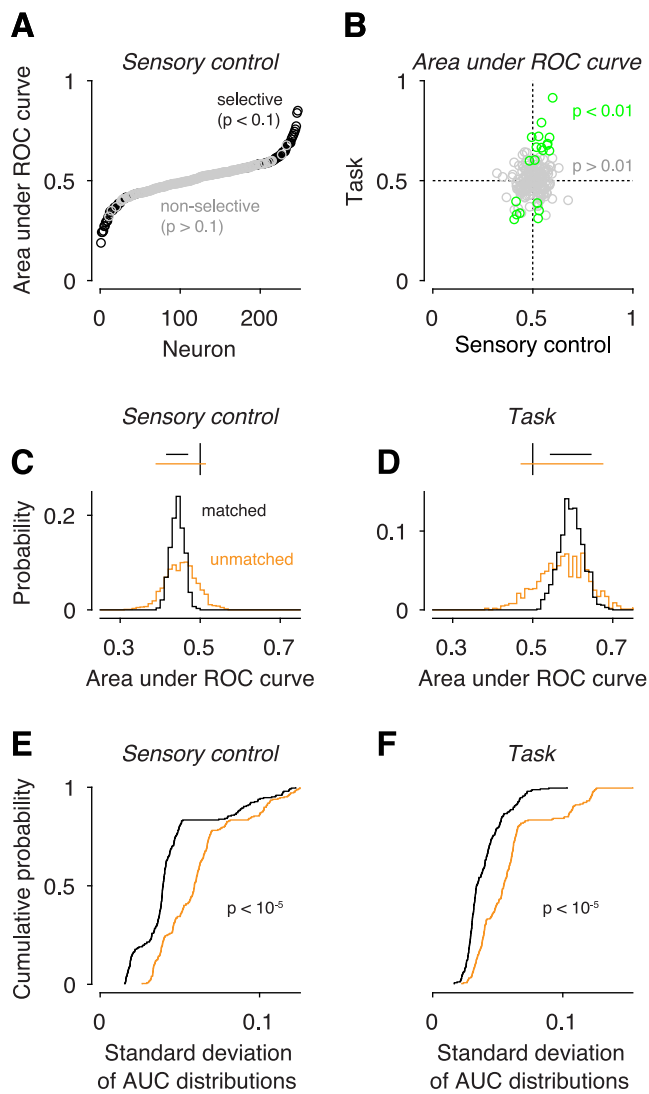


Figure 5. Without matching eye positions, neural responses are more variable, reducing the number of neurons modulated during cue evaluation. **A**, Population summary of AUC values in the sensory control condition without eye-position matching. **B**, Discrimination performance of nonselective (based on sensory control) neurons during task performance ($n = 178$). Conventions as in Figure 3. **C**, Distributions of AUC values for one example neuron (M85-56-13), separately for matched (black) and unmatched eye positions (orange) measured in the sensory control condition. Distributions were created by randomly resampling trials 1000 times. Inset, CIs (horizontal lines) for the mean AUC values, relative to chance performance (0.5, vertical line). **D**, Same as in **C**, but for another example neuron measured during task performance (M85-62-34). **E**, Cumulative distributions of SDs summarizing the width of single-neuron AUC distributions in the sensory control condition, separately for matched (black) and unmatched eye positions (orange). **F**, Same as in **E**, but during task performance.

Would we have observed comparable effects had we not controlled for eye position? To address this question, we recomputed AUC distributions by randomly selecting the same number of trials, but regardless of the eye positions. We found the number of neurons modulated by task context to be substantially reduced (Fig. 5). In the sensory control condition, a larger fraction of neurons failed to discriminate between Go and Stop stimulus, which effectively increased the pool of nonselective neurons ($n = 178$ of 247, Fig. 5A, gray data points). From this pool of nonselective neurons, however, only 11.24% (20 of 178, Fig. 5B, green data points) signaled the identity of the stimulus during the task, a fraction that was significantly smaller compared with the fraction obtained after matching eye positions (30.4%, $p < 0.00004$, χ^2 test). Matching eye

positions made a difference because it reduced trial-by-trial variability in firing rates. As a consequence, individual neurons were more likely to be found selective in the sensory control condition, as illustrated for one example neuron in Figure 5C. Without matching eye positions, trial-by-trial variability in firing rates was relatively high, and the distribution of AUC values obtained by randomly resampling trials was relatively broad (orange histogram, mean = 0.45, SD = 0.04). Its confidence region (orange horizontal line at top) included chance performance (black vertical line), and the neuron would therefore be considered nonselective. With matched eye positions, however, trial-by-trial firing rates became less variable, the distribution of AUC values was narrower (black histogram, mean = 0.44, SD = 0.02), and chance performance was clearly outside the confidence limits (black horizontal line), such that the neuron would now be excluded from the nonselective pool. Across the population, therefore, matching eye position reduced the size of the nonselective pool. In the same way, matching eye positions increased the number of neurons that could discriminate the stimuli during the task, as illustrated with a second neuron in Figure 5D. Without matching eye positions, the AUC distribution was relatively broad (orange histogram, mean = 0.58, SD = 0.06); matching eye positions made this distribution tighter (black histogram, mean = 0.60, SD = 0.03), and performance for decoding stimulus identity significantly different from chance level (confidence limits at top). The observation that matching eye positions sharpened the distributions of AUC values was true across the population of recorded neurons (Fig. 5E,F). We determined, for each neuron, the SD of the AUC distribution and compared the distributions of SDs with and without matching eye positions. Both during sensory control (Fig. 5E) and during task performance (Fig. 5F), the SDs of the AUC distributions were smaller under matched (black traces) than unmatched eye positions (orange traces, $p < 0.00001$ in both cases, two-sample Kolmogorov–Smirnov test). We conclude that, had we not matched eye position, we would have substantially underestimated the number of V1 neurons that were modulated by the process of evaluating cues.

The improvements in discriminability seen during the task could not be explained by any differences in running between sensory control and task conditions. While running behavior was under tight control during task performance, it was unconstrained in the sensory control condition, where mice could not earn a reward. It might therefore be possible that the changes in V1 discriminability between task and sensory control condition do not reflect the context of the visual task, but rather differences in running (Niell and Stryker, 2010; Ayaz et al., 2013; Erisken et al., 2014). To address this question, we focused on the sensory control condition and asked whether running per se, outside the context of the task, would affect discriminability of single neurons. We found that, with the exception of 1 mouse, the animals were also running, in the sensory control condition, on a substantial percentage of trials ($35.6 \pm 1.9\%$, on average). Where possible, we exploited this behavioral variability and separated single-trial firing rates based on whether the mouse was running or sitting ($n = 71$ of the 115 neurons). Consistent with previous reports (Niell and Stryker, 2010; Saleem et al., 2013; Erisken et al., 2014; Dadarlat and Stryker, 2017), we found a fraction of V1 neurons, whose firing rates were modulated by running (15 of 71 neurons, 21.13%, $p < 0.05$ for each neuron, unpaired t test). Although running had a general effect on average firing rates, it did not, however, affect how well V1 neurons could discriminate the cues. We computed AUC values and asked whether V1 discriminability, measured during sitting, would be any different if

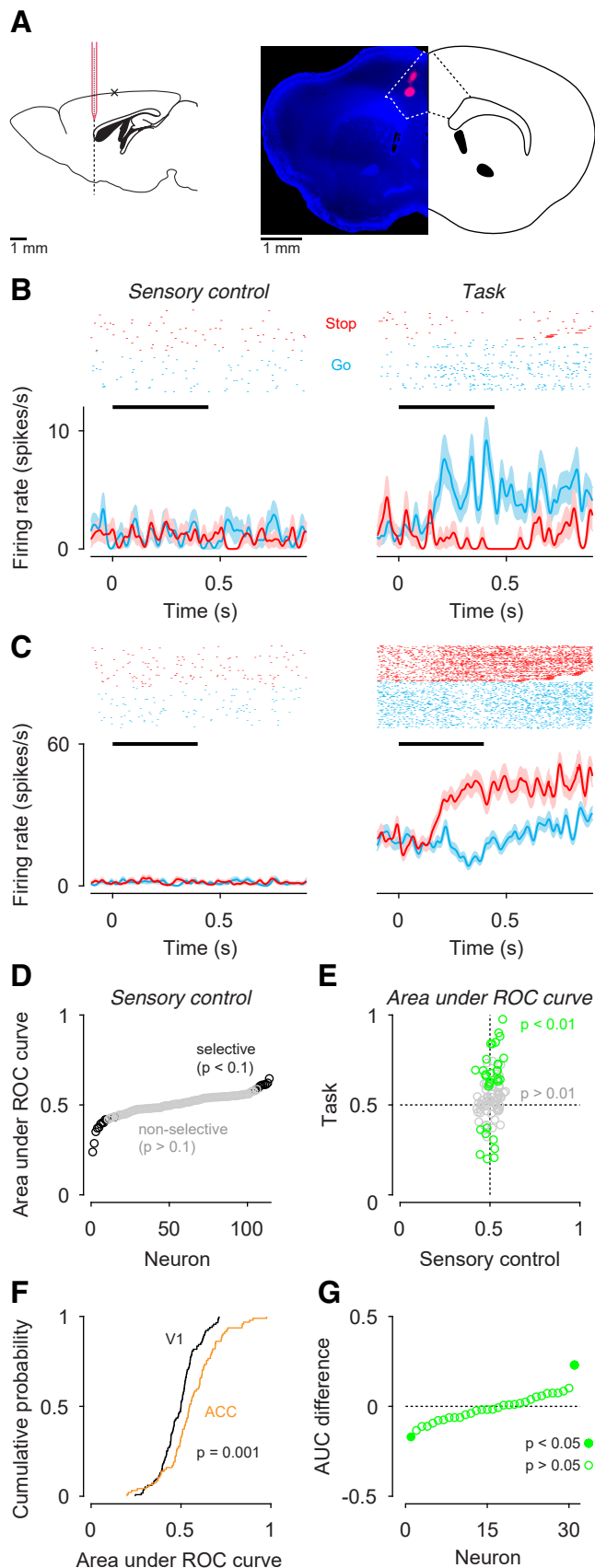


Figure 6. In ACC, cue evaluation has a markedly stronger impact than in V1, and preferences in the population are biased toward the cue promising reward. **A**, Histological reconstruction of recording sites in an example session. Left, Sagittal view. Silicon probe is shown in red. Dashed vertical line indicates the position of the coronal section shown on the right. Cross represents the location of bregma. Probes were coated with a lipophilic tracer (pink)

the mouse was running. On average, mean AUC values were very similar (sitting: 0.52, running: 0.51, $p = 0.28$, paired t test), and only 4 of 71 neurons (5.6%) showed a significant difference in AUC values (permutation test, $p < 0.05$). This observation is consistent with imaging data, where the relative selectivity for two grating stimuli was also not affected by running behavior (Poort et al., 2015). We therefore conclude that running per se cannot account for the improved discriminability of V1 neurons during task performance.

To gauge the task-dependent modulations in V1, we compared them against potential cue evaluation signatures in prefrontal cortex, a key area for many aspects of behavioral control. We focused on ACC for two reasons. First, ACC plays a prominent role in foraging-like behaviors, where the benefits of certain actions have to be evaluated relative to the required efforts (Walton et al., 2002; Rudebeck et al., 2006; Kennerley et al., 2009; Hillman and Bilkey, 2010). Second, in mouse cortex, ACC sends direct projections to V1, providing a network for top-down modulation of visual processing (Zhang et al., 2014, 2016; Fiser et al., 2016; Leinweber et al., 2017).

We recorded, using the same paradigm, from ACC and found a similar fraction of neurons that was modulated during cue evaluation; discriminative power, however, was much stronger than in area V1, and population preferences were biased toward the cue promising reward (Fig. 6). We recorded from $n = 3$ mice (12 sessions) targeting the ACC just anterior of bregma (Fig. 6A); this part of ACC sends topographically organized projections to V1 (Zhang et al., 2016; Leinweber et al., 2017). In many ACC neurons, selectivity emerged for Go versus Stop cues during the task. The example neuron shown in Figure 6B, for instance, gave almost no response to either cue in the sensory control condition (left, AUC = 0.54, $p > 0.1$), but strongly signaled the presence of the Go cue during the task (AUC = 0.72, $p < 0.01$). We also observed, although less frequently, neurons with the opposite pattern of responses, such as the example shown in Figure 6C (left: AUC = 0.44, $p > 0.1$; right: AUC = 0.22, $p < 0.01$). Across the population, 82.5% (94 of 114) of ACC neurons could not discriminate the cues in the sensory control condition (Fig. 6D, gray data points, $p > 0.1$), a fraction of nonselective neurons that was significantly larger than observed in V1, even without matching eye positions (i.e., Fig. 5A, $p = 0.033$, χ^2 test). Of these nonselective ACC neurons, 34.04% (32 of 94) signaled the identity of the cue during the task (Fig. 6E, green data points, $p < 0.01$). While the proportion of neurons affected by evaluating cues seemed comparable to area V1, two differences stood out: (1) discriminative power, assessed by the magnitude of AUC values, was consistently stronger in ACC than in V1 (Fig. 6F, $p = 0.001$, two-sample Kolmogorov–Smirnov test); and (2) modulations in ACC were not as balanced as in V1: among the modulated ACC neurons, the majority (75%) responded more strongly to the cue

before insertion. Right, Coronal view. Dashed outline in the section indicates the anterior cingulate region, following Franklin and Paxinos (2013). **B**, Spike rasters and density functions in response to the Go (blue) and Stop cue (red) for one example neuron (M302-44-13), measured in the sensory control (left) and task condition (right). **C**, Same as in **B**, but for a second example neuron (M312-42-37). **D**, Population summary of AUC values in the sensory control condition ($n = 114$). **E**, Discrimination performance of nonselective neurons during task performance ($n = 94$). Conventions as in Figure 3. **F**, Cumulative distributions of mean AUC values during task performance, separately for the populations of neurons recorded from V1 (black, $n = 115$) and ACC (orange, $n = 94$). **G**, Differences in AUC values, based on trials in the sensory control condition, during which the mouse was either running or sitting ($n = 31$). Filled markers represent neurons with significant differences.

predicting a reward, a percentage significantly larger than in V1 ($p = 0.015$, χ^2 test). Analogous to V1, we also examined whether the changes in discriminability had any simple relation to the act of running. We focused on the sensory control condition, in which mice were running around cue onset on almost half of the trials ($44.55 \pm 5.04\%$, $n = 12$ sessions), and compared AUC values computed separately for running versus sitting trials. Across the population of discriminating ACC neurons ($n = 31$, Fig. 6G, open circles), only 2 showed a statistically significant difference between sitting versus running AUCs (closed circles, permutation test, $p < 0.05$). These analyses show that running per se does not influence how well ACC neurons discriminate visual cues.

Discussion

Here, we have assessed how the behavioral demands of evaluating visual cues affected their neural representations in mouse V1 and ACC. In our task, the animal's commitment to a potentially rewarding action had to rely on visual cues, which differed in terms of global shape, but provided equivalent visual stimulation to RFs in cortex. Tightly controlling locomotion and eye positions, we found differential responses to locally identical visual cues in $\sim 30\%$ of V1 neurons; this proportion was substantially smaller when we did not account for eye positions. In ACC, much stronger selectivity emerged during cue evaluation, consistent with its prominent role in behavioral control. While preferences for either cue were balanced in the V1 population, preferences in ACC were biased toward the cue promising reward. Together, these experiments demonstrate distinct signatures of cue evaluation in primary visual and cingulate cortex of the mouse.

Isolating cue evaluation signatures in mouse V1 is challenging because its neural activity can reflect multiple behavioral influences; our task was designed to reduce the impact of such influences, but it also has its shortcomings. Key features of our task, such as self-initiation of trials ensuring constant task engagement, constant running speed, and a delayed reward, allowed us to compare responses to the cues during the task, while controlling for the impact of arousal (Vinck et al., 2015; Reimer et al., 2016), locomotion (Niell and Stryker, 2010; Eriskin et al., 2014; Dadarlat and Stryker, 2017), and task engagement (Jurjut et al., 2017; Pho et al., 2018; Jacobs et al., 2020). Yet, to assess baseline neural discriminability, we relied on the sensory control condition, during which the temporal structure of stimulus presentation and the overall arousal level of the mice were different. Although neural discriminability did not depend on locomotion per se, we cannot rule out that stimulus timing or arousal contributed to the difference in discriminability between sensory control and task condition. We also did not monitor orofacial features, such as movements of the face, the nose, or whiskers (Musall et al., 2019; Stringer et al., 2019; Salkoff et al., 2020), whose impact on V1 activity can be substantial during unconstrained behavior (Stringer et al., 2019) but might be less pervasive when mice are engaged in a visual task (Musall et al., 2019).

One of our findings is that substantial modulations of V1 responses were revealed only under tight control of eye positions. Even under head fixation, mice make saccadic eye movements (Sakatani and Isa, 2007; Payne and Raymond, 2017; Meyer et al., 2018, 2020; Samonds et al., 2018), whose size can depend on stimulus properties (Samonds et al., 2018) and whose frequency increases with running (Niell and Stryker, 2010; Keller et al., 2012; Ayaz et al., 2013; Bennett et al., 2013). Broadly consistent

with the notion that saccades in head-fixed mice are related to attempted head movements (Meyer et al., 2020), we found that saccades were reliably preceded by acceleration. Systematic differences in eye position across behavioral conditions (Keller et al., 2012; Liang et al., 2020) required a stringent eye position matching procedure (Roelfsema et al., 1998) because simply collecting more trials would not alleviate such systematic differences. As we show, stratifying mouse V1 responses removes variability related to eye position, which might otherwise mask or reduce effects of interest. Indeed, had we not considered eye position, we would have grossly underestimated the percentage of modulated V1 neurons.

A key feature of our behavioral task is that mice self-initiate each trial by running (see also Marques et al., 2018), which we chose to aim for a constant level of task engagement. One might suspect that this requirement for running negatively affects performance, given previous reports of poorer visual performance during hyperaroused states, including running (McGinley et al., 2015; McBride et al., 2019; Neske et al., 2019; Salkoff et al., 2020). We found, however, that running is not detrimental to visual performance in our task, with a post-learning average d' of almost 3. Similarly, in earlier work, running also did not compromise motion coherence thresholds during direction discrimination in random dot patterns (Marques et al., 2018). One potential explanation for this apparent contradiction might be that, in Go/No-go tasks without self-initiation of trials, periods of running or hyperarousal might coincide with lower task engagement, which might underlie the poorer visual performance. A similar argument has recently been proposed for the low arousal case, where trials indexed by high amplitudes of low-frequency oscillations were linked to reduced task engagement more than to impaired performance (Jacobs et al., 2020).

Differential neural responses in V1 to identical visual stimulation, under comparable running behavior and eye positions, could reflect several task-related contexts, such as reward expectancy or learned categorical representations. Reward expectancy can shape activity in V1 of rodents (Shuler and Bear, 2006; Chubykin et al., 2013; Poort et al., 2015) and macaques (Stănişor et al., 2013). In macaque V1, if the amount of a fluid reward is manipulated and independently assigned to either of two stimuli, multiunit responses to the same stimulus can become stronger with increasing values of relative reward (Stănişor et al., 2013). Such a straight relation, however, did not exist in our single-neuron data: only half the population responded stronger to the reward-predicting cue; the other half responded stronger to the cue predicting no reward. We would argue, however, that there is no *a priori* reason that the cue predicting a reward is the only one that is behaviorally relevant. In our paradigm, the cue signaling the absence of reward might be just as relevant, if the goal is to save time and energy. Alternatively, the differential processing of the two cues might not reflect the value of reward, but rather represent a category representation emerging in the context of the task. Training macaques in categorical discrimination of similar shapes, for instance, can increase selectivity of neurons in ventral stream areas (Logothetis et al., 1995; Baker et al., 2002). Remarkably, in inferior temporal cortex, selectivity for stimulus categories can be stronger in a categorization task than during passive viewing (McKee et al., 2014). The differential responses we observed in mouse V1 might in a similar way reflect the fact that the mouse has learned to categorize the two stimuli.

In contrast to the balanced selectivity we observed in area V1, preferences in ACC were biased toward the stimulus that promised a reward; this biased selectivity in ACC was task-specific

because it only emerged in response to the behavioral demands. Neural populations at higher processing stages often exhibit pronounced biases for specific stimuli. For instance, in macaques trained to discriminate visual stimuli, the majority of neurons recorded in the lateral intraparietal area responded most strongly to one particular stimulus (Fitzgerald et al., 2013). Such biased selectivity might be beneficial in perceptual tasks with binary or discrete outcomes because the overall level of activity could then be used by downstream areas to infer stimulus identity and commit toward an action. Biased selectivity has also been observed in mice trained to discriminate two orientations: 88% of neurons imaged in PPC responded more strongly to a rewarded than to an unrewarded orientation (Pho et al., 2018). These and our findings suggest that, in the mouse, stimulus representations transition along the cortical hierarchy from a balanced to a biased scheme. Future work will have to clarify under which behavioral conditions biased selectivity emerges, and where in cortex the transition occurs from balanced to biased distributions of preferences.

What might be the neural circuits underlying the task-dependent modulation we observed in area V1? Although we have no direct evidence, several lines of research indicate ACC as a prime candidate. ACC is important for reward-guided action selection (Doya, 2008; Kolling et al., 2016; Shenhav et al., 2016). In foraging-like behaviors, responses of ACC neurons represent the benefits of certain actions, relative to the required effort (Walton et al., 2002; Rudebeck et al., 2006; Kennerley et al., 2009; Hillman and Bilkey, 2010; Kolling et al., 2012). Effort-based decision-making might be one of the processes that is relevant in our task because mice have to commit to running bouts to harvest a reward. Furthermore, ACC sends direct projections to mouse V1, which can carry top-down signals that can shape activity of V1 neurons (Zhang et al., 2014, 2016; Fiser et al., 2016; Leinweber et al., 2017; Huda et al., 2020). Consistent with the idea that ACC contributes to the selectivity emerging in V1, we found that neurons in ACC became strikingly selective during cue evaluation. Conclusive demonstrations, however, for V1 modulations in our task by ACC will require simultaneous recordings from both areas (e.g., Steinmetz et al., 2019) or optogenetic suppression of ACC terminals over V1 (e.g., Zhang et al., 2014).

References

- Andermann ML, Kerlin AM, Reid RC (2010) Chronic cellular imaging of mouse visual cortex during operant behavior and passive viewing. *Front Cell Neurosci* 4:3.
- Ayaz A, Saleem AB, Scholvinck ML, Carandini M (2013) Locomotion controls spatial integration in mouse visual cortex. *Curr Biol* 23:890–894.
- Aydin C, Couto J, Giugliano M, Farrow K, Bonin V (2018) Locomotion modulates specific functional cell types in the mouse visual thalamus. *Nat Commun* 9:4882.
- Baker CI, Behrmann M, Olson CR (2002) Impact of learning on representation of parts and wholes in monkey inferotemporal cortex. *Nat Neurosci* 5:1210–1216.
- Barnett AG, van der Pols JC, Dobson AJ (2005) Regression to the mean: what it is and how to deal with it. *Int J Epidemiol* 34:215–220.
- Bennett C, Arroyo S, Hestrin S (2013) Subthreshold mechanisms underlying state-dependent modulation of visual responses. *Neuron* 80:350–357.
- Briggs F, Mangun GR, Usrey WM (2013) Attention enhances synaptic efficacy and the signal-to-noise ratio in neural circuits. *Nature* 499:476–480.
- Buzsaki G, Mizuseki K (2014) The log-dynamic brain: how skewed distributions affect network operations. *Nat Rev Neurosci* 15:264–278.
- Chen Y, Martinez-Conde S, Macknik SL, Bereshpolova Y, Swadlow HA, Alonso JM (2008) Task difficulty modulates the activity of specific neuronal populations in primary visual cortex. *Nat Neurosci* 11:974–982.
- Chubykin AA, Roach EB, Bear MF, Shuler MG (2013) A cholinergic mechanism for reward timing within primary visual cortex. *Neuron* 77:723–735.
- Clancy KB, Orsolic I, Mrcic-Flogel TD (2019) Locomotion-dependent remapping of distributed cortical networks. *Nat Neurosci* 22:778–786.
- Dadgarlat MC, Stryker MP (2017) Locomotion enhances neural encoding of visual stimuli in mouse V1. *J Neurosci* 37:3764–3775.
- Dombeck DA, Khabbaz AN, Collman F, Adelman TL, Tank DW (2007) Imaging large-scale neural activity with cellular resolution in awake, mobile mice. *Neuron* 56:43–57.
- Doya K (2008) Modulators of decision making. *Nat Neurosci* 11:410–416.
- Duan CA, Erlich JC, Brody CD (2015) Requirement of prefrontal and mid-brain regions for rapid executive control of behavior in the rat. *Neuron* 86:1491–1503.
- Erisken S, Vaiceliunaite A, Jurjut O, Fiorini M, Katzner S, Busse L (2014) Effects of locomotion extend throughout the mouse early visual system. *Curr Biol* 24:2899–2907.
- Fiser A, Mahringer D, Oyibo HK, Petersen AV, Leinweber M, Keller GB (2016) Experience-dependent spatial expectations in mouse visual cortex. *Nat Neurosci* 19:1658–1664.
- Fitzgerald JK, Freedman DJ, Fanini A, Bennur S, Gold JJ, Assad JA (2013) Biased associative representations in parietal cortex. *Neuron* 77:180–191.
- Franklin KB, Paxinos G (2013) *The mouse brain in stereotaxic coordinates*, Ed 4. Amsterdam: Academic.
- Gavornik JP, Bear MF (2014) Learned spatiotemporal sequence recognition and prediction in primary visual cortex. *Nat Neurosci* 17:732–737.
- Gescheider GA (1997) *Psychophysics: the fundamentals*, Ed 3. Mahwah, NJ: Erlbaum.
- Glickfeld LL, Histed MH, Maunsell JH (2013) Mouse primary visual cortex is used to detect both orientation and contrast changes. *J Neurosci* 33:19416–19422.
- Goard MJ, Pho GN, Woodson J, Sur M (2016) Distinct roles of visual, parietal, and frontal motor cortices in memory-guided sensorimotor decisions. *eLife* 5:e13764.
- Hanks TD, Kopec CD, Brunton BW, Duan CA, Erlich JC, Brody CD (2015) Distinct relationships of parietal and prefrontal cortices to evidence accumulation. *Nature* 520:220–223.
- Hazan L, Zugaro M, Buzsaki G (2006) Klusters, NeuroScope, NDManager: a free software suite for neurophysiological data processing and visualization. *J Neurosci Methods* 155:207–216.
- Henschke JU, Dylida E, Katsanevaki D, Dupuy N, Currie SP, Amvrosiadis T, Papan JM, Rochefort NL (2020) Reward association enhances stimulus-specific representations in primary visual cortex. *Curr Biol* 30:1866–1880. e5.
- Heumann D, Leuba G, Rabinowicz T (1977) Postnatal development of the mouse cerebral neocortex: II. Quantitative cytoarchitectonics of visual and auditory areas. *J Hirnforsch* 18:483–500.
- Hill DN, Mehta SB, Kleinfeld D (2011) Quality metrics to accompany spike sorting of extracellular signals. *J Neurosci* 31:8699–8705.
- Hillman KL, Bilkey DK (2010) Neurons in the rat anterior cingulate cortex dynamically encode cost-benefit in a spatial decision-making task. *J Neurosci* 30:7705–7713.
- Histed MH, Carvalho LA, Maunsell JH (2012) Psychophysical measurement of contrast sensitivity in the behaving mouse. *J Neurophysiol* 107:758–765.
- Huda R, Sipe GO, Breton-Provencher V, Cruz KG, Pho GN, Adam E, Gunter LM, Sullins A, Wickersham IR, Sur M (2020) Distinct prefrontal top-down circuits differentially modulate sensorimotor behavior. *Nat Commun* 11:6007.
- Jacobs EA, Steinmetz NA, Peters AJ, Carandini M, Harris KD (2020) Cortical state fluctuations during sensory decision making. *Curr Biol* 30:4944–4955.e7.
- Jurjut O, Georgieva P, Busse L, Katzner S (2017) Learning enhances sensory processing in mouse V1 before improving behavior. *J Neurosci* 37:6460–6474.
- Keller GB, Bonhoeffer T, Hubener M (2012) Sensorimotor mismatch signals in primary visual cortex of the behaving mouse. *Neuron* 74:809–815.
- Kennerley SW, Dahmubed AF, Lara AH, Wallis JD (2009) Neurons in the frontal lobe encode the value of multiple decision variables. *J Cogn Neurosci* 21:1162–1178.
- Kim H, ährlund-Richter S, Wang X, Deisseroth K, Carlén M (2016) Prefrontal parvalbumin neurons in control of attention. *Cell* 164:208–218.

- Kolling N, Behrens TE, Mars RB, Rushworth MF (2012) Neural mechanisms of foraging. *Science* 336:95–98.
- Kolling N, Wittmann MK, Behrens TE, Boorman ED, Mars RB, Rushworth MF (2016) Value, search, persistence and model updating in anterior cingulate cortex. *Nat Neurosci* 19:1280–1285.
- Krumin M, Lee JJ, Harris KD, Carandini M (2018) Decision and navigation in mouse parietal cortex. *eLife* 7:e42583.
- Kvitsiani D, Ranade S, Hangya B, Taniguchi H, Huang JZ, Kepecs A (2013) Distinct behavioural and network correlates of two interneuron types in prefrontal cortex. *Nature* 498:363–366.
- Lee SH, Kwan AC, Zhang S, Phoumthipphavong V, Flannery JG, Masmanidis SC, Taniguchi H, Huang ZJ, Zhang F, Boyden ES, Deisseroth K, Dan Y (2012) Activation of specific interneurons improves V1 feature selectivity and visual perception. *Nature* 488:379–383.
- Leinweber M, Ward DR, Sobczak JM, Attinger A, Keller GB (2017) A sensorimotor circuit in mouse cortex for visual flow predictions. *Neuron* 95:1420–1432.e5.
- Liang L, Fratzl A, Reggiani JD, El Mansour O, Chen C, Andermann ML (2020) Retinal inputs to the thalamus are selectively gated by arousal. *Curr Biol* 30:3923–3934.
- Licata AM, Kaufman MT, Raposo D, Ryan MB, Sheppard JP, Churchland AK (2017) Posterior parietal cortex guides visual decisions in rats. *J Neurosci* 37:4954–4966.
- Liu P, Sun YJ, Li Y, Zhang LL, Tao HW (2010) Intervening inhibition underlies simple-cell receptive field structure in visual cortex. *Nat Neurosci* 13:89–96.
- Loftus GR, Masson ME (1994) Using CIs in within-subject designs. *Psychon Bull Rev* 1:476–490.
- Logothetis NK, Pauls J, Poggio T (1995) Shape representation in the inferior temporal cortex of monkeys. *Curr Biol* 5:552–563.
- Logothetis NK, Kayser C, Oeltermann A (2007) In vivo measurement of cortical impedance spectrum in monkeys: implications for signal propagation. *Neuron* 55:809–823.
- Lopes G, Bonacchi N, Frazao J, Neto JP, Atallah BV, Soares S, Moreira L, Matias S, Itskov PM, Correia PA, Medina RE, Calcaterra L, Dreosti E, Paton JJ, Kampff AR (2015) Bonsai: an event-based framework for processing and controlling data streams. *Front Neuroinform* 9:7.
- Macmillan NA, Creelman CD (2005) *Detection theory: a user's guide*, Ed 2. Mahwah, NJ: Erlbaum.
- Marques T, Summers MT, Fioreze G, Fridman M, Dias RF, Feller MB, Petreanu L (2018) A role for mouse primary visual cortex in motion perception. *Curr Biol* 28:1703–1713.e6.
- Maunsell JH (2015) Neuronal mechanisms of visual attention. *Annu Rev Vis Sci* 1:373–391.
- McBride EG, Lee SY, Callaway EM (2019) Local and global influences of visual spatial selection and locomotion in mouse primary visual cortex. *Curr Biol* 29:1592–1605.e5.
- McGinley MJ, David SV, McCormick DA (2015) Cortical membrane potential signature of optimal states for sensory signal detection. *Neuron* 87:179–192.
- McKee JL, Riesenhuber M, Miller EK, Freedman DJ (2014) Task dependence of visual and category representations in prefrontal and inferior temporal cortices. *J Neurosci* 34:16065–16075.
- Meyer AF, Poort J, O'Keefe J, Sahani M, Linden JF (2018) A head-mounted camera system integrates detailed behavioral monitoring with multichannel electrophysiology in freely moving mice. *Neuron* 100:46–60.e7.
- Meyer AF, O'Keefe J, Poort J (2020) Two distinct types of eye-head coupling in freely moving mice. *Curr Biol* 30:2116–2130.e6.
- Mitzdorf U (1985) Current source-density method and application in cat cerebral cortex: investigation of evoked potentials and EEG phenomena. *Physiol Rev* 65:37–100.
- Montijn JS, Olcese U, Pennartz CMA (2016) Visual stimulus detection correlates with the consistency of temporal sequences within stereotyped events of V1 neuronal population activity. *J Neurosci* 36:8624–8640.
- Moore T, Zirnsak M (2017) Neural mechanisms of selective visual attention. *Annu Rev Psychol* 68:47–72.
- Murray EA, Rudebeck PH (2018) Specializations for reward-guided decision-making in the primate ventral prefrontal cortex. *Nat Rev Neurosci* 19:404–417.
- Musall S, Kaufman MT, Juavinett AL, Gluf S, Churchland AK (2019) Single-trial neural dynamics are dominated by richly varied movements. *Nat Neurosci* 22:1677–1686.
- Neske GT, Nestvogel D, Steffan PJ, McCormick DA (2019) Distinct waking states for strong evoked responses in primary visual cortex and optimal visual detection performance. *J Neurosci* 39:10044–10059.
- Nicholson C, Freeman JA (1975) Theory of current source-density analysis and determination of conductivity tensor for anuran cerebellum. *J Neurophysiol* 38:356–368.
- Niell CM, Stryker MP (2010) Modulation of visual responses by behavioral state in mouse visual cortex. *Neuron* 65:472–479.
- Pakan JM, Lowe SC, Dylida E, Keemink SW, Currie SP, Coutts CA, Rochefort NL (2016) Behavioral-state modulation of inhibition is context-dependent and cell type specific in mouse visual cortex. *eLife* 5:e14985.
- Payne HL, Raymond JL (2017) Magnetic eye tracking in mice. *eLife* 6:e29222.
- Pho GN, Goard MJ, Woodson J, Crawford B, Sur M (2018) Task-dependent representations of stimulus and choice in mouse parietal cortex. *Nat Commun* 9:2596.
- Poort J, Khan AG, Pachitariu M, Nemri A, Orsolich I, Krupic J, Bauza M, Sahani M, Keller GB, Mrsic-Flogel TD, Hofer SB (2015) Learning enhances sensory and multiple non-sensory representations in primary visual cortex. *Neuron* 86:1478–1490.
- Quiroga RQ, Nadasdy Z, Ben-Shaul Y (2004) Unsupervised spike detection and sorting with wavelets and superparamagnetic clustering. *Neural Comput* 16:1661–1687.
- R Core Team (2017) *A language and environment for statistical computing*. Vienna: R Core Team.
- Ramesh RN, Burgess CR, Sugden AU, Gyetvan M, Andermann ML (2018) Intermingled ensembles in visual association cortex encode stimulus identity or predicted outcome. *Neuron* 100:900–915.e9.
- Reimer J, McGinley MJ, Liu Y, Rodenkirch C, Wang Q, McCormick DA, Tolias AS (2016) Pupil fluctuations track rapid changes in adrenergic and cholinergic activity in cortex. *Nat Commun* 7:13289.
- Roelfsema PR, Lamme VA, Spekreijse H (1998) Object-based attention in the primary visual cortex of the macaque monkey. *Nature* 395:376–381.
- Rudebeck PH, Walton ME, Smyth AN, Bannerman DM, Rushworth MF (2006) Separate neural pathways process different decision costs. *Nat Neurosci* 9:1161–1168.
- Sakatani T, Isa T (2007) Quantitative analysis of spontaneous saccade-like rapid eye movements in C57BL/6 mice. *Neurosci Res* 58:324–331.
- Saleem AB, Ayaz A, Jeffery KJ, Harris KD, Carandini M (2013) Integration of visual motion and locomotion in mouse visual cortex. *Nat Neurosci* 16:1864–1869.
- Saleem AB, Diamanti EM, Fournier J, Harris KD, Carandini M (2018) Coherent encoding of subjective spatial position in visual cortex and hippocampus. *Nature* 562:124–127.
- Salkoff DB, Zaghera E, McCarthy E, McCormick DA (2020) Movement and performance explain widespread cortical activity in a visual detection task. *Cereb Cortex* 30:421–437.
- Samonds JM, Geisler WS, Priebe NJ (2018) Natural image and receptive field statistics predict saccade sizes. *Nat Neurosci* 21:1591–1599.
- Scholz FW, Stephens MA (1987) K-sample Anderson-Darling tests. *J Am Statist Assoc* 82:918.
- Schroeder CE, Mehta AD, Givre SJ (1998) A spatiotemporal profile of visual system activation revealed by current source density analysis in the awake macaque. *Cereb Cortex* 8:575–592.
- Shadlen MN, Kiani R (2013) Decision making as a window on cognition. *Neuron* 80:791–806.
- Shenhav A, Cohen JD, Botvinick MM (2016) Dorsal anterior cingulate cortex and the value of control. *Nat Neurosci* 19:1286–1291.
- Shuler MG, Bear MF (2006) Reward timing in the primary visual cortex. *Science* 311:1606–1609.
- Speed A, Del Rosario J, Mikail N, Haider B (2020) Spatial attention enhances network, cellular and subthreshold responses in mouse visual cortex. *Nat Commun* 11:505.
- Stahl JS, van Alphen AM, De Zeeuw CI (2000) A comparison of video and magnetic search coil recordings of mouse eye movements. *J Neurosci Methods* 99:101–110.
- Stanislaw H, Todorov N (1999) Calculation of signal detection theory measures. *Behav Res Methods Instrum Comput* 31:137–149.
- Stăniş or L, van der Togt C, Pennartz CM, Roelfsema PR (2013) A unified selection signal for attention and reward in primary visual cortex. *Proc Natl Acad Sci USA* 110:9136–9141.

- Steinmetz NA, Zarka-Haas P, Carandini M, Harris KD (2019) Distributed coding of choice, action and engagement across the mouse brain. *Nature* 576:266–273.
- Stringer C, Pachitariu M, Steinmetz N, Reddy CB, Carandini M, Harris KD (2019) Spontaneous behaviors drive multidimensional, brainwide activity. *Science* 364:255.
- Vinck M, Batista-Brito R, Knoblich U, Cardin JA (2015) Arousal and locomotion make distinct contributions to cortical activity patterns and visual encoding. *Neuron* 86:740–754.
- Wallace DJ, Greenberg DS, Sawinski J, Rulla S, Notaro G, Kerr JND (2013) Rats maintain an overhead binocular field at the expense of constant fusion. *Nature* 498:65–69.
- Walton ME, Bannerman DM, Rushworth MF (2002) The role of rat medial frontal cortex in effort-based decision making. *J Neurosci* 22:10996–11003.
- Wang Q, Gao E, Burkhalter A (2011) Gateways of ventral and dorsal streams in mouse visual cortex. *J Neurosci* 31:1905–1918.
- Wimmer RD, Schmitt LI, Davidson TJ, Nakajima M, Deisseroth K, Halassa MM (2015) Thalamic control of sensory selection in divided attention. *Nature* 526:705–709.
- Yatsenko D, Walker EY, Tolia AS (2018) DataJoint: a simpler relational data model. arXiv:1807.11104.
- Zhang S, Xu M, Kamigaki T, Hoang Do JP, Chang WC, Jenvay S, Miyamichi K, Luo L, Dan Y (2014) Selective attention: long-range and local circuits for top-down modulation of visual cortex processing. *Science* 345:660–665.
- Zhang S, Xu M, Chang WC, Ma C, Hoang Do JP, Jeong D, Lei T, Fan JL, Dan Y (2016) Organization of long-range inputs and outputs of frontal cortex for top-down control. *Nat Neurosci* 19:1733–1742.

5 V1 microcircuits underlying mouse visual behavior

This chapter is reproduced from an article published in *Current Opinion in Neurobiology*. The article can be found under <https://www.sciencedirect.com/science/article/abs/pii/S0959438818302046>. The full citation is:

Katzner, S., Born, G., & Busse, L. (2019). V1 microcircuits underlying mouse visual behavior. *Current Opinion in Neurobiology*, 58, 191–198.

Declaration of author contributions

Laura Busse and Steffen Katzner conceptualized the paper. Laura Busse, Steffen Katzner, and Gregory Born wrote the original draft. Laura Busse and Steffen Katzner edited the manuscript. Laura Busse, Steffen Katzner, and Gregory Born visualized the data. Laura Busse supervised the project.

Personal contributions

G.B. assembled the panels for Fig. 2. G.B. also contributed to writing the draft, focusing on the section “Top-down modulation of sensory processing in mouse V1”. Finally, G.B. edited the manuscript.

Rights and permissions

”Please note that, as the author of this Elsevier article, you retain the right to include it in a thesis or dissertation, provided it is not published commercially. Permission is not required, but please ensure that you reference the journal as the original source.”

Retrieved from <https://s100.copyright.com/AppDispatchServlet#formTop> on 14.11.2021.

V1 microcircuits underlying mouse visual behavior

Steffen Katzner¹, Gregory Born^{1,2} and Laura Busse^{1,3}

Visual behavior is based on the concerted activity of neurons in visual areas, where sensory signals are integrated with top-down information. In the past decade, the advent of new tools, such as functional imaging of populations of identified single neurons, high-density electrophysiology, virus-assisted circuit mapping, and precisely timed, cell-type specific manipulations, has advanced our understanding of the neuronal microcircuits underlying visual behavior. Studies in head-fixed mice, where such tools can routinely be applied, begin to provide new insights into the neural code of primary visual cortex (V1) underlying visual perception, and the micro-circuits of attention, predictive processing, and learning.

Addresses

¹ Division of Neurobiology, Department Biology II, LMU Munich, 82151 Munich, Germany

² Graduate School of Systemic Neuroscience (GSN), LMU Munich, 82151 Munich, Germany

³ Bernstein Center for Computational Neuroscience, 82151 Munich, Germany

Corresponding author: Busse, Laura (busse@bio.lmu.de)

Current Opinion in Neurobiology 2019, 58:191–198

This review comes from a themed issue on **Computational neuroscience**

Edited by **Máté Lengyel** and **Brent Doiron**

<https://doi.org/10.1016/j.conb.2019.09.006>

0959-4388/© 2019 Elsevier Ltd. All rights reserved.

Introduction

How do we see? This simple question does not have a simple answer. Vision is a complex process that starts with the absorption of light by the photoreceptors in the retina, which convey to downstream circuits the information necessary for perception and action. Essential for visual behavior are several processes, such as the encoding and transformation of visual representations across the visual hierarchy, the selection of salient or otherwise relevant information, the integration of visual inputs with learned priors or predictions for scene interpretation, and the translation into appropriate behavioral actions.

Within the last two decades, experiments in head-fixed mice have enabled researchers to investigate the neural basis of visual behavior on the microcircuit level. Rapid

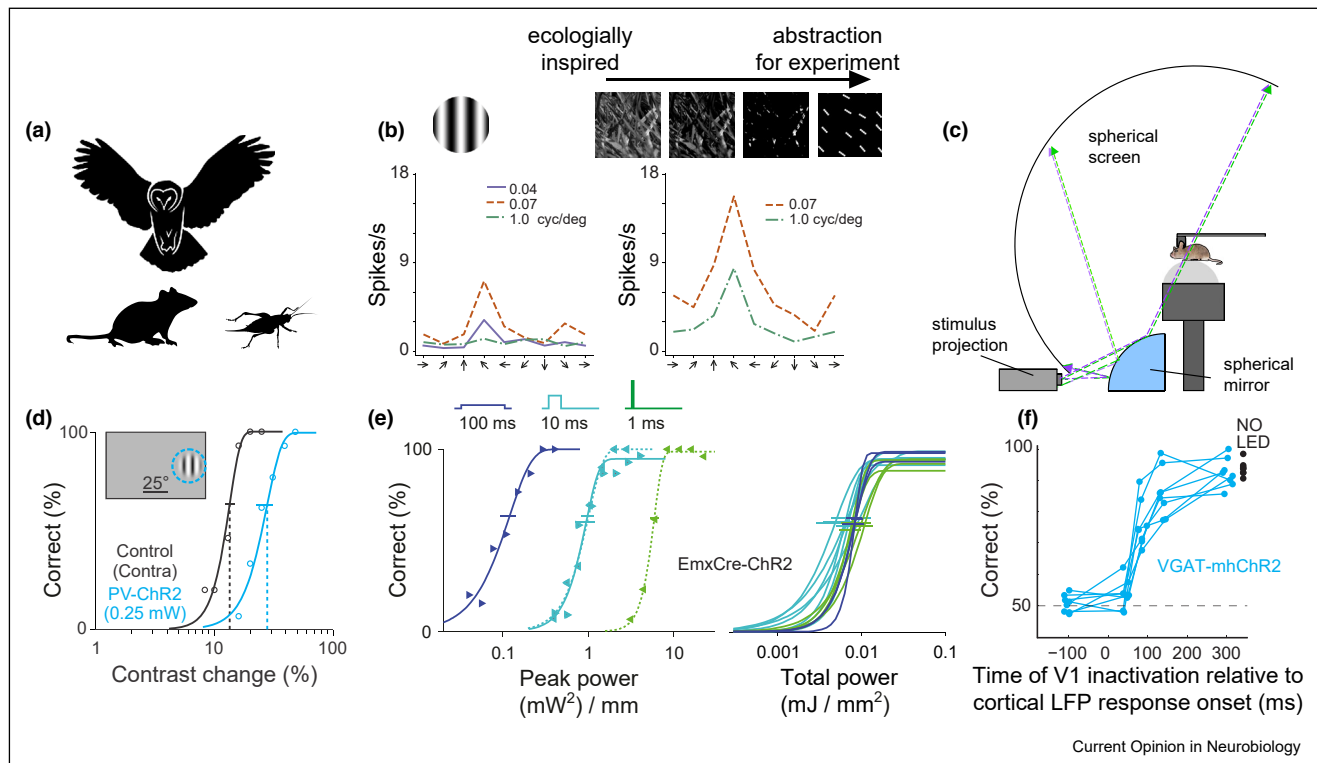
progress has been made, thanks to the availability of techniques that cannot as readily be used in other mammals. Examples are long-term monitoring of populations of identified single neurons using two-photon imaging with genetically encoded calcium indicators [1], and cell-type or projection-specific optogenetic manipulations [2]. Here, we survey this progress by focusing on *in vivo* studies in the head-fixed mouse, review how neural microcircuits in V1 support visual behavior and relate, where possible, experimental findings to computational models of visual function.

The mouse as a model system for visually guided behavior

While working with mice allows the interrogation of neuronal microcircuits at unprecedented detail, their suitability as a model system for visual behavior has often been called into question. Indeed, mice have large visual receptive fields (RFs, e.g. ~ 20 deg in V1 [3]) and poor spatial acuity in laboratory vision tests [4]. Yet, mice can discriminate not only simple, but also higher-order visual stimuli [5,6], as well as natural scenes [7]. Furthermore, they exhibit interesting and ecologically relevant visual behaviors: vision is their only sense to detect avian overhead predators [8,9], and is essential to orient themselves accurately towards prey and approach it from the distance [10] (Figure 1a).

It is becoming increasingly clear that considering the natural habitat of mice in the design and display of visual stimuli is likely to advance our understanding of mouse vision and visual behavior. For instance, preferences for spatial frequency in mouse V1 are concentrated below 0.08 cyc/deg, if measured with standard, artificial grating stimuli [11,12]. However, probing mouse V1 with more complex stimuli that mimic the optic flow experienced by running through grass (Figure 1b), revealed reliable, highly selective responses for orientation and direction, even at high spatial frequencies [13*]. Such adaptations in tuning might be understood in the context of efficient coding theory [14,15], which posits that perceptual systems have evolved towards transmission of as much information as possible, given the statistics of the natural environment and biological constraints of the nervous system. Relatedly, if performance in a natural task, such as object localization or identification, is taken as starting point, Bayesian ideal observer analysis [16] can provide a framework for extracting the most task-relevant stimulus features and hence infer representations for natural stimuli. Developing custom display solutions for optimal stimulation of the mouse's large field of view [12,17,18], and providing color inputs with wavelengths appropriate

Figure 1



Mouse vision and neural codes in V1. **(a)** Ethological visually guided behaviors in the mouse: avoidance of aerial predators [8,9] and prey capture [10]. **(b)** Comparison of V1 responses (example cell) to grating stimuli (left) and visual stimuli inspired by the mouse's visual habitat, here: patches of grass (right). These flow stimuli evoke higher firing rates and responses, which remain well tuned even for spatial frequencies so far considered beyond the resolution of the mouse (adapted from [13^{*}]). **(c)** Custom projection and display devices to provide panoramic input of appropriate wavelength to the mouse's large field of view (Euler and Busse, unpublished). **(d)** Psychometric curve of an example mouse (single session) in a contrast change detection experiment, during control trials (black) and trials with V1 inactivation (blue) over V1 regions encoding the visual stimulus (inset). V1 inactivation systematically impairs perceptual performance, that is, shifts the psychometric curve to the right, providing evidence for a link between V1 activity and visual behavior (adapted from [30]). **(e)** Behavioral report of optogenetic V1 pyramidal cell stimulation can be well predicted by the total amount of light delivered. Example mouse, two sessions (adapted from [38^{*}]). **(f)** During precisely timed, optogenetic inactivation of V1, behavioral performance in an orientation discrimination task is to large degree restored, even if as little as the initial ~80 ms of the stimulus-evoked V1 response is left intact (adapted from [34^{**}]).

for their UV-sensitive cones [17–20] (Figure 1c), will likely reveal visual capabilities of mice that surpass what has so far been recognized [18], and will allow further testing of theories relating environment statistics to neural representations and task performance.

Do mice use the thalamocortical pathway for visual behavior?

Given the prominence of subcortical visual pathways in rodents, it has been imperative for studies of mouse visual behavior to demonstrate that, like in other mammals, specific visual tasks rely on thalamocortical pathways, in particular on V1. In the mouse, as much as 88% of retinal ganglion cells (RGCs) target the superior colliculus (SC) and most RGCs projecting to the dorsolateral geniculate nucleus of the thalamus (dLGN) have an axon collateral to SC [21]. In SC, neurons are selective for direction and orientation [22], and organized in maps with

orientation columns [23,24]. Consistent with the importance of SC for visual behavior in rodents, ablation of primary visual cortex seems to have little impact on the detection and orientation towards salient visual stimuli [25,26]. Similarly, muscimol-induced inactivation of gerbil primary auditory cortex has little impact on behavioral performance in a sound detection task [27], and mice trained to detect objects using their whiskers can rapidly recover their performance level after ablation of barrel cortex [28], suggesting that across sensory systems rodents might not require primary cortices to detect simple stimuli. Remarkably, SC can have powerful control over visual cortex [29]: in posthinal cortex, an extrastriate visual area, neural responses seem to remain intact after V1 inactivation, but they are abolished upon silencing SC. Despite the prominent role of the SC, short-term inactivation of V1 consistently demonstrated impairments of performance during orientation discrimination

[30–33,34**,35], motion perception [36], and detection of changes in stimulus contrast [30] (Figure 1d). Importantly, impairments in orientation discrimination performance seem to be strongest for low-contrast stimuli [32], and rather moderate suppression of firing rates can substantially elevate perceptual thresholds [30]. Together, these studies are consistent with a critical link between activity in mouse V1 and perceptual performance in a range of visual tasks.

Inactivating V1 in order to pinpoint its specific functions, however, comes with caveats. First, diminished behavioral performance during inactivation experiments could arise from effects unspecific to vision. A stronger case is thus made if V1 suppression impairs behavioral performance only in vision tasks, and not in a variant of the task in a different sensory modality [31]. Second, since V1 sends numerous projections to subcortical structures, manipulating V1 activity will inevitably also affect output targets, such as SC [37]. Hence, even if inactivation is targeted to area V1, it is challenging to ultimately rule out the involvement of SC in mouse visual perception.

The code and microcircuits for sensation and perception in mouse V1

While it seems that activity in mouse V1 is necessary for image-forming vision, it is less clear how many of its neurons are required for perception. This question has been elegantly tested in the somatosensory system's barrel cortex, where rats can report juxtacellular current injections into single neurons, leading to ~10–15 additional action potentials. Behavioral reports of such nanostimulation were most reliable if the stimulation targeted strongly responsive pyramidal cells in deep layers [39,40] or fast-spiking inhibitory interneurons [40,41]. Potentially related are findings of single 'hub' neurons in superficial layers of rodent V1, which exert widespread control over the cortical population: The induction of burst spiking in single neurons could change, in ~40% of the cases, global brain state as assessed by the local field potential (LFP) [42]. Induced bursts also affected, within a radius of ~100 μm , spiking activity in <1.7% of excitatory neurons [43,44] and in 29% of somatostatin-positive (SOM+) inhibitory interneurons [43]. The strong recruitment of inhibition resonates well with recent findings, where holographic optogenetic activation of a single pyramidal cell in L2/3 of mouse V1 induced a pattern of activity consistent with feature competition, in which similarly tuned neurons predominantly suppress each other [45**]. Together, these studies point towards an important role of V1 L2/3 circuits in suppressing redundant information and promoting sparse coding [46].

How activation of inhibitory interneurons in V1 influences visual perception is a matter of debate. One study reported that driving V1 parvalbumin-positive inhibitory

interneurons (PV+) improved discriminability (d') for orientation [47]; however, the interpretation of these behavioral data is not straightforward, because they do not rule out the possibility that optogenetic stimulation affected task compliance [38*,48]. The opposite conclusions were reached by other studies, in which activation of PV+ interneurons impaired contrast discrimination, particularly in perceptually limited, threshold-level sensory conditions [48]. Interestingly, a similar decline in performance was observed for activation of somatostatin-positive (SOM+) interneurons, while activation of vasoactive intestinal peptide (VIP+) interneurons improved perceptual thresholds [48], potentially via the well-characterized disinhibitory VIP+ \rightarrow SOM+ \rightarrow pyramidal cell circuit [49]. An important next step will be a detailed characterization of visual perception under a wide range of optogenetic stimulation intensities. Such an approach would allow one to assess whether varying drive to the targeted interneurons changes perception in qualitatively different ways. This could potentially reconcile discrepancies between previous studies.

How relevant is spike timing in mouse V1 for driving visually guided behavior? A few studies causally tested, in the context of perception, predictions of theoretical models concerning the relevance of precise timing and synchronicity [50] versus the necessity of rate coding given chaotic network dynamics and noisy single neurons [51]. While single neuron nanostimulation in somatosensory cortex demonstrated that detection performance improved with the irregularity of the induced spike train [41], results in V1 obtained during larger-scale optogenetic stimulation of pyramidal cells rather suggest that the exact timing of spikes does not matter, at least in simple detection tasks [38*]. Indeed, detection performance of direct, low-intensity V1 optogenetic stimulation seems to depend only on total light energy, that is, the product of pulse intensity and duration, with little effect of stimulation frequency [38*] (Figure 1e). At least for the type of V1 stimulation employed, which increased spiking on average by ~1.1 spikes/s over 100 ms, behavior could be well approximated by a linear integration of spikes occurring within this stimulation window in a population of noisy neurons. These experiments elegantly and powerfully establish the capabilities of readout [52]; to which degree this result generalizes to more naturalistic stimulation patterns and is sufficient for explaining performance in complex, sensory tasks remain important open questions.

Which V1 spikes are critical for visual perception? Exploiting the power of precisely timed optogenetic suppression of V1 activity, Scanziani and colleagues could show that the first 40–80 ms of V1 activity are sufficient for mice to perform a simple orientation discrimination task (45 deg, [34**]) (Figure 1f). Remarkably, within this initial 80 ms of V1 response, the majority of V1 neurons

discriminating the stimulus had a response difference of ~ 1 spike. This highlights that the first V1 spikes, probably mostly representing the initial feedforward sweep, can reliably drive behavior, at least in simple discrimination tasks.

Finally, two-photon functional imaging — currently still limited to the temporal scale of calcium indicators — allows to determine in large neuronal populations, which features of the neural code correlate with task performance. The heterogeneity of V1 L2/3 responses both before and during stimulus presentation, but not mean activity, seems a good candidate for predicting single trial detection performance and reaction time [53], and differs between active task performance and passive viewing [54^{*}]. Other studies, however, have found that populations of V1 L2/3 neurons during orientation discrimination predominantly encoded stimulus identity as opposed to delayed behavioral choice [33], and did not alter selectivity after reward contingencies had been reversed [54^{*}]. One goal for the future will be to investigate questions of population coding and behavior with more complex stimuli and tasks, at higher temporal resolution, on a trial-by-trial basis, and in individual animals [52]. Furthermore, our most detailed knowledge of the neural circuits underlying visual behavior in the mouse currently arises from layers 2/3 of primary visual cortex. In the future, it will be important to expand these investigations to other layers and areas beyond the primary visual cortex, whose potential function in mouse visual behavior remains largely unknown.

Top-down modulation of sensory processing in mouse V1

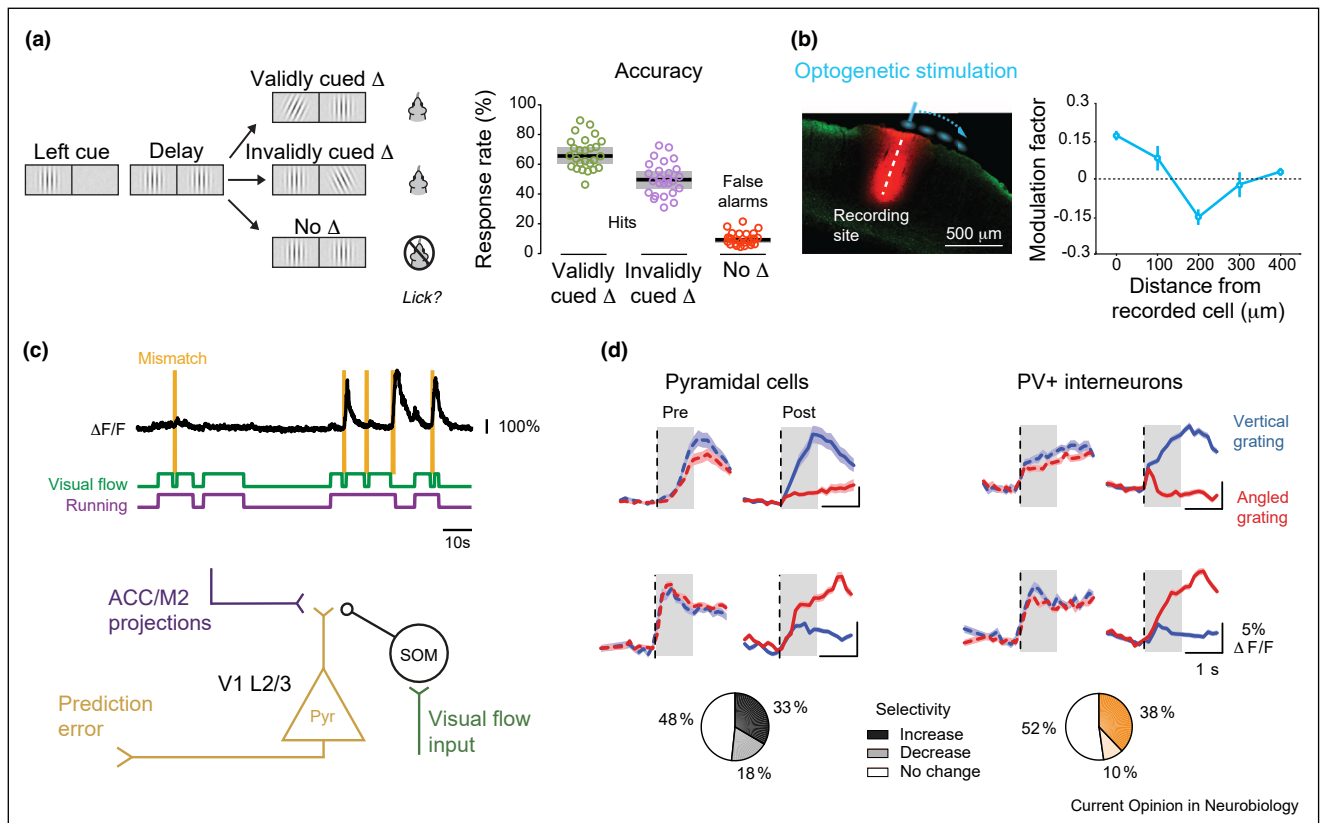
A fundamental task of sensory systems is to select behaviorally relevant information and enhance its neural representation, commonly referred to as selective attention. Selective visual attention has long been studied in primates, but recent work has shown that attention can also be probed in head-fixed mice [55^{*}]. Indeed, in carefully designed spatial cueing tasks (Figure 2a), mice showed higher accuracy, faster reaction times, and enhanced perceptual sensitivity after valid compared to invalid cues [55^{*}]; such results are characteristic signatures of selective visual attention. This key demonstration has opened up the possibility to relate perceptual improvements by attention to activity in V1 microcircuits, and to identify the neural source and signals controlling visual attention. Experiments on the microcircuits of attention would also allow testing predictions of a biophysically inspired computational model, which postulates specific roles for different types of interneurons in the attentional modulation of sensory responses [56].

One candidate source for attentional modulation of V1 responses is the anterior cingulate region of prefrontal cortex (ACC), which sends long-range, monosynaptic projections to V1 innervating pyramidal cells and all three

major classes of inhibitory interneurons (PVs, SOMs, VIPs) [57,58]. In anesthetized mice, optogenetic stimulation of ACC projections terminating in V1 recruited these interneurons, whose concerted activity produced a pattern of pyramidal cell responses similar to the center-surround profile of spatial attention [58] (Figure 2b). It has also been reported that optogenetic stimulation of ACC improved behavioral performance during orientation discrimination [58], which is consistent with a functional relevance of those projections during task performance.

According to the influential framework of predictive coding, early processing stages are less concerned with selecting and representing stimulus features, but rather compare incoming sensory signals against an internal model of the world [59–61]. The predictive coding framework postulates a hierarchical processing scheme, where higher-level stages send predictions of sensory inputs to lower levels. Lower-level stages compare predicted against actual sensory input and might signal prediction errors, which are used to update the model. How these key components of the predictive coding framework might be implemented by neural circuits in mouse cortex has been tested in a series of studies, in which mice were navigating virtual reality (VR) environments [57,62,63,64^{**},65]. VR environments allow sudden perturbations of the optic flow, creating visual input that deviates from what would be expected based on self-motion. Two-photon calcium imaging revealed that such mismatches evoked responses in a population of layer 2/3 V1 neurons [62,65] (Figure 2c), consistent with prediction error signals. Such mismatch signals required that the animals experienced the coupling between optic flow and self-motion, because mismatch responses were absent in a separate group of animals receiving identical visual stimulation without visuomotor coupling [64^{**}]. The predictions themselves are thought to be conveyed by subregions of the ACC and secondary motor cortex (M2). ACC/M2 provide, via topographically organized, monosynaptic projections, to V1 layer 2/3 neurons motor-related signals [57]. Motor-related signals in ACC/M2 projections were found to be correlated with the optic flow expected by self-movement, and this correlation was restored, after additional practice, in VR environments, where the coupling of optic flow to the animal's movement direction was inverted [57]. Finally, a circuit in layer 2/3 of mouse V1 has been proposed that could potentially implement the computation of prediction errors (Figure 2c). Layer 2/3 'mismatch' neurons integrate motor-related, excitatory input and inhibitory input from SOM+ interneurons driven by the visual optic flow. Without perturbations, the excitatory motor-input and the inhibitory visual input cancel out; if perturbations stop the optic flow, however, SOM+ activity decreases and this release of inhibition allows the mismatch neuron to signal a prediction error [64^{**}].

Figure 2



Top-down modulations of V1 circuits. **(a)** The adaptation of classic spatial cueing tasks to head-fixed mice opens up the possibility to study microcircuits of attentional selection. Left: in the experimental setup, the animal is facing two screens, one of which displays a cue grating at the beginning of the trial. After the following delay period, where the grating is presented on both screens, the animal needs to lick if either of the two gratings changes its orientation and refrain from licking if the orientations remain the same. Right: behavioral performance is better in trials in which the cue is valid (i.e. presented at the same location at which a later change in orientation needs to be detected) compared to trials in which the cue is invalid (adapted from [55]). **(b)** In anesthetized mice, optogenetic activation of ACC projections over V1 results in center-surround modulation. Left: laser stimulation sites (blue) relative to the recording site (red). Right: Spatial profile of response modulation, averaged across the population of recorded neurons. A facilitatory center and a suppressive surround are reminiscent of spatial attention effects (adapted from [58]). **(c)** A predictive coding interpretation of V1 responses. Top: Sudden halts (yellow) of optic flow in a VR environment can elicit 'mismatch' responses from a population of L2/3 V1 pyramidal cells. Bottom: The proposed microcircuit generating these responses integrates excitatory signals from ACC/M2 (purple) signaling predicted optic flow and inhibitory inputs from SOM+ neurons (orange) driven by the visual optic flow (green). If visual and predicted optic flow match, these inputs cancel; in case of 'mismatches' the pyramidal cell produces a prediction error (adapted from [64]). **(d)** Top: During orientation discrimination learning, individual pyramidal cells and PV+ interneurons develop a preference for one or the other grating stimuli. Bottom: Population summary of changes in selectivity for these two neuron types (adapted from [67]).

VR experiments with rodents also highlight the intimate relation between vision and navigation. As mice navigate a virtual corridor lined by visual stimuli, responses of V1 neurons to identical stimuli were found to be selective for the animal's spatial position in the corridor [66,63]. V1 selectivity for spatial position closely corresponded to the spatial position encoded in the hippocampal area CA1, and population activity in both regions seemed to reflect the animal's subjective estimate of position [66].

Key ideas behind theories of selective attention or predictive processing already imply that neural representations in V1 are not static, but depend on context and

experience. How experience, or learning, affects sensory processing in V1 circuits can be investigated elegantly in the mouse, where the activity of populations of identified single neurons can be tracked across recording sessions. Longitudinal two-photon calcium imaging during learning of a visual detection task, for instance, revealed decreasing responses of layer 4 neurons, the primary target of bottom-up inputs, yet increasing activity in top-down projections from the retrosplinal cortex [68]. Consistent with such learning-related strengthening of top-down influences on V1 processing, two studies have reported that L2/3 neurons can acquire ramp-like responses, possibly encoding the timing of the behaviorally relevant stimulus [31,68].

Besides strengthening top-down signals, learning can also improve V1 stimulus processing [31,32]. Indeed, learning to discriminate stimulus orientation made responses more reliable in neurons that already preferred either orientation before learning; other neurons developed such relative preference during learning [31] (Figure 2d). On the microcircuit-level, a methodological tour de force combining longitudinal functional imaging with cell type identification by post-mortem immunohistochemistry [67**] could reveal differential effects of learning on multiple classes of inhibitory interneurons. With learning, PV+ neurons acquired substantial stimulus selectivity (Figure 2d), which could be modeled as increased functional connectivity between pyramidal and PV+ cells with similar preferences. The model also revealed that the magnitude of learning-related increases in stimulus preference of pyramidal cells was inversely related to their pre-learning coupling strength with SOM+ neurons. Thus, SOM+ neurons might be responsible for gating learning-induced effects in V1. Consistent with a role in gating learning-induced changes, the activity of SOM+ interneurons was found to be reduced during learning [68], and rather decorrelated from the local network [67**]. Thus, a release from inhibition during learning might be important to promote plasticity in V1 [68], where optogenetic activation of SOM+ neurons could, to some degree, reverse learning-induced changes [68].

Although learning-related improvements in behavioral performance are often paralleled by changes in sensory processing, the time course for behavioral and neural measures of learning can also dissociate. During classical conditioning of orientation discrimination, for instance, sensory processing in mouse V1 improved before successful discrimination was evident in the animal's licking behavior [32]. This observation might be related to reports from the auditory system, showing elegantly that behavioral readouts of learning can systematically underestimate the acquisition of task knowledge [69]. These findings provide important constraints for theories of learning, and highlight the need to quantify learning precisely in individual animals, and to carefully choose behavioral indicators of progress.

Conclusions and outlook

We reviewed recent work on how microcircuits in V1, and projections from top-down sources, might serve visual behavior of the mouse. While rapid progress has been made in understanding the role of V1 upper layers and their specific inputs, much less is understood about the role of lower-layer circuits and inter-laminar connectivity. A new wave of discoveries is likely to come from recordings with high-density CMOS-based electrodes [70], sampling from distributed areas of the brain [71], or from brain-wide functional imaging methods [72], which promise to frame V1 computations in the brain-wide network of regions active during visual behavior.

Conflict of interest statement

Nothing declared.

Acknowledgements

This work was supported by the German Research Foundation (LB: BU 1808/5-1; project number 276693517 SFB 1233, TP10; SFB 870, TP19).

References and recommended reading

Papers of particular interest, published within the period of review, have been highlighted as:

- of special interest
 - of outstanding interest
1. Lin MZ, Schnitzer MJ: **Genetically encoded indicators of neuronal activity**. *Nat Neurosci* 2016, **19**:1142-1153.
 2. Kim CK, Adhikari A, Deisseroth K: **Integration of optogenetics with complementary methodologies in systems neuroscience**. *Nat Rev Neurosci* 2017, **18**:222-235.
 3. Niell CM, Stryker MP: **Highly selective receptive fields in mouse visual cortex**. *J Neurosci* 2008, **28**:7520-7536.
 4. Prusky GT, West PWR, Douglas RM: **Behavioral assessment of visual acuity in mice and rats**. *Vis Res* 2000, **40**:2201-2209.
 5. Khastkhoudeh Z, Jurjut O, Katzner S, Busse L: **Mice can use second-order, contrast-modulated stimuli to guide visual perception**. *J Neurosci* 2016, **36**:4457-4469.
 6. Schnabel UH, Bossens C, Lorteije JAM, Self MW, Beeck de HO, Roelfsema PR: **Figure-ground perception in the awake mouse and neuronal activity elicited by figure-ground stimuli in primary visual cortex**. *Sci Rep* 2018, **8**:1-14.
 7. Yu Y, Hira R, Stirman JN, Yu W, Smith IT, Smith SL: **Mice use robust and common strategies to discriminate natural scenes**. *Sci Rep* 2018, **8**:1379.
 8. Yilmaz M, Meister M: **Rapid innate defensive responses of mice to looming visual stimuli**. *Curr Biol* 2013, **23**:2011-2015.
 9. De Franceschi G, Vivattanasarn T, Saleem AB, Solomon SG: **Vision guides selection of freeze or flight defense strategies in mice**. *Curr Biol* 2016, **26**:2150-2154.
 10. Hoy JL, Yavorska I, Wehr M, Niell CM: **Vision drives accurate approach behavior during prey capture in laboratory mice**. *Curr Biol* 2016, **26**:3046-3052.
 11. Gao E, DeAngelis GC, Burkhalter A: **Parallel input channels to mouse primary visual cortex**. *J Neurosci* 2010, **30**:5912-5926.
 12. Marshel JH, Garrett ME, Nauhaus I, Callaway EM: **Functional specialization of seven mouse visual cortical areas**. *Neuron* 2011, **72**:1040-1054.
 13. Dyballa L, Hoseini MS, Dadarlat MC, Zucker SW, Stryker MP: **Flow stimuli reveal ecologically appropriate responses in mouse visual cortex**. *Proc Natl Acad Sci U S A* 2018, **115**:11304-11309.
 - Using novel visual stimuli inspired by the optic flow likely experienced by the mouse while running through patchy grass, this study demonstrates that neurons in mouse V1 can be responsive and selective at spatial frequencies higher than previously appreciated.
 14. Barlow H: **Possible principles underlying the transformations of sensory messages – MIT Press Scholarship**. *Sensory Communication*. Cambridge, MA: MIT Press; 1961, 217-234.
 15. Attneave F: **Some informational aspects of visual perception**. *Psychol Rev* 1954, **61**:183-193.
 16. Geisler WS: **Visual perception and the statistical properties of natural scenes**. *Annu Rev Psychol* 2008, **59**:167-192.
 17. Rhim I, Coello-Reyes G, Ko H, Nauhaus I: **Maps of cone opsin input to mouse V1 and higher visual areas**. *J Neurophysiol* 2017. [jn.00849.2016](https://doi.org/10.1152/jn.00849.2016).
 18. Denman DJ, Luviano JA, Ollerenshaw DR, Cross S, Williams D, Buice MA, Olsen SR, Reid RC: **Mouse color and wavelength-**

- specific luminance contrast sensitivity are non-uniform across visual space.** *eLife* 2018, **7**:e31209.
19. Tan Z, Sun W, Chen TW, Kim D, Ji N: **Neuronal representation of ultraviolet visual stimuli in mouse primary visual cortex.** *Sci Rep* 2015, **5**:12597.
 20. Denman DJ, Siegle JH, Koch C, Reid RC, Blanche TJ: **Spatial organization of chromatic pathways in the mouse dorsal lateral geniculate nucleus.** *J Neurosci: Off J Soc Neurosci* 2017, **37**:1102-1116.
 21. Ellis EM, Gauvain G, Sivyer B, Murphy GJ: **Shared and distinct retinal input to the mouse superior colliculus and dorsal lateral geniculate nucleus.** *J Neurophysiol* 2016, **116**:602-610.
 22. Wang L, Sarnaik R, Rangarajan K, Liu X, Cang J: **Visual receptive field properties of neurons in the superficial superior colliculus of the mouse.** *J Neurosci* 2010, **30**:16573-16584.
 23. Ahmadlou M, Heimel JA: **Preference for concentric orientations in the mouse superior colliculus.** *Nat Commun* 2015, **6**: ncomms7773.
 24. Feinberg EH, Meister M: **Orientation columns in the mouse superior colliculus.** *Nature* 2015, **519**:229-232.
 25. Schneider GE: **Two visual systems.** *Science* 1969, **163**:895-902.
 26. Petruno SK, Clark RE, Reinagel P: **Evidence that primary visual cortex is required for image, orientation, and motion discrimination by rats.** *PLOS ONE* 2013, **8**:e56543.
 27. Caras ML, Sanes DH: **Top-down modulation of sensory cortex gates perceptual learning.** *Proc Natl Acad Sci U S A* 2017, **114**:9972-9977.
 28. Hong YK, Lacefield CO, Rodgers CC, Bruno RM: **Sensation, movement and learning in the absence of barrel cortex.** *Nature* 2018, **561**:542-546.
 29. Beltramo R, Scanziani M: **A collicular visual cortex: neocortical space for an ancient midbrain visual structure.** *Science* 2019, **363**:64-69.
 30. Glickfeld LL, Histed MH, Maunsell JHR: **Mouse primary visual cortex is used to detect both orientation and contrast changes.** *J Neurosci* 2013, **33**:19416-19422.
 31. Poort J, Khan AG, Pachitariu M, Nemri A, Orsolic I, Krupic J, Bauza M, Sahani M, Keller GB, Mrsic-Flogel TD *et al.*: **Learning enhances sensory and multiple non-sensory representations in primary visual cortex.** *Neuron* 2015, **86**:1478-1490.
 32. Jurjut O, Georgieva P, Busse L, Katzner S: **Learning enhances sensory processing in mouse V1 before improving behavior.** *J Neurosci* 2017, **37**:6460-6474.
 33. Goard MJ, Pho GN, Woodson J, Sur M: **Distinct roles of visual, parietal, and frontal motor cortices in memory-guided sensorimotor decisions.** *eLife* 2016, **5**:e13764.
 34. Resulaj A, Ruediger S, Olsen SR, Scanziani M: **First spikes in visual cortex enable perceptual discrimination.** *eLife* 2018, **7**: e34044.
- Using precisely timed optogenetic inactivation of primary visual cortex, this study demonstrates that the first stimulus-evoked spikes can be sufficient for orientation discrimination.
35. Zatka-Haas P, Steinmetz NA, Carandini M, Harris KD: **Distinct contributions of mouse cortical areas to visual discrimination.** *bioRxiv* 2019:501627.
 36. Marques T, Summers MT, Fioreze G, Fridman M, Dias RF, Feller MB, Petreanu L: **A role for mouse primary visual cortex in motion perception.** *Curr Biol* 2018, **28**:1703-1713.e6.
 37. Ahmadlou M, Tafreshiha A, Heimel JA: **Visual cortex limits pop-out in the superior colliculus of awake mice.** *Cereb Cortex* 2017, **27**:5772-5783.
 38. Histed MH, Maunsell JHR: **Cortical neural populations can guide behavior by integrating inputs linearly, independent of synchrony.** *Proc Natl Acad Sci U S A* 2014, **111**:E178-E187.
- This study tested the ability to detect direct, optogenetic activation of V1 excitatory neurons and found that detection performance was driven by the total amount of light delivered, irrespective of the exact pattern or frequency of stimulation. V1 electrophysiological recordings showed that the light-induced changes in firing rates were small, and behavior reflected the integration of the total number of spikes over the 100 ms of stimulation.
39. Houweling AR, Brecht M: **Behavioural report of single neuron stimulation in somatosensory cortex.** *Nature* 2008, **451**:65-68.
 40. Tanke N, Borst JGG, Houweling AR: **Single-cell stimulation in barrel cortex influences psychophysical detection performance.** *J Neurosci* 2018, **38**:2057-2068.
 41. Doron G, von Heimendahl M, Schlattmann P, Houweling AR, Brecht M: **Spiking irregularity and frequency modulate the behavioral report of single-neuron stimulation.** *Neuron* 2014, **81**:653-663.
 42. Li CyT, Poo M, Dan mY: **Burst spiking of a single cortical neuron modifies global brain state.** *Science* 2009, **324**:643-646.
 43. Kwan AC, Dan Y: **Dissection of cortical microcircuits by single-neuron stimulation in vivo.** *Curr Biol* 2012, **22**:1459-1467.
 44. Meyer JF, Golshani P, Smirnakis SM: **The effect of single pyramidal neuron firing within layer 2/3 and layer 4 in mouse V1.** *Front Neural Circuits* 2018:12.
 45. Chettih SN, Harvey CD: **Single-neuron perturbations reveal feature-specific competition in V1.** *Nature* 2019, **567**:334.
- Using holographic optogenetic stimulation of single V1 L2/3 pyramidal cells the authors demonstrate suppression between similarly tuned neurons, pointing towards feature competition and sparse coding.
46. Olshausen BA, Field DJ: **Emergence of simple-cell receptive field properties by learning a sparse code for natural images.** *Nature* 1996, **381**:607-609.
 47. Lee SH, Kwan AC, Zhang S, Phoumthippavong V, Flannery JG, Masmanidis SC, Taniguchi H, Huang ZJ, Zhang F, Boyden ES *et al.*: **Activation of specific interneurons improves V1 feature selectivity and visual perception.** *Nature* 2012, **488**:379-383.
 48. Cone JJ, Scantlen MD, Histed MH, Maunsell JHR: **Different Inhibitory Interneuron Cell Classes Make Distinct Contributions to Visual Contrast Perception.** *ENEURO* 2019:6. ENEURO.0337-18.2019.
 49. Pfeffer CK, Xue M, He M, Huang ZJ, Scanziani M: **Inhibition of inhibition in visual cortex: the logic of connections between molecularly distinct interneurons.** *Nat Neurosci* 2013, **16**:1068-1076.
 50. Fries P: **Rhythms for cognition: communication through coherence.** *Neuron* 2015, **88**:220-235.
 51. van Vreeswijk C, Sompolinsky H: **Chaos in neuronal networks with balanced excitatory and inhibitory activity.** *Science* 1996, **274**:1724-1726.
 52. Panzeri S, Harvey CD, Piasini E, Latham PE, Fellin T: **Cracking the neural code for sensory perception by combining statistics, intervention, and behavior.** *Neuron* 2017, **93**:491-507.
 53. Montijn JS, Goltstein PM, Pennartz CM: **Mouse V1 population correlates of visual detection rely on heterogeneity within neuronal response patterns.** *eLife* 2015:4.
 54. Pho GN, Goard MJ, Woodson J, Crawford B, Sur M: **Task-dependent representations of stimulus and choice in mouse parietal cortex.** *Nat Commun* 2018, **9**:2596.
- This study compares V1 and PPC neurons in terms of selectivity for visual input and choice signals. While activity V1 is largely driven by visual stimuli and rather insensitive to the mapping between stimuli and choice, PPC activity is task-dependent and strongly correlated with behavioral choices.
55. Wang L, Krauzlis RJ: **Visual selective attention in mice.** *Curr Biol* 2018, **28**:676-685.e4.
- The authors develop several variants of a spatial cueing task for head-fixed mice, in which behavior shows hallmarks of attentional selection. This development opens up the possibility to study, in the mouse, microcircuits of selective visual attention.
56. Buia CI, Tiesinga PH: **Role of interneuron diversity in the cortical microcircuit for attention.** *J Neurophysiol* 2008, **99**:2158-2182.

57. Leinweber M, Ward DR, Sobczak JM, Attinger A, Keller GB: **A sensorimotor circuit in mouse cortex for visual flow predictions.** *Neuron* 2017, **95**:1420–1432.e5.
58. Zhang S, Xu M, Kamigaki T, Hoang Do JP, Chang WC, Jenvey S, Miyamichi K, Luo L, Dan Y: **Selective attention. Long-range and local circuits for top-down modulation of visual cortex processing.** *Science (New York, N.Y.)* 2014, **345**:660–665.
59. Rao RPN, Ballard DH: **Predictive coding in the visual cortex: a functional interpretation of some extra-classical receptive-field effects.** *Nat Neurosci* 1999, **2**:79–87.
60. Spratling MW: **Predictive coding as a model of response properties in cortical area V1.** *J Neurosci* 2010, **30**:3531–3543.
61. Keller GB, Mrsic-Flogel TD: **Predictive processing: a canonical cortical computation.** *Neuron* 2018, **100**:424–435.
62. Keller GB, Bonhoeffer T, Hübener M: **Sensorimotor mismatch signals in primary visual cortex of the behaving mouse.** *Neuron* 2012, **74**:809–815.
63. Fiser A, Mahringer D, Oyibo HK, Petersen AV, Leinweber M, Keller GB: **Experience-dependent spatial expectations in mouse visual cortex.** *Nat Neurosci* 2016, **19**:1658–1664.
64. Attinger A, Wang B, Keller GB: **Visuomotor coupling shapes the functional development of mouse visual cortex.** *Cell* 2017, **169**:1291–1302.e14.
- This study demonstrates that responses to sensorimotor mismatch in V1 L2/3 neurons require experience with normal sensorimotor coupling. In addition, the study proposes a microcircuit for computation of prediction error signals consisting of convergent inputs to ‘mismatch neurons’ of motor-related inputs and inhibitory inputs from SOM+ neurons, encoding the sensory stimulus. Under normal conditions, these inputs cancel; during sudden halts of the visual optic flow, the ‘mismatch’ neuron is released from inhibition and signals a mismatch response.
65. Zmarz P, Keller GB: **Mismatch receptive fields in mouse visual cortex.** *Neuron* 2016, **92**:766–772.
66. Saleem AB, Diamanti EM, Fournier J, Harris KD, Carandini M: **Coherent encoding of subjective spatial position in visual cortex and hippocampus.** *Nature* 2018, **562**:124–127.
- This study highlights the intimate relation between vision and navigation. It shows that identical visual stimuli lining the walls of a virtual corridor at different spatial positions elicit differential responses in neurons of mouse V1. Furthermore, not only hippocampal representations but also those in V1 seem to reflect subjective estimates of the mouse’s spatial position.
67. Khan AG, Poort J, Chadwick A, Blot A, Sahani M, Mrsic-Flogel TD, Hofer SB: **Distinct learning-induced changes in stimulus selectivity and interactions of GABAergic interneuron classes in visual cortex.** *Nat Neurosci* 2018, **21**:851–859.
- Combining longitudinal two-photon calcium imaging of populations of single neurons with post-mortem immunohistochemical identification of cell types, this study demonstrates that learning differentially shapes stimulus selectivity and functional connectivity of L2/3 pyramidal neurons, and PV+, SOM+, and VIP+ inhibitory interneurons. During learning, both pyramidal and PV+ cells increase their stimulus preference and their preference-specific functional coupling. Pre-learning coupling of SOM+ neurons to pyramidal cells was found to be inversely related to learning-related increases in preferences, suggesting that SOM+ might gate learning.
68. Makino H, Komiyama T: **Learning enhances the relative impact of top-down processing in the visual cortex.** *Nat Neurosci* 2015, **18**:1116–1122.
69. Kuchibhotla KV, Sten TH, Papadoyannis ES, Elnozahy S, Fogelson KA, Kumar R, Boubenec Y, Holland PC, Ostojic S, Froemke RC: **Dissociating task acquisition from expression during learning reveals latent knowledge.** *Nat Commun* 2019, **10**:1–13.
70. Jun JJ, Steinmetz NA, Siegle JH, Denman DJ, Bauza M, Barbarits B, Lee AK, Anastassiou CA, Andrei A, Aydn Ç *et al.*: **Fully integrated silicon probes for high-density recording of neural activity.** *Nature* 2017, **551**:24636.
71. Steinmetz N, Zatka-Haas P, Carandini M, Harris K: **Distributed correlates of visually-guided behavior across the mouse brain.** *bioRxiv* 2018:474437.
72. Macé E, Montaldo G, Trenholm S, Cowan C, Brignall A, Urban A, Roska B: **Whole-brain functional ultrasound imaging reveals brain modules for visuomotor integration.** *Neuron* 2018, **100**:1241–1251.e7.

6 Discussion

This thesis describes contextual modulations of visual processing in mouse V1 and dLGN with a focus on the role of feedback signals. In particular, we show that CT feedback can in dLGN affect processing of naturalistic stimuli by increasing the response gain and by promoting tonic firing mode (Spacek et al., 2021). Moreover, we reveal that CT feedback sculpts spatial integration in dLGN by enhancing surround suppression and sharpening RFs (Born et al., 2021). These results integrate, at least in part, well with studies carried out in other species (Andolina et al., 2013; Hasse and Briggs, 2017a; Jones et al., 2012) and modalities (Alitto and Usrey, 2003; Ergenzinger et al., 1998; Zhang et al., 1997). At the level of V1, we reveal that a large fraction of neurons responds preferentially to either a rewarded or an unrewarded cue (Wal et al., 2021). This effect might be established by feedback connections from the ACC, whose neurons project to V1 and for which we describe a similar phenomenon. In the last part, we summarize current literature on mouse V1 microcircuits mediating visually-guided behavior with an emphasis on the role of top-down modulations for sensory processing in V1 (Katzner et al., 2019).

6.1 The role of feedback

Although the general purpose of feedback is still debated, most functions of feedback enable the organism to rapidly adjust sensory processing to changing contexts. These functions include changing the firing mode of neurons, controlling their response gain, and shaping their tuning properties.

6.1.1 Firing mode

A crucial component of context-dependent processing at the level of the thalamus might be the firing mode of relay cells. Relay cells can respond to incoming stimuli in either the burst or the tonic firing mode. The tonic firing mode is characterized by regularly fired, sodium-mediated action potentials and a firing rate that increases approximately linearly with the driving input, yielding a high dynamic range (Sherman, 2001; Lu et al., 1992). Therefore, this processing regime seems particularly well suited for the precise encoding of surrounding stimuli. The burst firing mode, on the other hand, is defined by a rapid train of sodium action potentials that ride on top of a slow calcium spike. Although it has been argued that spikes within a burst might encode sensory

information (Mease et al., 2017), the prevailing idea is that the burst spikes represent all-or-none responses (Sherman, 2001; Lu et al., 1992). These nonlinear responses have a high probability of triggering an action potential in downstream cortical neurons and might thus serve as a wake-up call to cortex (Sherman, 2001). Such wake-up calls might be particularly useful for detecting sudden changes in the sensory input.

In **Manuscript 1** (Born et al., 2021) and **Manuscript 2** (Spacek et al., 2021), we found that suppressing CT feedback increased in dLGN burst ratios. Conversely, activating CT feedback reduced burst ratios (Born et al., 2021). Burst spikes depend on voltage-gated T-type channels which only become de-inactivated when the neurons membrane potential becomes sufficiently hyperpolarized for at least 100 ms (Sherman, 2001). Hence, this result is in line with CT feedback acting via its direct excitatory route and supports previous findings: Mease et al. (2014), for instance, juxtacellularly probed responses to whisker deflections in the mouse somatosensory thalamus and revealed that optogenetic activation of L6CT neurons in barrel cortex reduced the probability of thalamic bursts. Yet, these observations are contrasted by findings from Olsen et al. (2012) and Bortone et al. (2014) who activated and inactivated corticothalamic feedback to dLGN respectively and found no significant change in burst ratios. Thus, to resolve this conflict, further studies are needed.

6.1.2 Gain control

By fitting a threshold linear model to dLGN responses under control conditions and under conditions in which CT feedback was suppressed, we were able to show that CT feedback modulates dLGN firing rates by a divisive mechanism (Spacek et al., 2021). Gain modulations occur in both subcortical and cortical structures and are suggested to play an important role for a wide range of cognitive functions such as multimodal integration, learning, and sensory processing (Ferguson and Cardin, 2020). In excitatory neurons of mouse primary auditory cortex, for example, repeated exposure to a sound reduces, by recruitment of SOM+ interneurons, the gain of frequency tuning (Natan et al., 2017), and L6CT pyramidal cells in V1 control, via translaminar PV+ inhibitory interneurons (Bortone et al., 2014; Frandolig et al., 2019), the gain across cortical layers (Olsen et al., 2012; Bortone et al., 2014; Frandolig et al., 2019).

For a long time, it has been thought that subtractive modulations would arise from hyperpolarizing inputs while divisive modulations were attributed to shunting inhibi-

tion. Modelling the effects of shunting inhibition, however, resulted in subtractive changes (Holt and Koch, 1997). An alternative explanation is the so-called “synaptic noise” (Shu et al., 2003; Chance et al., 2002). Synaptic noise describes the extent to which a neuron’s membrane potential fluctuates due to synaptic inputs and seems in cat V1 together with changes in depolarization and input resistance responsible for evoking gain modulations (Cardin et al., 2008). These factors are indeed also affected by CT feedback (Béhuret et al., 2015) which, combined with fluctuations in the recruitment of T-type channels, can alter the slope of the input-output function of thalamic relay cell (Béhuret et al., 2015; Wolfart et al., 2005). CT feedback can also influence the retino-thalamo-cortical transmission by eliciting NMDA plateau potentials in distal dendrites of relay cells (Augustinaite et al., 2014). If the relay cell is in burst mode, an NMDA spike can switch the neuron to tonic mode, and if already in tonic mode, the excitatory potential increases the probability of the relay cell to respond to incoming retinal inputs. Supporting this notion, Przybyszewski et al. (2000), showed that feedback projections from macaque V1 multiplicatively modulate contrast-tuning of dLGN parvocellular neurons.

CT feedback can thus alter the sensitivity of neurons at an early processing stage and contribute to the dynamic encoding range necessary for an organism to detect both subtle and prominent inputs (Ferguson and Cardin, 2020).

6.1.3 Contextual modulation in mouse V1

Contextual modulations are not restricted to the thalamus but occur also upstream in the primary sensory cortices. In mouse V1, we found that a substantial fraction of neurons develops selective responses to one of two visual cues that signal either a missing or an upcoming reward (Wal et al., 2021). Reward modulations have previously been reported in rodent V1 (Poort et al., 2015; Shuler, 2006; Chubykin et al., 2013), where neurons can predict the timing of a reward (Shuler, 2006). While it has been suggested that reward timing in V1 is established by local circuits together with cholinergic inputs from the basal forebrain (Chubykin et al., 2013), Stanisor et al. (2013) found that the strength with which neurons in macaque V1 are modulated by a reward is correlated with top-down attentional influences. This suggests that reward modulation in V1 could, at least in part, be mediated by feedback connections. In line with this idea, we found selective response patterns also in the mouse ACC, which sends feedback projections to V1 (Leinweber et al., 2017; Zhang et al., 2014).

Even though we cannot rule out that the modulations we observed are better explained by other contextual influences, such as those due to the global shape of the stimuli (Baker et al., 2002; Logothetis et al., 1995; McKee et al., 2014), they nevertheless might help the animal to discriminate between two behaviorally-relevant cues.

6.1.4 Predictive coding

Another prominent idea regarding the role of feedback for sensory processing comes from the predictive coding framework (Rao and Ballard, 1999; Clark, 2013; Keller and Mrsic-Flogel, 2018). According to the predictive coding idea, higher processing stages acquire, through experience, a model of the external world, which generates specific predictions about incoming sensory information. These predictions are conveyed via feedback signals to lower processing stages, where they are compared with external feedforward inputs. Only the difference between the actual sensory input and the prediction is then passed on to the next processing stage in the form of an error signal. Based on the error signal the model representation is updated.

A prominent example of a predictive signal can be traced back to Helmholtz (Von Helmholtz, 1867) who coined the term corollary discharge. Corollary discharge describes the sensory consequence that is predicted based on an efference copy, i.e. a copy of the motor command, and that enables the organism to distinguish own movements from external movements. Neurophysiological evidence for this idea has been found in different species and processing domains. Trying to understand why we perceive a stable visual world, regardless of saccadic or rapid eye movements, Sommer and Wurtz (2006) found that neurons in the frontal eye field of macaques receive, via the thalamus, corollary discharges from neurons in the superior colliculus based on which they shift their RFs. Moreover, Keller and Hahnloser (2009) reported neurons in the zebra finch' auditory forebrain that seem to detect mismatches between the bird's model of a song and the actually perceived song.

In mice, predictive processing has been studied in the primary visual cortex. Keller et al. (2012) recorded from neurons in layer 2/3 of mouse V1, while the animals, being headfixed over a spherical treadmill, navigated through a virtual corridor. Interestingly, they found a fraction of neurons that predominantly responded when the visual feedback was not coupled to the movement of the mice and hence elicited a mismatch. Crucially, these mismatch signals are experience-dependent, which is in line with the idea

that they reflect sensory-driven violations of a learned model (Attinger et al., 2017). It has been proposed that prediction of this model are sent in form of excitatory motor signals from neurons in the ACC/M2 to neurons in L2/3 of V1 (Leinweber et al., 2017). These neurons are also targeted by somatostatin-positive inhibitory neurons that encode the visual flow. If the visual flow is in accordance with top-down mediated motor commands, inhibitory and excitatory inputs are cancelled out, otherwise a mismatch signal is elicited (Attinger et al., 2017).

Adopting the idea of predictive coding to contextual influences on spatial integration, surround suppression can be understood as the successful prediction of a local stimulus from the global spatial pattern. The stronger response to a small stimulus can, on the other hand, be viewed as a mismatch signal, that is generated because the local input could not be predicted by the larger context (Rao and Ballard, 1999). In fact, a computational model based on predictive coding was able to recapitulate many aspects of the V1 classical and extraclassical RF properties, including surround suppression (Spratling, 2010). Thus, CT feedback-mediated effects on surround suppression observed in our study can be explained in the framework of predictive coding.

From the predictive coding framework one can also derive specific hypotheses regarding the effects of CT feedback for processing artificial vs. naturalistic stimuli. That is, CT feedback should be particularly engaged for naturalistic stimuli since they should more closely match the model of the external world. In line with this idea, we found effects of CT feedback on firing rate to be more consistent and stronger for naturalistic movie clips than for drifting gratings (Spacek et al., 2021).

6.1.5 State-dependent modulations in dLGN

While activity in both cortex and thalamus is known to depend on the behavioral state of the animal, the effects of corticothalamic feedback have traditionally been probed in anesthetized animals (Briggs and Usrey, 2011). This is problematic because, first, anaesthesia might affect higher processing stages stronger than lower processing stages and therefore alter in particular the influence of feedback projections (Makino and Komiyama, 2015; Keller et al., 2020; Briggs and Usrey, 2011). In line with this notion, Makino and Komiyama (2015) found that administering in mice a mixture of ketamine and xylazine had little effect on the response profile of the feedforward-recipient layer 4 neurons while strongly suppressing feedback from the retrosplenial cortex to V1. Sec-

only, recordings in anesthetized animals do not allow to answer important questions regarding interactions between effects of CT feedback and behavioral state.

In **Manuscript 2** (Spacek et al., 2021), we recorded in mouse dLGN responses to naturalistic movie clips and manipulate CT feedback during different behavioral states. Our results show that although effects of locomotion mimic those of CT feedback, the two influences act largely independent. This is indeed similar to what has been described for state-dependent modulations in the superior colliculus, which are suggested to be independent of corticotectal inputs: In a recent study, Schröder et al. (2020) used two-photon calcium imaging to record from neurons in the mouse SC. When comparing the response properties of SC neurons during different arousal levels, as assessed by the pupil size, they found both neurons whose responses were positively modulated by arousal as well as neurons that were negatively modulated by arousal. Importantly, when optogenetically inactivating V1, this pattern persisted.

Although we found that effects of CT feedback and behavioral state were overall independent, we indeed revealed two subtle interactions. That is, CT feedback affected dLGN firing rates and burst ratios less strongly during periods of quiescence than during periods of locomotion. Importantly, locomotion is associated with a more desynchronized brain state (Niell and Stryker, 2010). A relationship between brain state and CT feedback effects has previously been reported by Wörgötter et al. (1998), who measured the effect of inactivating CT feedback on responses in the dLGN of anaesthetized cats while monitoring EEG activity. They found that during more desynchronized states CT feedback effects are more prominent. Also stressing the link between CT feedback and arousal-dependent modulations in mouse dLGN, a recent study showed that suppressing V1 by administering muscimol significantly reduced the correlation between dLGN firing rates and pupil size (Molnár et al., 2021).

Although our results speak in favor of dLGN processing being modulated by behavioral state and CT feedback independently, the current paradigm shift from recordings in anaesthetized to recordings in awake animals will hopefully contribute to further clarify the matter.

6.2 Diversity of L6 CT feedback

6.2.1 Anatomical diversity

CT feedback arises from the upper part of the deepest cortical layer, layer 6a, from where long-range axonal projections are sent to the thalamus by a distinct population of pyramidal cells (Frandonig et al., 2019; Gouwens et al., 2019). Even though this population, which in mice makes up about 65% of excitatory neurons in layer 6 (Olsen et al., 2012), is locally confined, it is not homogeneous. On a morphological level one can discriminate between two subtypes, one of which has a shorter apical dendrite reaching up to layer 4, while the apical dendrite of the second subtype extends to the most superficial layers (Olsen et al., 2012). Using unsupervised clustering algorithms recent studies determined three L6CT subtypes based on electrophysiological and morphological properties and two subtypes based on transcriptomics (Gouwens et al., 2019; Tasic et al., 2016). Single-cell RNA sequencing on L6CT neurons in the mouse barrel cortex could show that their transcriptional heterogeneity reflects in part their different laminar locations and projection patterns (Chevéé et al., 2018). CT neurons in the upper part of L6a send axonal projections to the first-order thalamic nucleus of the somatosensory system, the ventral posterior medial nucleus (VPM), and the thalamic reticular nucleus (TRN), whereas CT neurons in the lower part of layer 6a innervate the VPM and the higher-order thalamic nucleus of the somatosensory system, the posterior medial nucleus (Frandonig et al., 2019). Also, in primate V1, L6 can be subdivided into two tiers based on the projection target of its corticogeniculate neurons. Corticogeniculate neurons in the upper tier of L6 innervate the parvocellular layers of the dLGN, whereas corticogeniculate neurons in the lower tier project mainly to the magnocellular layers (Lund et al., 1975; Conley and Raczkowski, 1990; Fitzpatrick et al., 1994).

6.2.2 Functional diversity

How is this diversity in the CT population reflected on a functional level? Functional properties of L6CT neurons remain relatively unexplored, mainly owing to their deep location. Although L6CT neurons in mouse V1 share specific response properties, such as their ultrasparse firing and their strong orientation selectivity (Vélez-Fort et al., 2014), corticogeniculate cells in ferrets, rabbits, and monkeys display heterogeneous tuning (Harvey, 1978; Tsumoto and Suda, 1980; Swadlow and Weyand, 1987; Briggs and Usrey, 2005). Tuning properties that are suited to functionally cluster corticogenic-

ulate cells are, for instance, contrast sensitivity or temporal frequency tuning (Stoelzel et al., 2017; Briggs and Usrey, 2009). In primate V1, it has been shown that corticogeniculate neurons can be clustered based on their antidromic latencies and the degree to which their response is modulated by the temporal frequency of a drifting grating into three groups. Compared to simple cells, fast and slow complex cells are more sensitive to low contrast stimuli, prefer higher temporal frequencies, and display stronger surround suppression. The two complex cell population, on the other hand, differ with respect to their orientation and direction selectivity: Fast complex cells show sharper orientation tuning and are more sensitive to the direction in which the grating is drifting. In sum, the three populations display response properties that closely resemble those found in feedforward processing streams, which suggests that CT feedback is organized in segregated channels (Briggs and Usrey, 2009).

While our studies add important insights into the role of feedback for sensory processing in the mouse visual system, our approach of optogenetically manipulating CT feedback in PV-Cre and Ntsr1-Cre mice does not do justice to the diversity within the L6CT population. To gain a more complete understanding of CT feedback, future studies would greatly benefit from mice strains in which specific L6CT subpopulation could be targeted.

6.3 Manipulating CT feedback

In addition, our approach of suppressing L6CT neurons at the level of the cell body cannot rule out that thalamic activity is affected by other poly-synaptic routes. It is known that L6CT neurons have cortical axons collaterals which change the gain across cortical layers, including neurons in layer 5 (Bortone et al., 2014; Kim et al., 2014; Olsen et al., 2012). In the visual system, layer 5 pyramidal cells project to the superior colliculus (SC). Tectogeniculate neurons in the SC, in turn, provide driving input to the dorsolateral shell of the dLGN (Bickford et al., 2015; Cang et al., 2018).

Future studies should therefore manipulate CT feedback by inhibiting in the thalamus CT axon terminals. However, optogenetic inhibition of axon terminals remains difficult. While opening GtACRs can have, due to the high chloride concentration in axons, excitatory effects, photoactivating proton pumps at terminal sites can lead to a pH-dependent influx of calcium, which can in turn increase spontaneous neurotransmitter release (Mahn et al., 2016; Wiegert et al., 2017). A solution to this problem

is a targeting-enhanced mosquito homologue of the vertebrate encephalopsin, eOPN3. Light-activating eOPN3 recruits G protein-coupled receptors at the presynaptic terminals which, by reducing intracellular calcium concentrations, inhibits vesicle release (Mahn et al., 2021).

6.4 Conclusions and Outlook

The shift in model organism from anaesthetized cats and primates to awake mice in combination with the advent of genetic tools and steadily improving recording techniques has significantly facilitated the dissection and understanding of neural circuits, including the anatomy and the functional role of L6 corticothalamic projections. As established by the manuscripts in this thesis, L6 corticothalamic projections are highly structured and affect sensory processing in thalamocortical neurons on multiple levels, including their firing mode and their spatial integration properties.

These insights contribute to an emerging view, according to which the thalamus does not simply relay sensory information from the periphery to the cortex but rather constitutes an important processing stage at which cortical neurons can, via feedback connections, actively alter their inputs. Despite adding valuable information to this view, many interesting questions remain unanswered. For instance, do CT feedback connections in the mouse consist of parallel processing streams similar to what has been shown in primates; what is the relative contribution of inhibitory neurons in the TRN and in first-order thalamic nuclei to feedback-mediated inhibitory effects; and do these effects persist if we control for influences that are mediated by other polysynaptic corticofugal pathways?

Contextual modulations are not restricted to the thalamus but extend throughout the sensory systems. In mouse V1, we show that a large fraction of neurons is preferentially engaged by a rewarded or an unrewarded stimulus. Although we find a similar pattern at the level of the ACC, a structure that sends projections to V1, we cannot resolve the relationship between the two effects. An important follow-up question is therefore to which extent are the tuning preferences found at the level of V1 mediated by top-down projections from ACC.

Lastly, while we have probed contextual modulations in experimental setting that allowed us to optimally control any source of variance, investigating contextual modu-

lations and their link to feedback connections under more complex, ecologically relevant conditions will yield a more complete understanding of feedback.

7 Bibliography

- Agam, Y., Liu, H., Papanastassiou, A., Buia, C., Golby, A. J., Madsen, J. R., and Kreiman, G. (2010). Robust Selectivity to Two-Object Images in Human Visual Cortex. *Current Biology*, 20(9):872–879.
- Alberio, L., Locarno, A., Saponaro, A., Romano, E., Bercier, V., Albadri, S., Simeoni, F., Moleri, S., Pelucchi, S., Porro, A., Marcello, E., Barsotti, N., Kukovetz, K., Boender, A. J., Contestabile, A., Luo, S., Moutal, A., Ji, Y., Romani, G., Beltrame, M., Del Bene, F., Di Luca, M., Khanna, R., Colecraft, H. M., Pasqualetti, M., Thiel, G., Tonini, R., and Moroni, A. (2018). A light-gated potassium channel for sustained neuronal inhibition. *Nature Methods*, 15(11):969–976.
- Alitto, H. J. and Usrey, W. M. (2003). Corticothalamic feedback and sensory processing. *Current Opinion in Neurobiology*, 13(4):440–445.
- Alitto, H. J. and Usrey, W. M. (2008). Origin and Dynamics of Extraclassical Suppression in the Lateral Geniculate Nucleus of the Macaque Monkey. *Neuron*, 57(1):135–146.
- Allman, J., Miezin, F., and McGuinness, E. (1985). Stimulus Specific Responses from Beyond the Classical Receptive Field: Neurophysiological Mechanisms for Local-Global Comparisons in Visual Neurons. *Annual Review of Neuroscience*, 8(1):407–430.
- Andolina, I. M., Jones, H. E., and Sillito, A. M. (2013). Effects of cortical feedback on the spatial properties of relay cells in the lateral geniculate nucleus. *Journal of Neurophysiology*, 109(3):889–899.
- Andolina, I. M., Jones, H. E., Wang, W., and Sillito, A. M. (2007). Corticothalamic feedback enhances stimulus response precision in the visual system. *Proceedings of the National Academy of Sciences*, 104(5):1685–1690.
- Andrews, T. J. and Ewbank, M. P. (2004). Distinct representations for facial identity and changeable aspects of faces in the human temporal lobe. *NeuroImage*, 23(3):905–913.
- Angelucci, A. and Bressloff, P. C. (2006). Contribution of feedforward, lateral and feedback connections to the classical receptive field center and extra-classical recep-

- tive field surround of primate V1 neurons. In *Progress in Brain Research*, volume 154, pages 93–120. Elsevier.
- Angelucci, A., Levitt, J. B., Walton, E. J. S., Hupé, J.-M., Bullier, J., and Lund, J. S. (2002). Circuits for Local and Global Signal Integration in Primary Visual Cortex. *Journal of Neuroscience*, 22(19):8633–8646.
- Angelucci, A. and Sainsbury, K. (2006). Contribution of feedforward thalamic afferents and corticogeniculate feedback to the spatial summation area of macaque V1 and LGN. *Journal of Comparative Neurology*, 498(3):330–351.
- Arshavsky, V. Y., Lamb, T. D., and Pugh, E. N. (2002). G Proteins and Phototransduction. *Annual Review of Physiology*, 64(1):153–187.
- Atallah, B. V., Bruns, W., Carandini, M., and Scanziani, M. (2012). Parvalbumin-Expressing Interneurons Linearly Transform Cortical Responses to Visual Stimuli. *Neuron*, 73(1):159–170.
- Attinger, A., Wang, B., and Keller, G. B. (2017). Visuomotor Coupling Shapes the Functional Development of Mouse Visual Cortex. *Cell*, 169(7):1291–1302.
- Augustinaite, S. and Kuhn, B. (2020). Complementary Ca²⁺ Activity of Sensory Activated and Suppressed Layer 6 Corticothalamic Neurons Reflects Behavioral State. *Current Biology*, 30(20):3945–3960.
- Augustinaite, S., Kuhn, B., Helm, P. J., and Heggelund, P. (2014). NMDA Spike/Plateau Potentials in Dendrites of Thalamocortical Neurons. *Journal of Neuroscience*, 34(33):10892–10905.
- Aydın, Ç., Couto, J., Giugliano, M., Farrow, K., and Bonin, V. (2018). Locomotion modulates specific functional cell types in the mouse visual thalamus. *Nature Communications*, 9(1):1–12.
- Baker, C. I., Behrmann, M., and Olson, C. R. (2002). Impact of learning on representation of parts and wholes in monkey inferotemporal cortex. *Nature Neuroscience*, 5(11):1210–1216.
- Barbaresi, P., Spreafico, R., Frassoni, C., and Rustioni, A. (1986). GABAergic neurons are present in the dorsal column nuclei but not in the ventroposterior complex of rats. *Brain Research*, 382(2):305–326.

- Béhuret, S., Deleuze, C., and Bal, T. (2015). Corticothalamic Synaptic Noise as a Mechanism for Selective Attention in Thalamic Neurons. *Frontiers in Neural Circuits*, 9:80.
- Berkes, P., Orban, G., Lengyel, M., and Fiser, J. (2011). Spontaneous Cortical Activity Reveals Hallmarks of an Optimal Internal Model of the Environment. *Science*, 331(6013):83–87.
- Bickford, M. E. (2016). Thalamic Circuit Diversity: Modulation of the Driver/Modulator Framework. *Frontiers in Neural Circuits*, 9:86.
- Bickford, M. E., Zhou, N., Krahe, T. E., Govindaiah, G., and Guido, W. (2015). Retinal and Tectal "Driver-Like" Inputs Converge in the Shell of the Mouse Dorsal Lateral Geniculate Nucleus. *Journal of Neuroscience*, 35(29):10523–10534.
- Binzegger, T. (2004). A Quantitative Map of the Circuit of Cat Primary Visual Cortex. *Journal of Neuroscience*, 24(39):8441–8453.
- Blakemore, C. and Tobin, E. (1972). Lateral inhibition between orientation detectors in the cat's visual cortex. *Experimental Brain Research*, 15(4):439–440.
- Bokor, H., Acsady, L., and Deschenes, M. (2008). Vibrissal Responses of Thalamic Cells That Project to the Septal Columns of the Barrel Cortex and to the Second Somatosensory Area. *Journal of Neuroscience*, 28(20):5169–5177.
- Bonin, V. (2005). The Suppressive Field of Neurons in Lateral Geniculate Nucleus. *Journal of Neuroscience*, 25(47):10844–10856.
- Born, G., Schneider-Soupiadis, F. A., Erisken, S., Vaiceliunaite, A., Lao, C. L., Mo-barhan, M. H., Spacek, M. A., Einevoll, G. T., and Busse, L. (2021). Corticothalamic feedback sculpts visual spatial integration in mouse thalamus. *Nature Neuroscience*.
- Bortone, D. S., Olsen, S. R., and Scanziani, M. (2014). Translaminar Inhibitory Cells Recruited by Layer 6 Corticothalamic Neurons Suppress Visual Cortex. *Neuron*, 82(2):474–485.
- Bosking, W. H., Zhang, Y., Schofield, B., and Fitzpatrick, D. (1997). Orientation Selectivity and the Arrangement of Horizontal Connections in Tree Shrew Striate Cortex. *Journal of Neuroscience*, 17(6):2112–2127.

- Bowman, E. M., Brown, V. J., Kertzman, C., Schwarz, U., and Robinson, D. L. (1993). Covert orienting of attention in macaques. I. Effects of behavioral context. *Journal of Neurophysiology*, 70(1):431–443.
- Briggs, F. and Usrey, W. M. (2005). Temporal properties of feedforward and feedback pathways between the thalamus and visual cortex in the ferret. *Thalamus and Related Systems*, 3(02):133.
- Briggs, F. and Usrey, W. M. (2009). Parallel Processing in the Corticogeniculate Pathway of the Macaque Monkey. *Neuron*, 62(1):135–146.
- Briggs, F. and Usrey, W. M. (2011). Corticogeniculate feedback and visual processing in the primate. *Journal of Physiology*, 589(1):33–40.
- Busse, L. (2018). The influence of locomotion on sensory processing and its underlying neuronal circuits. *e-Neuroforum*, 24(1):A41–A51.
- Cang, J., Savier, E., Barchini, J., and Liu, X. (2018). Visual Function, Organization, and Development of the Mouse Superior Colliculus. *Annual Review of Vision Science*, 4(1):239–262.
- Cardin, J. A., Palmer, L. A., and Contreras, D. (2008). Cellular Mechanisms Underlying Stimulus-Dependent Gain Modulation in Primary Visual Cortex Neurons In Vivo. *Neuron*, 59(1):150–160.
- Cavanaugh, J. R., Bair, W., and Movshon, J. A. (2002). Nature and Interaction of Signals From the Receptive Field Center and Surround in Macaque V1 Neurons. *Journal of Neurophysiology*, 88(5):2530–2546.
- Chance, F. S., Abbott, L., and Reyes, A. D. (2002). Gain Modulation from Background Synaptic Input. *Neuron*, 35(4):773–782.
- Chevée, M., Robertson, J. D. J., Cannon, G. H., Brown, S. P., and Goff, L. A. (2018). Variation in Activity State, Axonal Projection, and Position Define the Transcriptional Identity of Individual Neocortical Projection Neurons. *Cell Reports*, 22(2):441–455.
- Chubykin, A. A., Roach, E. B., Bear, M. F., and Shuler, M. G. H. (2013). A Cholinergic Mechanism for Reward Timing within Primary Visual Cortex. *Neuron*, 77(4):723–735.

- Clark, A. (2013). Whatever next? Predictive brains, situated agents, and the future of cognitive science. *Behavioral and Brain Sciences*, 36(3):181–204.
- Conley, M. and Raczkowski, D. (1990). Sublaminar organization within layer VI of the striate cortex in Galago. *Journal of Comparative Neurology*, 302(2):425–436.
- Crabtree, J. W. (2018). Functional Diversity of Thalamic Reticular Subnetworks. *Frontiers in Systems Neuroscience*, 12:41.
- Crabtree, J. W. and Killackey, H. P. (1989). The Topographic Organization and Axis of Projection within the Visual Sector of the Rabbit's Thalamic Reticular Nucleus. *European Journal of Neuroscience*, 1(1):94–109.
- Crandall, S. R. and Cox, C. L. (2012). Local Dendrodendritic Inhibition Regulates Fast Synaptic Transmission in Visual Thalamus. *Journal of Neuroscience*, 32(7):2513–2522.
- Crandall, S. R., Cruikshank, S. J., and Connors, B. W. (2015). A Corticothalamic Switch: Controlling the Thalamus with Dynamic Synapses. *Neuron*, 86(3):768–782.
- Crick, F. (1984). Function of the thalamic reticular complex: The searchlight hypothesis. *Proceedings of the National Academy of Sciences*, 81(14):4586–4590.
- de Labra, C., Rivadulla, C., Grieve, K., Marino, J., Espinosa, N., and Cudeiro, J. (2007). Changes in Visual Responses in the Feline dLGN: Selective Thalamic Suppression Induced by Transcranial Magnetic Stimulation of V1. *Cerebral Cortex*, 17(6):1376–1385.
- De Souza, E. B. and Van Loon, G. R. (1986). Brain serotonin and catecholamine responses to repeated stress in rats. *Brain Research*, 367(1-2):77–86.
- DeAngelis, G. C., Freeman, R. D., and Ohzawa, I. (1994). Length and width tuning of neurons in the cat's primary visual cortex. *Journal of Neurophysiology*, 71(1):347–374.
- Deisseroth, K. (2011). Optogenetics. *Nature Methods*, 8(1):26–29.
- Denman, D. J. and Contreras, D. (2016). On Parallel Streams through the Mouse Dorsal Lateral Geniculate Nucleus. *Frontiers in Neural Circuits*, 10:20.

- Deschenes, M. and Hu, B. (1990). Electrophysiology and Pharmacology of the Corticothalamic Input to Lateral Thalamic Nuclei: An Intracellular Study in the Cat. *European Journal of Neuroscience*, 2(2):140–152.
- Deschênes, M., Veinante, P., and Zhang, Z.-W. (1998). The organization of corticothalamic projections: Reciprocity versus parity. *Brain Research Reviews*, 28(3):286–308.
- Desimone, R. and Duncan, J. (1995). Neural Mechanisms of Selective Visual Attention. *Annual Review of Neuroscience*, 18(1):193–222.
- Devinsky, O., Morrell, M. J., and Vogt, B. A. (1995). Contributions of anterior cingulate cortex to behaviour. *Brain*, 118(1):279–306.
- Diamanti, E. M., Reddy, C. B., Schröder, S., Muzzu, T., Harris, K. D., Saleem, A. B., and Carandini, M. (2021). Spatial modulation of visual responses arises in cortex with active navigation. *eLife*, 10:e63705.
- Ergenzinger, E., Glasier, M., Hahm, J., and Pons, T. (1998). Cortically induced thalamic plasticity in the primate somatosensory system. *Nature Neuroscience*, 1(3):226–229.
- Erisken, S., Vaiceliunaite, A., Jurjut, O., Fiorini, M., Katzner, S., and Busse, L. (2014). Effects of Locomotion Extend throughout the Mouse Early Visual System. *Current Biology*, 24(24):2899–2907.
- Escabí, M. A., Miller, L. M., Read, H. L., and Schreiner, C. E. (2003). Naturalistic Auditory Contrast Improves Spectrotemporal Coding in the Cat Inferior Colliculus. *Journal of Neuroscience*, 23(37):11489–11504.
- Evangelio, M., García-Amado, M., and Clascá, F. (2018). Thalamocortical Projection Neuron and Interneuron Numbers in the Visual Thalamic Nuclei of the Adult C57BL/6 Mouse. *Frontiers in Neuroanatomy*, 12:27.
- Felleman, D. J. and Van Essen, D. C. (1991). Distributed Hierarchical Processing in the Primate Cerebral Cortex. *Cerebral Cortex*, 1(1):1–47.
- Fenko, L., Yizhar, O., and Deisseroth, K. (2011). The Development and Application of Optogenetics. *Annual Review of Neuroscience*, 34(1):389–412.

- Ferguson, K. A. and Cardin, J. A. (2020). Mechanisms underlying gain modulation in the cortex. *Nature Reviews Neuroscience*, 21(2):80–92.
- Fiser, A., Mahringer, D., Oyibo, H. K., Petersen, A. V., Leinweber, M., and Keller, G. B. (2016). Experience-dependent spatial expectations in mouse visual cortex. *Nature Neuroscience*, 19(12):1658–1664.
- Fitzpatrick, D., Usrey, W. M., Schofield, B. R., and Einstein, G. (1994). The sublamina organization of corticogeniculate neurons in layer 6 of macaque striate cortex. *Visual Neuroscience*, 11(2):307–315.
- Frandonig, J. E., Matney, C. J., Lee, K., Kim, J., Chevée, M., Kim, S.-J., Bickert, A. A., and Brown, S. P. (2019). The Synaptic Organization of Layer 6 Circuits Reveals Inhibition as a Major Output of a Neocortical Sublamina. *Cell Reports*, 28(12):3131–3143.
- Fu, Y. (2010). Phototransduction in Rods and Cones. In *Webvision: The Organization of the Retina and Visual System [Internet]*, page 38. University of Utah Health Sciences Center.
- Garcia-Lazaro, J., Ahmed, B., and Schnupp, J. (2006). Tuning to Natural Stimulus Dynamics in Primary Auditory Cortex. *Current Biology*, 16(3):264–271.
- Gentet, L. J. and Ulrich, D. (2004). Electrophysiological characterization of synaptic connections between layer VI cortical cells and neurons of the nucleus reticularis thalami in juvenile rats. *European Journal of Neuroscience*, 19(3):625–633.
- Ghanem, A. and Conzelmann, K.-K. (2016). G gene-deficient single-round rabies viruses for neuronal circuit analysis. *Virus Research*, 216:41–54.
- Gilbert, C. D., Das, A., Ito, M., Kapadia, M., and Westheimer, G. (1996). Spatial integration and cortical dynamics. *Proceedings of the National Academy of Sciences*, 93(2):615–622.
- Gilbert, C. D. and Li, W. (2013). Top-down influences on visual processing. *Nature Reviews Neuroscience*, 14(5):350–363.
- Gilbert, C. D. and Sigman, M. (2007). Brain States: Top-Down Influences in Sensory Processing. *Neuron*, 54(5):677–696.

- Gilbert, C. D. and Wiesel, T. N. (1990). The influence of contextual stimuli on the orientation selectivity of cells in primary visual cortex of the cat. *Vision Research*, 30(11):1689–1701.
- Godwin, D. W., Vaughan, J. W., and Sherman, S. M. (1996). Metabotropic glutamate receptors switch visual response mode of lateral geniculate nucleus cells from burst to tonic. *Journal of Neurophysiology*, 76(3):1800–1816.
- Golshani, P., Liu, X.-B., and Jones, E. G. (2001). Differences in quantal amplitude reflect GluR4- subunit number at corticothalamic synapses on two populations of thalamic neurons. *Proceedings of the National Academy of Sciences*, 98(7):4172–4177.
- Gong, S., Doughty, M., Harbaugh, C. R., Cummins, A., Hatten, M. E., Heintz, N., and Gerfen, C. R. (2007). Targeting Cre Recombinase to Specific Neuron Populations with Bacterial Artificial Chromosome Constructs. *Journal of Neuroscience*, 27(37):9817–9823.
- Gouwens, N. W., Sorensen, S. A., Berg, J., Lee, C., Jarsky, T., Ting, J., Sunkin, S. M., Feng, D., Anastassiou, C. A., Barkan, E., Bickley, K., Blesie, N., Braun, T., Brouner, K., Budzillo, A., Caldejon, S., Casper, T., Castelli, D., Chong, P., Crichton, K., Cuhaciyani, C., Daigle, T. L., Dalley, R., Dee, N., Desta, T., Ding, S.-L., Dingman, S., Doperalski, A., Dotson, N., Egdorf, T., Fisher, M., de Frates, R. A., Garren, E., Garwood, M., Gary, A., Gaudreault, N., Godfrey, K., Gorham, M., Gu, H., Habel, C., Hadley, K., Harrington, J., Harris, J. A., Henry, A., Hill, D., Josephsen, S., Kebede, S., Kim, L., Kroll, M., Lee, B., Lemon, T., Link, K. E., Liu, X., Long, B., Mann, R., McGraw, M., Mihalas, S., Mukora, A., Murphy, G. J., Ng, L., Ngo, K., Nguyen, T. N., Nicovich, P. R., Oldre, A., Park, D., Parry, S., Perkins, J., Potekhina, L., Reid, D., Robertson, M., Sandman, D., Schroedter, M., Slaughterbeck, C., Soler-Llavina, G., Sulc, J., Szafer, A., Tasic, B., Taskin, N., Teeter, C., Thatra, N., Tung, H., Wakeman, W., Williams, G., Young, R., Zhou, Z., Farrell, C., Peng, H., Hawrylycz, M. J., Lein, E., Ng, L., Arkhipov, A., Bernard, A., Phillips, J. W., Zeng, H., and Koch, C. (2019). Classification of electrophysiological and morphological neuron types in the mouse visual cortex. *Nature Neuroscience*, 22(7):1182–1195.
- Govorunova, E. G., Sineshchekov, O. A., Janz, R., Liu, X., and Spudich, J. L. (2015).

- Natural light-gated anion channels: A family of microbial rhodopsins for advanced optogenetics. *Science*, 349(6248):647–650.
- Guillery, R., Feig, S., and Lozsádi, D. (1998). Paying attention to the thalamic reticular nucleus. *Trends in Neurosciences*, 21(1):28–32.
- Gulyas, B., Lagae, L., Eysel, U., and Orban, G. A. (1990). Corticofugal feedback influences the responses of geniculate neurons to moving stimuli. *Experimental Brain Research*, 79(2):441–446.
- Guo, K., Robertson, R. G., Mahmoodi, S., and Young, M. P. (2005). Centre-surround interactions in response to natural scene stimulation in the primary visual cortex. *European Journal of Neuroscience*, 21(2):536–548.
- Guo, W., Clause, A. R., Barth-Maron, A., and Polley, D. B. (2017). A Corticothalamic Circuit for Dynamic Switching between Feature Detection and Discrimination. *Neuron*, 95(1):180–194.
- Hall, I. C., Sell, G. L., Chester, E. M., and Hurley, L. M. (2012). Stress-evoked increases in serotonin in the auditory midbrain do not directly result from elevations in serum corticosterone. *Behavioural Brain Research*, 226(1):41–49.
- Hanson, J. L. and Hurley, L. M. (2014). Context-dependent fluctuation of serotonin in the auditory midbrain: The influence of sex, reproductive state and experience. *Journal of Experimental Biology*, 217(4):526–535.
- Harris, J. A., Mihalas, S., Hirokawa, K. E., Whitesell, J. D., Choi, H., Bernard, A., Bohn, P., Caldejon, S., Casal, L., Cho, A., Feiner, A., Feng, D., Gaudreault, N., Gersen, C. R., Graddis, N., Groblewski, P. A., Henry, A. M., Ho, A., Howard, R., Knox, J. E., Kuan, L., Kuang, X., Lecoq, J., Lesnar, P., Li, Y., Luviano, J., McConoughey, S., Mortrud, M. T., Naeemi, M., Ng, L., Oh, S. W., Ouellette, B., Shen, E., Sorensen, S. A., Wakeman, W., Wang, Q., Wang, Y., Williford, A., Phillips, J. W., Jones, A. R., Koch, C., and Zeng, H. (2019). Hierarchical organization of cortical and thalamic connectivity. *Nature*, 575(7781):195–202.
- Harvey, A. (1978). Characteristics of corticothalamic neurons in area 17 of the cat. *Neuroscience Letters*, 7(2-3):177–181.

- Hasse, J. M. and Briggs, F. (2017a). Corticogeniculate feedback sharpens the temporal precision and spatial resolution of visual signals in the ferret. *Proceedings of the National Academy of Sciences*, 114(30):E6222–E6230.
- Hasse, J. M. and Briggs, F. (2017b). A cross-species comparison of corticogeniculate structure and function. *Visual Neuroscience*, 34.
- Hembrook-Short, J. R., Mock, V. L., and Briggs, F. (2017). Attentional Modulation of Neuronal Activity Depends on Neuronal Feature Selectivity. *Current Biology*, 27(13):1878–1887.
- Herzog, M. H. and Clarke, A. M. (2014). Why vision is not both hierarchical and feedforward. *Frontiers in Computational Neuroscience*, 8:135.
- Hirsch, J. A., Wang, X., Sommer, F. T., and Martinez, L. M. (2015). How Inhibitory Circuits in the Thalamus Serve Vision. *Annual Review of Neuroscience*, 38(1):309–329.
- Holt, G. R. and Koch, C. (1997). Shunting Inhibition Does Not Have a Divisive Effect on Firing Rates. *Neural Computation*, 9(5):1001–1013.
- Hoogland, P. V., Welker, E., and Van der Loos, H. (1987). Organization of the projections from barrel cortex to thalamus in mice studied with Phaseolus vulgaris-leucoagglutinin and HRP. *Experimental Brain Research*, 68(1):73–87.
- Hupé, J. M., James, A. C., Payne, B. R., Lomber, S. G., Girard, P., and Bullier, J. (1998). Cortical feedback improves discrimination between figure and background by V1, V2 and V3 neurons. *Nature*, 394(6695):784–787.
- Hvoslef-Eide, M., Nilsson, S. R. O., Hailwood, J. M., Robbins, T. W., Saksida, L. M., Mar, A. C., and Bussey, T. J. (2018). Effects of anterior cingulate cortex lesions on a continuous performance task for mice. *Brain and Neuroscience Advances*, 2:239821281877296.
- Ichida, J. M. and Casagrande, V. A. (2002). Organization of the feedback pathway from striate cortex (V1) to the lateral geniculate nucleus (LGN) in the owl monkey (*Aotus trivirgatus*). *Journal of Comparative Neurology*, 454(3):272–283.

- Jackman, S. L., Turecek, J., Belinsky, J. E., and Regehr, W. G. (2016). The calcium sensor synaptotagmin 7 is required for synaptic facilitation. *Nature*, 529(7584):88–91.
- Jacob, S. N. and Nienborg, H. (2018). Monoaminergic Neuromodulation of Sensory Processing. *Frontiers in Neural Circuits*, 12:51.
- Jeon, D., Kim, S., Chetana, M., Jo, D., Ruley, H. E., Lin, S.-Y., Rabah, D., Kinet, J.-P., and Shin, H.-S. (2010). Observational fear learning involves affective pain system and Cav1.2 Ca²⁺ channels in ACC. *Nature Neuroscience*, 13(4):482–488.
- Jones, H. E., Andolina, I. M., Ahmed, B., Shipp, S. D., Clements, J. T. C., Grieve, K. L., Cudeiro, J., Salt, T. E., and Sillito, A. M. (2012). Differential Feedback Modulation of Center and Surround Mechanisms in Parvocellular Cells in the Visual Thalamus. *Journal of Neuroscience*, 32(45):15946–15951.
- Jones, H. E. and Sillito, A. M. (1994). The Length - Response Properties of Cells in the Feline Perigeniculate Nucleus. *European Journal of Neuroscience*, 6(7):1199–1204.
- Kaila, K., Price, T. J., Payne, J. A., Puskarjov, M., and Voipio, J. (2014). Cation-chloride cotransporters in neuronal development, plasticity and disease. *Nature Reviews Neuroscience*, 15(10):637–654.
- Kanwisher, N., McDermott, J., and Chun, M. M. (1997). The Fusiform Face Area: A Module in Human Extrastriate Cortex Specialized for Face Perception. *Journal of Neuroscience*, 17(11):4302–4311.
- Kanwisher, N. and Yovel, G. (2006). The fusiform face area: A cortical region specialized for the perception of faces. *Philosophical Transactions of the Royal Society B: Biological Sciences*, 361(1476):2109–2128.
- Kapadia, M. K., Ito, M., Gilbert, C. D., and Westheimer, G. (1995). Improvement in visual sensitivity by changes in local context: Parallel studies in human observers and in V1 of alert monkeys. *Neuron*, 15(4):843–856.
- Katzner, S., Born, G., and Busse, L. (2019). V1 microcircuits underlying mouse visual behavior. *Current Opinion in Neurobiology*, 58:191–198.
- Kayama, Y., Shosaku, A., and Doty, R. (1984). Cryogenic blockade of the visual cortico-thalamic projection in the rat. *Experimental Brain Research*, 54(1):157–165.

- Keller, A. J., Roth, M. M., and Scanziani, M. (2020). Feedback generates a second receptive field in neurons of the visual cortex. *Nature*, 582(7813):545–549.
- Keller, G. B., Bonhoeffer, T., and Hübener, M. (2012). Sensorimotor Mismatch Signals in Primary Visual Cortex of the Behaving Mouse. *Neuron*, 74(5):809–815.
- Keller, G. B. and Hahnloser, R. H. R. (2009). Neural processing of auditory feedback during vocal practice in a songbird. *Nature*, 457(7226):187–190.
- Keller, G. B. and Mrsic-Flogel, T. D. (2018). Predictive Processing: A Canonical Cortical Computation. *Neuron*, 100(2):424–435.
- Khan, A. G. and Hofer, S. B. (2018). Contextual signals in visual cortex. *Current Opinion in Neurobiology*, 52:131–138.
- Kim, J., Matney, C. J., Blankenship, A., Hestrin, S., and Brown, S. P. (2014). Layer 6 Corticothalamic Neurons Activate a Cortical Output Layer, Layer 5a. *Journal of Neuroscience*, 34(29):9656–9664.
- Kirchberger, L., Mukherjee, S., Schnabel, U. H., van Beest, E. H., Barsegyan, A., Levelt, C. N., Heimel, J. A., Lorteije, J. A. M., van der Togt, C., Self, M. W., and Roelfsema, P. R. (2021). The essential role of recurrent processing for figure-ground perception in mice. *Science Advances*, 7(27):eabe1833.
- Kirchgessner, M. A., Franklin, A. D., and Callaway, E. M. (2020). Context-dependent and dynamic functional influence of corticothalamic pathways to first- and higher-order visual thalamus. *Proceedings of the National Academy of Sciences*, 117(23):13066–13077.
- Klink, P. C., Dagnino, B., Gariel-Mathis, M.-A., and Roelfsema, P. R. (2017). Distinct Feedforward and Feedback Effects of Microstimulation in Visual Cortex Reveal Neural Mechanisms of Texture Segregation. *Neuron*, 95(1):209–220.
- Knierim, J. J. and van Essen, D. C. (1992). Neuronal responses to static texture patterns in area V1 of the alert macaque monkey. *Journal of Neurophysiology*, 67(4):961–980.
- Lamme, V. A. and Roelfsema, P. R. (2000). The distinct modes of vision offered by feedforward and recurrent processing. *Trends in Neurosciences*, 23(11):571–579.

- Land, P. W., Buffer, S. A., and Yaskosky, J. D. (1995). Barreloids in adult rat thalamus: Three-dimensional architecture and relationship to somatosensory cortical barrels. *Journal of Comparative Neurology*, 355(4):573–588.
- Larkum, M. (2013). A cellular mechanism for cortical associations: An organizing principle for the cerebral cortex. *Trends in Neurosciences*, 36(3):141–151.
- Lee, S.-H. and Dan, Y. (2012). Neuromodulation of Brain States. *Neuron*, 76(1):209–222.
- Lee, T. S. and Mumford, D. (2003). Hierarchical Bayesian inference in the visual cortex. *Journal of the Optical Society of America A*, 20(7):1434.
- Leinweber, M., Ward, D. R., Sobczak, J. M., Attinger, A., and Keller, G. B. (2017). A Sensorimotor Circuit in Mouse Cortex for Visual Flow Predictions. *Neuron*, 95(6):1420–1432.
- Lennie, P. (1998). Single Units and Visual Cortical Organization. *Perception*, 27(8):889–935.
- Li, Y., Lopez-Huerta, V. G., Adiconis, X., Levandowski, K., Choi, S., Simmons, S. K., Arias-Garcia, M. A., Guo, B., Yao, A. Y., Blosser, T. R., Wimmer, R. D., Aida, T., Atamian, A., Naik, T., Sun, X., Bi, D., Malhotra, D., Hession, C. C., Shema, R., Gomes, M., Li, T., Hwang, E., Krol, A., Kowalczyk, M., Peça, J., Pan, G., Halassa, M. M., Levin, J. Z., Fu, Z., and Feng, G. (2020). Distinct subnetworks of the thalamic reticular nucleus. *Nature*, 583(7818):819–824.
- Li, Y.-t., Ibrahim, L. A., Liu, B.-h., Zhang, L. I., and Tao, H. W. (2013). Linear transformation of thalamocortical input by intracortical excitation. *Nature Neuroscience*, 16(9):1324–1330.
- Liang, L., Fratzl, A., Reggiani, J. D., El Mansour, O., Chen, C., and Andermann, M. L. (2020). Retinal Inputs to the Thalamus Are Selectively Gated by Arousal. *Current Biology*, 30(20):3923–3934.
- Livingstone, M. and Hubel, D. (1988). Segregation of form, color, movement, and depth: Anatomy, physiology, and perception. *Science*, 240(4853):740–749.
- Logothetis, N. K., Pauls, J., and Poggio, T. (1995). Shape representation in the inferior temporal cortex of monkeys. *Current Biology*, 5(5):552–563.

- Lomber, S. G. (1999). The advantages and limitations of permanent or reversible deactivation techniques in the assessment of neural function. *Journal of Neuroscience Methods*, 86(2):109–117.
- Lu, S. M., Guido, W., and Sherman, S. M. (1992). Effects of membrane voltage on receptive field properties of lateral geniculate neurons in the cat: Contributions of the low-threshold Ca²⁺ conductance. *Journal of Neurophysiology*, 68(6):2185–2198.
- Lund, J. S., Lund, R. D., Hendrickson, A. E., Bunt, A. H., and Fuchs, A. F. (1975). The origin of efferent pathways from the primary visual cortex, area 17, of the macaque monkey as shown by retrograde transport of horseradish peroxidase. *Journal of Comparative Neurology*, 164(3):287–303.
- Madisen, L., Mao, T., Koch, H., Zhuo, J.-m., Berenyi, A., Fujisawa, S., Hsu, Y.-W. A., Garcia, A. J., Gu, X., Zanella, S., Kidney, J., Gu, H., Mao, Y., Hooks, B. M., Boyden, E. S., Buzsáki, G., Ramirez, J. M., Jones, A. R., Svoboda, K., Han, X., Turner, E. E., and Zeng, H. (2012). A toolbox of Cre-dependent optogenetic transgenic mice for light-induced activation and silencing. *Nature Neuroscience*, 15(5):793–802.
- Mahn, M., Gibor, L., Patil, P., Cohen-Kashi Malina, K., Oring, S., Printz, Y., Levy, R., Lampl, I., and Yizhar, O. (2018). High-efficiency optogenetic silencing with soma-targeted anion-conducting channelrhodopsins. *Nature Communications*, 9(1):4125.
- Mahn, M., Prigge, M., Ron, S., Levy, R., and Yizhar, O. (2016). Biophysical constraints of optogenetic inhibition at presynaptic terminals. *Nature Neuroscience*, 19(4):554–556.
- Mahn, M., Saraf-Sinik, I., Patil, P., Pulin, M., Bitton, E., Karalis, N., Bruentgens, F., Palgi, S., Gat, A., Dine, J., Wietek, J., Davidi, I., Levy, R., Litvin, A., Zhou, F., Sauter, K., Soba, P., Schmitz, D., Lüthi, A., Rost, B. R., Wiegert, J. S., and Yizhar, O. (2021). Efficient optogenetic silencing of neurotransmitter release with a mosquito rhodopsin. *Neuron*, 109(10):1621–1635.
- Makino, H. and Komiyama, T. (2015). Learning enhances the relative impact of top-down processing in the visual cortex. *Nature Neuroscience*, 18(8):1116–1122.
- Malach, R., Amir, Y., Harel, M., and Grinvald, A. (1993). Relationship between intrinsic connections and functional architecture revealed by optical imaging and in vivo

- targeted biocytin injections in primate striate cortex. *Proceedings of the National Academy of Sciences*, 90(22):10469–10473.
- Malyshev, A., Roshchin, M., Smirnova, G., Dolgikh, D., Balaban, P., and Ostrovsky, M. (2017). Chloride conducting light activated channel GtACR2 can produce both cessation of firing and generation of action potentials in cortical neurons in response to light. *Neuroscience Letters*, 640:76–80.
- Martin, P. R. and Solomon, S. G. (2011). Information processing in the primate visual system. *Journal of Physiology*, 589(1):29–31.
- Martinez-Garcia, R. I., Voelcker, B., Zaltsman, J. B., Patrick, S. L., Stevens, T. R., Connors, B. W., and Cruikshank, S. J. (2020). Two dynamically distinct circuits drive inhibition in the sensory thalamus. *Nature*, 583(7818):813–818.
- Martinez-Trujillo, J. C. and Treue, S. (2004). Feature-Based Attention Increases the Selectivity of Population Responses in Primate Visual Cortex. *Current Biology*, 14(9):744–751.
- Mattis, J., Tye, K. M., Ferenczi, E. A., Ramakrishnan, C., O’Shea, D. J., Prakash, R., Gunaydin, L. A., Hyun, M., Fenno, L. E., Gradinaru, V., Yizhar, O., and Deisseroth, K. (2012). Principles for applying optogenetic tools derived from direct comparative analysis of microbial opsins. *Nature Methods*, 9(2):159–172.
- McAlonan, K. (2006). Attentional Modulation of Thalamic Reticular Neurons. *Journal of Neuroscience*, 26(16):4444–4450.
- McAlonan, K., Cavanaugh, J., and Wurtz, R. H. (2008). Guarding the gateway to cortex with attention in visual thalamus. *Nature*, 456(7220):391–394.
- McClurkin, J. W. and Marrocco, R. T. (1984). Visual cortical input alters spatial tuning in monkey lateral geniculate nucleus cells. *Journal of Physiology*, 348(1):135–152.
- McCormick, D. A. and Pape, H. C. (1990). Noradrenergic and serotonergic modulation of a hyperpolarization-activated cation current in thalamic relay neurones. *Journal of Physiology*, 431(1):319–342.
- McCormick, D. A. and von Krosigk, M. (1992). Corticothalamic activation modulates thalamic firing through glutamate “metabotropic” receptors. *Proceedings of the National Academy of Sciences*, 89(7):2774–2778.

- McKee, J. L., Riesenhuber, M., Miller, E. K., and Freedman, D. J. (2014). Task Dependence of Visual and Category Representations in Prefrontal and Inferior Temporal Cortices. *Journal of Neuroscience*, 34(48):16065–16075.
- Mease, R. A., Krieger, P., and Groh, A. (2014). Cortical control of adaptation and sensory relay mode in the thalamus. *Proceedings of the National Academy of Sciences*, 111(18):6798–6803.
- Mease, R. A., Kuner, T., Fairhall, A. L., and Groh, A. (2017). Multiplexed Spike Coding and Adaptation in the Thalamus. *Cell Reports*, 19(6):1130–1140.
- Metherate, R., Cox, C., and Ashe, J. (1992). Cellular bases of neocortical activation: Modulation of neural oscillations by the nucleus basalis and endogenous acetylcholine. *Journal of Neuroscience*, 12(12):4701–4711.
- Molnár, B., Sere, P., Bordé, S., Koós, K., Zsigri, N., Horváth, P., and Lőrincz, M. L. (2021). Cell Type-Specific Arousal-Dependent Modulation of Thalamic Activity in the Lateral Geniculate Nucleus. *Cerebral Cortex Communications*, 2(2):tgab020.
- Montero, V. M. (2000). Attentional activation of the visual thalamic reticular nucleus depends on ‘top-down’ inputs from the primary visual cortex via corticogeniculate pathways. *Brain Research*, 864(1):95–104.
- Montero, V. M., Guillery, R. W., and Woolsey, C. N. (1977). Retinotopic organization within the thalamic reticular nucleus demonstrated by a double label autoradiographic technique. *Brain Research*, 138(3):407–421.
- Moore, T. and Armstrong, K. M. (2003). Selective gating of visual signals by microstimulation of frontal cortex. *Nature*, 421(6921):370–373.
- Moran, J. and Desimone, R. (1985). Selective attention gates visual processing in the extrastriate cortex. *Science*, 229(4715):782–784.
- Morgan, J. L. and Lichtman, J. W. (2020). An Individual Interneuron Participates in Many Kinds of Inhibition and Innervates Much of the Mouse Visual Thalamus. *Neuron*, 106(3):468–481.
- Murphy, P., Duckett, S. G., and Sillito, A. (1999). Feedback Connections to the Lateral Geniculate Nucleus and Cortical Response Properties. *Science*, 286(5444):1552–1554.

- Murphy, P. C. and Sillito, A. M. (1987). Length tuning in the visual pathway. *Nature*, 329(6141):727–729.
- Nassi, J. J. and Callaway, E. M. (2009). Parallel processing strategies of the primate visual system. *Nature Reviews Neuroscience*, 10(5):360–372.
- Nassi, J. J., Lomber, S. G., and Born, R. T. (2013). Corticocortical Feedback Contributes to Surround Suppression in V1 of the Alert Primate. *Journal of Neuroscience*, 33(19):8504–8517.
- Natan, R. G., Rao, W., and Geffen, M. N. (2017). Cortical Interneurons Differentially Shape Frequency Tuning following Adaptation. *Cell Reports*, 21(4):878–890.
- Nelson, J. and Frost, B. (1978). Orientation-selective inhibition from beyond the classic visual receptive field. *Brain Research*, 139(2):359–365.
- Niell, C. M. and Stryker, M. P. (2010). Modulation of Visual Responses by Behavioral State in Mouse Visual Cortex. *Neuron*, 65(4):472–479.
- O’Connor, D. H., Fukui, M. M., Pinsk, M. A., and Kastner, S. (2002). Attention modulates responses in the human lateral geniculate nucleus. *Nature Neuroscience*, 5(11):1203–1209.
- Ogden, T. E. (1960). On the Function of Corticothalamic Neurons. *Science*, 131(3392):40–40.
- Olsen, S. R., Bortone, D. S., Adesnik, H., and Scanziani, M. (2012). Gain control by layer six in cortical circuits of vision. *Nature*, 483(7387):47–52.
- Pecka, M., Han, Y., Sader, E., and Mrsic-Flogel, T. D. (2014). Experience-Dependent Specialization of Receptive Field Surround for Selective Coding of Natural Scenes. *Neuron*, 84(2):457–469.
- Pinault, D. (2004). The thalamic reticular nucleus: Structure, function and concept. *Brain Research Reviews*, 46(1):1–31.
- Pinto, L., Goard, M. J., Estandian, D., Xu, M., Kwan, A. C., Lee, S.-H., Harrison, T. C., Feng, G., and Dan, Y. (2013). Fast modulation of visual perception by basal forebrain cholinergic neurons. *Nature Neuroscience*, 16(12):1857–1863.

- Piscopo, D. M., El-Danaf, R. N., Huberman, A. D., and Niell, C. M. (2013). Diverse Visual Features Encoded in Mouse Lateral Geniculate Nucleus. *Journal of Neuroscience*, 33(11):4642–4656.
- Polack, P.-O., Friedman, J., and Golshani, P. (2013). Cellular mechanisms of brain state-dependent gain modulation in visual cortex. *Nature Neuroscience*, 16(9):1331–1339.
- Poort, J., Khan, A. G., Pachitariu, M., Nemri, A., Orsolich, I., Krupic, J., Bauza, M., Sahani, M., Keller, G. B., Mrsic-Flogel, T. D., and Hofer, S. B. (2015). Learning Enhances Sensory and Multiple Non-sensory Representations in Primary Visual Cortex. *Neuron*, 86(6):1478–1490.
- Posner, M. I. (1980). Orienting of Attention. *Quarterly Journal of Experimental Psychology*, 32(1):3–25.
- Przybylski, A. W., Gaska, J. P., Foote, W., and Pollen, D. A. (2000). Striate cortex increases contrast gain of macaque LGN neurons. *Visual Neuroscience*, 17(4):485–494.
- Radnikow, G. and Feldmeyer, D. (2018). Layer- and Cell Type-Specific Modulation of Excitatory Neuronal Activity in the Neocortex. *Frontiers in Neuroanatomy*, 12:1.
- Rao, R. P. N. and Ballard, D. H. (1999). Predictive coding in the visual cortex: A functional interpretation of some extra-classical receptive-field effects. *Nature Neuroscience*, 2(1):79–87.
- Resulaj, A., Ruediger, S., Olsen, S. R., and Scanziani, M. (2018). First spikes in visual cortex enable perceptual discrimination. *eLife*, 7:e34044.
- Rieke, F., Bodnar, D., and Bialek, W. (1995). Naturalistic stimuli increase the rate and efficiency of information transmission by primary auditory afferents. *Proceedings of the Royal Society of London. Series B: Biological Sciences*, 262(1365):259–265.
- Rikhye, R. V. and Sur, M. (2015). Spatial Correlations in Natural Scenes Modulate Response Reliability in Mouse Visual Cortex. *Journal of Neuroscience*, 35(43):14661–14680.

- Rockland, K. S. and Knutson, T. (2000). Feedback connections from area MT of the squirrel monkey to areas V1 and V2. *Journal of Comparative Neurology*, 425(3):345–368.
- Román Rosón, M., Bauer, Y., Kotkat, A. H., Berens, P., Euler, T., and Busse, L. (2019). Mouse dLGN Receives Functional Input from a Diverse Population of Retinal Ganglion Cells with Limited Convergence. *Neuron*, 102(2):462–476.
- Saleem, A. B., Diamanti, E. M., Fournier, J., Harris, K. D., and Carandini, M. (2018). Coherent encoding of subjective spatial position in visual cortex and hippocampus. *Nature*, 562(7725):124–127.
- Schneider, K. A. and Kastner, S. (2009). Effects of Sustained Spatial Attention in the Human Lateral Geniculate Nucleus and Superior Colliculus. *Journal of Neuroscience*, 29(6):1784–1795.
- Schröder, S., Steinmetz, N. A., Krumin, M., Pachitariu, M., Rizzi, M., Lagnado, L., Harris, K. D., and Carandini, M. (2020). Arousal Modulates Retinal Output. *Neuron*, 107(3):487–495.
- Serre, T., Kreiman, G., Kouh, M., Cadieu, C., Knoblich, U., and Poggio, T. (2007). A quantitative theory of immediate visual recognition. In *Progress in Brain Research*, volume 165, pages 33–56. Elsevier.
- Sherman, S. (2001). Tonic and burst firing: Dual modes of thalamocortical relay. *Trends in Neurosciences*, 24(2):122–126.
- Sherman, S. M. (2007). The thalamus is more than just a relay. *Current Opinion in Neurobiology*, 17(4):417–422.
- Sherman, S. M. and Guillery, R. W. (1996). Functional organization of thalamocortical relays. *Journal of Neurophysiology*, 76(3):1367–1395.
- Sherman, S. M. and Guillery, R. W. (1998). On the actions that one nerve cell can have on another: Distinguishing ”drivers” from ”modulators”. *Proceedings of the National Academy of Sciences*, 95(12):7121–7126.
- Sherman, S. M. and Guillery, R. W. (2002). The role of the thalamus in the flow of information to the cortex. *Philosophical Transactions of the Royal Society of London. Series B: Biological Sciences*, 357(1428):1695–1708.

- Shu, Y., Hasenstaub, A., Badoual, M., Bal, T., and McCormick, D. A. (2003). Barrages of Synaptic Activity Control the Gain and Sensitivity of Cortical Neurons. *Journal of Neuroscience*, 23(32):10388–10401.
- Shuler, M. G. (2006). Reward Timing in the Primary Visual Cortex. *Science*, 311(5767):1606–1609.
- Siegle, J. H., Jia, X., Durand, S., Gale, S., Bennett, C., Graddis, N., Heller, G., Ramirez, T. K., Choi, H., Luviano, J. A., Groblewski, P. A., Ahmed, R., Arkhipov, A., Bernard, A., Billeh, Y. N., Brown, D., Buice, M. A., Cain, N., Caldejon, S., Casal, L., Cho, A., Chvilicek, M., Cox, T. C., Dai, K., Denman, D. J., de Vries, S. E. J., Dietzman, R., Esposito, L., Farrell, C., Feng, D., Galbraith, J., Garrett, M., Gelfand, E. C., Hancock, N., Harris, J. A., Howard, R., Hu, B., Hytnen, R., Iyer, R., Jessett, E., Johnson, K., Kato, I., Kiggins, J., Lambert, S., Lecoq, J., Ledochowitsch, P., Lee, J. H., Leon, A., Li, Y., Liang, E., Long, F., Mace, K., Melchior, J., Millman, D., Mollenkopf, T., Nayan, C., Ng, L., Ngo, K., Nguyen, T., Nicovich, P. R., North, K., Ocker, G. K., Ollerenshaw, D., Oliver, M., Pachitariu, M., Perkins, J., Reding, M., Reid, D., Robertson, M., Ronellenfitch, K., Seid, S., Slaughterbeck, C., Stoecklin, M., Sullivan, D., Sutton, B., Swapp, J., Thompson, C., Turner, K., Wakeman, W., Whitesell, J. D., Williams, D., Williford, A., Young, R., Zeng, H., Naylor, S., Phillips, J. W., Reid, R. C., Mihalas, S., Olsen, S. R., and Koch, C. (2021). Survey of spiking in the mouse visual system reveals functional hierarchy. *Nature*, 592(7852):86–92.
- Sillito, A. M., Cudeiro, J., and Jones, H. E. (2006). Always returning: Feedback and sensory processing in visual cortex and thalamus. *Trends in Neurosciences*, 29(6):307–316.
- Sillito, A. M. and Jones, H. E. (2002). Corticothalamic interactions in the transfer of visual information. *Philosophical Transactions of the Royal Society of London. Series B: Biological Sciences*, 357(1428):1739–1752.
- Sillito, A. M., Kemp, J. A., and Berardi, N. (1983). The cholinergic influence on the function of the cat dorsal lateral geniculate nucleus (dLGN). *Brain Research*, 280(2):299–307.
- Simoncelli, E. P. and Olshausen, B. A. (2001). Natural Image Statistics and Neural Representation. *Annual Review of Neuroscience*, 24(1):1193–1216.

- Sommer, M. A. and Wurtz, R. H. (2006). Influence of the thalamus on spatial visual processing in frontal cortex. *Nature*, 444(7117):374–377.
- Spacek, M. A., Born, G., Crombie, D., Bauer, Y., Liu, X., Katzner, S., and Busse, L. (2021). Robust effects of corticothalamic feedback during naturalistic visual stimulation. *bioRxiv*.
- Spratling, M. W. (2010). Predictive Coding as a Model of Response Properties in Cortical Area V1. *Journal of Neuroscience*, 30(9):3531–3543.
- Stanisor, L., van der Togt, C., Pennartz, C. M. A., and Roelfsema, P. R. (2013). A unified selection signal for attention and reward in primary visual cortex. *Proceedings of the National Academy of Sciences*, 110(22):9136–9141.
- Stettler, D. D., Das, A., Bennett, J., and Gilbert, C. D. (2002). Lateral Connectivity and Contextual Interactions in Macaque Primary Visual Cortex. *Neuron*, 36(4):739–750.
- Stoelzel, C. R., Bereshpolova, Y., Alonso, J.-M., and Swadlow, H. A. (2017). Axonal Conduction Delays, Brain State, and Corticogeniculate Communication. *Journal of Neuroscience*, 37(26):6342–6358.
- Sundberg, S. C., Lindström, S. H., Sanchez, G. M., and Granseth, B. (2018). Cre-expressing neurons in visual cortex of Ntsr1-Cre GN220 mice are corticothalamic and are depolarized by acetylcholine. *Journal of Comparative Neurology*, 526(1):120–132.
- Swadlow, H. A. and Weyand, T. G. (1987). Corticogeniculate neurons, corticotectal neurons, and suspected interneurons in visual cortex of awake rabbits: Receptive-field properties, axonal properties, and effects of EEG arousal. *Journal of Neurophysiology*, 57(4):977–1001.
- Szabadics, J. (2006). Excitatory Effect of GABAergic Axo-Axonic Cells in Cortical Microcircuits. *Science*, 311(5758):233–235.
- Tasic, B., Menon, V., Nguyen, T. N., Kim, T. K., Jarsky, T., Yao, Z., Levi, B., Gray, L. T., Sorensen, S. A., Dolbeare, T., Bertagnolli, D., Goldy, J., Shapovalova, N., Parry, S., Lee, C., Smith, K., Bernard, A., Madisen, L., Sunkin, S. M., Hawrylycz, M., Koch, C., and Zeng, H. (2016). Adult mouse cortical cell taxonomy revealed by single cell transcriptomics. *Nature Neuroscience*, 19(2):335–346.

- Thiele, A. (2013). Muscarinic Signaling in the Brain. *Annual Review of Neuroscience*, 36(1):271–294.
- Tong, F., Nakayama, K., Moscovitch, M., Weinrib, O., and Kanwisher, N. (2000). Response Properties of the Human Fusiform Face Area. *Cognitive Neuropsychology*, 17(1-3):257–280.
- Treue, S. and Maunsell, J. H. R. (1996). Attentional modulation of visual motion processing in cortical areas MT and MST. *Nature*, 382:539–541.
- Tsumoto, T., Creutzfeldt, O. D., and Legéndy, C. R. (1978). Functional organization of the corticofugal system from visual cortex to lateral geniculate nucleus in the cat. *Experimental Brain Research*, 32(3):345–364.
- Tsumoto, T. and Suda, K. (1980). Three groups of cortico-geniculate neurons and their distribution in binocular and monocular segments of cat striate cortex. *Journal of Comparative Neurology*, 193(1):223–236.
- Turecek, R. and Trussell, L. O. (2001). Presynaptic glycine receptors enhance transmitter release at a mammalian central synapse. *Nature*, 411(6837):587–590.
- Urbain, N. and Deschenes, M. (2007). A New Thalamic Pathway of Vibrissal Information Modulated by the Motor Cortex. *Journal of Neuroscience*, 27(45):12407–12412.
- Van den Bergh, G., Zhang, B., Arckens, L., and Chino, Y. M. (2010). Receptive-field properties of V1 and V2 neurons in mice and macaque monkeys. *Journal of Comparative Neurology*, 518(11):2051–2070.
- Vangeneugden, J., van Beest, E. H., Cohen, M. X., Lorteije, J. A., Mukherjee, S., Kirchberger, L., Montijn, J. S., Thamizharasu, P., Camillo, D., Levelt, C. N., Roelfsema, P. R., Self, M. W., and Heimel, J. A. (2019). Activity in Lateral Visual Areas Contributes to Surround Suppression in Awake Mouse V1. *Current Biology*, 29(24):4268–4275.
- Vélez-Fort, M., Rousseau, C. V., Niedworok, C. J., Wickersham, I. R., Rancz, E. A., Brown, A. P., Strom, M., and Margrie, T. W. (2014). The Stimulus Selectivity and Connectivity of Layer Six Principal Cells Reveals Cortical Microcircuits Underlying Visual Processing. *Neuron*, 83(6):1431–1443.

- Vinje, W. E. and Gallant, J. L. (2000). Sparse Coding and Decorrelation in Primary Visual Cortex During Natural Vision. *Science*, 287(5456):1273–1276.
- Von Helmholtz, H. (1867). *Handbuch der physiologischen Optik: mit 213 in den Text eingedruckten Holzschnitten und 11 Tafeln*, volume 9. Voss.
- Wal, A., Klein, F. J., Born, G., Busse, L., and Katzner, S. (2021). Evaluating Visual Cues Modulates Their Representation in Mouse Visual and Cingulate Cortex. *Journal of Neuroscience*, 41(15):3531–3544.
- Walker, E. Y., Sinz, F. H., Cobos, E., Muhammad, T., Froudarakis, E., Fahey, P. G., Ecker, A. S., Reimer, J., Pitkow, X., and Tolias, A. S. (2019). Inception loops discover what excites neurons most using deep predictive models. *Nature Neuroscience*, 22(12):2060–2065.
- Wang, L. and Krauzlis, R. J. (2018). Visual Selective Attention in Mice. *Current Biology*, 28(5):676–685.
- Wang, Q. and Burkhalter, A. (2007). Area map of mouse visual cortex. *Journal of Comparative Neurology*, 502(3):339–357.
- Webb, B. S., Tinsley, C. J., Barraclough, N. E., Easton, A., Parker, A., and Derrington, A. M. (2002). Feedback from V1 and inhibition from beyond the classical receptive field modulates the responses of neurons in the primate lateral geniculate nucleus. *Visual Neuroscience*, 19(5):583–592.
- Wells, M. F., Wimmer, R. D., Schmitt, L. I., Feng, G., and Halassa, M. M. (2016). Thalamic reticular impairment underlies attention deficit in *Ptchd1Y/-* mice. *Nature*, 532(7597):58–63.
- Wickersham, I. R., Finke, S., Conzelmann, K.-K., and Callaway, E. M. (2007). Retrograde neuronal tracing with a deletion-mutant rabies virus. *Nature Methods*, 4(1):47–49.
- Wiegert, J. S., Mahn, M., Prigge, M., Printz, Y., and Yizhar, O. (2017). Silencing Neurons: Tools, Applications, and Experimental Constraints. *Neuron*, 95(3):504–529.

- Wikipedia contributors (2021). Andromeda galaxy — Wikipedia, the free encyclopedia. https://en.wikipedia.org/w/index.php?title=Andromeda_Galaxy&oldid=1032624178. [Online; accessed 15-July-2021].
- Wimmer, R. D., Schmitt, L. I., Davidson, T. J., Nakajima, M., Deisseroth, K., and Halassa, M. M. (2015). Thalamic control of sensory selection in divided attention. *Nature*, 526(7575):705–709.
- Winer, J. A., Miller, L. M., Lee, C. C., and Schreiner, C. E. (2005). Auditory thalamo-cortical transformation: Structure and function. *Trends in Neurosciences*, 28(5):255–263.
- Wolfart, J., Debay, D., Le Masson, G., Destexhe, A., and Bal, T. (2005). Synaptic background activity controls spike transfer from thalamus to cortex. *Nature Neuroscience*, 8(12):1760–1767.
- Wörgötter, F., Nelle, E., Li, B., and Funke, K. (1998). The influence of corticofugal feedback on the temporal structure of visual responses of cat thalamic relay cells. *Journal of Physiology*, 509(3):797–815.
- Xue, J., Carney, T., Ramoa, A., and Freeman, R. (1988). Binocular interaction in the perigeniculate nucleus of the cat. *Experimental Brain Research*, 69(3).
- Yizhar, O., Fenno, L. E., Davidson, T. J., Mogri, M., and Deisseroth, K. (2011). Optogenetics in Neural Systems. *Neuron*, 71(1):9–34.
- Zhang, F., Gradinaru, V., Adamantidis, A. R., Durand, R., Airan, R. D., de Lecea, L., and Deisseroth, K. (2010). Optogenetic interrogation of neural circuits: Technology for probing mammalian brain structures. *Nature Protocols*, 5(3):439–456.
- Zhang, S., Xu, M., Kamigaki, T., Do, J. P. H., Chang, W.-C., Jenvay, S., Miyamichi, K., Luo, L., and Dan, Y. (2014). Long-range and local circuits for top-down modulation of visual cortex processing. *Science*, 345(6197):660–665.
- Zhang, Y., Suga, N., and Yan, J. (1997). Corticofugal modulation of frequency processing in bat auditory system. *Nature*, 387(6636):900–903.

8 Supplements

8.1 Acknowledgements

First and foremost I would like to thank my supervisor Laura Busse for her strong support throughout the past years. Her thoughtful and motivating mentorship have made my PhD such a pleasant experience, and I am very grateful for all the opportunities she has provided me with.

Further, I would like to thank Steffen for introducing me to the beauty of behavioral experiments and for always being a reliable partner when it came to discussing the last important soccer games.

I very much appreciate having had the valuable input from my TAC-members Prof. Tobias Rose and Prof. Anton Sirota. Their expertise helped me to successfully complete my PhD-project.

I would also like to thank all members of the neurobiology department and especially all Busse lab members for their scientific input as well as for creating a very enjoyable environment.

I am grateful for having been able to complete this thesis in the excellent framework of the Graduate School for Systemic Neurosciences, and for the additional support I received from the Joachim Herz Stiftung.

Lastly, I would like to thank my friends and family.

8.2 List of Publications

Born, G.,* Schneider-Soupiadis, F. A.*, Erisken, S.*, Vaicelunaite, A., Mobarhan, M. H., Lao, C. L., Spacek, M. A., Einevoll, G. T., & Busse, L. (2021). Corticothalamic feedback sculpts visual spatial integration in mouse thalamus. *Nature Neuroscience*.

Dignath, D.*, Born, G.*, Eder, A., Topolinski, S., & Pfister, R. (2021). Imitation of action-effects increases social affiliation. *Psychological Research*, 85(5), 1922–1933.

Spacek, M. A., Born, G., Crombie, D., Bauer, Y., Liu, X., Katzner, S. A., & Busse, L. (2021). Robust effects of cortical feedback on thalamic firing mode during naturalistic stimulation. *bioRxiv*, 776237.

Wal, A., Klein, F. J., Born G., Busse, L., & Katzner, S. (2021). Evaluating visual cues modulates their representation in mouse visual and cingulate cortex. *Journal of Neuroscience*, 41(15), 3531–3544.

Katzner, S., Born, G., & Busse, L. (2019). V1 microcircuits underlying mouse visual behavior. *Current Opinion in Neurobiology*, 58, 191–198.

8.3 Affidavit

Eidesstattliche Versicherung/Affidavit

Hiermit versichere ich an Eides statt, dass ich die vorliegende Dissertation "The Effect of Feedback on Sensory Processing in the Mouse Early Visual System" selbstständig angefertigt habe, mich außer der angegebenen keiner weiteren Hilfsmittel bedient und alle Erkenntnisse, die aus dem Schrifttum ganz oder annähernd übernommen sind, als solche kenntlich gemacht und nach ihrer Herkunft unter Bezeichnung der Fundstelle einzeln nachgewiesen habe.

I hereby confirm that the dissertation "The Effect of Feedback on Sensory Processing in the Mouse Early Visual System" is the result of my own work and that I have only used sources or materials listed and specified in the dissertation.

München, den
Munich, date

Unterschrift
Signature

8.4 Author Contributions

Born, G.,* Schneider-Soupiadis, F. A.*, Erisken, S.*, Vaicelunaite, A., Mobarhan, M. H., Lao, C. L., Spacek, M. A., Einevoll, G. T., & Busse, L. (2021). Corticothalamic feedback sculpts visual spatial integration in mouse thalamus. *Nature Neuroscience*.

Laura Busse, Sinem Erisken, Gregory Born, Felix A. Schneider-Soupiadis and Agne Vaiceliunaite conceptualized the study. Milad H. Mobarhan and Gaute T. Einevoll developed the methodology. Gregory Born, Sinem Erisken, Felix A. Schneider-Soupiadis, Martin A. Spacek, Mobarhan H. Milad and Laura Busse developed the software. Gregory Born, Felix A. Schneider-Soupiadis, Sinem Erisken and Laura Busse performed the formal analysis. Gregory Born, Felix A. Schneider-Soupiadis, Sinem Erisken, Agne Vaiceliunaite and Martin A. Spacek performed the experimental investigations. Chu Lan Lao provided resources. Martin A. Spacek, Gregory Born, Sinem Erisken, Laura Busse and Felix A. Schneider-Soupiadis curated the data. Gregory Born, Sinem Erisken, Felix A. Schneider-Soupiadis and Laura Busse wrote the original draft. All authors wrote and edited the manuscript. Gregory Born, Felix A. Schneider-Soupiadis, Sinem Erisken and Laura Busse visualized the data. Laura Busse supervised the project, and Laura Busse and Gregory Born acquired funding.

Spacek, M. A., Born, G., Crombie, D., Bauer, Y., Liu, X., Katzner, S. A., & Busse, L. (2021). Robust effects of cortical feedback on thalamic firing mode during naturalistic stimulation. *bioRxiv*, 776237.

Laura Busse and Martin A. Spacek conceptualized the study. Martin A. Spacek and Davide Crombie developed the methodology. Martin A. Spacek, Steffen Katzner, Gregory Born, Davide Crombie, Yannik Bauer, and Xinyu Liu wrote the software. Steffen Katzner performed the formal analysis. Martin A. Spacek and Yannik Bauer performed the investigation. Martin A. Spacek, Gregory Born, Davide Crombie, and Laura Busse curated the data. Laura Busse and Gregory Born wrote the original draft. Laura Busse, Steffen Katzner, Martin A. Spacek, Gregory Born, and Davide Crombie reviewed and edited the manuscript. Martin A. Spacek, Gregory Born, and Steffen Katzner visualized the data. Laura Busse acquired funding, supervised, and administered the project.

Wal, A., Klein, F. J., Born G., Busse, L., & Katzner, S. (2021). Evaluating visual cues modulates their representation in mouse visual and cingulate cortex. *Journal of Neuroscience*, 41(15), 3531–3544.

Alexandra Wal, Frederike J. Klein, and Gregory Born performed the research. Alexandra Wal, Frederike J. Klein, Gregory Born, and Laura Busse edited the paper. Laura Busse and Steffen Katzner designed the research. Steffen Katzner analyzed the data and wrote the paper.

Katzner, S., Born, G., & Busse, L. (2019). V1 microcircuits underlying mouse visual behavior. *Current Opinion in Neurobiology*, 58, 191–198.

Laura Busse, and Steffen Katzner conceptualized the paper. Laura Busse, Steffen Katzner, and Gregory Born wrote the original draft. Laura Busse and Steffen Katzner edited the manuscript. Laura Busse, Steffen Katzner, and Gregory Born visualized the data. Laura Busse supervised the project.

Gregory Born

Prof. Dr. Laura Busse

Place, date

Place, date

Felix A. Schneider-Soupiadis

Dr. Sinem Erisken

Place, date

Place, date